ISBN 91-628-2804-5
LUNFD6/(NFFL-7150) 1997

The search for a standard model Higgs at the LHC and electron identification using transition radiation in the ATLAS tracker

Thesis Submitted for the Degree of
Doctor of Philosophy in Physics
by

Ulrik Egede

DEPARTMENT OF PHYSICS, LUND UNIVERSITY, 1998

ISBN 91-628-2804-5
LUNFD6/(NFFL-7150) 1997

The search for a standard model Higgs at the LHC and electron identification using transition radiation in the ATLAS tracker

By due permission of the faculty of mathematics and natural sciences at Lund University, to be publicly discussed at the lecture hall B of the Department of Physics, January 16th 1998 at 2.15pm for the degree of Doctor of Philosophy

by

Ulrik Egede

Elementary Particle Physics,
Lund University,
Box 118,
SE-221 00 Lund,
Sweden.

Contents

Abstract

The Large Hadron Collider (LHC) will be ready for proton-proton collisions in the year 2005 and the ATLAS detector will be one of the two experiments at the LHC which will explore a new and higher energy range for particle physics. In this thesis, an analysis of the power of the ATLAS detector to detect a Standard Model Higgs boson has been performed. It is shown that it will be possible to discover a Higgs particle across the complete mass range from the lower limit defined by the reach of the LEP2 collider experiments to the upper theoretical limit around 1 TeV. The role of the inner tracking detector of ATLAS for the detection of conversions and the identification of the primary vertex in the detection of a Higgs particle in the $H \to \gamma\gamma$ decay channel is demonstrated with a detailed detector simulation. The identification of a 1 TeV Higgs particle requires a good understanding of both the signal and the backgrounds. The related uncertainties are covered in detail and it is shown that the Higgs can be identified in the $H \to W^+W^- \to l\nu jj$, $H \to ZZ \to l^+l^-\nu\bar{\nu}$ and $H \to ZZ \to l^+l^-jj$ decay channels. The Transition Radiation Tracker (TRT) is a combined tracking an electron identification device which will be a part of the inner tracking detector of ATLAS. For a prototype of the TRT the electron identification performance is analysed and it is shown that the full scale TRT together with the calorimeters will provide the electron identification power required for a clean electron and photon signal at the LHC. For the prototype a rejection factor of 100 against pions was achieved with an electron efficiency of 90%. The importance of the TRT for a clear detection of a Higgs particle is demonstrated.

Preface

This thesis covers the topic of Higgs physics at the Large Hadron Collider and the development of the Transition Radiation Tracker (TRT) for the ATLAS experiment. It covers the work I have performed in the period from December 1993 to November 1997 at the Department of Elementary Particle Physics in Lund as a member of the ATLAS collaboration.

Following a short review in chapter 1 of the new physics accessible with the Large Hadron Collider, chapter 2 is a general description of the Higgs theory within the Standard Model. The more specific parts of the theory concerning the dominant production mechanisms and experimentally favoured decay modes are covered as well.

The theory behind the creation and detection of transition radiation is treated in chapter 3 followed in chapter 4 by a description of the ATLAS detector with special emphasis on the TRT.

The first analysis part of the thesis is on the electron identification power of a prototype of the TRT placed in a testbeam. The description of the testbeam, the treatment of the data and the results on electron identification are covered in chapter 5 and has in addition been submitted for publication [1].

The second analysis part is on Higgs simulations in the ATLAS detector. Chapter 6 describes the general simulation framework of physics simulations with the ATLAS detector and the tools developed especially for the Higgs analysis presented in this thesis. Two extreme points for the mass of the Higgs particle was selected for a detailed analysis.

In chapter 7 a Higgs particle with mass around 100 GeV decaying to two photons was analysed. The analysis focused on the use of the Inner Detector to improve the mass resolution, and to reject the background from QCD-jet events.

In chapter 8 the decay modes of a Higgs particle with a mass of 1 TeV are reviewed and the backgrounds are analysed with special attention to the theoretical uncertainties. New to the analysis in ATLAS is a proper evaluation of the effect of pile-up on tag jets and the use of a charged track veto in the central detector region.

Significant parts of the work presented in this thesis has gone into the ATLAS Technical Proposal [2], the ATLAS Calorimeter Technical Design Report [3] and the ATLAS Inner Detector Technical Design Report [4, 5]. Therefore, it is a part of the

documentation that underwent the LHCC[1] referee process, and contributed to the approval of the ATLAS detector.

The work presented can be assumed to have been performed in its majority by the author unless specific citations are provided. Throughout this thesis equations and results are presented in natural units where $c = 1$ and $\hbar = 1$. For physics processes where either of the massive W or Z vector bosons participate the letter V is used.

[1] The Large Hadron Collider Committee, the LHCC makes recommendations to the CERN Research Board.

Chapter 1

The Large Hadron Collider

The Large Hadron Collider (LHC) is the next generation collider at CERN. It will be built in the 27 km tunnel where the LEP collider is situated today and will start operation in June 2005. The collider will have two counter-rotating proton beams each with an energy of 7 TeV giving a total collision energy of 14 TeV. The LHC will take advantage of the existing accelerator complex at CERN to create the proton beams and accelerate them.

The Large Hadron Collider is the natural choice as the next step for particle physics. For the last many years discoveries of new particles have been dominated by hadron colliders extending the accessible energy range upwards. In this way the LHC can be seen as a discovery machine with a dynamic range of discovery from energy scales of 5 MeV in the case of B-physics to a few TeV for the discovery of new vector bosons or quark compositeness.

The theory for electroweak interactions had great success with the prediction and finally the discovery of the W and Z vector bosons at the proton-antiproton Sp$\bar{\text{p}}$S collider at CERN. In the electroweak theory it is, however, not sufficient with the four vector bosons responsible for the electroweak interactions since all particles in such a theory will be massless. The vector bosons can acquire mass by introducing a scalar doublet to break the symmetry between the four vector bosons. By assigning each fermion a coupling to the scalar field proportional to the mass of the particle the same scalar field can describe the masses of all known particles.

With the scalar field, the Higgs field, there is associated a Higgs particle which, if discovered, will be strong proof of this mass creation theory. However, the Higgs particle has not been seen and the field is open for discoveries at the LHC. While the standard model is a kind of minimal model there are many other models within the branch of supersymmetric theories which predict a forest of new particles within the range of the LHC.

To extent the reach of new physics to as high mass scales as possible and to increase the production cross section of the processes of interest as seen in fig. 1.1 it would be preferable to increase the centre of mass energy above the 14 TeV of the LHC. The magnetic field strength required to force the particle beams around

in the collider increases linearly with the beam energy. The highest operational magnetic field for affordable superconducting magnets is 8.65 T which together with the requirement that the LHC has to fit inside the existing LEP tunnel gives the maximum energy of 7 TeV energy for the beams.

With the beam energy limited, another way to increase the rate of events with interesting physics is to increase the luminosity. The event rate of a specific process is given as

$$n_x = \sigma_x \mathcal{L} \tag{1.1}$$

where $\mathcal{L}$ is the luminosity and σ_x the cross section of the process. The cross section is at a given centre of mass energy a fixed number dependent on the specific physics process only while the luminosity is controlled by the parameters of the collider. The luminosity is for a collider

$$\mathcal{L} = \frac{1}{4\pi} \frac{N^2 f}{t A_{\mathrm{T}}}, \tag{1.2}$$

where N is the number of protons in each bunch, t the time between individual bunches, A_{T} the transverse dimension of the bunches at the interaction points and f the fraction of bunch positions actually containing protons.

The time between the bunches is limited by the requirement that there should be no additional interactions on each side of the interaction region. For the LHC the bunch crossing time will be 25 ns corresponding to a bunch separation of 7.5 m. The transverse dimensions of the beam can at the interaction point be squeezed down to 15 μm. To be able to fill new bunches into the LHC and operate the beam dump it is necessary to order the proton bunches in bunch trains followed by some empty bunches. In total 2835 of the 3557 available spaces with 25 ns separation will contain protons corresponding to $f = 0.80$.

The only remaining way to increase the luminosity is to increase the number of protons in each bunch. This is limited by electromagnetic forces between the colliding bunches.

The maximal luminosity achievable will be close to $2 \cdot 10^{34}$ cm^{-2}s^{-1} but to be in a stable region the nominal luminosity is fixed at 10^{34} cm^{-2}s^{-1}. For the first years of running it is foreseen to run at low luminosity $\mathcal{L}_{\mathrm{low}} = 10^{33}$ cm^{-2}s^{-1} and only gradually increasing it to the high luminosity $\mathcal{L}_{\mathrm{high}} = 10^{34}$ cm^{-2}s^{-1}.

The requirements on the luminosity from physics can be seen from fig. 1.1. The number of observed events is given as

$$n_{\mathrm{obs}} = \mathcal{L}\sigma \; Br \; T\varepsilon, \tag{1.3}$$

with T the effective time the machine is running, Br the branching ratio of the selected decay and ε the detection efficiency. A standard year at the LHC is supposed to give a total running time of $T = 10^7$ s. Taking as an example the creation of a 500 GeV Higgs particle, the cross section is 3 pb and the branching ratio for the favourable H $\rightarrow$ ZZ decay with the Z bosons decaying to leptons is around 0.1%. At low luminosity this gives just below 50 events a year before taking any detection

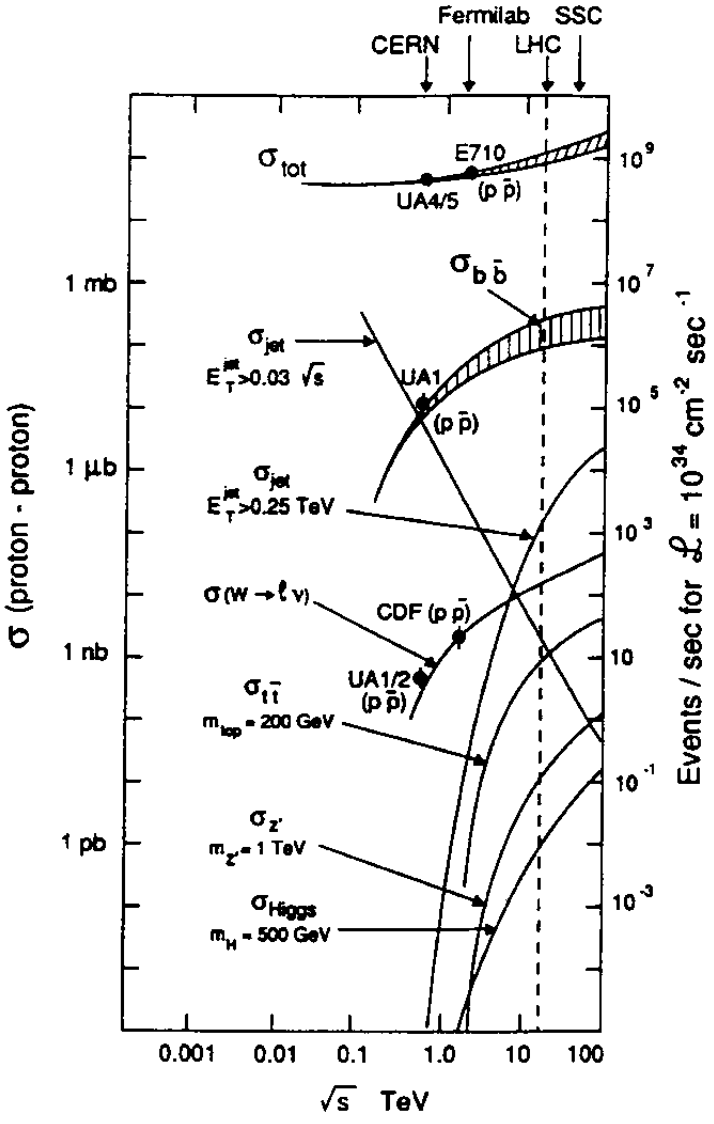

Figure 1.1: Expected cross section as a function of energy in the centre of mass system for proton-proton collisions. Note the difference between the total inelastic cross section and the cross section for physics processes like Higgs production. From [6].

efficiencies into account. Clearly a luminosity of 10^{34} cm^{-2}s^{-1} or higher is required to identify a Higgs particle in this decay mode. The first years with the LHC can, however, be used for physics processes with higher cross sections such as B-physics, studies of the top quark and searches for supersymmetric particles.

The high requirement on luminosity is the reason for the choice of a proton-proton collider. For while a proton-antiproton collider has the advantage that both counter-rotating beams can be kept in the same beam pipe, producing the enormous amounts of antiprotons required for the high luminosity is not realistic and would be more expensive than the proton-proton solution with separate beam pipes. The charge asymmetry introduced with a proton-proton collider is not a serious problem for the physics analysis.

The number of simultaneous proton-proton inelastic interactions taken place in each bunch crossing is given as a Poisson distribution with an average of

$$<n> = \frac{\mathcal{L}\sigma_{\mathrm{ie}}t}{f}. \tag{1.4}$$

At high luminosity this gives an average of 22 simultaneous inelastic interactions in each event with an expected value of the inelastic cross section $\sigma_{\mathrm{ie}} = 70$ mb. Each of the interactions give rise to many tracks from the interaction region thus giving events with many hundred tracks. The cross section from elastic scattering of the protons and diffractive events will not be seen by the detectors as it is only the inelastic scatterings that give rise to particles at sufficient high angles with respect to the beam axis.

The events with production of high mass objects such as vector bosons or Higgs particles are often called physics events. The term is misleading since all interactions of course contain physics but the dominating QCD-jet processes with low energy transfer are believed to contain little unknown physics and are thus regarded as background without any (new) physics information.

The difference between the total cross section and the cross section of the interesting physics is in many cases greater than ten orders of magnitude. The absolute majority of interactions, called minimum bias events, are fusion processes of gluons or quarks with a small energy transfer resulting in events with many hadrons of low momentum and nothing else. To identify the interesting events in the background requires some clear signatures. One of these is the identification of leptons with high transverse momentum[1]. Leptons have a very low rate in minimum bias events but can be found in selected decay modes of most physics processes. The strong need for lepton identification has driven the design of the LHC detectors as will be seen in chapter 4.

[1]Transverse momentum, p_{T}, is throughout this thesis defined as the momentum perpendicular to the *beam* axis of the LHC.

Chapter 2

Higgs physics at the LHC

The Standard Model of particle physics developed about 25 years ago has been a major success. With the prediction of the neutral currents and the masses of the heavy vector bosons some of the major elements of the theory were demonstrated. On the level of precision physics, the last many years of data produced by LEP1 at the Z^0 resonance in e^+e^- collisions, has shown that the standard model also describe the different radiative corrections with remarkable accuracy. There are at present no experimental results which are not satisfactory described by the Standard Model.

This chapter will treat the physics behind a Standard Model Higgs sector. After a short introduction to the Higgs mechanism the main part of the chapter will be aimed at the production and decay channels of a Higgs particle produced in the proton collisions at the LHC. Some comments will be given on alternative theories extending or replacing the standard model.

2.1 The standard model Higgs

The electroweak sector of the standard model is described as a SU(2)×U(1) gauge theory. In its basic form it describes all the electroweak interactions between fermions by the exchange of massless vector bosons. No details will be given here on the basic framework of the SU(2)×U(1) theory; the derivation can be found in [7] or any other text book on quantum field theory.

The Lagrangian density of the free massless boson fields can be written as the sum of the U(1) gauge field B_μ and the three real SU(2) gauge fields W^i_μ, $i = 1, 2, 3$. It takes the form

$$\mathcal{L}^{\mathrm{B}} = -\frac{1}{4} F_{\mathrm{B}\mu\nu}(x) F^{\mu\nu}_{\mathrm{B}}(x) - \frac{1}{4} F^i_{\mathrm{W}\mu\nu}(x) F^{i\mu\nu}_{\mathrm{W}}(x), \tag{2.1}$$

where the field tensors are defined as

$$F^{\mu\nu}_{\mathrm{B}} = \partial^\nu B^\mu - \partial^\mu B^\nu \tag{2.2}$$

$$F^{i\mu\nu}_{\mathrm{W}} = \partial^\nu W^{i\mu} - \partial^\mu W^{i\nu}. \tag{2.3}$$

Through the transformation

$$\mathrm{A}_\mu = \cos\theta_\mathrm{W}\,\mathrm{B}_\mu + \sin\theta_\mathrm{W}\,\mathrm{W}^3_\mu \tag{2.4}$$

$$\mathrm{Z}_\mu = \sin\theta_\mathrm{W}\,\mathrm{B}_\mu - \cos\theta_\mathrm{W}\,\mathrm{W}^3_\mu \tag{2.5}$$

$$\mathrm{W}^\pm_\mu = \frac{1}{\sqrt{2}}\left(\mathrm{W}^1_\mu \mp \mathrm{i}\mathrm{W}^2_\mu\right) \tag{2.6}$$

where the Weinberg angle θ_W is a free parameter, the Lagrangian describing the free vector boson field can be written as

$$\mathcal{L}^\mathrm{B} = -\frac{1}{4}F_{\mu\nu}(x)F^{\mu\nu}(x) - \frac{1}{2}F^\dagger_{\mathrm{W}\mu\nu}(x)F^{\mu\nu}_\mathrm{W}(x) - \frac{1}{4}F_{\mathrm{Z}\mu\nu}(x)F^{\mu\nu}_\mathrm{Z}(x), \tag{2.7}$$

where $F^{\mu\nu}$ is now the electromagnetic field tensor and $F^{\mu\nu}_\mathrm{W}$, $F^{\mu\nu}_\mathrm{Z}$ the field tensors for the $\mathrm{W}^\pm$ and Z fields. The W and Z fields can be made massive by including the terms

$$m^2_\mathrm{W}W^\dagger_\mu(x)W^\mu(x) + \frac{1}{2}m^2_\mathrm{Z}Z_\mu(x)Z^\mu(x). \tag{2.8}$$

Introducing masses in this way, however, causes the Lagrangian density no longer to be invariant under the U(1) gauge transformation

$$\psi(x) \to \psi'(x) = e^{\mathrm{i}Y\xi(x)}\psi(x) \tag{2.9}$$

where ψ is the different boson fields with weak hypercharge Y and $\xi(x)$ any differentiable function. The Lagrangian including the mass terms will neither be invariant under SU(2) gauge transformations. Ignoring the lack of Gauge invariance results in a theory which is not renormalisable and thus only adequate for describing tree level processes.

Spontaneous symmetry breaking is the way to give the W and Z vector bosons mass while keeping the gauge theory $\mathrm{SU}(2)\times\mathrm{U}(1)$ invariant.

2.1.1 Spontaneous symmetry breaking

The Goldstone model is a simple model with spontaneous symmetry breaking. Starting with a classical theory, take a Lagrangian density

$$\mathcal{L} = \partial^\mu\varphi^*\partial_\mu\varphi - V(\varphi), \tag{2.10}$$

where φ is a complex field

$$\varphi = \frac{\sqrt{2}}{2}[\varphi_1 + \mathrm{i}\varphi_2], \tag{2.11}$$

and $V(\varphi)$ the potential energy

$$V(\varphi) = \mu^2|\varphi|^2 + \lambda|\varphi|^4. \tag{2.12}$$

The constants μ^2, λ are real with λ positive to make the total field energy bounded from below. The Lagrangian is invariant under the global U(1) transformation describing rotations in the complex plane. It should be noted that φ is a function of the spacetime coordinate x which is suppressed to simplify the notation.

Requiring that the vacuum, the lowest energy state, is invariant under Lorentz transformations and translations implies that $\varphi(x)$ is a constant in this vacuum state. Two different possibilities exist for the vacuum state depending on the parameter μ^2.

If μ^2 is positive the situation is quite normal with the minimum potential energy when $\varphi = 0$. If instead μ^2 is negative, the minimum energy no longer corresponds to a unique value of φ but is instead degenerate with the minimum as a ring in the complex plane

$$\varphi_{V_{\min}} = \sqrt{\frac{-\mu^2}{2\lambda}} e^{\mathrm{i}\theta}, \quad 0 \leq \theta < 2\pi. \tag{2.13}$$

As the Lagrangian (2.10) is invariant under rotations in the complex plane of φ each direction is equally good and setting $\theta = 0$ such that

$$\varphi_{V_{\min}} = \sqrt{\frac{-\mu^2}{2\lambda}} \equiv \frac{v}{\sqrt{2}} \tag{2.14}$$

can be done without loss of generalisation. A theory where the vacuum has less symmetry than the Lagrangian is called a theory with spontaneous symmetry breaking. The deviation from the chosen minimum can be described by the two real fields σ and η defined through

$$\varphi = \frac{\sqrt{2}}{2}[v + \sigma + \mathrm{i}\eta]. \tag{2.15}$$

The Lagrangian (2.10) rewritten in terms of σ and η is

$$\begin{aligned} \mathcal{L} = &\frac{1}{2}\partial^\mu\sigma\partial_\mu\sigma - \lambda v^2\sigma^2 + \frac{1}{2}\partial^\mu\eta\partial_\mu\eta \\ &- \lambda v\sigma[\sigma^2 + \eta^2] - \frac{1}{4}\lambda[\sigma^2 + \eta^2]^2 + c \end{aligned} \tag{2.16}$$

with c a constant of interest only for general relativity. Taking the higher order terms as interaction terms the free Lagrangian reads

$$\mathcal{L} = \frac{1}{2}\partial^\mu\sigma\partial_\mu\sigma - \lambda v^2\sigma^2 + \frac{1}{2}\partial^\mu\eta\partial_\mu\eta. \tag{2.17}$$

It is seen that σ and η in fact are two real Klein-Gordon fields. By quantising these fields the Lagrangian (2.17) describes two different spin 0 particle fields. The σ bosons will have mass

$$m_\sigma = v\sqrt{2\lambda} \tag{2.18}$$

arising from the σ^2 term while the η bosons will be massless. The masslessness of the η bosons are a direct consequence of the minimum being degenerate. The remaining

terms from (2.16) can be treated as interactions among the σ and η particles through perturbation theory.

From the above situation it can be seen how the spontaneous symmetry breaking of the U(1) symmetry caused by the degenerate energy minimum of the Lagrangian (2.10) creates a pertubative theory with a massive scalar boson.

2.1.2 The Higgs mechanism

What is called the Higgs mechanism is the extension of the spontaneous symmetry breaking to create massive vector bosons in a gauge invariant theory. Here it will be shown for a U(1) theory. The idea is to replace the normal derivative in (2.10) with the covariant derivative

$$D_\mu = \partial_\mu + \mathrm{i}qA_\mu. \tag{2.19}$$

Adding the Lagrangian of the free gauge field A_μ, results in

$$\mathcal{L} = D^\mu\varphi^* D_\mu\varphi - V(\varphi) - \frac{1}{4}F_{\mu\nu}F^{\mu\nu}. \tag{2.20}$$

This new Lagrangian is now invariant under the U(1) gauge transformation

$$\begin{aligned} \varphi(x) &\to \varphi'(x) = \varphi(x)e^{\mathrm{i}q\xi(x)} \\ A_\mu(x) &\to A'_\mu(x) = A_\mu(x) + \partial_\mu\xi(x), \end{aligned} \tag{2.21}$$

with ξ any differentiable function. Continuing in exactly the same way as for the Goldstone model with a negative μ^2 and expressing the Lagrangian in terms of the variables σ and η as defined in (2.15) the result is

$$\begin{aligned} \mathcal{L} = &\frac{1}{2}\partial^\mu\sigma\partial_\mu\sigma - \lambda v^2\sigma^2 + \frac{1}{2}\partial^\mu\eta\partial_\mu\eta \\ &- \frac{1}{4}F_{\mu\nu}F^{\mu\nu} + \frac{1}{2}q^2v^2A_\mu A^\mu \\ &+ qvA^\mu\partial_\mu\eta \\ &+ \text{higher order terms.} \end{aligned} \tag{2.22}$$

The Lagrangian clearly has a massive vector boson field A and two scalar fields σ, η with η massless, but unfortunately also a term $A^\mu\partial_\mu\eta$ which does not fit in. It can not be understood as a pertubative interaction term since it is quadratic in the fields as the terms for the free field are. However, a careful analysis [7] shows that the Lagrangian (2.22) has one degree of freedom too much. This extra degree of freedom can be absorbed by choosing a specific gauge, ie. performing a gauge transformation of the type (2.21), where $\varphi(x)$ has the form

$$\varphi(x) = \frac{\sqrt{2}}{2}[v + \sigma(x)]. \tag{2.23}$$

Such a gauge transformation is always possible and the chosen gauge is called the unitary gauge. In this gauge the η field disappears and what is left is the Lagrangian

$$\begin{aligned}\mathcal{L} = & \frac{1}{2}\partial^\mu\sigma\partial_\mu\sigma - \lambda v^2\sigma^2 \\ & - \frac{1}{4}F_{\mu\nu}F^{\mu\nu} + \frac{1}{2}q^2v^2A_\mu A^\mu \\ & + \text{higher order terms.}\end{aligned} \tag{2.24}$$

In summary, it is seen that a complex scalar field and a massless vector field, both with two degrees of freedom, in (2.20) as a result of the Higgs mechanism was transformed in (2.24) into one real scalar field with one degree of freedom and a massive vector boson field with 3 degrees of freedom. A massless spin 1 particle has two transverse polarised states while a massive spin 1 particle has an additional longitudinal polarised state. It should be noted that the η field only disappears if the η bosons are massless. As shown in section 2.1.1 this requires the vacuum state to be degenerate ie. the Higgs mechanism will only work with a degenerate vacuum.

The Higgs mechanism was demonstrated here for a U(1) gauge invariant Lagrangian. To extend it to the SU(2)×U(1) gauge invariant Lagrangian of the electroweak theory is relatively simple. The starting point is a Lagrangian with a complex scalar doublet and four massless vector bosons. Counting degrees of freedom gives four from the scalars and eight from the vector bosons.

Through the Higgs mechanism the Lagrangian is transformed into one real scalar, three massive vector and one massless vector boson. The massless vector boson is of course to be identified with the photon and the single remaining scalar with the Higgs boson. Counting degrees of freedom again gives one from the Higgs, two from the photon and nine from the massive vector bosons, again adding up to twelve.

Introducing the masses of the vector bosons with one doublet of complex scalars is the simplest scenario, in principle an infinite number of scalar fields can be introduced. The simplest supersymmetric models instead have five scalar fields left after the Higgs mechanism: a doublet of charged scalars, two neutral scalars and one neutral pseudoscalar.

The masses of the particles in the standard model are given as

$$m_{\mathrm{H}} = \sqrt{2\lambda}v, \quad m_{\mathrm{W}} = \frac{1}{2}vg, \quad m_{\mathrm{Z}} = \frac{m_{\mathrm{W}}}{\cos\theta_{\mathrm{W}}}, \tag{2.25}$$

where g is the weak coupling constant and θ_{W} the Weinberg angle. Using

$$v^2 = \frac{\sqrt{2}}{2G_{\mathrm{f}}}, \quad \alpha = \frac{g^2\sin^2\theta_{\mathrm{W}}}{4\pi}, \tag{2.26}$$

where G_{F} is the Fermi constant and α the fine structure constant, the vector boson masses can be expressed through G_{F}, α and $\sin\theta_{\mathrm{W}}$. With the Fermi constant measured from the muon lifetime and the Weinberg angle from the relative cross sections of neutral current ($\nu_\mu + \mathrm{p} \to \nu_\mu + \mathrm{X}$) and charge current ($\nu_\mu + \mathrm{p} \to \mu + \mathrm{X}$) processes it was possible to predict the masses of the vector bosons. Their discovery at the UA1

and UA2 experiments at the CERN Sp$\bar{\text{p}}$S was a great victory for the electroweak theory.

The vacuum expectation value is easily extracted as

$$v = \frac{2m_{\mathrm{W}}}{g} = 246 \text{ GeV}, \tag{2.27}$$

but there is no way to measure the value of λ before a discovery of the Higgs. As discussed in section 2.5 self consistency of the standard model sets an upper limit on the Higgs mass around 1 TeV. Experimental Higgs mass limits are discussed in section 2.4.

For reference the full electroweak and Higgs sector part of the standard model Lagrangian is given. It takes the form

$$\mathcal{L} = \mathcal{L}_0 + \mathcal{L}_{\mathrm{FB}} + \mathcal{L}_{\mathrm{FH}} + \mathcal{L}_{\mathrm{BB}} + \mathcal{L}_{\mathrm{BH}} + \mathcal{L}_{\mathrm{HH}} \tag{2.28}$$

where $\mathcal{L}_0$ is the Lagrangian of the free fields

$$\begin{aligned}
\mathcal{L}_0 = {} & \bar{\psi}_{\mathrm{f}}(\mathrm{i}\partial\!\!\!/ - m_{\mathrm{f}})\psi_{\mathrm{f}} \\
& - \frac{1}{4}F_{\mu\nu}F^{\mu\nu} \\
& - \frac{1}{2}F^{\dagger}_{\mathrm{W}\mu\nu}F^{\mu\nu}_{\mathrm{W}} + m^2_{\mathrm{W}}W^{\dagger}_{\mu}W^{\mu} \\
& - \frac{1}{4}F_{\mathrm{Z}\mu\nu}F^{\mu\nu}_{\mathrm{Z}} + \frac{1}{2}m^2_{\mathrm{Z}}Z_{\mu}Z^{\mu} \\
& + \frac{1}{2}\partial^{\mu}\sigma\partial_{\mu}\sigma - \frac{1}{2}m^2_{\mathrm{H}}\sigma^2,
\end{aligned} \tag{2.29}$$

and the remaining terms the interaction between fermions and bosons, fermions and the Higgs, bosons and bosons, bosons and the Higgs and finally Higgs self interactions. Only the fermion Higgs interaction term

$$\mathcal{L}_{\mathrm{FH}} = -\frac{1}{v}m_{\mathrm{f}}\bar{\psi}_{\mathrm{f}}\psi_{\mathrm{f}}\sigma \tag{2.30}$$

which will be important later is given here. A sum over all fermions is implicitly assumed in (2.29) and (2.30) with some terms obviously disappearing if the neutrinos are massless.

A remarkable feature of introducing massive fermions in the theory is that their interaction terms in the Lagrangian become proportional to their mass as seen in (2.30). While this makes it impossible to put constraints on the Higgs mass and the fermion masses, it has the consequence that the Higgs particle will couple to the fermions in proportion to their mass. The supersymmetric extensions of the Standard Model have different predictions for the coupling constants and hence a measurement of several coupling constants can be used to look into the theory behind the Higgs mechanism.

2.2 Higgs Production

The dominating Higgs production mechanism at the LHC will be the gluon fusion process for all possible Higgs masses. Other processes with their Feynman diagrams in fig. 2.1 are also of interest because of the special signatures they can provide for the identification of the Higgs. In fig. 2.2 the cross section is shown as a function of the standard model Higgs mass. At the highest masses a significant part of the cross section is from vector boson fusion.

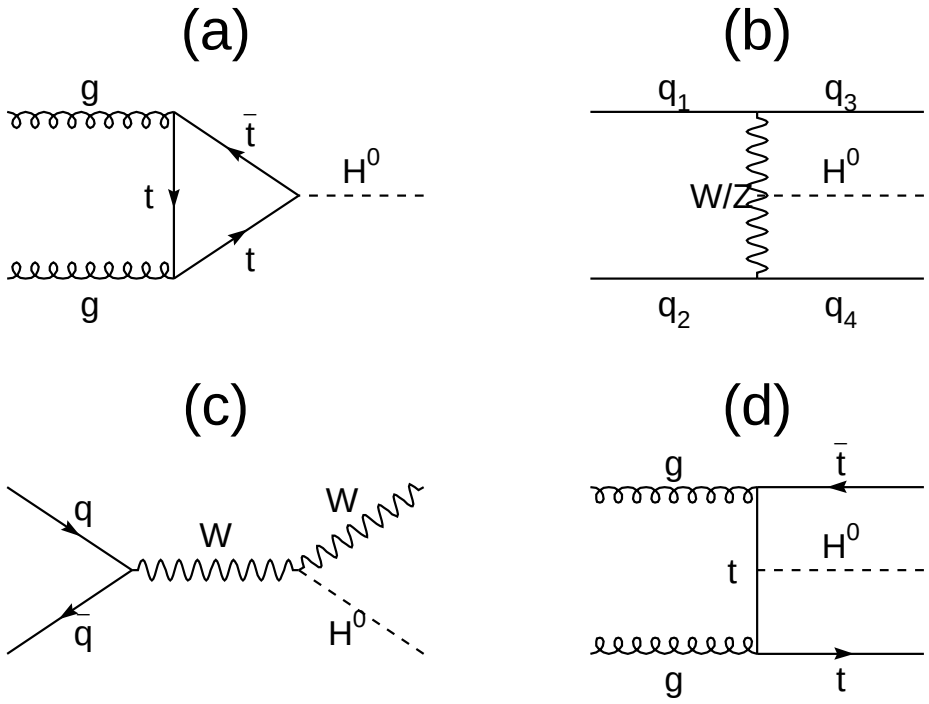

Figure 2.1: The most important processes for Higgs production at hadron colliders. Gluon fusion (a), vector boson fusion (b), Associative production with W (c) and an example of the diagrams having associative production with a top pair (d).

2.2.1 Gluon fusion

The gluon fusion process for Higgs production, shown in fig. 2.1, can be calculated from the width of the H $\rightarrow$ gg decay (section 2.3.4) and the gluon structure function. The loop is totally dominated by the top quark because of the strong Higgs coupling

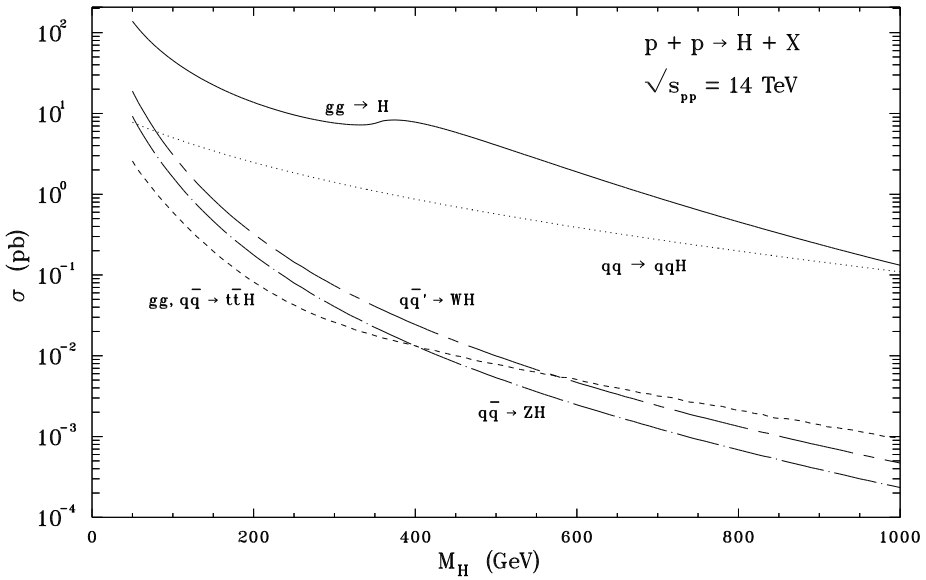

Figure 2.2: The production cross section of the standard model Higgs boson. Across the complete possible mass range the gluon fusion process is dominating. From [8].

to the heavy top quark. The cross section for the basic gluon to Higgs process is

$$\hat{\sigma}(\mathrm{gg} \to \mathrm{H}) = \frac{(2\pi)^4}{2m_\mathrm{H}^2} \int \frac{1}{(2\pi)^3} \frac{\mathrm{d}^3 p}{2E} \delta^4(p_{\mathrm{g}_1} + p_{\mathrm{g}_2} - p) |\mathcal{M}|^2 \tag{2.31}$$

$$= \frac{8\pi^2 \Gamma_{\mathrm{H}\to\mathrm{gg}}}{N_\mathrm{g}^2 m_\mathrm{H}} \int \frac{\mathrm{d}^3 p}{E} \delta^4(p_{\mathrm{g}_1} + p_{\mathrm{g}_2} - p) \tag{2.32}$$

$$= \frac{8\pi^2 \Gamma_{\mathrm{H}\to\mathrm{gg}}}{N_\mathrm{g}^2 m_\mathrm{H}} \delta(\hat{s} - m_\mathrm{H}^2) \tag{2.33}$$

with the width of the gluon decay inserted using (2.42) and (2.78), $N_\mathrm{g} = 8$ the number of different gluons and $\hat{s} = x_1 x_2 s$ the squared energy of the gluon pair[1].

To get the full cross section the gluon cross section has to be integrated with the structure functions of the gluons

$$\sigma_0(\mathrm{pp} \to \mathrm{H}) = \iint \mathrm{d}x_1 \mathrm{d}x_2 x_1 g(x_1, m_\mathrm{H}^2) x_2 g(x_2, m_\mathrm{H}^2) \hat{\sigma}(\mathrm{gg} \to \mathrm{H}). \tag{2.34}$$

The lowest order cross section given in (2.34) has large corrections from higher order QCD diagrams. The increase in cross section from higher order diagrams is

[1] The delta function is a zero width approximation of the Higgs. For a heavy Higgs it should be replaced by a Breit-Wigner distribution.

conventionally defined as the *K-factor*

$$K = \frac{\sigma_{\mathrm{HO}}}{\sigma_{\mathrm{LO}}} \tag{2.35}$$

where LO (HO) refer to lowest (higher) order results. The K-factor for gluon fusion is in [9] evaluated in a next-to-leading order calculation and gives $K = 1.5$ almost independent of the Higgs mass.

The value of the cross section including the K-factor has two main uncertainties. The first is from the gluon structure function which still has a large uncertainty in the low x region. The cross section using a large set of todays best available structure functions was calculated in [8] and their relative differences shown in fig. 2.3. It can be seen that they differ by around 20% which can be taken as the theoretical uncertainty from the gluon structure function. At the time of data taking for the LHC it can be expected to have much better structure functions available with data from HERA, the Tevatron and even the LHC itself.

The second uncertainty in the gluon fusion cross section is from corrections above the next-to-leading order. The cross section changes with the renormalisation scale μ as an effect of un-calculated higher order effects. By changing μ between $m_{\mathrm{H}}/2$ and $2m_{\mathrm{H}}$ it is in [9] concluded that the remaining uncertainties from higher order effects is below 15%.

The uncertainty in the cross section arising from uncertainties in the top quark mass are small and will be insignificant with an improved measurement of the top mass at the starting time of the LHC.

The production of the Higgs through gluon fusion is sensitive to a fourth generation of quarks. Because the Higgs couples in proportion to the fermion mass, a heavier generation of quarks is not suppressed in the process fig. 2.1a as would be expected for a loop process with a heavier particle in the loop. Including a fourth generation of very heavy quarks will more than double the cross section as shown in fig. 2.4. This has the consequence that the Higgs cross section is sensitive to a fourth generation of quarks even if the quarks are too heavy for a direct discovery at the LHC. The mass range is limited by the scale of new physics where the standard model breaks down.

2.2.2 Vector boson fusion

The process of Higgs production through vector boson fusion shown in fig. 2.1b will only be important for high Higgs masses where the coupling to longitudinal polarised vector bosons is strong (see section 2.3.1).

At the high energies where a heavy Higgs particle is created the vector bosons act essentially as massless particles and can be treated as particles present inside the colliding protons. With this simplification the full process in fig. 2.1b can be separated into a calculation of the vector boson structure function in the proton and a calculation of Higgs production in colliding vector boson beams. The method is called the effective W approximation.

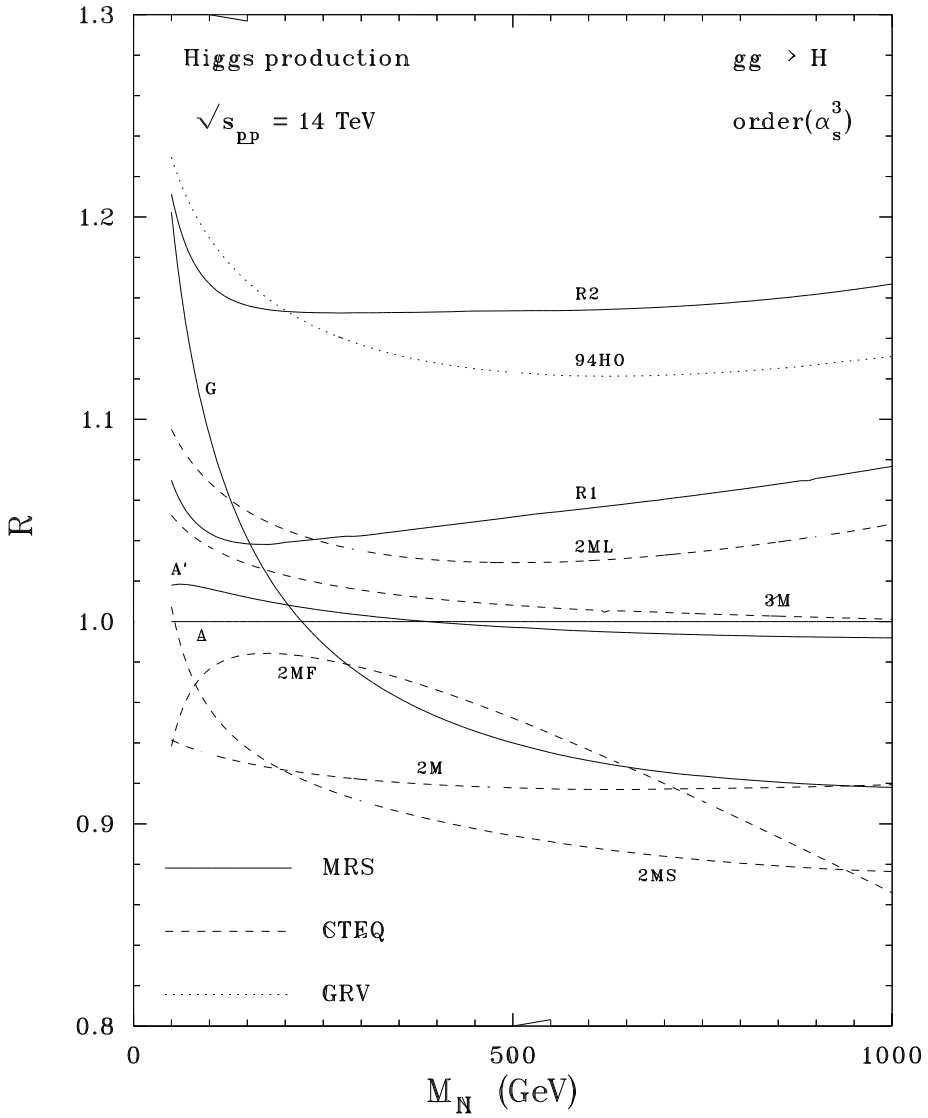

Figure 2.3: Ratios of Higgs production rate through gluon fusion for the structure functions MRS(A,A',G,R1,R2), CTEQ(2M,2MS,2MF,2ML,3M) and GRVHO94 as the function of the Higgs mass. All production rates are relative to the MRS(A) structure function. From [8].

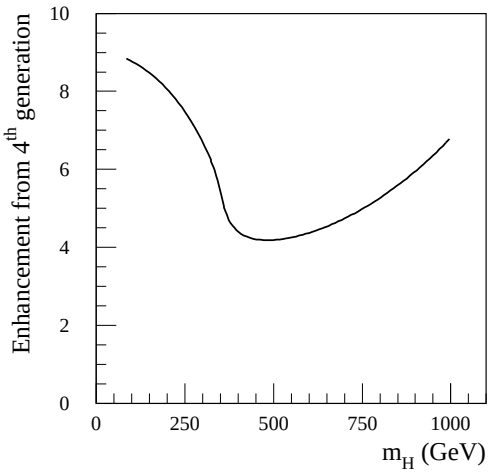

Figure 2.4: The enhancement in the Higgs production cross section from gluon fusion if a fourth very heavy generation of quarks exists.

Following the derivation in [10] the cross section for production of a particle X in the fusion of two vector bosons can be written as

$$\sigma(\mathrm{q_1 q_2} \to \mathrm{q_1' q_2' X}) = \frac{16\pi^2}{\hat{s} m_{\mathrm{X}}} \sum_{\lambda} \int_{m_{\mathrm{X}}^2/\hat{s}}^{1} \frac{\mathrm{d}x}{x} F_\lambda(x) F_\lambda(\frac{m_{\mathrm{X}}^2}{\hat{s}x}) \Gamma_\lambda(\mathrm{X} \to \mathrm{VV}), \tag{2.36}$$

where F_λ is the structure function for the vector boson V with partial width Γ_λ in the state with polarisation λ, $\hat{s} = x_1 x_2 s$ the centre of mass energy squared of the two colliding quarks and q_1', q_2' denoting the two outgoing quarks.

For the production of a Higgs, the decay width described in section 2.3.1 is dominated by the longitudinal polarised state. Ignoring the small contribution from the transverse polarised states the cross section for a heavy Higgs can be written as

$$\sigma(\mathrm{q_1 q_2} \to \mathrm{q_1' q_2' H}) = \frac{16\pi^2}{\hat{s} m_{\mathrm{H}}} \sum_{\mathrm{V=W,Z}} \int_{m_{\mathrm{H}}^2/\hat{s}}^{1} \frac{\mathrm{d}x}{x} F_L(x) F_L(\frac{m_{\mathrm{H}}^2}{\hat{s}x}) \Gamma_L(\mathrm{H} \to \mathrm{VV}). \tag{2.37}$$

To get the full cross section for the Higgs from vector boson fusion the cross section above has to be convoluted with the structure functions of the incoming quarks. For all possible values of the Higgs mass the cross section is below the gluon fusion process, but with the additional signature of the two outgoing quarks participating in the process the identification will be easier in this production channel for a large Higgs mass. Chapter 8 details how a heavy Higgs can be identified with the use of the forward jets.

2.2.3 Associate production

Even if the cross sections for the associative Higgs production shown in fig. 2.1c and fig. 2.1d are low compared to the total Higgs cross section, they can be of interest since the final states have some clear signatures which can be used in the difficult intermediate mass region for the Higgs (section 2.6.1). The calculated cross section are shown in fig. 2.2.

The associative production with a W vector boson was first mentioned in [11] where the expression for the cross section in a slightly more modern notation is

$$\begin{aligned}\sigma(\mathrm{pp} \to \mathrm{WH} + \mathrm{X}) = \frac{g^4}{768\pi} \iint \frac{1}{3}[x_1 f_u(x_1, Q^2) x_2 f_{\bar{d}}(x_2, Q^2) + \\ x_2 f_u(x_2, Q^2) x_1 f_{\bar{d}}(x_1, Q^2)] \cdot \\ f_{\mathrm{W}}(x_1 x_2 s) \mathrm{d}x_1 \mathrm{d}x_2\end{aligned} \tag{2.38}$$

for $\mathrm{W}^+\mathrm{H}$ production. For the $\mathrm{W}^-\mathrm{H}$ production the quark f_u, f_d and anti-quark $f_{\bar{u}}$, $f_{\bar{d}}$ structure functions are interchanged. The value of f_{W} is given by the expression

$$\begin{aligned}f_{\mathrm{W}}(y) = \frac{1}{y}\sqrt{1 - \frac{(m_{\mathrm{H}} + m_{\mathrm{W}})^2}{y}}\sqrt{1 - \frac{(m_{\mathrm{H}} - m_{\mathrm{W}})^2}{y}} \cdot \\ \left\{\left[1 - \frac{(m_{\mathrm{H}} + m_{\mathrm{W}})^2}{y}\right]\left[1 - \frac{(m_{\mathrm{H}} - m_{\mathrm{W}})^2}{y}\right] + 12\frac{m_{\mathrm{W}}^2}{y}\right\} \cdot \\ \frac{1}{(1 - m_{\mathrm{W}}/y)^2}.\end{aligned} \tag{2.39}$$

For a Higgs mass of 150 GeV the production cross section is around 1 pb or 4% of the gluon fusion cross section. With the present structure functions available the uncertainty in the cross section is around 30%. However, this uncertainty can to a large extent be reduced by using single W production as a reference process [12]. At LHC energies it is estimated that

$$\frac{\sigma(\mathrm{pp} \to \mathrm{WH} + \mathrm{X})}{\sigma(\mathrm{pp} \to \mathrm{W} + \mathrm{X})} \simeq 3.5 \cdot 10^{-8} \tag{2.40}$$

with the uncertainty from structure functions instead now only 7%. This way of reducing the uncertainty in production cross section from reference processes could also be employed for other production channels.

The other associative production of interest is the $\mathrm{Ht\bar{t}}$ process. The cross section was first calculated by Kunszt in [13] with further details in [14]. Since ten different Feynman diagrams contribute to the process just in lowest order the calculation is complicated and no derivation will be given here. For Higgs masses below 200 GeV the cross section is around a factor 5 below the cross section for associative production with a W, while for Higgs masses above 500 GeV it reaches above the WH cross section but is still far below the gluon fusion cross section.

In the case of a supersymmetric Higgs sector the cross sections for the fermionic and bosonic associative production will change in different ways from the standard model values.

2.3 Higgs decays

With the Higgs decaying directly into pairs of all massive particles, and through loop diagrams even into pairs of massless gluons and photons, the field of Higgs physics is large. After a discovery of a Higgs particle it will be important to detect the Higgs decay into several decay channels to check if the coupling strength is in proportion to the mass for all fermions as the standard model predicts.

The partial width of the Higgs to the dominant decay modes will be calculated analytically at the lowest order in the sections 2.3.1 to 2.3.4. The total width and the branching ratios are plotted in fig. 2.5 and fig. 2.6. They are calculated with the program HDECAY [15] which includes the dominant higher order corrections to the decay widths.

It is clear from the figure that branching ratios change dramatically across the possible range of the Higgs mass making it necessary to have different strategies for the Higgs identification depending on its mass.

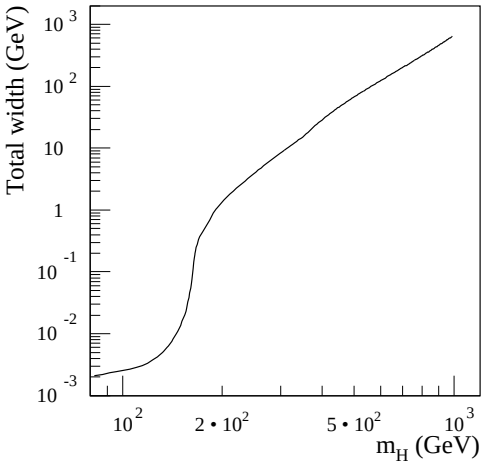

Figure 2.5: The total width of the standard model Higgs. Note how the width approaches the value of the mass itself for a very heavy Higgs.

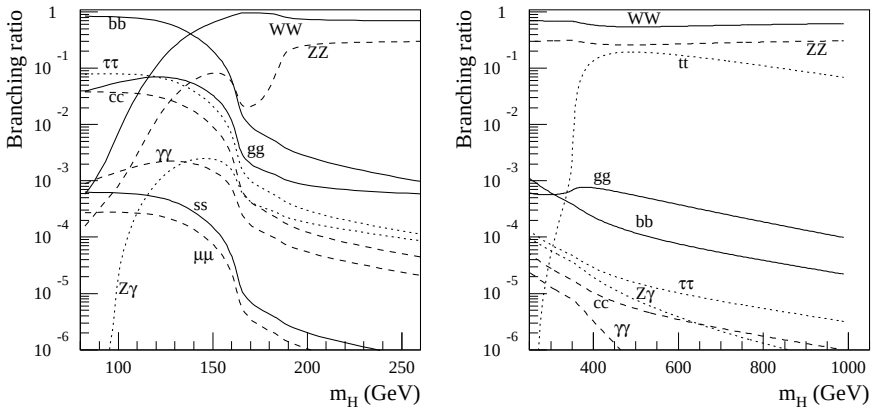

Figure 2.6: The branching ratio of a standard model Higgs for all decays with a branching ratio above 10^{-6}.

2.3.1 Vector boson decay

Starting from the Feynman rule for the HZZ vertex [7] in fig. 2.7 the partial Higgs width $\Gamma_{\mathrm{H}\to\mathrm{ZZ}}$ can be calculated. The matrix element is

$$\mathrm{i}\mathcal{M}_{\mathrm{H}\to\mathrm{ZZ}} = \sum_{\lambda,\rho} \mathrm{i}g\frac{m_{\mathrm{Z}}}{\cos\theta_{\mathrm{W}}} g_{\mu\nu}\epsilon^{*\mu}_{1\lambda}\epsilon^{*\nu}_{2\rho} \tag{2.41}$$

with ϵ_1, ϵ_2 the polarisation vectors of the two Z bosons with polarisation indices λ, ρ. For the two-body decay to two equal mass particles the differential decay rate [16] is

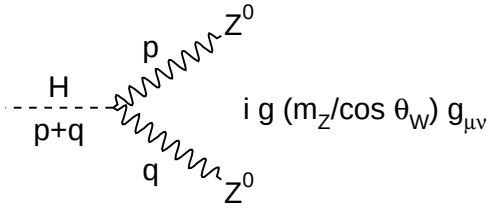

Figure 2.7: The decay of a Higgs boson to two Z^0 bosons with four momentum p, q and the Feynman rule for the vertex.

given as

$$\frac{\mathrm{d}\Gamma}{\mathrm{d}\Omega} = \frac{\sqrt{\lambda(m_{\mathrm{H}}^2, m_{\mathrm{Z}}^2, m_{\mathrm{Z}}^2)}}{64\pi^2 m_{\mathrm{H}}^3}|\mathcal{M}|^2\mathcal{S} \tag{2.42}$$

with λ a quadratic form

$$\sqrt{\lambda(m_{\mathrm{H}}^2, m_{\mathrm{Z}}^2, m_{\mathrm{Z}}^2)} = m_{\mathrm{H}}^2 \sqrt{1 - \left(\frac{2m_{\mathrm{Z}}}{m_{\mathrm{H}}}\right)^2} \tag{2.43}$$

and

$$\mathcal{S} = \prod_k n_k^{-1} = 2^{-1} \tag{2.44}$$

where n is the number of identical final state particles of type k. The squared matrix element can from (2.41) be written as

$$|\mathcal{M}|^2 = \left(\frac{g\, m_{\mathrm{Z}}}{\cos\theta_{\mathrm{W}}}\right)^2 \sum_{\lambda,\rho} g_{\mu\nu} \epsilon_{1\lambda}^{*\mu} \epsilon_{2\rho}^{*\nu} g_{\alpha\beta} \epsilon_{1\lambda}^{\alpha} \epsilon_{2\rho}^{\beta} \tag{2.45}$$

The summation over the three polarisation states of the massive Z bosons [16] is

$$\sum_{\lambda} \epsilon_{\lambda}^{\mu} \epsilon_{\lambda}^{*\nu} = -g^{\mu\nu} + \frac{p^{\mu} p^{\nu}}{m_{\mathrm{Z}}^2}, \tag{2.46}$$

which is just the Lorentz covariant generalisation of having three orthonormal polarisation vectors e_{λ} in the rest frame of the Z where

$$\sum_{\lambda} \mathrm{e}_{\lambda}^{i} \mathrm{e}_{\lambda}^{j} = \delta^{ij}. \tag{2.47}$$

The squared matrix element (2.45) can now be simplified as

$$|\mathcal{M}|^2 = \left(\frac{g\, m_{\mathrm{Z}}}{\cos\theta_{\mathrm{W}}}\right)^2 g_{\mu\nu} \left(-g^{\mu\alpha} + \frac{p^{\mu} p^{\alpha}}{m_{\mathrm{Z}}^2}\right) g_{\alpha\beta} \left(-g^{\nu\beta} + \frac{q^{\nu} q^{\beta}}{m_{\mathrm{Z}}^2}\right) \tag{2.48}$$

$$= \left(\frac{g\, m_{\mathrm{Z}}}{\cos\theta_{\mathrm{W}}}\right)^2 \left(-g_{\nu}{}^{\alpha} + \frac{p_{\nu} p^{\alpha}}{m_{\mathrm{Z}}^2}\right) \left(-g^{\nu}{}_{\alpha} + \frac{q^{\nu} q_{\alpha}}{m_{\mathrm{Z}}^2}\right) \tag{2.49}$$

$$= \left(\frac{g\, m_{\mathrm{Z}}}{\cos\theta_{\mathrm{W}}}\right)^2 \left(4 - \frac{p_{\alpha} p^{\alpha}}{m_{\mathrm{Z}}^2} - \frac{q^{\nu} q_{\nu}}{m_{\mathrm{Z}}^2} + \frac{p_{\nu} q^{\nu} p^{\alpha} q_{\alpha}}{m_{\mathrm{Z}}^4}\right) \tag{2.50}$$

$$= \left(\frac{g\, m_{\mathrm{Z}}}{\cos\theta_{\mathrm{W}}}\right)^2 \left(2 + \frac{(p \cdot q)^2}{m_{\mathrm{Z}}^4}\right). \tag{2.51}$$

where p and q are the 4 momentum of the two Z bosons. Now using that

$$m_{\mathrm{H}}^2 = (p+q)^2 = p^2 + q^2 + 2p \cdot q = 2m_{\mathrm{Z}}^2 + 2p \cdot q \tag{2.52}$$

or

$$p \cdot q = \frac{m_{\mathrm{H}}^2 - 2m_{\mathrm{Z}}^2}{2} \tag{2.53}$$

the squared matrix element is further reduced to

$$|\mathcal{M}|^2 = \left(\frac{g\, m_{\mathrm{Z}}}{\cos\theta_{\mathrm{W}}}\right)^2 \left(2 + \frac{\left(m_{\mathrm{H}}^2 - 2m_{\mathrm{Z}}^2\right)^2}{4m_{\mathrm{Z}}^4}\right) \tag{2.54}$$

$$= \left(\frac{g\, m_{\mathrm{H}}^2}{2m_{\mathrm{Z}}\cos\theta_{\mathrm{W}}}\right)^2 \left(1 - \frac{4m_{\mathrm{Z}}^2}{m_{\mathrm{H}}^2} + \frac{12m_{\mathrm{Z}}^4}{m_{\mathrm{H}}^4}\right) \tag{2.55}$$

$$= \left(\frac{g\, m_{\mathrm{H}}^2}{2m_{\mathrm{W}}}\right)^2 \left(1 - \frac{4m_{\mathrm{Z}}^2}{m_{\mathrm{H}}^2} + \frac{12m_{\mathrm{Z}}^4}{m_{\mathrm{H}}^4}\right). \tag{2.56}$$

The decay rate can be written as

$$\Gamma_{\mathrm{H}\to\mathrm{ZZ}} = \int \mathrm{d}\Omega \frac{\mathrm{d}\Gamma}{\mathrm{d}\Omega} \tag{2.57}$$

$$= \frac{g^2}{512\pi^2}\frac{m_{\mathrm{H}}^3}{m_{\mathrm{W}}^2}\sqrt{1 - \left(\frac{2m_{\mathrm{Z}}}{m_{\mathrm{H}}}\right)^2}\left(1 - \frac{4m_{\mathrm{Z}}^2}{m_{\mathrm{H}}^2} + \frac{12m_{\mathrm{Z}}^4}{m_{\mathrm{H}}^4}\right)\int \mathrm{d}\Omega \tag{2.58}$$

$$= \frac{g^2}{128\pi}\frac{m_{\mathrm{H}}^3}{m_{\mathrm{W}}^2}\sqrt{1 - \left(\frac{2m_{\mathrm{Z}}}{m_{\mathrm{H}}}\right)^2}\left(1 - \frac{4m_{\mathrm{Z}}^2}{m_{\mathrm{H}}^2} + \frac{12m_{\mathrm{Z}}^4}{m_{\mathrm{H}}^4}\right). \tag{2.59}$$

The width of the Higgs decaying to $\mathrm{W}^+\mathrm{W}^-$ is the same as the calculation above, except that the two decay particles are not equal leading to a factor two larger result from (2.44). In a notation with scaling variables the results can be given as

$$\Gamma_{\mathrm{H}\to\mathrm{ZZ}} = \frac{g^2}{128\pi}\frac{m_{\mathrm{H}}^3}{m_{\mathrm{W}}^2}\sqrt{1 - x_{\mathrm{Z}}}\left(1 - x_{\mathrm{Z}} + \frac{3x_{\mathrm{Z}}^2}{4}\right) \tag{2.60}$$

$$\Gamma_{\mathrm{H}\to\mathrm{WW}} = \frac{g^2}{64\pi}\frac{m_{\mathrm{H}}^3}{m_{\mathrm{W}}^2}\sqrt{1 - x_{\mathrm{W}}}\left(1 - x_{\mathrm{W}} + \frac{3x_{\mathrm{W}}^2}{4}\right) \tag{2.61}$$

where

$$x_{\mathrm{Z}} = 4\frac{m_{\mathrm{Z}}^2}{m_{\mathrm{H}}^2}, \quad x_{\mathrm{W}} = 4\frac{m_{\mathrm{W}}^2}{m_{\mathrm{H}}^2}. \tag{2.62}$$

It is the longitudinal polarisation that is responsible for the second part of the sum in (2.46) and by following this part onwards to (2.60) it is seen that the transverse polarisation only enters with powers of $x_{\mathrm{Z}}/x_{\mathrm{W}}$ or higher. At high Higgs masses the Higgs coupling to vector mesons is thus totally dominated by the longitudinal vector boson states.

2.3.2 Fermionic decays

The Higgs particle couples to all fermions proportional to their mass so the coupling to a pair of top quarks is by far the strongest. If the Higgs mass is below the double

top mass the dominant fermionic decay will be to bottom quarks. The Feynman diagram for the vertex is given in fig. 2.8 resulting in the matrix element

$$\mathrm{i}\mathcal{M}_{\mathrm{H}\to\mathrm{f}\bar{\mathrm{f}}} = \mathrm{i}\frac{g m_{\mathrm{f}}}{2m_{\mathrm{W}}}\bar{u}(p)v(q). \tag{2.63}$$

The matrix element squared and summed over the spin states s, s' of the fermions

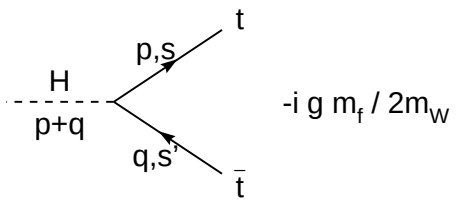

Figure 2.8: The decay of a Higgs boson to two fermions t, $\bar{\mathrm{t}}$ with four momentum p, q and spin states s, s', and the Feynman rule for the vertex.

is then following [16] given as

$$|\mathcal{M}|^2 = \frac{g^2 m_{\mathrm{f}}^2}{4m_{\mathrm{W}}^2}\sum_{s,s'}\{\bar{u}_s(p)v_{s'}(q)\}\{\bar{u}_s(p)v_{s'}(q)\}^* \tag{2.64}$$

$$= \frac{g^2 m_{\mathrm{f}}^2}{4m_{\mathrm{W}}^2}\mathrm{Tr}\left\{\sum_s(\bar{u}(p)u(p))\sum_{s'}(\bar{v}(q)v(q))\right\} \tag{2.65}$$

$$= \frac{g^2 m_{\mathrm{f}}^2}{4m_{\mathrm{W}}^2}\mathrm{Tr}\{(\not{p}+m_{\mathrm{f}})(\not{q}-m_{\mathrm{f}})\} \tag{2.66}$$

$$= \frac{g^2 m_{\mathrm{f}}^2}{4m_{\mathrm{W}}^2}\left(\mathrm{Tr}\{\not{p}\not{q}\} - m_{\mathrm{f}}^2\mathrm{Tr}\{I\}\right) \tag{2.67}$$

$$= \frac{g^2 m_{\mathrm{f}}^2}{4m_{\mathrm{W}}^2}\,4(p\cdot q - m_{\mathrm{f}}^2) \tag{2.68}$$

$$= \frac{g^2 m_{\mathrm{f}}^2 m_{\mathrm{H}}^2}{2m_{\mathrm{W}}^2}\left(1-\frac{4m_{\mathrm{f}}^2}{m_{\mathrm{H}}^2}\right), \tag{2.69}$$

where (2.53) was used in the last line. Using (2.42) and making the trivial angular integration then gives

$$\Gamma_{\mathrm{H}\to\mathrm{f}\bar{\mathrm{f}}} = \frac{N_c g^2 m_{\mathrm{f}}^2 m_{\mathrm{H}}}{32\pi m_{\mathrm{W}}^2}\left(1-\frac{4m_{\mathrm{f}}^2}{m_{\mathrm{H}}^2}\right)^{3/2}, \tag{2.70}$$

where a colour factor has been explicitly introduced (3 for quarks, else 1).

The radiative corrections for the Higgs decay to bottom quarks are treated in detail in [17, 18, 19] for both electroweak and QCD type corrections. In the interesting

mass range for the decay (80 GeV< m_{H} <150 GeV) the absolute value of the QCD corrections are large leading to almost a factor two reduction in the width [20]. In [17] the remaining uncertainty in the decay width from the non-calculated $\mathcal{O}(\alpha_s^3)$ corrections is estimated to 5%.

2.3.3 Two photon decay

Since the photon is massless there is no coupling between the standard model Higgs and the photon. However, the decay is possible through loop processes with either fermions or bosons in the loop. For an extended Higgs sector charged scalars can also enter. Feynman diagrams for the lowest order processes are shown in fig. 2.9.

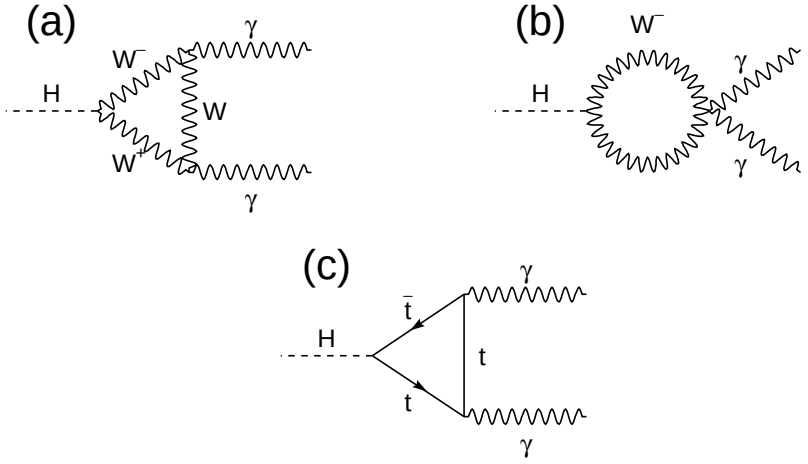

Figure 2.9: Feynman diagrams in the Standard Model for the Higgs decay to two photons in lowest order.

The calculation of the matrix element for the decay is rather complicated and involves dimensional regularisation of the infinities arising from the loop. The end result for the squared matrix element is [20]

$$|\mathcal{M}|^2 = \frac{g^2 m_{\mathrm{H}}^4}{32\pi^2 m_{\mathrm{W}}^2} \left| \sum_i \alpha N_c e_i^2 F_i \right|^2 , \tag{2.71}$$

with the sum over all scalars, fermions and bosons in the loop with charge e_i and colour factor N_c (3 for quarks else 1). The factor F is given as

$$F_{\mathrm{boson}} = 2 + 3\tau + 3\tau(2-\tau)f(\tau), \tag{2.72}$$

$$F_{\mathrm{fermion}} = -2\tau(1 + (1-\tau)f(\tau)), \tag{2.73}$$

$$F_{\mathrm{scalar}} = \tau(1 - \tau f(\tau)) \tag{2.74}$$

when

$$f(\tau) = \begin{cases} \left[\sin^{-1}(\sqrt{(1/\tau)}\right]^2 & \text{if } \tau \geq 1 \\ -\frac{1}{4}\left[\log\left(\frac{1+\sqrt{1-\tau}}{1-\sqrt{1-\tau}}\right) - \mathrm{i}\pi\right]^2 & \text{if } \tau < 1, \end{cases} \tag{2.75}$$

and

$$\tau = \left(\frac{2m_i}{m_{\mathrm{H}}}\right)^2. \tag{2.76}$$

The term F_{fermion} disappears for small τ which means that light quarks and leptons are insignificant. The only fermion participating is the top quark. For bosons the loop only contains the charged W.

The F parameters for the top and W contributions scaled with the colour factor are plotted in fig. 2.10 for the Higgs mass range where the decay is of interest. It can be seen how the fermion and boson loops have opposite signs but with the W loop dominating. Adding a fourth family with the lepton and the two quarks having masses above 500 GeV will give a near cancellation in the matrix element. A possible scalar particle in the loop will only have a small influence following (2.74).

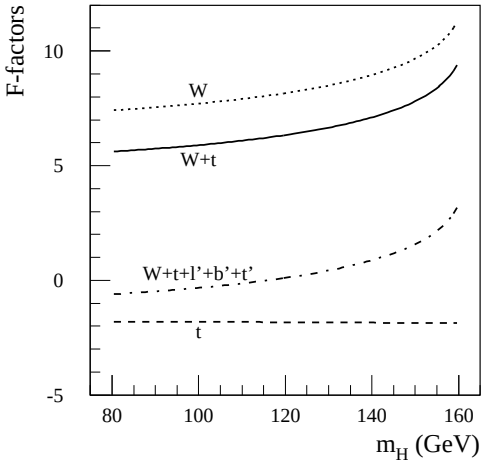

Figure 2.10: The contribution from the W and top quark loop to the matrix element in the $\mathrm{H} \to \gamma\gamma$ decay. The sum of the two and the influence of adding a 4th heavy family $(\mathrm{l}', \nu', \mathrm{b}', \mathrm{t}')$ is also shown.

The width of the $\mathrm{H} \to \gamma\gamma$ decay channel is now easily obtained using (2.42) and

performing the trivial angular integration. The result is

$$\Gamma_{\mathrm{H}\to\gamma\gamma} = \frac{\alpha^2 g^2 m_{\mathrm{H}}^3}{1024\pi^3 m_{\mathrm{W}}^2}\left|\sum_i N_c e_i^2 F_i\right|^2, \tag{2.77}$$

which always gives a branching ratio below 0.3% due to the much larger width of the $\mathrm{H}\to\mathrm{b\bar{b}}$ decay. The two photon signature is, however, clean and as will be seen in section 2.6.1 an important decay channel at the LHC. Adding a fourth family will reduce the branching ratio by more than a factor 8 if the Higgs mass is below 140 GeV.

The radiative corrections to the $\mathrm{H}\to\gamma\gamma$ decay width are relatively simple as they only affect the top quark loop and neither the W loop nor the final state photons. The corrections are below 3% [21] and thus of limited importance.

2.3.4 Two gluon decay

With the branching ratio for the $\mathrm{H}\to\gamma\gamma$ decay already calculated in the preceding section, the decay of the Higgs to two gluons is relatively easy. As the gluons have no coupling to vector bosons or scalars only a diagram similar to the diagram of fig. 2.9c will contribute to the $\mathrm{H}\to\mathrm{gg}$ decay. In (2.71) the factor $\alpha N_c e_i^2$ has to be replaced by α_s^2 to take the different coupling into account and a factor 2 should be added to the decay width giving a decay width (2.77) since the two final state particles are no longer identical. The decay width is

$$\Gamma_{\mathrm{H}\to\mathrm{gg}} = \frac{\alpha_s^2 g^2 m_{\mathrm{H}}^3}{512\pi^3 m_{\mathrm{W}}^2}\left|\sum_i F_i\right|^2, \tag{2.78}$$

where now only fermions should be included in the loop. As was the case for the photon decay, all quarks but the top quark have an insignificant contribution to the total decay width.

Even if the branching ratio to gluons is around a factor 40 higher than the two photon branching ratio the decay is of no interest at the LHC[2]. The two gluons will during the fragmentation evolve into a two jet system which will have a rate many orders of magnitude below the rate for two-jet production at the LHC. However, as it was already seen in section 2.2.1 the Higgs-gluon coupling is very important in the production process of a Higgs at the LHC. The effects of radiative corrections to the decay width, which are large and positive, were treated in section 2.2.1.

2.4 Experimental results on Higgs searches

The experimental bounds on the Higgs mass come from the experiments at the LEP $\mathrm{e^+e^-}$ storage ring. The mass range accessible continues to rise as the centre of mass energy in the collisions increases during the LEP2 upgrade. The decay channel investigated is the so called Higgs-strahlung process shown in fig. 2.11.

[2]For a future linear e^+e^- collider the $\mathrm{H}\to\mathrm{gg}$ decay is potentially possible to detect.

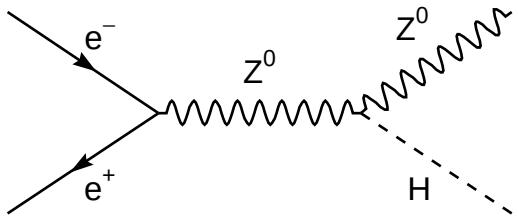

Figure 2.11: Higgs-strahlung, the dominant production process for a standard model Higgs at LEP2.

The best Higgs mass limits at the moment are from data collected with a maximal centre of mass energy of 172 GeV. In articles submitted for publication the limits are: 70.7 GeV (ALEPH) [22], 69.5 GeV (L3) [23] and 65.0 GeV (OPAL) [24]. The ultimate Higgs mass reach for LEP2, at a collision energy of 192 GeV and with an integrated luminosity of 150 pb^{-1} for each experiment, is estimated to be 95 GeV [25]. No other experiments are expected to raise this limit further before the start of the LHC.

As can be seen the overlap between LEP2 and the LHC for Higgs masses is rather small and that makes it important that the detectors at the LHC will have ultimate performance in the difficult region of an intermediate mass Higgs.

Before the discovery of the top quark at the Tevatron its mass was quite well known from the top quark effect on lower energy processes through radiative corrections. The same is to some extent true for the Higgs. While the electroweak radiative corrections at the one loop level are proportional to

$$\frac{m_{\mathrm{t}}^2 - m_{\mathrm{b}}^2}{m_{\mathrm{W}}^2} \quad \text{or} \quad \frac{m_{\mathrm{t}}^2}{m_{\mathrm{Z}}^2} \tag{2.79}$$

they are for radiative corrections involving the Higgs proportional to

$$\log \frac{m_{\mathrm{H}}}{m_{\mathrm{Z}}} \tag{2.80}$$

thus making the uncertainties in the Higgs mass predictions much larger than was the case for the top quark mass before its direct discovery.

Precision measurements of $\sin\theta_{\mathrm{W}}$, m_{t}, α_s, m_{Z} and α give an over-determined system from which limits on the Higgs mass can be extracted. Assuming a standard model Higgs sector it is in [26] shown that a Higgs mass of the order 130 GeV gives the best fit to data and an upper limit of 430 GeV is claimed as a 95% confidence limit. Combining precision measurements from the LEP and Tevatron experiments gives the indirect measurement $m_{\mathrm{H}} = 115^{+116}_{-66}$ GeV with 420 GeV as a 95% confidence limit [27]. As an interesting remark it can from (2.80) be seen that the indirect measurement $m_{\mathrm{H}} \simeq m_{\mathrm{Z}}$ is equivalent to the conclusion that no radiative corrections involving the Higgs particle have been measured.

2.5 A theoretical limit on the Higgs mass

Several more or less precise arguments can set the upper limit for a standard model Higgs particle. All of them follows the line that the standard model breaks down if the Higgs mass is pushed too far upwards. The theoretical bounds will be reviewed below while the detection methods for a very heavy Higgs will be treated in chapter 8.

2.5.1 The triviality bound

An upper limit on the Higgs mass can be given from what is called the triviality bound. The simplified Goldstone model (section 2.1.1) having a single scalar is used to illustrate the process. Using the renormalisation group equations as in [20] a running value of the coupling λ is obtained

$$\lambda(Q) = \frac{\lambda(v)}{1 - \frac{3}{4\pi^3}\log\frac{Q^2}{v^2}\lambda(v)} \tag{2.81}$$

where v is the vacuum expectation value (2.27) and the Higgs mass (at tree level) given as

$$m_{\mathrm{H}} = v\sqrt{2\lambda(v)}. \tag{2.82}$$

It can be seen that if no new physics enters equation (2.81) has to be valid for all values of Q; but keeping λ finite as $Q \to \infty$ forces $\lambda(v)$ to zero. This implies a non-interacting theory called a *trivial* theory. If instead imagining that the standard model is embedded in a more complete theory having new physics at an energy scale Λ_{NP} the requirement can be loosened to something like

$$\lambda(\Lambda_{\mathrm{NP}}) \lesssim 1 \tag{2.83}$$

thus setting a maximal value on $\lambda(v)$ giving an upper limit on the Higgs mass from (2.81) and (2.82). Setting Λ_{NP} at the Planck scale $m_{\mathrm{Pl}} \simeq 10^{19}$ GeV and requiring that the pertubative approach is valid for all energies gives the low limit $m_{\mathrm{H}} \lesssim 140$ GeV. Defining a lower energy of the cutoff will give a larger allowed range for the Higgs mass. The implementation of lattice theory also makes it possible to loosen the requirement that λ is in the pertubative regime for all values of λ below Λ_{NP}.

Using the full electroweak Lagrangian (2.28) does not change the conclusion from the simplified discussion above, but it is necessary to use it to get better numerical values. To imagine the largest possible Higgs mass the scale of new physics has to be pressed far down. It seems natural that $m_{\mathrm{H}} \lesssim \mathcal{O}(\Lambda_{\mathrm{NP}})$ as a Higgs with mass above the scale of new physics can not be defined as a standard model Higgs any longer. Just using this requirement sets $m_{\mathrm{H}} \lesssim 1000$ GeV as seen in fig. 2.12 having the value

$$(m_{\mathrm{H}}^{\max})^2 = \frac{8\pi^2 v^2}{3\log\frac{\Lambda_{\mathrm{NP}}}{v^2}} \tag{2.84}$$

where the top quark coupling is ignored. The line $m_{\mathrm{H}}^{\max} = \Lambda_{\mathrm{NP}}$ is also plotted.

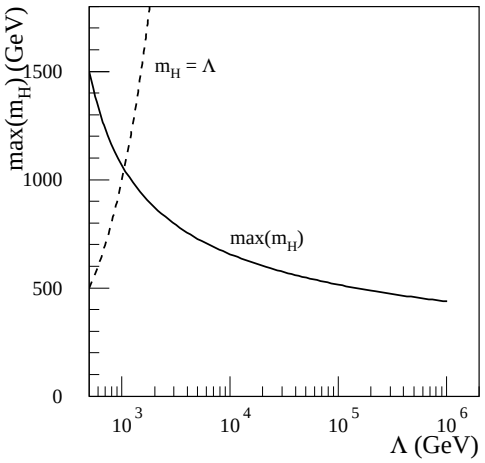

Figure 2.12: The maximal possible Higgs mass with a given scale $\Lambda_{\rm NP}$ for new physics. The dashed line marks $m_{\rm H}^{\rm max} = \Lambda_{\rm NP}$.

However, using (2.82) to define $m_{\rm H}$ is wrong since the tree level value will have large radiative corrections for $m_{\rm H} \gg v$. Using (2.81) to define the Higgs mass instead from $\lambda(m_{\rm H})$ results in no upper limit on the Higgs mass but the result is not reliable since pushing $m_{\rm H}$ to the maximal value will exactly evaluate λ in the non-pertubative region to get the value $m_{\rm H}$. In [28] this problem has been treated with care taking into account the high top quark mass and up to two loop effects. In fig. 2.13, taken from the article, a band is given for the maximal Higgs mass with a given scale of new physics. The width of the band shows the uncertainty in the value of the Higgs mass where the pertubative approach breaks down.

The work presented in [29] uses lattice gauge theory on the scalar sector of the Standard Model to set an absolute bound on the Higgs mass and not just a limit from a breakdown of perturbation theory. From numerical analysis it is concluded that $m_{\rm H} \lesssim 710$ GeV thus giving a upper limit similar to the limit from perturbation theory. The theoretical uncertainty on the upper mass is evaluated to ± 60 GeV. The bounding condition on the new physics scale was that the standard model can describe physics accurately below the double Higgs mass.

2.5.2 The width of the Higgs

The width of a heavy Higgs is given by the sum of (2.60) and (2.61) in the limit $x_{\rm V} \to 0$ (V=W,Z). The leading term is proportional to $m_{\rm H}^3$ and given as

$$\Gamma_{\rm H} = \frac{3g^2}{128\pi m_{\rm W}^2} m_{\rm H}^3 \simeq 0.5 \text{ TeV}^{-2}\, m_{\rm H}^3. \tag{2.85}$$

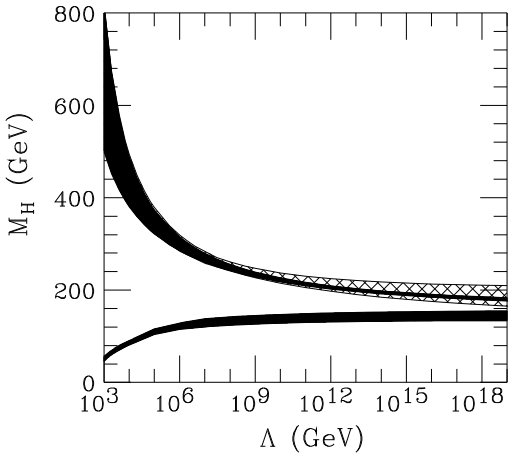

Figure 2.13: The Higgs mass where the pertubative approach breaks down including two loop effects. The upper band reflects the uncertainty in the calculation. The lower band is a lower limit on the Higgs mass from stability arguments of the theory and will not be commented on further.

As already seen in section 2.3.1 the width is totally dominated by the longitudinal polarised state of the vector boson.

Taking (2.85) to the very limit where the width of the Higgs is equal to the mass gives a kind of upper limit on the Higgs mass of 1.4 TeV. At least the concept of the Higgs as a particle disappears and complete VV $\rightarrow$ VV scattering has to be considered.

2.5.3 $WW \rightarrow WW$ scattering

The complete set of Feynman diagrams for $W^+W^- \rightarrow W^+W^-$ scatteringare shown in fig. 2.14. For $s, m_H \gg m_W, mZ$ only the diagrams with the Higgs in the s and t channel are important. The matrix element using these is in [30] given as

$$\mathcal{M}(W_L^+ W_L^- \rightarrow W_L^+ W_L^-) = A(s) + A(t) \tag{2.86}$$

where s is the squared centre of mass energy and t, u defined as

$$t = -\frac{s}{2}(1 - \cos\theta) \tag{2.87}$$

$$u = -\frac{s}{2}(1 + \cos\theta) \tag{2.88}$$

in the situation with elastic scattering of equal mass particles and θ the scattering angle in the CM system. A in (2.86) is the scattering amplitude

$$A(s) = -\frac{m_H^2}{v^2}\left(1 + \frac{m_H^2}{s - m_H^2 + im_H\Gamma_H\Theta(s)}\right) \tag{2.89}$$

with Θ the step function.

To conserve unitarity it is required that the scattering amplitude is below unity for all isospin states and partial waves. The 3 isospin states $T(I)$ are given as

$$T(0) = 3A(s) + A(t) + A(u) \tag{2.90}$$
$$T(1) = A(t) - A(u) \tag{2.91}$$
$$T(2) = A(t) + A(u) \tag{2.92}$$

which can be further expanded into partial waves according to

$$a_l^I = \frac{1}{64\pi} \int_{-1}^{1} \mathrm{d}(\cos\theta) P_l(\cos\theta) T(I). \tag{2.93}$$

As an example the strength of the J = 0 partial wave can be calculated. The simple form $P_0 = 1$ of the lowest order Legendre polynomial makes the integrals easy.

$$\int_{-1}^{1} \mathrm{d}(\cos\theta) P_0(\cos\theta) A(s) = 2A(s), \tag{2.94}$$
$$\int_{-1}^{1} \mathrm{d}(\cos\theta) P_0(\cos\theta) A(t) = \frac{2}{s} \int_{-s}^{0} A(t)\mathrm{d}t \tag{2.95}$$
$$= -\frac{2m_{\mathrm{H}}^2}{sv^2} \int_{-s}^{0} \left(1 + \frac{m_{\mathrm{H}}^2}{t - m_{\mathrm{H}}^2}\right) \mathrm{d}t \tag{2.96}$$
$$= \frac{2m_{\mathrm{H}}^2}{sv^2} \left(\frac{m_{\mathrm{H}}^2}{s} \log(1 + s/m_{\mathrm{H}}^2) - 1\right), \tag{2.97}$$
$$\int_{-1}^{1} \mathrm{d}(\cos\theta) P_0(\cos\theta) A(u) = \frac{2}{s} \int_{0}^{-s} A(u)\mathrm{d}u \tag{2.98}$$
$$= -\int_{-1}^{1} \mathrm{d}(\cos\theta) P_0(\cos\theta) A(t). \tag{2.99}$$

Inserted in the calculation of the amplitudes

$$a_0^0 = \frac{1}{64\pi}\int_{-1}^{1} \mathrm{d}(\cos\theta) P_0(\cos\theta) T(0) \tag{2.100}$$

$$= \frac{1}{64\pi} 6A(s) \tag{2.101}$$

$$= -\frac{3m_{\mathrm{H}}^2}{32\pi v^2}\left(1 + \left(\frac{s}{m_{\mathrm{H}}^2} - 1 + \mathrm{i}\frac{3m_{\mathrm{H}}^2}{32\pi v^2}\right)^{-1}\right) \tag{2.102}$$

$$a_0^1 = \frac{1}{64\pi}\int_{-1}^{1} \mathrm{d}(\cos\theta) P_0(\cos\theta) T(1) \tag{2.103}$$

$$= \frac{1}{32\pi}\int_{-1}^{1} \mathrm{d}(\cos\theta) P_0(\cos\theta) A(t) \tag{2.104}$$

$$= \frac{m_{\mathrm{H}}^2}{16\pi s v^2}\left(\frac{m_{\mathrm{H}}^2}{s}\log(1 + s/m_{\mathrm{H}}^2) - 1\right) \tag{2.105}$$

$$a_0^2 = \frac{1}{64\pi}\int_{-1}^{1} \mathrm{d}(\cos\theta) P_0(\cos\theta) T(2) \tag{2.106}$$

$$= 0 \tag{2.107}$$

Requiring the partial wave unitarity $|a_0| < 1$ sets the limit $m_{\mathrm{H}} < 1.0$ TeV for all values of $\sqrt{s}$. The limit can not be taken all too serious since it drives the pertubative approach of partial waves into the region of non-pertubative analysis where $|a_0| = \mathcal{O}(1)$.

2.5.4 A value for the maximal Higgs mass

Each of the arguments for an upper limit on the Standard Model Higgs mass presented above have small problems mainly lying in the fact that they predict the breakdown of perturbation theory thus predicting a strongly interacting high energy sector of vector boson interactions. The whole concept of the Higgs mechanism as a pertubative expansion around the vacuum expectation value also breaks down.

Lattice theory should in principle be able to avoid this limitation but so far calculations have only been made with a simplified model with the heavy quarks excluded. However, it seems clear that the standard model can not survive without modifications if the Higgs mass is above 1 TeV. Quite small corrections to the standard model can allow higher Higgs masses so a limit at 1 TeV should in no way limit the search at the LHC for Higgs like objects with even higher masses.

2.6 Higgs searches at the LHC

2.6.1 An intermediate mass Higgs ($m_{\mathrm{Z}} < m_{\mathrm{H}} < 2m_{\mathrm{Z}}$)

To find a Higgs particle below the threshold for the $\mathrm{H} \to \mathrm{ZZ}$ decay and above the limit set by the searches at LEP2 will be difficult. The obvious way to detect a Higgs

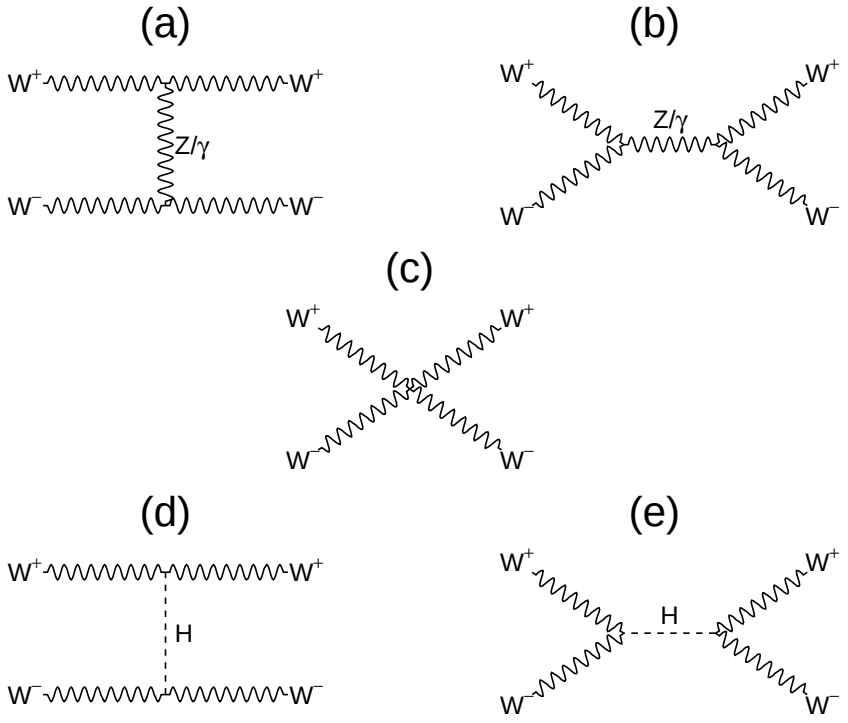

Figure 2.14: The complete gauge invariant set of Feynman diagrams for $W^+W^- \to W^+W^-$ scattering.

would be in the dominant $H \to b\bar{b}$ channel but with the b-quarks fragmenting into jets this channel will be overwhelmed by the di-jet rate. Also the $H \to b\bar{b}$ decay lacks any trigger as it neither has high jet energies nor isolated leptons in the final state. A more favourable situation can be obtained by either looking at associative production or at one of the rarer decays.

With the Higgs produced together with either a top quark pair or a vector boson (section 2.2.3) the problem of getting a trigger for the Higgs events are solved by requiring a high energy lepton from one of the top quarks or the vector boson decay. The HZ production is already suppressed in comparison with the HW and taking the factor three lower branching ratio for leptonic decays into account the HZ production mode is of limited interest as the rate will be low.

The next handle for the decay is to identify the jets with b-quarks. The method called b-tagging is based either on the long lifetime of the b-quarks which causes secondary vertices or on the high amount of leptons in B meson decays. While the

HW mode will in general have two b-quarks in the final state the $Ht\bar{t}$ will have four as $t \to b$. The use of multiple b-tagging can provide a larger rejection of jets and thus counteract the lower cross section for $Ht\bar{t}$ production in the interesting mass range.

The $H \to b\bar{b}$ decay gives further problems in the reconstruction. The Higgs mass has to be reconstructed from two jets giving trouble with invisible energy from escaping neutrinos and energy lost outside the jet cone. As a result the reconstructed mass peak will be wide. The $Ht\bar{t}$ channel also suffers from the combinatorial problem of selecting the correct combination of b-jets.

The other way of identifying a Higgs in the intermediate mass region is to select an exotic decay as the $H \to \gamma\gamma$ decay. The trigger is two isolated electromagnetic clusters. While the channel suffers from a branching ratio around 10^{-3} the backgrounds are also much lower than in the case of the $H \to b\bar{b}$ decay due to the clear signature of two isolated photons in the final state. The main backgrounds are from direct photon production and jets faking photons. Both the signal and the backgrounds for the $H \to \gamma\gamma$ decay will be treated in chapter 7.

In the upper limit of the mass interval with a Higgs mass above 130 GeV the branching ratio to vector bosons reaches significant levels. However, at least one of the vector bosons will not be on the mass shell. The obvious decay channel is $H \to ZZ^* \to l^+l^-l^+l^-$ where a mass constraint can be made on one of the lepton pairs while the other pair is given to have an invariant mass below m_Z. Looking on fig. 2.6 a funny shape of the branching ratio to Z-bosons can be seen for Higgs masses in the interval 150 GeV $< m_H <$ 190 GeV. It is caused by a threshold effect where the decay to two W bosons on the mass shell turns possible but still at least one of the Z bosons needs to be below the mass shell.

The main irreducible background for the $H \to ZZ^*$ decay is direct ZZ^* and $Z\gamma^*$ production with decays to four leptons. A good mass resolution is required to reduce this continuum background. The most important reducible backgrounds are $t\bar{t}$ and $Zb\bar{b}$ production again with four leptons in the final state. The main cuts to reduce the background is isolated electrons, a mass cut on one of the lepton pairs to the Z mass, and a requirement for the other lepton pair to have an invariant mass above 20 GeV. The last cut mainly reduces the background from the $Z\gamma^*$ and $Zb\bar{b}$ processes.

2.6.2 A heavy Higgs ($2m_Z < m_H \lesssim 650$ GeV)

If a standard model Higgs is having a mass above twice the Z mass the discovery will be easy through the decay channel $H \to ZZ \to l^+l^-l^+l^-$. This is called the golden channel for Higgs decays. Both lepton pairs will have an on-shell Z mass making it possible to reduce many types of backgrounds.

The main irreducible background is direct ZZ production, but a requirement for at least one of the Z bosons to have a transverse momentum above half the Higgs mass will strongly suppress this background. The upper mass limit for detecting the Higgs in this decay channel is given by the reduced production rate and the increased width of the Higgs. A larger width of the signal increases the irreducible continuum background as is shown for the $H \to \gamma\gamma$ decay channel in section 7.1 but the reduced

rate is the most serious problem. As an example fewer than 200 Higgs particles with $m_{\mathrm{H}} = 700$ GeV decay in the $\mathrm{H} \to \mathrm{ZZ} \to \mathrm{l^+l^-l^+l^-}$ channel in a year at high luminosity. Taking into account the kinematic cuts and detecting efficiencies hardly any particles are left for detection.

2.6.3 A very heavy Higgs ($m_{\mathrm{H}} \gtrsim 650$ GeV)

With the fixed collision energy of the LHC the production cross section of a Higgs particle falls with an increasing Higgs mass. The rate in a selective decay channel like the four lepton channel is thus no longer high enough for the highest Higgs masses. With the decays to vector bosons totally dominating, the only possible detection channels left, are with at least one of the vector bosons decaying to neutrinos or jets.

The decay channel $\mathrm{H} \to \mathrm{W^+W^-} \to \mathrm{l}\nu\mathrm{jj}$, where j denotes a jet from a quark in the W decay, has a branching ratio of just below 30% giving it a rate some 50 times higher than the four lepton channel from $\mathrm{H} \to \mathrm{ZZ}$ decays. However, the background from direct jW and $\mathrm{t\bar{t}}$ production are large and can only be reduced requiring forward jets in the event. The decay channel $\mathrm{H} \to \mathrm{ZZ} \to \mathrm{l^+l^-}\nu\bar{\nu}$ which has a six times larger branching ratio than the four lepton channel could also be interesting.

The large width of a heavy Higgs also makes it impossible to observe a mass peak. For methods relying on just counting events it is even more important to have a good rejection of the background. More details on how to observe a Higgs particle with $m_{\mathrm{H}} = 1$ TeV can be found in chapter 8.

2.7 No Higgs particle at all

It is also possible that there will be no Higgs like particle at all. This would destroy the nice theory giving mass to the vector bosons but would not be in contradiction to any experimental results. Many different theories are available to define such a situation among them the so-called technicolour models. As a first test of a new theory it has to be unitary in the scattering amplitudes (2.93).

Taking the unitarisation instead as a definition, several effective models can be developed where $|a_l^I|$ is kept below unity for all energies [30, 31] either by keeping the complex value for higher energies when it reaches $|a_l^I|$=1, or by redefining the amplitude as

$$a_l^{I\prime} = \frac{a_l^I}{1 - \mathrm{i}a_l^I}. \tag{2.108}$$

From an analysis done in just the leptonic decay channel ($\mathrm{W^+W^-} \to \mathrm{l^+}\nu\mathrm{l^-}\nu$) it is in [31] concluded that the different models without any Higgs boson would reveal an excess in the $\mathrm{W^+W^-} \to \mathrm{W^+W^-}$ scattering with data from one year at high luminosity (100 $\mathrm{fb^{-1}}$). However, to distinguish between the different models will require much more data.

Chapter 3

Transition radiation detectors

Transition radiation is a radiation in the X-ray region, that arises when ultrarelativistic particles cross a boundary between 2 media with different dielectric constants. It depends strongly on the relativistic γ factor of the particle which makes it usable for particle identification at energies where time of flight methods or detection of Cherenkov radiation no longer work. As an example, the large mass difference between electrons and pions makes it possible to separate electrons from pions in an energy interval from 0.5 GeV to 200 GeV.

To build a detector based on transition radiation is far from easy though since the number of X-ray photons from a single boundary are of the order α, the fine structure constant.

The theory here is mainly based on the review articles [32] and [33] and the section on applications to detectors on [34] and [35].

3.1 Transition radiation from a single boundary

The simplest situation creating transition radiation is with only one boundary as indicated in fig. 3.1. In both media the solution to the inhomogeneous Maxwell equations including the particle gives rise to a continuous energy loss ($\mathrm{d}E/\mathrm{d}x$) as will be described in detail in section 3.4.2. However, to fulfil the boundary conditions on the surface between the two media it is necessary to add solutions to the homogenous Maxwell equations: this homogenous solution is the transition radiation.

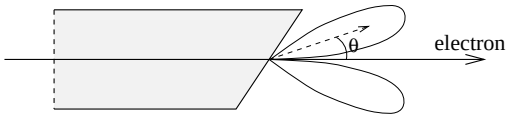

Figure 3.1: Transition radiation created at a single boundary between 2 media. The angle θ is highly exaggerated.

For the electric field at the boundary, in the limit of ultra-relativistic particles, the electric field is apart from some numeric constants

$$\vec{e}(\omega,\vec{\theta}) = \frac{\vec{\theta}}{\gamma^{-2}+\theta^2+\xi_1^2} - \frac{\vec{\theta}}{\gamma^{-2}+\theta^2+\xi_2^2}. \tag{3.1}$$

with a similar formula for the magnetic field $\vec{h}(\omega,\vec{\theta})$. $\vec{\theta}$ is the difference between the unit vectors in the direction of the particle and the radiation, γ is the relativistic gamma factor of the particle and ω the frequency of the radiation. For the two media ξ_i is defined as

$$\xi_i = \frac{\omega_{\mathrm{P}_i}}{\omega}, \tag{3.2}$$

where ω_{P_i} is the plasma frequency of a material i with electron density n_{e_i} considered as an electron gas,

$$\omega_{\mathrm{P}_i}^2 = \frac{4\pi\alpha n_{\mathrm{e}_i}}{m_{\mathrm{e}}} \simeq (28.8\ \mathrm{eV})^2 \frac{Z\rho}{A}, \tag{3.3}$$

with Z, A the atomic number and weight, α the fine structure constant and ρ the density. The definition of θ can be seen in fig. 3.1.

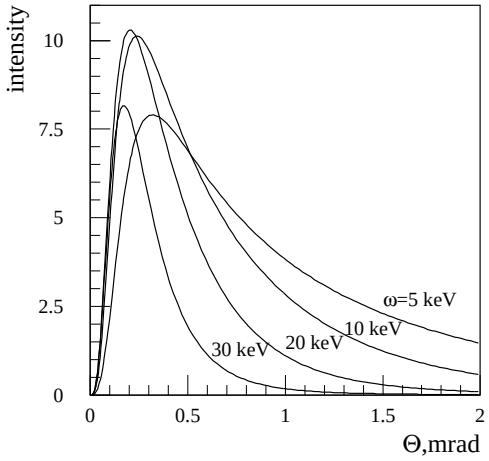

Figure 3.2: The angular distribution $\frac{\mathrm{d}^2W}{\mathrm{d}\omega\mathrm{d}\theta}$ of transition radiation from a single boundary between polypropylene and air for a 4 GeV electron ($\gamma = 8000$).

The energy radiated per solid angle per unit frequency takes the form

$$\begin{aligned}\frac{\mathrm{d}^2W}{\mathrm{d}\omega\mathrm{d}\Omega} &= \left|\vec{e}(\omega,\vec{\theta}) \times \vec{h}(\omega,\vec{\theta})\right| \\ &= \frac{\alpha}{\pi^2}\left|\frac{\theta}{\gamma^{-2}+\theta^2+\xi_1^2} - \frac{\theta}{\gamma^{-2}+\theta^2+\xi_2^2}\right|^2.\end{aligned} \tag{3.4}$$

The angular distribution is illustrated in fig. 3.2.

Performing the angular integration in (3.4) the total energy radiated per unit frequency is

$$\frac{\mathrm{d}W}{\mathrm{d}\omega} = \frac{\alpha}{\pi}\left(\frac{\xi_1^2+\xi_2^2+2\gamma^{-2}}{\xi_1^2-\xi_2^2}\log\frac{\gamma^{-2}+\xi_1^2}{\gamma^{-2}+\xi_2^2}-2\right) \tag{3.5}$$

or after a further integration over frequency

$$W = \frac{2\alpha\gamma\omega_{\mathrm{P}_1}}{3}, \tag{3.6}$$

under the assumption $\omega_{\mathrm{P}_2} \ll \omega_{\mathrm{P}_1}$.

In this ideal situation the transition radiation is proportional to γ but the proportionality cannot be preserved in a practical detector.

Taking into account a low energy cutoff on the detected photons, which will exist in all detectors, the number of photons emitted from a single boundary is

$$n_\gamma = \int_{\omega_{\min}}^{\infty}\frac{1}{\omega}\frac{\mathrm{d}W}{\mathrm{d}\omega}\mathrm{d}\omega \simeq 0.5\alpha \tag{3.7}$$

with $\omega_{\min} = 0.15\gamma\omega_{\mathrm{P}}$ as an example. The main problem for detectors based on transition radiation is (3.7), the number of emitted photons from a single surface is low, and hence many surfaces are needed. However, many closely packed surfaces also offer the possibility to use interference to create a threshold detector.

3.2 Radiators with many layers

A unit with many boundaries, a radiator, can be achieved using foils placed closely together as shown in fig. 3.3.

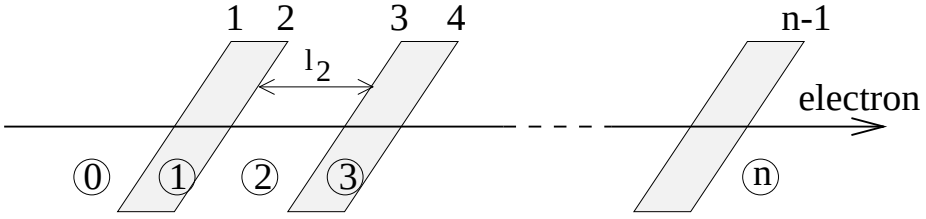

Figure 3.3: A radiator with many boundaries. The boundaries are numbered from 1 to $n-1$ and the media with encircled numbers from 1 to n.

With one boundary two different stationary solutions to the Maxwell equations have to be matched, but with many boundaries a general solution is complicated. As seen in equation (3.4) and fig. 3.2 the radiation is for relativistic particles sharply peaked in the forward direction and from (3.5) with the energy concentrated in the

X-ray region. Hence backwards radiation and reflections can be ignored. With this simplification the electric field at the end of the radiator is given as a sum of the fields from the individual boundaries taking interference and absorption into account,

$$\vec{E}(\omega,\vec{\theta}) = \sum_{j=1}^{n-1} \vec{e}^{j}(\omega,\vec{\theta}) \exp\left(-\sum_{\mathrm{m}\geq\mathrm{j}}^{\mathrm{n}-1} \sigma_{\mathrm{m}} + \mathrm{i}\varphi_{\mathrm{m}}\right). \tag{3.8}$$

$\vec{e}^{j}$ is the single surface amplitude as in (3.1) with the media surrounding boundary j substituting ξ_1 and ξ_2. The absorption coefficient σ_m is given as

$$\sigma_m = \frac{l_m}{\lambda_m} \tag{3.9}$$

where λ_m is the absorption length in the medium and l_m the length of the medium along the particle path. The difference in phase φ_m for transition radiation from different layers, caused by different times for the particle and the photons to cross the layers, is

$$\varphi_{\mathrm{m}} = \frac{\omega l_{\mathrm{m}}}{v} - \vec{k}_{\mathrm{m}} \cdot \vec{l}_{\mathrm{m}} \tag{3.10}$$

where v is the velocity of the particle, $\vec{k}_{\mathrm{m}}$ the wave vector of the photon with frequency ω and $\vec{l}_{\mathrm{m}}$ the vector between the crossing points of the boundaries and the particle as illustrated in fig. 3.4.

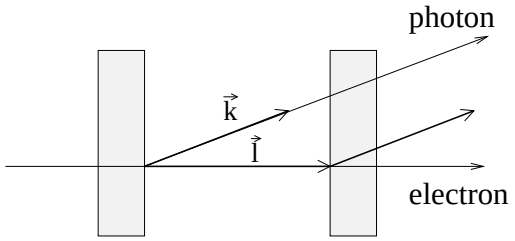

Figure 3.4: The phase difference of transition radiation from different boundaries is affected by the wave vector in the media, the velocity of the particle and the distance between the boundaries.

The phase difference can be simplified using

$$\epsilon_{\mathrm{m}} = 1 - \xi_{\mathrm{m}}^2 \tag{3.11}$$

$$k_{\mathrm{m}} = \sqrt{\epsilon_{\mathrm{m}}}\omega \simeq \left(1 - \frac{1}{2}\xi_{\mathrm{m}}^2\right)\omega \tag{3.12}$$

$$\frac{1}{v} \simeq 1 + \frac{\gamma^{-2}}{2} \tag{3.13}$$

$$\vec{k}_{\mathrm{m}} \cdot \vec{l}_{\mathrm{m}} = k_{\mathrm{m}} l_{\mathrm{m}} \cos\theta \simeq k_{\mathrm{m}} l_{\mathrm{m}} \left(1 - \frac{1}{2}\theta^2\right) \tag{3.14}$$

resulting in

$$\varphi_{\mathrm{m}} = \frac{(\gamma^{-2} + \theta^2 + \xi_{\mathrm{m}}^2)\omega l_{\mathrm{m}}}{2}. \tag{3.15}$$

Defining the formation length

$$z_{\mathrm{m}} = \frac{2}{(\gamma^{-2} + \theta^2 + \xi_{\mathrm{m}}^2)\omega} \tag{3.16}$$

it is seen that with $l_{\mathrm{m}} \ll z_{\mathrm{m}}$ the two boundaries of the m'th media will have negative interference, i.e. they add up with opposite sign and equal magnitude in (3.8), resulting in no transition radiation. The interpretation is that creation of transition radiation is in fact a macroscopic effect and the effect that there is no transition radiation if the layers have below a certain thickness is called the formation zone effect.

For a single foil placed in a gas with no absorption

$$\left(\frac{\mathrm{d}^2W}{\mathrm{d}\omega\mathrm{d}\Omega}\right)_{1\text{ foil}} = 4\sin^2(\varphi_1/2)\left(\frac{\mathrm{d}^2W}{\mathrm{d}\omega\mathrm{d}\Omega}\right)_{1\text{ boundary}} \tag{3.17}$$

using (3.1), (3.4) and (3.8). Since the interference $\exp(\mathrm{i}\varphi_{\mathrm{m}})$ is included in the angular integration of the radiated energy it turns into a complicated integral. In the literature [32] it is expressed in terms of the dimensionless variables ν and Γ

$$\nu = \frac{2\omega}{l_1\omega_{\mathrm{P}_1}^2} \tag{3.18}$$

$$\Gamma = \frac{2\gamma}{l_1\omega_{\mathrm{P}_1}}. \tag{3.19}$$

The variables ν and Γ are defined such that $\nu, \Gamma > 1$ is the region where the transition radiation is strongly suppressed due to the formation zone effect.

For a single foil placed in vacuum

$$\left(\frac{\mathrm{d}W}{\mathrm{d}\omega}\right)_{1\text{ foil}}^{\text{vacuum}} = \frac{2\alpha}{\pi}G(\nu,\Gamma) \tag{3.20}$$

with $G(\nu,\Gamma)$ plotted in fig. 3.5. The broad maximum around $\nu = 1/\pi$ is important for the design of a detector as will be described in section 3.5. Equation (3.20) only applies to the case with vacuum outside the foils, $\omega_{\mathrm{P}_2} = 0$, but can be extended to the non-vacuum situation through the introduction of ω'_{P_i} and γ' defined as:

$$\omega'_{\mathrm{P}_1} = (\omega_{\mathrm{P}_1}^2 - \omega_{\mathrm{P}_2}^2)^{1/2} \tag{3.21}$$

$$\omega'_{\mathrm{P}_2} = 0 \tag{3.22}$$

$$\gamma' = (\gamma^{-2} + \omega_{\mathrm{P}_2}^2/\omega^2)^{-1/2}. \tag{3.23}$$

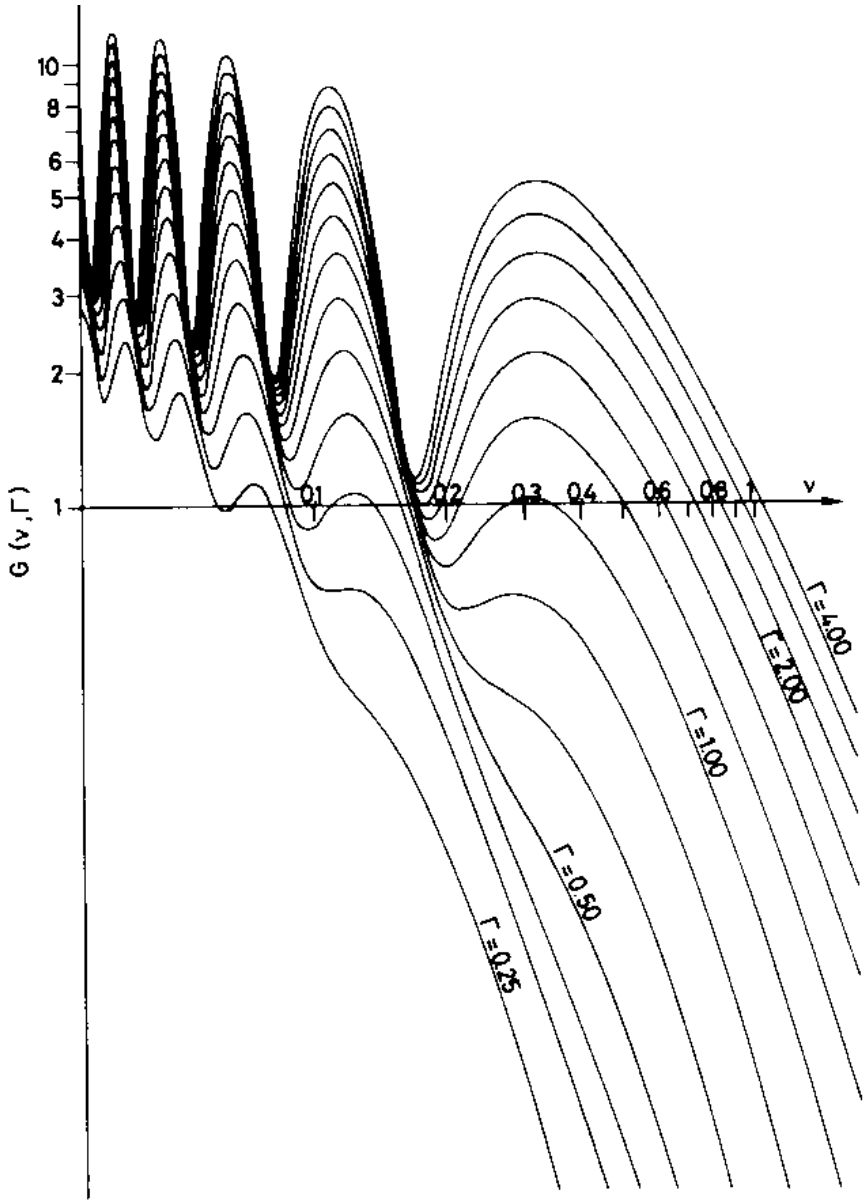

Figure 3.5: The transition radiation yield from a single foil expressed through the universal function $G(\nu, \Gamma)$. Note the broad maximum around $\nu = 1/\pi$. From [32].

In (3.1), (3.4) and (3.8) γ^{-2} and ξ_i^2 enters only in the combination $\gamma^{-2}+\xi_i^2$ which is preserved when substituting ω_{P_i} and γ by ω'_{P_i} and γ'. The substitution transforms the general case into the case with vacuum between the foils and (3.20) can be used in the form

$$\left(\frac{\mathrm{d}W}{\mathrm{d}\omega}\right)_{1\text{ foil}} = \frac{2\alpha}{\pi}G(\nu',\Gamma'), \tag{3.24}$$

where ν' and Γ' are defined using ω'_{P_1} and γ' in (3.18) and (3.19).

From (3.21) it is seen that $\omega'_{\mathrm{P}_1} < \omega_{\mathrm{P}_1}$ and $\gamma' < \gamma$ results in a lower yield from a detector with gas instead of vacuum between the foils. Also the nice feature of a linear response to γ as seen in (3.6) disappears. Instead there is a saturation in the transition radiation at

$$\gamma \geq \gamma'(\gamma=\infty) = \frac{\omega}{\omega_{\mathrm{P}_2}}. \tag{3.25}$$

3.3 N foils placed with regular spacing

In analogy to (3.17) the radiated energy from a radiator with N equal foils with regular spacing is

$$\left(\frac{\mathrm{d}^2W}{\mathrm{d}\omega\mathrm{d}\Omega}\right)_{\text{N foils}} = \left(\frac{\mathrm{d}^2W}{\mathrm{d}\omega\mathrm{d}\Omega}\right)_{1\text{ foil}} \left|\frac{1-C^{\mathrm{N}}}{1-C}\right|^2 \tag{3.26}$$

where

$$C = \exp\left(\mathrm{i}\varphi_1 + \mathrm{i}\varphi_2 - \frac{1}{2}\sigma_1 - \frac{1}{2}\sigma_2\right). \tag{3.27}$$

The mean value of the interference factor in (3.26) shows how much is gained from having several foils. It can be defined as an effective number of foils[1]

$$\mathrm{N_{eff}} = \frac{1-e^{-\mathrm{N}(\sigma_1+\sigma_2)}}{1-e^{-(\sigma_1+\sigma_2)}}. \tag{3.28}$$

For $\mathrm{N}\sigma \ll 1$ the yield is proportional to N while for $\mathrm{N} > 1/\sigma$ there is as much X-rays absorbed as new are generated resulting in a saturation with $\mathrm{N_{eff}} = 1/\sigma$.

From (3.26) and (3.27) its clear that there will be a dense interference pattern with resonances at emission angles θ where

$$\varphi_1 + \varphi_2 = 2p\pi, \quad p \text{ integer} \tag{3.29}$$

or

$$\frac{(\gamma^{-2}+\theta^2+\xi_1^2)\omega l_1}{2} + \frac{(\gamma^{-2}+\theta^2+\xi_2^2)\omega l_2}{2} = 2p\pi, \quad p \text{ integer} \tag{3.30}$$

[1] It is here assumed that the distance between the foils is larger than the formation zone.

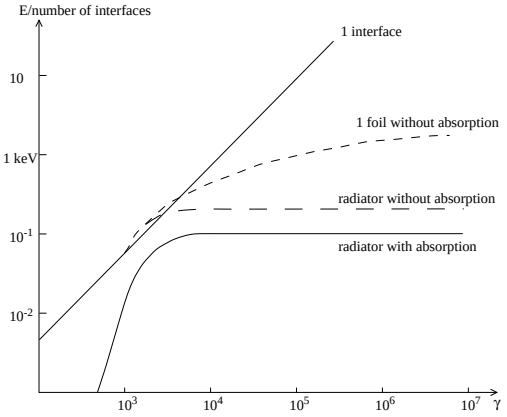

Figure 3.6: Energy radiated from a radiator with N foils compared to a single interface or 1 foil. The radiator has 400 layers of 20μm polypropylene with gaps of 180μm helium. It can clearly be seen how a detector with a multifoil radiator can act as a threshold detector. From [33] with minor corrections.

from (3.15). However, it is not possible to measure the angular distribution and after the integration of emission angles θ the distribution is similar to (3.24) as plotted in fig. 3.5, just scaled by N_{eff}. In fig. 3.6 the energy from a radiator with regular spaced foils is compared to the situation with a single interface or one foil. From the figure it is clear how a detector with a multifoil radiator can be used as a threshold detector for particle identification. Electrons exceeds a γ factor of 1000 at energies of 0.5 GeV while pions first pass this limit at 140 GeV. Hence in the large energy interval from 0.5 GeV to 140 GeV electrons will create full transition radiation while there will be practically no radiation from pions.

Radiators can be made of foam or fibres instead of regular foils. The irregularities in the thickness and spacing of the boundaries will cause a lower performance per unit length compared to regular foils. However, for practical solutions foam and fibres can have advantages in terms of larger flexibility in the fabrication and placement of the radiator.

3.4 The detection gas

The transition radiation created by the radiator has to be detected. Radiation in the keV range is best absorbed by an element with high atomic weight which has low lying atomic energy levels. Xenon is such an element and as a gas it can be implemented as detection gas in proportional chambers.

The detection gas registers both the energy from the absorbed photons and the ionisation from the primary particle. The particle identification is based on the difference between ionisation from a primary hadron and the sum of transition radiation

and ionisation from a primary electron. Thus a correct understanding of the ionisation in the detection gas is just as important as the understanding of the creation and absorption of transition radiation to evaluate the performance of a detector.

3.4.1 Absorption of transition radiation photons

The emission of X-rays from the radiator has to be matched to the absorption method used for the detection. If the ionisation of a gas is used for detection, the frequency response is rather limited with a high Z gas like Xe as the optimal choice. The absorption length for photons in the gas scales is approximately proportional to ω^3 in the range below 1 MeV where the photoelectric effect is dominant. Hence it is impossible for a practical gaseous detector to detect X-rays above 20 keV. The absorption length is defined as the length where a factor $1 - e^{-1}$ of the radiation is absorbed.

In fig. 3.7 is shown the absorption length for a pure xenon gas, the gas mixture chosen for the ATLAS TRT, polypropylene and Kapton. The absorption in a polypropylene radiator can be found by scaling the values for solid polypropylene with the air/foil proportion in the radiator.

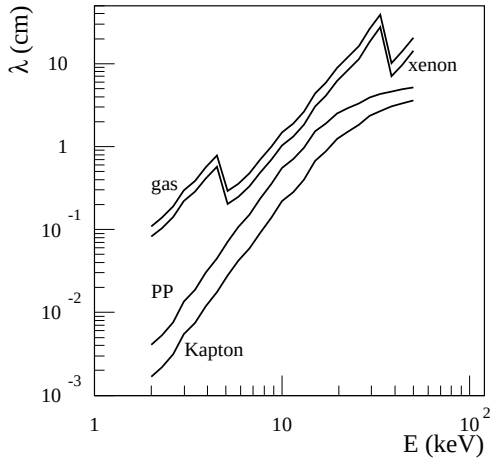

Figure 3.7: The absorption length for photons in xenon, the ATLAS TRT gas, Kapton and a polypropylene (PP) at standard temperature and pressure.

For high photon energies (above 20 keV) the detection efficiency is low as the photons pass straight through the detection gas; for low photon energies (below a few keV) the efficiency is low as well as most transition radiation photons are absorbed inside the radiator or in the walls surrounding the detection gas. Those two constraints define an optimal photon energy, ω_{gas}, for detection.

The foil thickness l_1 in a N-foil radiator can be adjusted to make the maximal output correspond to ω_{gas}. In fig. 3.5 is shown that the maximum output is around $\nu = 1/\pi$. Using (3.18) and (3.21)

$$l_{1_{\text{optimal}}} = \frac{2\pi\omega_{\text{gas}}}{\omega'^{\,2}_{\text{P}_1}}. \tag{3.31}$$

3.4.2 Ionisation from charged particles

Transition radiation photons are emitted in the in the same direction as the charged particle creating the radiation, hence the energy deposition in the detection gas will be from both the transition radiation photons and the ionisation caused by the same particle. As both pions and electrons will ionise the gas a detailed description of the ionisation is required for the understanding of the performance of a transition radiation detector for particle identification.

The Bethe-Bloch formula for the energy loss of a charged particle in a medium is well known but gives only the mean integrated energy loss. This is shown for a selection of materials in fig. 3.8. The relativistic rise makes the energy loss increase for $\beta\gamma$ above the minimum ionising point at $\beta\gamma = 3.5$. The rise is limited by the polarisation of the media which depends on the electron density and the relativistic rise is thus most suppressed for high density media. The result is that gases, with low electron density, have a large relativistic rise. For xenon at 1 atm the relativistic rise is around 75% [36].

The mean value of the total energy loss is given from the Bethe-Bloch formula but the fluctuations are large due to a low number of high energy ionisations. The energy loss distribution is given by the Landau distribution and shown in fig. 3.9. The long *Landau tail* towards high energies is a result of the large fluctuations in the high energy ionisations.

To simulate the true signal in a proportional chamber it is necessary to use a much more detailed model that gives the distribution of the individual ionisations along the track and their energies.

The photo absorption ionisation (PAI) model was first in detail described in [38]. It was developed using a semi-classical approach, that starts with the Maxwell equations for a charged particle traversing a medium with dielectric constant ε. In this way the energy loss is expressed as

$$\frac{\mathrm{d}E}{\mathrm{d}x} = \frac{e\vec{E}\cdot\vec{\beta}}{\beta} \tag{3.32}$$

where $\vec{\beta}$ is the velocity vector of the charged particle and $\vec{E}$ the electric field created by the particle itself evaluated at the point of the particle. Making a Fourier transform of the electric field the energy loss can instead be described as a continuous energy

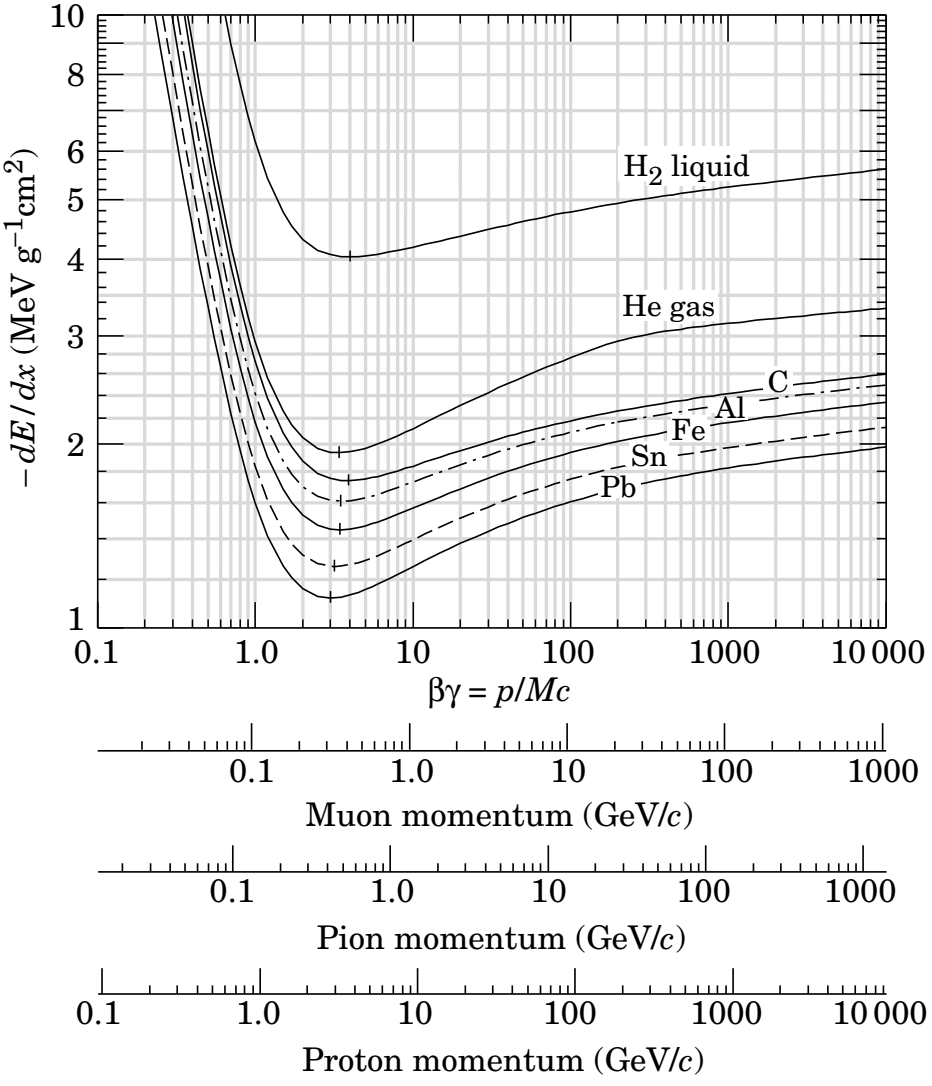

Figure 3.8: The energy loss of a charged particle in a range of materials. From [37].

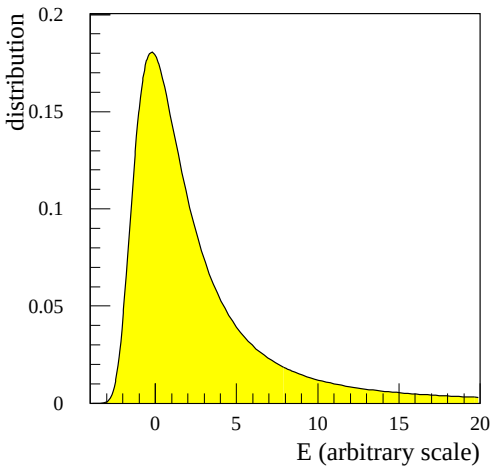

Figure 3.9: The Landau distribution of the total energy loss across a gas volume. Note the long *Landau tail* on the distribution.

loss in different frequency regions [38]. The result is

$$\begin{aligned}\frac{\mathrm{d}E}{\mathrm{d}x} = -\frac{\alpha}{\beta^2\pi}\int_0^\infty \mathrm{d}\omega \Big[\frac{n_\mathrm{e}}{Z}\sigma(\omega)\log[(1-\beta^2\varepsilon_1)^2+\beta^4\varepsilon_2^2]^{-1/2} \\ + \omega\left(\beta^2 - \frac{\varepsilon_1}{|\varepsilon|^2}\right)\Theta + \frac{n_\mathrm{e}}{Z}\sigma(\omega)\log\left(\frac{2m_\mathrm{e}\beta^2}{\omega}\right) \\ + \frac{1}{\omega}\int_0^\infty \mathrm{d}\omega'\frac{\sigma(\omega')}{Z}\Big]\end{aligned} \tag{3.33}$$

with $\varepsilon(\omega) = \varepsilon_1 + \mathrm{i}\varepsilon_2$ the dielectric constant, n_e the electron density, and Z the atomic number. The dielectric constant can be expressed by the atomic photo absorption cross section $\sigma(\omega)$ through the relations[2]

$$\varepsilon_2(\omega) = \frac{n_\mathrm{e}}{Z\omega}\sigma(\omega) \tag{3.34}$$

$$\varepsilon_1(\omega) = 1 + \frac{2}{\pi}\frac{n_\mathrm{e}}{Z}\int_0^\infty \mathrm{d}\omega'\frac{\sigma(\omega')}{\omega'^2-\omega^2}. \tag{3.35}$$

The only remaining term is $\Theta = \arg(1-\varepsilon^*\beta^2)$ which is responsible for the Cherenkov radiation. The photo absorption cross section is related directly to the absorption length in the gas through the relation

$$\lambda = \frac{A}{N_A\sigma} \tag{3.36}$$

[2] This is an approximation for low density media like a gas.

where A is the atomic weight and N_A Avogadros number. For composite gases a mean cross section weighted with the atomic weight of the different components will give an accuracy of a few percent in the absorption length [37]. Both the cross section and the absorption length for xenon is shown in fig. 3.10.

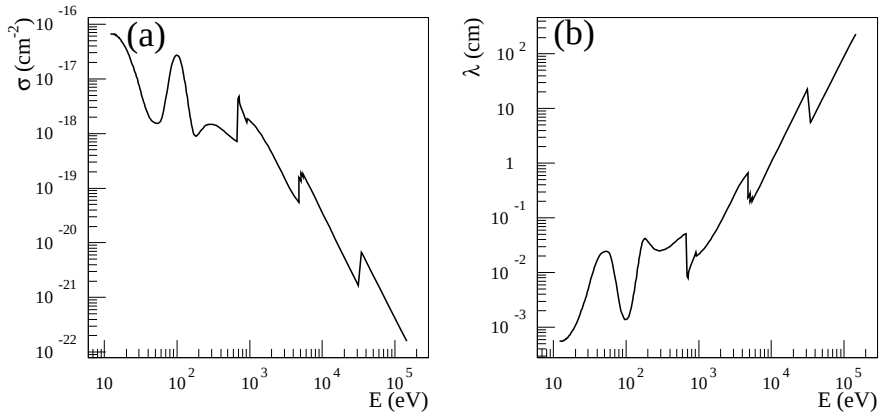

Figure 3.10: The photo absorption cross section (a) and the absorption length at 1 atm (b) for xenon.

The energy loss in (3.33) describes a continuous energy loss. It can, however, be reinterpreted as a number of discrete collisions with energy transfer ω. This is the semi-classical approach following the same line as Plancks derivation of the black body spectrum. The result following directly from (3.33) is

$$\left\langle \frac{\mathrm{d}E}{\mathrm{d}x} \right\rangle = -\int_0^\infty \mathrm{d}\omega n_\mathrm{e} \omega \frac{\mathrm{d}\sigma}{\mathrm{d}\omega}, \tag{3.37}$$

with the differential cross section

$$\begin{aligned} \frac{\mathrm{d}\sigma}{\mathrm{d}\omega} = -\frac{\alpha}{\beta^2 \pi} \Bigg[& \frac{\sigma(\omega)}{\omega Z} \log[(1-\beta^2\varepsilon_1)^2 + \beta^4 \varepsilon_2^2]^{-1/2} \\ & + \frac{1}{n_\mathrm{e}} \left(\beta^2 - \frac{\varepsilon_1}{|\varepsilon|^2} \right) \Theta + \frac{\sigma(\omega)}{\omega Z} \log \left(\frac{2 m_\mathrm{e} \beta^2}{\omega} \right) \\ & + \frac{1}{\omega^2} \int_0^\infty \mathrm{d}\omega' \frac{\sigma(\omega')}{Z} \Bigg]. \end{aligned} \tag{3.38}$$

3.5 Considerations for design

A practical transition radiation detector needs to take into account all the physics from the preceding sections. In most cases the length of the detector, L_det, is fixed

either as the length along the beamline in a fixed target experiment or as the radial space in a colliding beam detector.

With a fixed detector length, optimisation is required for.

- The composition of the foils and the gas between them in the radiator.
- The foil thickness l_1, to get the correct wavelength distribution of the transition radiation.
- The distance between the foils l_2, which needs to be large enough to avoid formation zone effects as derived in (3.16).
- The number of foils, N_{foil}, in front of a detecting gas.
- The gas composition and the thickness of the gas l_{gas} .

The choice of xenon as the detecting gas is obvious from its short absorption length as seen in fig. 3.7. With a gas thickness of around 0.5 cm there is large absorption up to 10 keV. In the figure is also seen that 4 keV photons have an absorption length of just 300 μm in a typical radiator foil giving only a small window for detecting transition radiation with $\omega_{gas} \simeq 7$ keV.

For the foil material where low absorption is important a low Z material is the best. Since lithium and beryllium are reactive materials the best practical choices are carbohydrates like polyethylene or polypropylene. The gas between the foils in the radiator has to have as low electron density as possible to achieve a low plasma frequency and thereby limit the saturation effect (3.25). Helium is this aspect is the best choice with $\gamma'_{max} = 26000$ while for air $\gamma'_{max} = 9600$ for a 7 keV photon energy.

With ω_{gas} and the radiator composition fixed the optimal foil thickness can be calculated from (3.31) and table 3.1 giving $l_{1_{optimal}} \simeq 20$ μm. The actual thickness of the foil has then to take into account a typical crossing angle between the particles and the foil.

Material	ω_P (keV)	ρ (g/cm^3)
polypropylene	20.87	0.935
helium	0.27	$0.18 \cdot 10^{-3}$
air	0.73	$1.29 \cdot 10^{-3}$
Kapton	24.5	1.39
xenon	1.42	$5.89 \cdot 10^{-3}$
$Xe/CF_4/CO_2$	1.70	$4.80 \cdot 10^{-3}$

Table 3.1: Plasma frequencies and densities for typical materials in a transition radiation detector and a 70/20/10 mixture of $Xe/CF_4/CO_2$.

To perform well for emission angles above $\theta > 0.2$ mrad (fig. 3.2) and for X-rays above 4 keV, (3.16) gives a minimum spacing of the foils of $l_{2_{minimal}} \simeq 1.3$ mm with air as the medium between the foils. For helium the minimum spacing is 2.2 mm.

The effective number of foils can now be calculated from (3.9) and fig. 3.7. The effective number of foils is below 35 for 5 keV X-rays. Hence not much is gained by having $N_{foil} > 35$.

Adding up the different lengths gives

$$l_{det} = N_{foil}(l_1 + l_2) + l_{gas} \approx 45 \text{ mm} \tag{3.39}$$

with only a small gain by increasing this length. At the same time the detector is not very efficient with an average number of photons

$$n_\gamma = 4 n_{\gamma_{\text{single boundary}}} N_{eff} \approx 0.5 \tag{3.40}$$

created for an electron passing. Or rephrased: only every second electron passing the detector will emit a single transition radiation photon. The factor four comes from the optimised thickness of the foil for positive interference.

The solution to the problem is to place multiple copies of the radiator and detection gas behind each other. This also opens up the possibility to combine the particle identification with tracking.

To measure the energy deposited as ionisation in the xenon gas there are 2 methods called the Q and the N method.

In the Q method, one measures with ADC's or FADC's the total energy deposited in the gas which is a sum of the transition radiation in the radiator and $\frac{dE}{dx}$ from the particle which also passes through the detecting gas. The method is sensitive to background from the Landau tail of $\frac{dE}{dx}$. Since the Q method is mainly sensitive to the X-rays with the highest energies, the number of foils can be enlarged in each layer because the absorption of X-rays in the radiator is only important for the soft part of the spectrum.

The N method instead, counts the number of clusters in the gas. A cluster is the volume of the gas where the ionisation from the electron knocked out by the X-ray photon is deposited. It typically has a diameter of 1 mm. This method is not very sensitive to $\frac{dE}{dx}$ since the main part of the ionisation is spatially spread out. The background mainly comes from δ-electrons which are electrons kicked out of the atomic shells by the primary particle with an energy high enough to make ionisation themselves.

While the Q method is expensive to implement for a multilayered detector with separate ADC's for each layer of detecting gas, the N-method can be incorporated in a multilayered detector in an elegant way. A threshold on the deposited energy in a single layer can give a simple yes/no answer if there was a cluster in a given layer. The probability for multiple clusters in a single layer is low and only a few clusters will be lost by just having a binary output. With a fixed probability for a cluster in each layer, particles passing all the layers will have a binomial distribution in the number of layers with a cluster registered.

The N method has to distinguish between two different binomial distributions from pions and electrons respectively for particle identification. The distributions have different average values and for binomial distributions there are no suffering from long Landau tails as with the Q method.

Since the total length of the detector is fixed and the length of each layer given by (3.39) also the number of layers is fixed. However, for the N method what counts is the mean number of clusters in all layers given by

$$<n_{\text{cluster}}> = N p_{\text{layer}} \tag{3.41}$$

where N is the number of layers and p_{layer} the probability for a cluster in each layer. This can also be expressed in terms of the number of detected clusters per unit length

$$A_{\text{TR}} = \frac{\mathrm{d}N_{\text{clusters detected}}}{\mathrm{d}L}. \tag{3.42}$$

While the lower limit on l_2, defined by the formation zone effect, is not very stringent the thickness of the Xe absorption layers are fixed and hence

$$N = \frac{L_{\text{det}}}{\mathrm{N}_{\text{foil}}(l_1 + l_2) + l_{\text{gas}}} \tag{3.43}$$

reaches a saturation when $\mathrm{N}_{\text{foil}} l_2$ is reduced to the point where $\mathrm{N}_{\text{foil}}(l_1 + l_2) = l_{\text{gas}}$. Detailed simulations using the model described in section 5.6 shows an optimal performance for $\mathrm{N}_{\text{foil}} \simeq 20$ and $l_2 \simeq 0.3$ mm. The maximal performance achievable is $A_{\text{TR}} \simeq 0.15$ cluster/cm [35].

3.6 Previous transition radiation detectors

Transition radiation detectors have been implemented in many different experiments in high energy physics mainly for electron pion separation but also for separation of pions and heavier hadrons. However, the relative mass difference between pions and kaons is so small that only a limited rejection power of kaons can be achieved for pion identification. A summary of specifications and performances of transition radiation detectors is given in table (3.2).

Experiments	R806	E715	NA34	UA6	UA2	E769	NA31	NA24
length (cm)	55	360	70	55	22	130	110	60
number layers	2	12	8	3	2	24	4	4
radiator	Li	CH_2	CH_2	Li	CH_2	CH_2	CH_2	CH_2
method	Q	N	N	Q	Q	N	Q	N
efficiency π (%)	5	0.06	0.05	10	8	2	10	0.5
efficiency e (%)	90	99	90	90	80	87	98.7	80

Table 3.2: Performance of detectors used for electron pion separation in different experiments. The *method* row refers to the Q and N method as described in section 3.5. The rejection is the efficiency for pions at the efficiency of electrons given in the row below. From [35] with minor changes of notation.

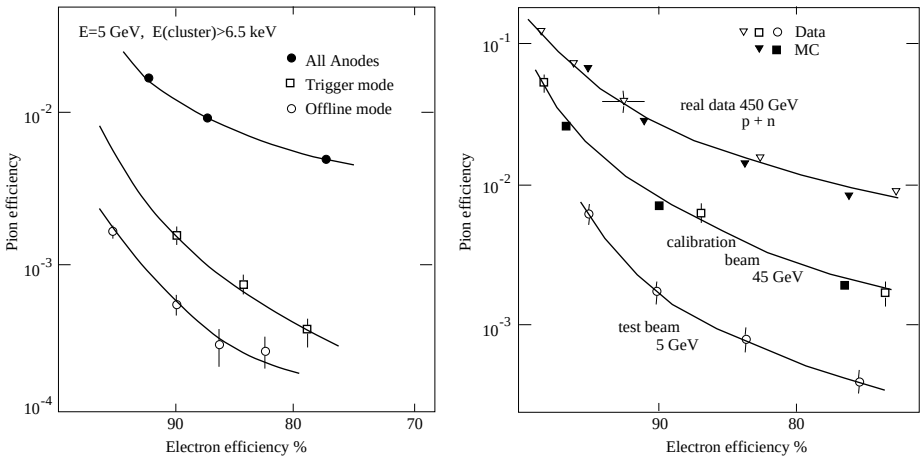

Figure 3.11: Performance of the HELIOS TRD. The first figure shows how the rejection power improves by including information on the position of the track. The information was first obtainable at the offline analysis. The second figure indicates the effect of having a high occupancy environment with many overlapping tracks in the proton-nucleus collisions. From [35].

The HELIOS TRD (NA34) is the only transition radiation detector which has combined the tracking and the transition radiation detection in the same way as is planned for the ATLAS TRT.

The HELIOS experiment was an experiment for to study lepton production in proton-nucleus collisions. To select the electrons in the busy environment of background hadrons a large rejection power was needed. This was achieved with a combination of an uranium/liquid argon calorimeter and a transition radiation detector. The TRD had 8 layers each consisting of 200 foils of 12.7μm polypropylene and a multiwire proportional chamber filled with xenon for the X-ray detection. In this detector it proved powerful to have the tracking together with the detection of transition radiation since this made it possible to sort out background from δ-electrons from other tracks as seen in fig. 3.11.

With the HELIOS TRD is was also proved that it is possible to operate a TRD with many overlapping tracks in the detector, however, with a reduced rejection of pions. The effect was fully understood as indicated in the second part of fig. 3.11 where both data points and Monte Carlo simulations are plotted.

Chapter 4

Design of the ATLAS detector

The ATLAS detector is a multi-purpose detector designed for physics studies at the LHC. The detector is optimised simultaneously for a long range of known and hypothetical processes; this introduces compromises for specific processes, but on the other hand gives a detector which is well prepared for the discovery of completely new phenomena. The overall design of ATLAS is shown in fig. 4.1. The detector is a cylinder with a total length of 42 m and a radius of 11 m.

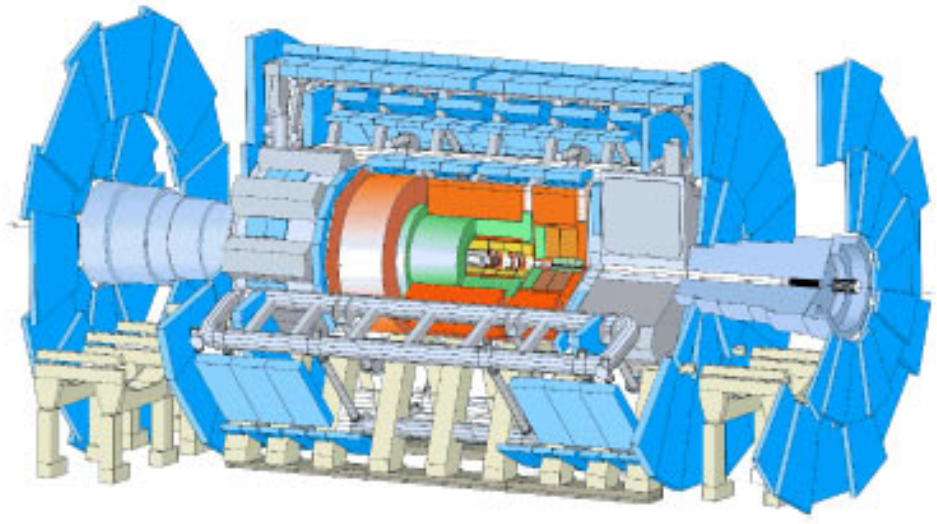

Figure 4.1: The design of the ATLAS detector. The detector is 42 m long and 22 m in diameter.

The coordinate system of ATLAS is a right-handed coordinate system with the x-axis pointing towards the centre of the LEP/LHC tunnel, and the z-axis along the tunnel. The y-axis is slightly tilted with respect to vertical from the general tilt of the tunnel. The coordinate system is shown in fig. 4.2. The pseudorapidity of particles from the primary vertex is defined as

$$\eta = -\log\tan\frac{\theta}{2} \tag{4.1}$$

where θ is the polar angle of the particle direction measured from the positive z-axis. Transverse momentum, p_{T}, is defined as the momentum perpendicular to the LHC beam axis.

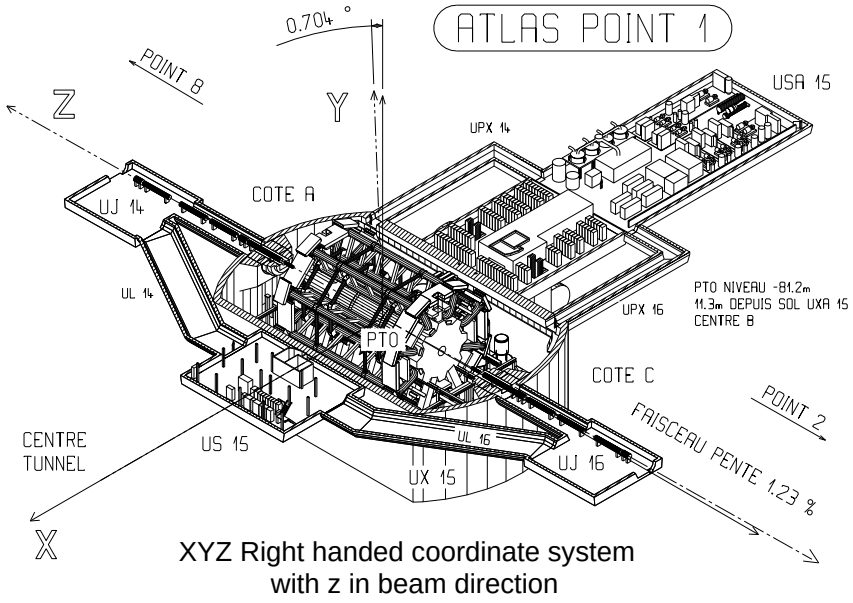

Figure 4.2: The coordinate system in the ATLAS detector. The general tilt of the LEP/LHC tunnel causes the y-axis to be slightly different from vertical.

Magnetic fields are required for charge identification and momentum measurements. ATLAS has a double configuration with a solenoid 2 T field close to the interaction point and a toroid 1–2 T field in the outermost part of the detector.

The inner tracking detector with half length 3.40 m and radius 1.15 m resides inside the solenoid and consist of silicon detectors and a straw tracker. The silicon layers are pixel layers closest to the interaction point and strip detectors outside this. The straw tracker is simultaneously a transition radiation detector adding to the electron identification power of ATLAS.

A liquid argon electromagnetic sampling calorimeter with layers of lead and liquid argon is placed outside the solenoid coil. In the forward direction it reaches down to $\eta = 3.2$. The hadronic calorimeter is a scintillator tile calorimeter in the central region and a continuation of the electromagnetic liquid argon calorimeter in the forward regions. The total dimensions of the calorimeter is 2.25 m in radius and a half length of 6.65 m.

The outermost part of the ATLAS detector is the muon system. The toroid magnetic field is made with an air core resulting in low multiple scattering for muons passing. The combination of a long barrel magnetic system with two inserted end-cap toroids makes the magnetic field reach to $\eta = 2.7$. The muon drift chambers are placed in three layers with one layer inside the magnetic field and a layer on each side. Fast trigger chambers with a lower resolution are implemented separately for the trigger system.

A special problem for a detector at the LHC is the large radiation doses. The complete ATLAS detector is subjected to radiation from low energy neutrons and accompanying photons from nuclear interactions. The neutrons are mostly created in the forward region ($|\eta| > 5$) but spread out in the complete detector with their low absorption rate. For the Inner Detector charged particles from the primary collisions will be an equally important factor. For the ATLAS detector to survive for at least 10 years, radiation hard technologies will be used for both the detectors and the readout electronics.

4.1 Magnet system

The solenoid magnet is placed inside the electromagnetic (EM) calorimeter. This is different from most other detector designs where the magnet is placed outside the EM calorimeter. The advantage of the small solenoid is a compact design. A small magnetic field in the EM calorimeter also reduces the transverse spread of showers. The major problem is the increased amount of material in front of the calorimeter which causes many particles to start showering before they reach the active part of the calorimeter.

The solenoid is a superconducting magnet kept at 4.5 K. To reduce the material the magnet does not have a separate cryostat but rather it shares the cryostat with the liquid argon calorimeter thus saving two cryostat walls. The half length of 2.65 m is considerably shorter than the inner tracking detector. This is a result of a compromise: a short coil reduces the material in front of the calorimeter; a long coil makes the magnetic field more uniform in the Inner Detector. The magnetic field along the z-direction drops from 2 T at the interaction point to around 0.5 T at the end of the Inner Detector.

The toroid magnet system is divided into one barrel part and two forward systems. With a toroid field, particles will across the complete pseudorapidity range, be almost perpendicular to the field. This means that the field integral $\int B\mathrm{d}l$, which is the important factor for momentum resolution, can be kept high even in the forward direction. The structure is open with 8 coils in the central region each in separate

cryostats. One of the rectangular shaped cryostats can be seen in the front of fig. 4.1. In the forward direction the toroid field is also formed by 8 superconducting coils but there placed in a common cryostat.

The low number of coils to form the toroid field results in a field strength that varies strongly with the ϕ coordinate. The field integral varies in the barrel from 2–6 Tm and in the end-caps from 4–8 Tm. This is not ideal but an economical necessity.

4.2 The muon system

The identification of leptons is important for an experiment working at a high energy proton-proton collider as already described in chapter 1. The ATLAS muon system serves a double purpose as a trigger to select events with high energy muons and as a precision muon spectrometer. The general layout of the muon system is shown in fig. 4.3.

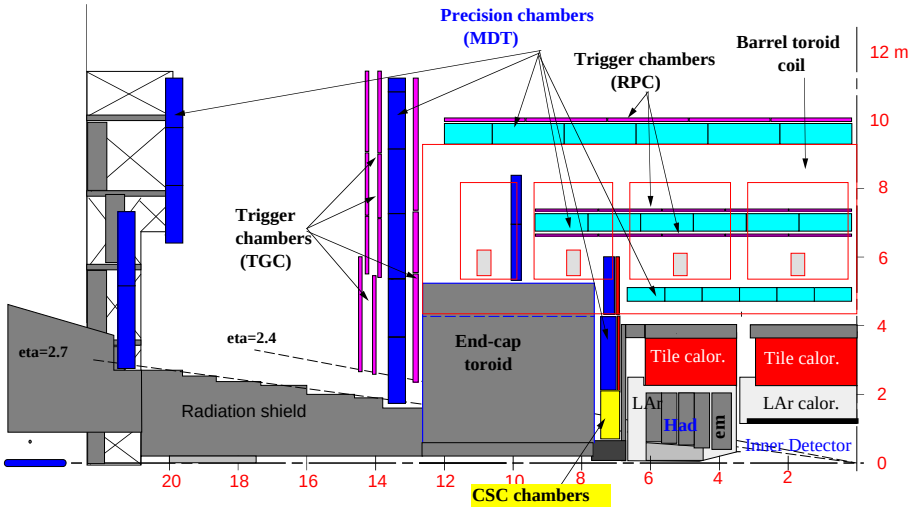

Figure 4.3: Side view of the muon system. The third layer of detectors in the forward region are mounted on the cavern wall.

In the most compact and cost efficient way the design of the muon system has to fulfil a set of conditions:

- A good transverse momentum resolution in the low p_T region. The limit is defined by the ability to detect the $H \rightarrow ZZ^*$ decay in the muon channel with a high suppression of the background. A resolution of around 1% is required for this.

- At the highest p_{T} the muon system should have sufficient resolution to give good charge identification for an identification of a $\mathrm{Z}' \to \mu\mu$ decay.
- A rapidity coverage $|\eta| < 3$. A smaller rapidity coverage will strongly reduce the number of events with a high mass object decaying to muons with all muons inside the covered region.
- A hermetic system to prevent particles to escape through holes.
- Measurement of spatial coordinates in 2 dimensions to provide good mass resolution.
- A low rate of both punch through hadrons and fake tracks.
- A trigger system for almost all physics channels. The requirement on rapidity coverage is similar to the requirement for the main muon system. For B-physics a maximal coverage for muons with transverse momentum down to 5 GeV is desirable.

Particles from the primary vertex traverse three sets of muon chambers. In the barrel part of the detector one set of chambers is placed inside the toroid and the momentum measured from the sagitta of the tracks. In the end-caps, where the toroid cryostat prevents chambers from being placed inside the magnetic field, the muon momentum is measured from the difference in entry and exit angle of the magnet.

The Monitored Drift Tube (MDT) chambers are proportional chambers made of aluminium tubes of 30 mm diameter and lengths varying from 70 cm to 630 cm. To measure the coordinate in the bending plane of the magnet the tubes are placed transverse to the beam axis. Each set of MDT's consist of 2 superlayers each with 3 or 4 layers of tubes. The many tubes in each set are required to reduce the level of fake tracks reconstructed from random associations of background hits and to provide 100% efficiency for each set. A single MDT set is shown in fig. 4.4.

Each MDT has a resolution of 80 μm which results in a momentum resolution

$$\frac{\Delta p_{\mathrm{T}}}{p_{\mathrm{T}}} < 10^{-4}\ \mathrm{GeV}^{-1} \cdot p \tag{4.2}$$

for tracks with $p_{\mathrm{T}} > 300$ GeV. For tracks with lower transverse momentum the resolution is limited by multiple scattering and the stopping power of the hadron calorimeter.

The MDT's are not used in the forward region because of their long tubes resulting in a too high rate. Instead Cathode Strip Chambers are used which are multiwire proportional chambers with a wire spacing of 2.5 mm. Cathode strips arranged perpendicular to the anode wires give a second coordinate in the readout which, together with the much finer granularity compared to the MDT's, make it possible to find tracks in the forward region where the track density is higher compared to the barrel region.

The drift tubes have a large diameter which results in a maximum drift-time of 480 ns which is much longer than the 25 ns spacing between the bunch crossings.

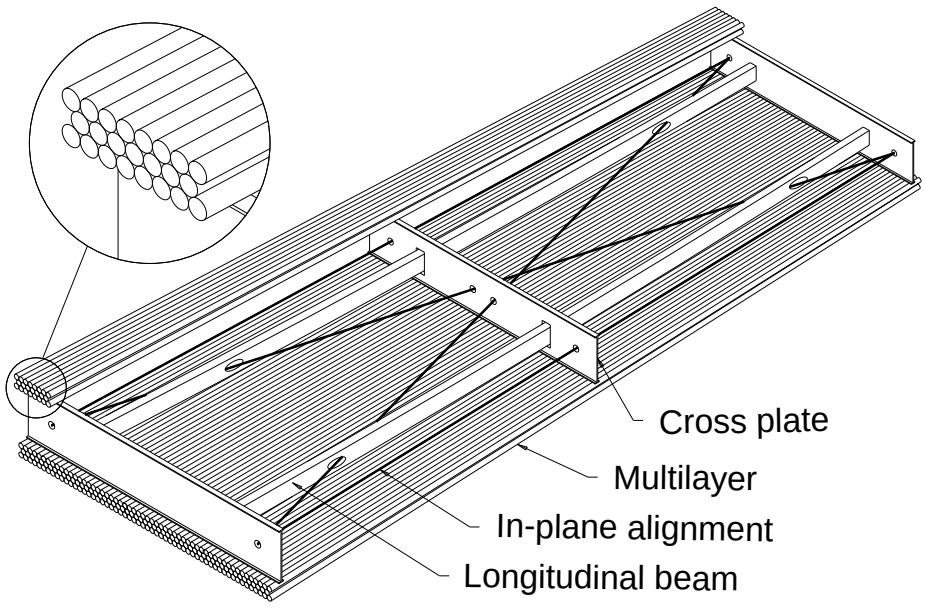

Figure 4.4: A set of Monitored Drift Tubes. Particles from the primary vertex traverse at least three such sets.

For this reason the tubes cannot be used for the trigger of the experiment. Instead special layers of trigger chambers are implemented.

A Resistive Plate Chamber (RPC) has a gas-gap between two resistive bakelite plates with metal strips. A uniform electric field between the plates creates avalanches when a particle cross the gas-gap and the induction from the avalanche is measured by the closest metal strips. The 2 mm thick gas-gap gives a fast detector with a 1 ns time resolution allowing the individual bunch crossings to be identified. The metal strips on each side of the detector are perpendicular to each other giving a position resolution of 1 cm in each plane. In the forward region the situation for the RPC's is the same as for the MDT's and multiwire proportional chambers are installed instead as trigger chambers.

Only the trigger chambers are read out for the level-1 trigger analysis. The lower spatial resolution of the trigger chambers provides a reduced but sufficient momentum resolution. Since the MDT's only give the η coordinate the trigger chambers also provide the φ coordinate for the tracks in the final analysis.

4.3 The calorimeter

A calorimeter is almost always divided into an electromagnetic and a hadronic calorimeter. The distinction is possible because of the different interaction behaviour

between the calorimeter and electrons/photons on one side and hadrons on the other side.

The development of electromagnetic showers from an incident electron or photon is a well understood process. The shower-to-shower variations in shape and registered energy are quite small for equal incident energy and hence a good resolution in the calorimeter also pays off in terms of a good resolution for the incoming particle energy. The size of an electromagnetic shower depends linearly on the radiation length X_0 of the calorimeter material.

The situation for incident hadrons is quite different. The nuclear processes involved show large variations in the amount of energy transferred to secondary $\pi^{\pm}$, π^0, neutrons etc. The neutral pions decay directly to photons and thus deposit their energy as electromagnetic showers. To compensate for this variation is difficult and the resolution in hadron energy is normally limited by the intrinsic variations in the shower and not the resolution of the calorimeter. The ratio between the response of the calorimeter for the purely hadronic and the purely electromagnetic part of the shower is called the e/h ratio. For a good energy resolution the value of e/h should be as close as possible to one. The size of hadronic showers depends linearly on the interaction length λ of the material which is always longer than the radiation length.

A calorimeter can be divided into a small electromagnetic (EM) calorimeter with high resolution closest to the interaction point and a larger hadronic calorimeter behind with a coarser resolution. A high density of the EM calorimeter makes the difference between radiation and interaction length large thus providing a good separation of the two types of showers and at the same time a compact EM calorimeter. To minimise the fluctuations in the response for the hadronic calorimeter a low Z material with interaction length and radiation length comparable is good. However, a compromise has to be made with the total size of the calorimeter which favours high density materials. A larger calorimeter means a larger muon system surrounding it and thus affects the cost of the total detector strongly.

Identification of electrons and photons are the most important issues for the calorimeters. The rate of QCD-jets is high and to be able to get a clean sample of electrons with transverse momentum above 20 GeV a rejection of QCD-jets at the level of 10^6 is required. Such a rejection can be achieved with a calorimeter of fine granularity in both the EM and hadronic part to identify isolated energy depositions from electrons/photons and to veto on hadronic energy behind the cluster in the EM calorimeter.

The design of the electromagnetic calorimeter is driven by the requirements for energy and spatial resolution for the Higgs processes involving decays to electrons or photons. The $H \rightarrow \gamma\gamma$ decay of a standard model Higgs has a large background and a mass resolution around 1% is required (see chapter 7). The dynamic range for the calorimeter ranges in transverse energy from around 1 GeV for electrons from B-meson decays to a few TeV for the decay of a heavy vector boson.

The reconstruction of jets is important for studies of quark compositeness. This sets stringent limits on the linearity of the hadronic calorimeter response at high energies. Also for the reconstruction of W bosons in hadronic decays the jet energy resolution is important as discussed in detail in chapter 8.

A measurement of missing transverse energy is a way to measure particles escaping the detector without interactions. This can either be neutrinos or stable supersymmetric particles. To identify missing transverse energy the calorimeter needs to have a good hermicity. This means that the rapidity coverage has to reach $|\eta| = 5$ and any cracks in the detector for cables and cooling has to be minimised. Also the hadronic calorimeter needs to be thick enough to avoid leakage of hadrons into the muon system which would both reduce the resolution in missing transverse energy and give background in the muon system. A compromise between the total size of the ATLAS detector, the stopping power of low energetic muons, an acceptable rate of punch through to the muon system and a good resolution in missing transverse energy, requires 11 absorption length of material in front of the muon system.

4.3.1 The liquid argon calorimeter

For the electromagnetic calorimeter in ATLAS is chosen a liquid argon sampling calorimeter. Layers of lead/stainless steel and liquid argon are interspaced. The lead gives the shower development with its short radiation length and the secondary electrons create ionisation in the narrow gaps of liquid argon. An inductive signal from the ionisation electrons drifting in the electric field across the gas-gap is registered by copper electrodes.

To achieve a low capacitance of the detecting elements and thereby a fast signal the lead plates have an accordion shape as shown in fig. 4.5. At the same time this creates a fully homogeneous calorimeter in the φ coordinate. In the central rapidity region there are four samplings:

Presampler A single thin layer of argon but no lead absorber in front. The purpose is to correct for the energy loss in the Inner Detector, solenoid and cryostat wall.

1st sampling The first sampling has a depth of 4.3 radiation lengths. The readout is, as seen in fig. 4.5, in thin η strips i.e. each strip has the size $(\Delta\eta \times \Delta\varphi) = (0.0031 \times 0.098)$. This provides an excellent resolution in the η coordinate for photon/π^0 separation. The φ coordinate is not suited for this since converted photons will open up in the magnetic field and produce clusters with widths similar to π^0 clusters.

2nd sampling The majority of the energy is deposited in the 16 radiation lengths of the second sampling. Clusters with energy below 50 GeV are fully contained and the noise can be reduced by not adding the 3rd sampling. For the position measurement of the cluster the 2 coordinates are equally important resulting in square cells of size $(\Delta\eta \times \Delta\varphi) = (0.0245 \times 0.0245)$.

3rd sampling Only the highest energy electrons will reach this deep in the detector. The clusters are at this point wide and the cell size can be doubled in the η direction without loss of resolution.

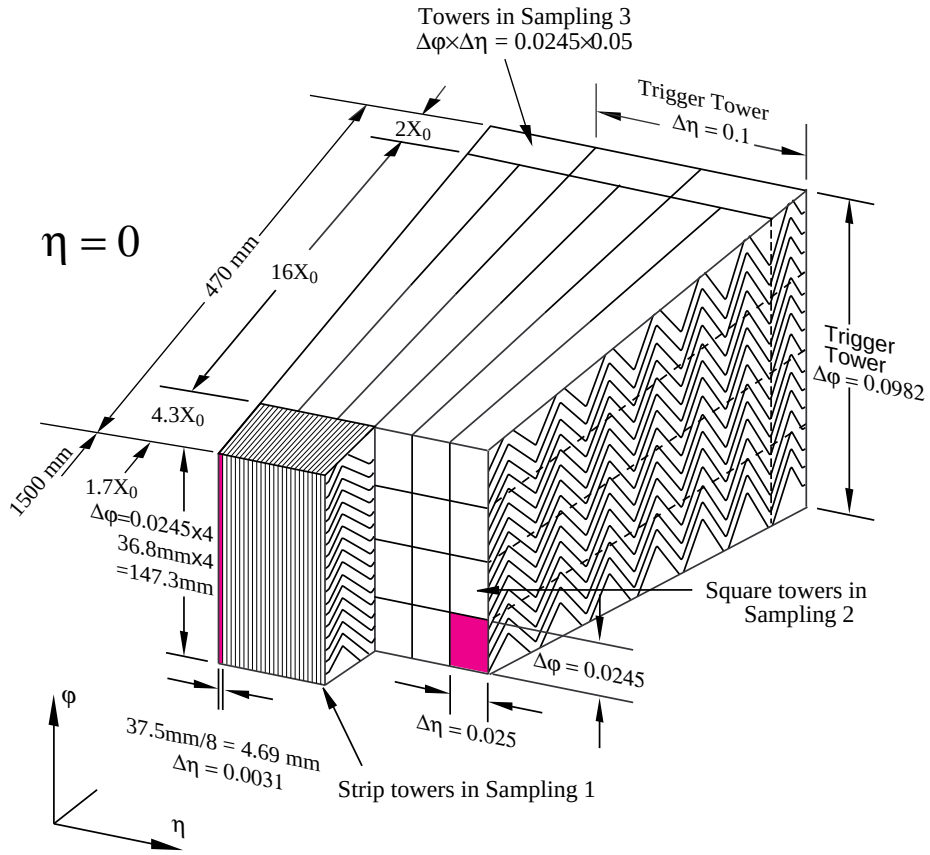

Figure 4.5: The structure of the barrel accordion calorimeter. The presampler is in front of the accordion.

In the end-cap there is less material in front of the calorimeter and the presampler can be avoided. The end-cap EM calorimeters start at $|\eta| = 1.5$ and continue down to $|\eta| = 3.2$ but with an increased cell size above $|\eta| = 2.5$. There is a crack with bad energy resolution where the end-cap and barrel calorimeters meet. A large effort has gone into reducing the size of the crack while still leaving space for cables and cooling for the Inner Detector.

The resolution of the EM calorimeter is

$$\frac{\Delta E}{E} = \frac{a}{\sqrt{E}} \oplus \frac{b}{E} \oplus c, \tag{4.3}$$

with energies measured in GeV. The sampling term a is defined by the number of lead/argon interfaces and is 8–11% depending on rapidity. Noise influences the resolution at the lowest energies through the term b which is of the order 400 MeV

when running at high luminosity. The constant term affects the resolution for high energy clusters and is limited by the calibration of the global energy scale and local variations in this. It is hard to predict but is believed to stay below 0.7%[1].

To withstand the high radiation levels in the forward region the hadronic calorimeter is also of liquid argon type in the end-caps. The design is simpler than the EM calorimeter and has parallel copper plates as absorbers placed perpendicular to the beam.

The very forward hadronic calorimeter with a coverage down to $|\eta| = 4.9$ is made of copper/tungsten. The choice of copper/tungsten is necessary to limit the width and depth of the showers from high energy jets close to the beam pipe, and to keep the background level low in the surrounding calorimeters from particles spraying out from the forward region. The calorimeter is a metal matrix with cylindrical holes. The holes have rods inside with a slightly smaller radius allowing for a liquid argon gap of just 250 μm. The small gap limits the sensitivity to pile-up effects which are large close to the beam pipe where energetic jets often hit the same area of the calorimeter.

4.3.2 The tile calorimeter

The tile calorimeter of ATLAS is the hadron calorimeter in the central rapidity region reaching out to $|\eta| = 1.7$ where the liquid argon hadronic calorimeter takes over. The tile calorimeter is a steel matrix with scintillators inserted as tiles as seen in fig. 4.6. The scintillator tiles are placed such that the shower passes through them from the side to improve the e/h ratio. Still, the tile calorimeter can not be termed as a compensating calorimeter since the e/h ratio has been measured to 1.3 in a prototype of the tile calorimeter.

The light created in the scintillators is read out with wavelength shifting fibres to photomultipliers placed on the outside of the calorimeter. The fibres absorb the blue light from the scintillators and reemit it at longer wavelengths where it reaches the photomultipliers through total reflection inside the fibres.

To improve the hermicity of the hadronic calorimeter two plugs in each side are inserted in the region where the cables and cooling from the EM calorimeter and the Inner Detector pass through. One of them, the crack scintillator, is a pure scintillator with no steel absorber. This design is forced by the limited space in the region. It plays an important role for the EM calorimeter as well since it is placed just in the difficult transition region between the barrel and end-cap EM calorimeter.

The resolution of the hadronic calorimeter will be

$$\frac{\Delta E}{E} = \begin{cases} \frac{50\%}{\sqrt{E}} \oplus 3\% & \text{for } |\eta| < 3 \\ \frac{100\%}{\sqrt{E}} \oplus 10\% & \text{for } 3 < |\eta| < 5 \end{cases} \tag{4.4}$$

where the constant term is dominated by the different response to the hadronic and electromagnetic part of the shower as a larger part of the total energy ends up as an electromagnetic shower at high energies.

[1] The contribution from local variation in the calorimeter has been measured on a prototype of the calorimeter and is well within the safety margin.

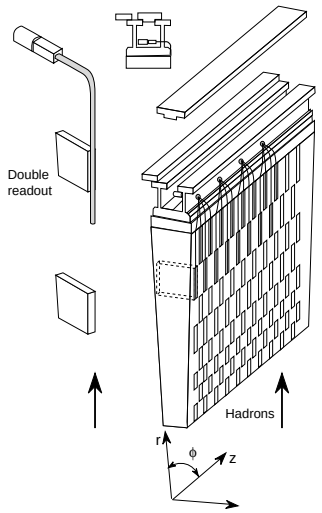

Figure 4.6: A module of the tile calorimeter. Notice how the scintillators attached to the light guides are placed with respect to the particles entering from below.

4.4 The Inner Detector

In the innermost part of ATLAS is placed a tracker. With finely segmented detectors it can reconstruct the tracks of charged particles in the magnetic field of the solenoid. The most important points for the Inner Detector are:

- Identification of individual particles in dense jets where the calorimeter cannot resolve the individual particles. At the same time the rate of fake tracks should be low.
- Momentum measurement in a large momentum range. Below a transverse momentum of 0.5 GeV the particles loop in the magnetic field and reconstruction is not possible. This lower limit affects the reconstruction of converted photons and J/Ψ decays.
- Charge identification of particles with large transverse momentum for the identification of a possible Z' decay. Increasing the magnetic field will improve the charge identification but at the same time increase the p_T limit for loopers.
- Distinguish between electrons and photons which create similar clusters in the EM calorimeter.
- Decay length reconstruction used for CP-violation studies in the B-system and for a B_s^0 mixing measurement.
- Tagging of jets originating from high energy b-quarks. The b-jets can be from a $H \to b\bar{b}$ decay or decays of supersymmetric particles. The tagging is done by

secondary vertex identification and through the identification of leptons from semileptonic B-meson decays.

- Electron/jet separation in addition to the separation already provided by the calorimeter.
- Momentum measurement of low energy muons which have large multiple scattering in the hadron calorimeter.
- Identification of the primary vertex in the presence of many vertices from overlying minimum bias events.

Good momentum resolution is provided with a reconstruction of the track along the full track length. This requires both good resolution of the individual detection elements and the possibility to link the individual measurements correctly together to tracks. This pattern recognition problem is treated in more detail in section 6.2.

In the barrel part of the Inner Detector where $|\eta| \lesssim 1$ all of the detecting elements are ordered in cylindrical structures while the two end-caps have the detecting elements placed in wheels. This assures that the particles pass all detecting elements with large incident angles.

In line with the coverage for the detection of electrons and muons in the calorimeter and muon system the coverage of the Inner Detector extends up to $|\eta| = 2.5$.

It is important to keep the amount of material in the Inner Detector low. Photon conversions, bremsstrahlung from electrons and nuclear interactions with pions all cause a degraded calorimeter performance. The large track density, however, requires detection elements with a fine granularity. The bunch crossing frequency of 40 MHz also forces the readout electronics to be placed directly on the detector and only transfer the information if a level-1 trigger occurs. There is clearly a compromise between tracking quality and tails in the calorimeter resolution that determines the amount of material. The material budget for the Inner Detector as presented in [4] is shown in fig. 4.7.

4.4.1 The silicon detectors

Two technologies are used for the ATLAS semiconductor tracker (SCT). Closest to the beam pipe are placed pixel detectors and further away silicon strip detectors.

In total, particles from the primary vertex pass at least seven layers of silicon detectors each providing a 2-dimensional coordinate. To reduce correlations between individual points the layers are spread out evenly along the tracks as shown in fig. 4.8.

Triggered by the wish to reduce the amount of material in the Inner Detector it was studied if the number of silicon layers passed could be reduced from seven to six [39]. The conclusion was, that the trigger and b-tagging performance would be seriously affected by such a change while the gain for the reconstruction in the electromagnetic calorimeter would only be marginal.

Silicon is a good material for tracking detectors. The small band gap in silicon means that the minimum energy to crate an electron/hole pair is just 3.6 eV. The net

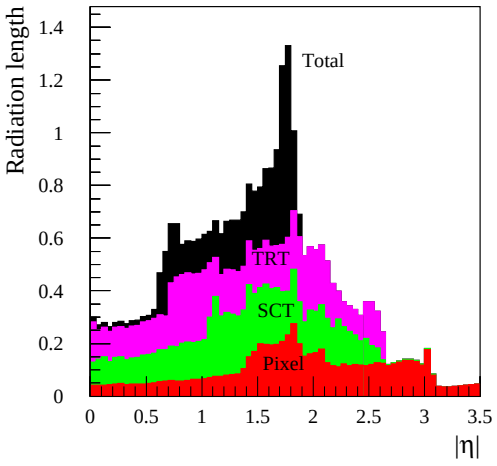

Figure 4.7: The material in the Inner Detector measured in radiation lengths.

effect of primary and secondary ionisation is around 80 electron/hole pairs per μm for a minimum ionising particle. A voltage applied across the substrate drift the electrons and holes towards the surface where they are detected.

The silicon strip detectors have a n type bulk with a single sided readout of n+ strips. This choice is believed to be the most radiation resistent. Radiation damage will cause the bulk material to change into a p type semiconductor with time but the detectors will still be functional. In each of the layers of the detector two single sided detectors are placed back to back. In one layer the strips are parallel to the beam pipe thus measuring the φ coordinate directly. The strips on the back side are rotated 40 mrad to give a stereo view and thereby reconstructing the z (r) coordinate as well in the barrel (end-cap). The choice of a small stereo angle is motivated by a redundancy in the φ coordinate which is crucial for the momentum reconstruction. Also a small stereo angle gives fewer ghost hits inside dense particle jets. Each strip in the detecting element will have a length of 12 cm and a width of 80 μm.

The pixel detectors have more square detecting elements of the size 50×400 μm thus giving a 2-dimensional coordinate with just one layer. The best resolution is in the φ coordinate. The pixel device is more expensive than silicon strip detectors and a less tested technology leading to the choice of only placing pixel detectors in the layers closest to the primary vertex.

The most important requirements for the pixel detectors are to provide secondary vertex information for full reconstruction of B-meson decays, and for b-tagging in top physics, a $H \rightarrow b\bar{b}$ decay and possible decays of supersymmetric particles. For pattern recognition the pixel detector is also important since, in spite of the close placement to the primary vertex, it has a very low occupancy. For the requirement of

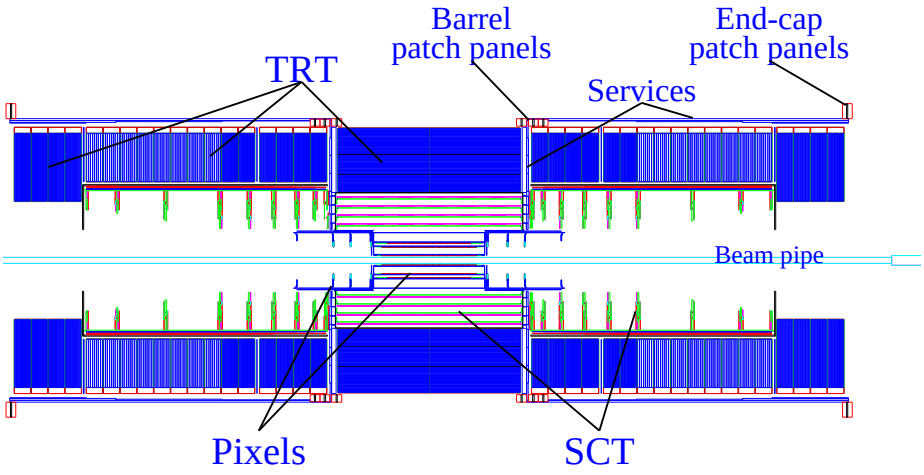

Figure 4.8: A side view of the Inner Detector layout.

identification of secondary vertices the first pixel layer has to be as close as possible to the beam pipe. In the present design the first layer almost touches the beam pipe at a radius of 4.8 cm. This layer will survive the first years of running at low luminosity and well maybe be replaced as it dies in the radiation from some years at high luminosity.

4.4.2 The Transition Radiation Tracker

The Transition Radiation Tracker (TRT) is placed between the silicon tracker and the solenoid. In this section the general layout will be described while the theory behind transition radiation was treated separately in chapter 3. It will be seen how the design closely follows the optimisation of a transition radiation detector and at the same time takes into account that it has to be a powerful tracking device.

The TRT consists of thin proportional chambers either in the form of straws embedded in fibres or with foils and straws in separate layers.

In total there are around 370 000 straws with 4 mm diameter in the TRT, which are placed radially in the end-cap and along the beam axis in the barrel region; these orientations are chosen to maximise the number of straws passed in all directions pointing away from the interaction point. Parameters for the TRT in tabular form can be found in table 3.1 and table 4.2.

The straws are filled with a xenon gas mixture ($70\%\mathrm{Xe}, 20\%\mathrm{CF_4}, 10\%\mathrm{CO_2}$). The xenon is for the absorption of transition radiation. $\mathrm{CF_4}$ enables the gas to have a faster drift-time for electrons, providing higher spatial resolution and reducing the influence from neighbouring bunch crossings at the LHC. A ($\mathrm{Xe/CF_4}$) gas mixture is not stable under high voltage so $\mathrm{CO_2}$ is added to stabilise the gas, thus preventing sparks and streamers inside the straw during operation. In the centre of the straw

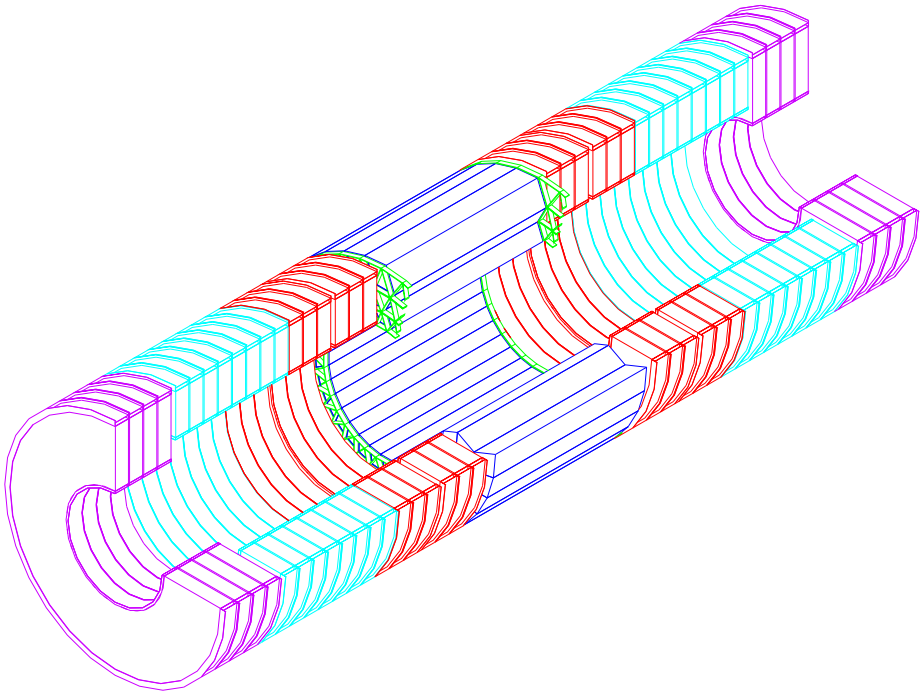

Figure 4.9: A 3-dimensional view of the Transition Radiation tracker (TRT). In the centre the barrel TRT and on each side the end-cap wheels.

Type	Parameter	Value
straw	radius	2 mm
	length	160 cm (barrel)
		$\sim$ 40 cm (end-cap)
wire	diameter	30 μm
	material	gold on tungsten
gas	pressure	1 atm
	temperature	$15 \pm 5^{\circ}$C
	gas gain	$2.5 \cdot 10^4$
	drift-time	$\lesssim$ 40 ns
	composition	70% Xe
		20% CF_4
		10% CO_2
fibre	material	PE/PP
	density	0.066 gcm^{-3}
	thickness	15 μm
foils	material	PE/PP
	thickness	17 μm

Table 4.1: A summary of the parameters of the TRT.

is a 30 μm gold covered tungsten wire. The gas gain in the straws will be $2.5 \cdot 10^4$ and the total drift-time approximately 40 ns and thus not fully contained within one bunch crossing.

In the end-cap the straws are placed in wheels where layers of radiator foils and layers of straws are interspaced. A 3-dimensional view of the barrel TRT and the end-cap wheels is shown in fig. 4.9. How the straws are placed in an end-cap wheel is shown in fig. 4.10. The foils are 17 μm thick with a 200-300μm spacing.

A more complicated structure is required in the barrel TRT where the lack of space prevents a solution with straws and radiator in separate layers. Instead the radiator will be put into all available space around the straws as sheets of loosely

Straw type	$r_{\min}$ (cm)	$r_{\max}$ (cm)	$\lvert z\rvert_{\min}$ (cm)	$\lvert z\rvert_{\max}$ (cm)	Number layers
barrel (short)	56	62	40	74	9
barrel (long)	62	107	0	74	64
end-Cap (short)	64	103	83	278	160
end-Cap (long)	48	103	282	335	64

Table 4.2: The TRT straw geometry. The short straws in the barrel pass through the full detector but are only active for $|z| > 40$ cm.

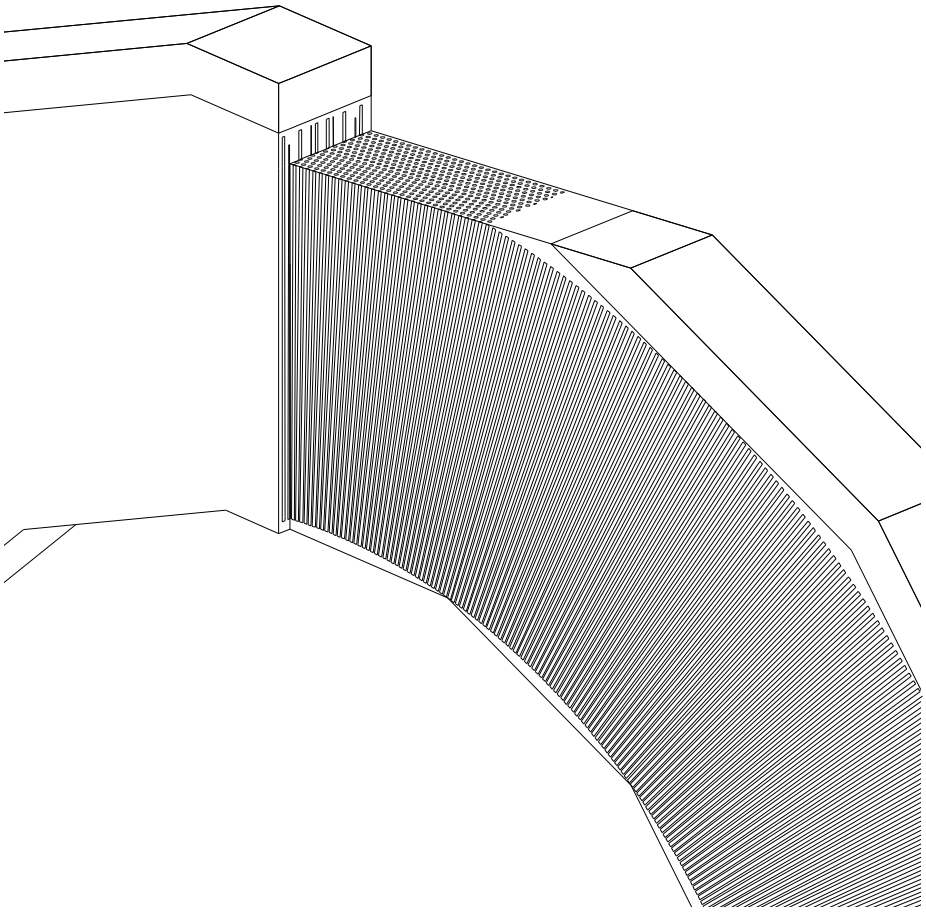

Figure 4.10: A small part of an end-cap wheel in the TRT. The radial placement of the straws can be seen. Foils creating transition radiation are placed between each layer.

packed fibres. The fibres are made of polypropylene/polyethylene which is a radiation resistent combination. Each fibre has a 15 μm diameter and experimental results have shown that a bulk density of around 0.06 g/cm^3 gives the fibre spacing that provides the maximal transition radiation yield. A magnified view of a polyethylene fibre material is shown in fig. 4.11.

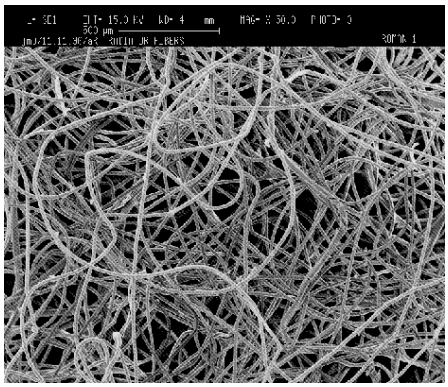

Figure 4.11: A magnification of a polyethylene fibre. The fibres are mainly aligned in the plane of the paper.

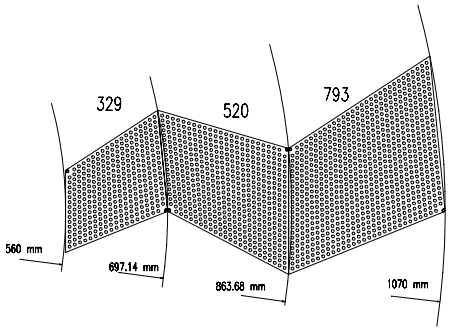

Figure 4.12: The placement of the straws in the barrel TRT. Each of the three layers has 32 chevron shaped modules with all modules in a given layer equal.

The optimal placement of the straws in the barrel TRT would be such that all straws had the same separation and no extra material was between the straws and the radiator. For mechanical reasons and to ease production this is not possible. Instead a modular structure has been chosen where the barrel TRT is divided into three layers each having 32 chevron shaped modules as seen in fig. 4.12. The chevron shaped modules fit into a support structure consisting of a stable triangular pattern. Many more details on the modular structure can be found in [40].

The strong point of the TRT in the tracker, is the large amount of hits on the individual tracks. While the silicon detectors provide in average seven space points on a track with 10–30 μm precision in the $r\varphi$ coordinate, the TRT gives above 35 hits for nearly all pseudorapidities with a resolution of 170 μm.

The number of hits on all reconstructed tracks in $H \to \gamma\gamma$ events at high luminosity is shown in fig. 4.13 as a function of the pseudorapidity. The 1σ spread in the number of hits on the tracks are plotted as error bars on the figure. The dip for $|\eta| \sim 0.9$ is caused by the transition from the barrel TRT to the end-cap TRT where tracks pass fewer straws. The dip has been minimised by lowering the inner radius of the barrel TRT to 56 cm. For $|z| < 40$ cm the wires in the innermost 9 layers are disconnected electrically to lower the occupancy in the straws but still provide hits on tracks in the transition region between the barrel and end-cap TRT.

The large number of hits on the tracks is powerful in the pattern recognition state

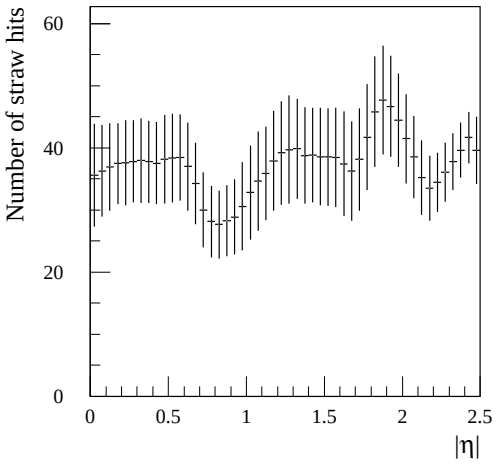

Figure 4.13: The number of hits in the TRT on tracks as a function of pseudorapidity. The error bars indicates the 1σ spread on the average.

where tracks are to be found in the detector. It will be treated in detail in section 6.2.

4.5 Trigger and computing aspects

For a detector at a proton-proton collider the trigger concept is of utmost importance. As already mentioned in chapter 1 the rate of interesting physics events is many orders of magnitude below the rate of minimum bias events. The bunch crossing rate is 40 MHz but it will only be possible to write events to tape at a rate below 100 Hz. This means that within seconds the data flow from the detector has to be reduced by a factor 400 000 which is only possible using several trigger levels.

The ATLAS trigger has three levels. At the first level only general features and a few detectors are read out while the level-3 trigger provides full scale physics analysis. The structure of the trigger is shown in fig. 4.14.

At the level-1 trigger only the calorimeters and the muon system is used. Fast readout is important, hence the muon system has special trigger chambers with a short drift-time but limited resolution. The data from the calorimeters are read out with a coarse $(\Delta\eta \times \Delta\varphi) = (0.1 \times 0.1)$ resolution. This reduces the bandwidth required for the readout and also reduces the total processing power required. The trigger algorithms are changeable and will to some extent be adjusted after data taking has started reflecting the present uncertainties in the minimum bias structure. The sub-detectors are treated individually at trigger level-1 and look for muons with $p_{\mathrm{T}} > 20$ GeV, isolated electromagnetic clusters with $E_{\mathrm{T}} > 30$ GeV, high energy hadronic jets or large missing transverse energy. An isolated cluster means that a

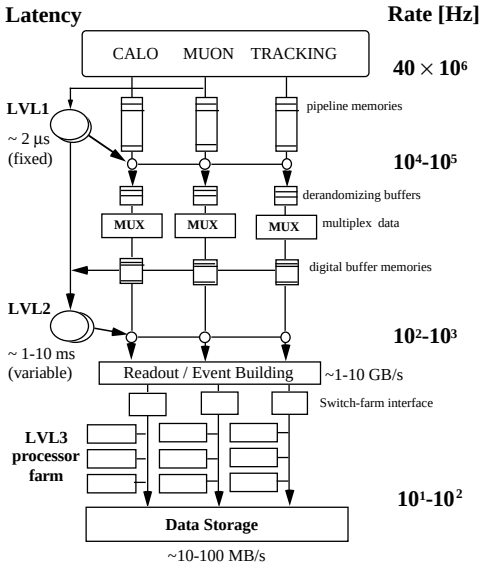

Figure 4.14: The structure of the 3 trigger levels in ATLAS.

region ($\Delta\eta \times \Delta\varphi$) around the central cluster contains low transverse energy.

More complicated triggers requiring two or more clusters/tracks also exists, an example of this is the trigger used for the $H \to \gamma\gamma$ decay which requires two isolated electromagnetic clusters with $E_T > 20$ GeV. All data is stored on the detector in pipelines of the readout electronics waiting for a trigger level-1 decision. After a fixed delay the data is either lost or read out by a trigger level-1 accept signal.

The level-2 trigger analyses data across different detectors and has access to data with full precision. The analysis takes place in a region, a so-called Region of Interest, around the direction in (η, φ) selected by the level-1 trigger. The main task of the level-2 trigger is to refine the analysis of the level-1 trigger inside this region of interest. Taking as an example again the $H \to \gamma\gamma$ decay, the trigger level-2 analysis calculates the cluster energy with the full resolution to refine the isolation cut. Jet events with energy deposition in the hadronic calorimeter behind the electromagnetic cluster are also rejected. In total this reduces the rate in the two photon trigger by a factor 25 with only a small loss of efficiency.

The Inner Detector is also involved in the level-2 trigger. For the isolated electron trigger the Inner Detector searches for tracks pointing towards the cluster. For electrons the p_T of the most energetic track should loosely match the E_T of the cluster.

When the LHC runs at low luminosity there will be special triggers for B-physics. This includes a level-1 trigger for isolated muons with $p_T > 6$ GeV and at level-2 a J/Ψ trigger in the TRT. This J/Ψ trigger will not run inside a small region of interest

but cover the entire TRT. The electron identification power of the TRT is important for this trigger to reject random combinations of hadrons from faking J/Ψ's.

The level-2 trigger does not run in a fixed time and will process many events in parallel. In total the trigger level-2 should reduce the trigger rate from 75 kHz to around 1 kHz which is the highest acceptable rate for the level-3 trigger.

The level-3 trigger analyses data in the full detector and will do more complicated physics analysis. Many physics channels will be covered by a trigger for $Z \to l^+l^-$ decays with a tight invariant mass cut around the Z mass. The $H \to \gamma\gamma$ decay is problematic at this trigger level since it will be required to store all events with a two photon invariant mass above 60 GeV or so. A strong rejection of π^0's faking photons is necessary for this. The level-3 trigger will reduce the data rate down to 100 Hz which is the highest acceptable rate for permanent storage of data.

The trigger system is sensitive to the theoretical uncertainties of the background levels to the physics channels. For this reason a factor two safety limit is build into the level-1 trigger where all thresholds are fully adjustable. For the level-2 trigger all analysis is programmable allowing for changes and upgrades of the software after the start of the LHC. For the level-3 trigger which will be based on standard workstations/PC's even the hardware can be upgraded to take advantage of the improved performance on the market.

Chapter 5

Testbeam analysis

In connection with the design of the transition radiation tracker (TRT) for ATLAS it is not sufficient to design and simulate the detector in the computer. Test modules are required to test both the mechanic and electronic solutions developed and for testing the performance of the detector.

For the development of the TRT the following prototypes have been tested at fixed target testbeams of the CERN Super Proton Synchrotron (SPS):

Single straws Single straws placed in the testbeam to measure properties straw signal and performance of the readout electronics. Often irradiated with an ^{55}Fe source to emulate the counting rate at high luminosity [41, 42].

TRD prototype The first prototype with straws embedded in a foam radiator. In total 192 straws in the detector. Used for electron identification studies [43].

Block prototype Four blocks of foam radiator with in total 864 parallel straws inserted. Used for tracking, pattern recognition and electron identification studies [44].

Radiator prototype An array with small straws and interchangeable radiator blocks. Used to evaluate the radiator performance [45].

Sector prototype Five 30° degree sectors of end-cap wheels with in total 2560 straws. Used for electron identification studies, tracking studies and long-term stability tests. The electron identification performance of the sector prototype will be described in detail in this chapter.

Barrel modules Different prototypes in reduced length of the barrel TRT modules. Used in the testbeam for studies of transition radiation performance [40].

The particle beams used in the testbeam has mostly been low rate electron and pion beams with energies ranging from 20 to 200 GeV. For the electron identification studies the 20 GeV beam is of special importance as it is close to the typical energy

of isolated electrons selected by the level-1 trigger in the ATLAS detector. Muon and photon beams have also been used for limited studies.

Many other prototypes have been built and tested for mechanical stability, electronics performance, radiation hardness etc. An overview of the obtained results can be found in [5].

In terms of the size and complexity of the data acquisition system and the amount of data collected, the testbeams with the prototypes can be compared to smaller fixed target experiments.

5.1 The Transition Radiation Tracker sector prototype

The prototype consists of five blocks containing 512 straws each. Each block, as seen in fig. 5.1, contains 16 layers of radial straws interleaved with radiator stacks, made of 17 polypropylene foils of 15 μm thickness and spaced on average by 265 μm. Each layer contains 32 straws positioned in a support frame with an accuracy of 100 μm. The total length of the detector is 780 mm. The support frames are staggered with respect to one another, in such a way as to minimise the fluctuations in the total number of straws crossed by beam particles as a function of their impact point on the prototype. The edges of the frames provide a common gas manifold for all the straws and the necessary electrical connections. One distributed blocking capacitance of 800 pF is connected to each group of 16 straws. No cross-talk was observed within the accuracy of the measurements, which was less than 1%. The inner part of the frames is constructed out of carbon fibre composite to minimise the amount of material. As a result, the average thickness of this inner support, including the straw fixations and end-plugs, is about 1.4% X_0 for particles crossing at normal incidence.

The straws have an inner diameter of 4 mm and have 60 μm thick walls made of coated polyamide film [42, 46]. The straws are reinforced with carbon fibres to increase the rigidity and to prevent the straws from creeping under variations of humidity and temperature. Their length was chosen to be 33 cm, due to the limited amount of space available inside the solenoidal magnet used for the 1995 measurements with the prototype. The front-end electronic chips are connected to printed-circuit boards situated at the outer radius of the frames.

The active gas in the straws was normally 70% Xe, 20% CF_4 and 10% CO_2. By examining the gas gain uniformity of all 2560 straws it was checked that 97% of the straws have a wire offset below 300 μm which guarantees stable operation under LHC conditions. All straws have been operating under high voltage in a stable way for several years. The sector prototype was operated at a gas flow of 0.05 cm^3/min per straw, which corresponds to about one volume per hour.

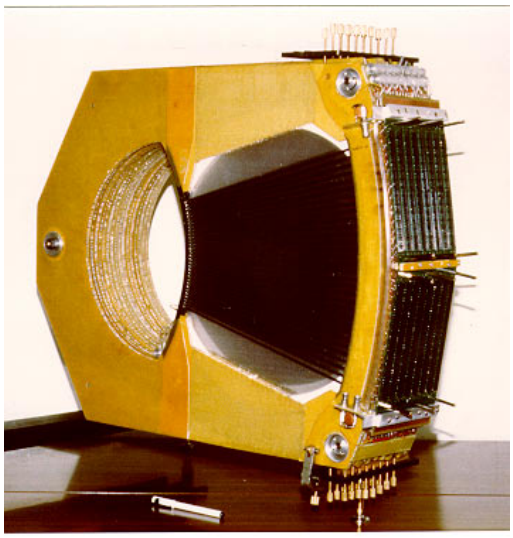

Figure 5.1: One of the five blocks in the TRT prototype before the electronics boards were mounted. The outermost layer of radially mounted straws can be seen.

5.2 Front-end electronics and readout

In addition to the stringent requirement to operate up to straw counting rates of 20 MHz at the LHC design luminosity, the final electronics of the TRT should fulfil requirements common to all types of LHC readout electronics:

- Radiation hardness.
- Low power consumption.
- Operation at a 40 MHz bunch crossing (BX) rate.
- Storage of data on detector for around 3 μs.
- Continuous readout at a rate of up to 75 kHz.
- Readout through high bandwidth links.
- Readout format compatible with level-2 trigger requirements.

As explained in detail below, many of these requirements were already implemented for the development version of the electronics on the prototype. The most significant difference is that the readout chips were not manufactured in a radiation hard process.

The long ion tail observed in the straw signal, characteristic of xenon gases, requires an accurate tail cancellation circuitry to avoid baseline shifts at counting

rates up to 20 MHz. A detailed analysis of the properties of the straw signal can be found in [41].

The transition radiation (TR) photons which are generated by electrons crossing the radiator foils between the straw layers deliver a point-like ionisation with an energy a few times higher than the ionisation from the particle itself, thus creating a short signal with high amplitude. Minimum ionising particles, on the other hand, produce extended ionisation with an average energy around 2 keV. The two signals can be distinguished by means of a fast preamplifier/shaper circuit combined with two discriminators, one with a low threshold ($\sim$ 0.2 keV), which efficiently registers signals from primary ionisation, and one with a high threshold ($\sim$ 6 keV), which registers a large fraction of the absorbed TR photons.

5.2.1 System overview

A simplified functional block diagram emphasising the readout channel for one straw is shown in fig. 5.2. The signal from the straw is processed in the preamplifier/shaper circuit. The output signal is compared in two discriminators with low and high threshold as described above, and the resulting two bits are latched and stored in the digital pipeline at the rising edge of the bunch crossing (BX) clock. If the low-threshold discriminator fired a 3-bit Gray encoded timing value is latched and stored in the pipeline. The three bits describe the time between the previous rising edge of the BX clock and the arrival of the signal, i.e. the drift-time in the straw. The pipeline stores five bits of information for each time slice of 25 ns over a period of around 3 μs (128 clock cycles).

Upon an accept signal from the level-1 trigger, the trigger decision logic selects the three relevant consecutive time slices and stores their information into a derandomiser (readout buffer). The data in the derandomiser are kept until an output enable signal is issued by the back-end electronics. The back-end unit reads out, packs and sends to the DAQ system the data from 512 channels. The back-end unit is also responsible for the slow control of the front-end circuits and the trigger level-1 management.

5.2.2 Transition Radiation Detector Analog (TRDA) chip

This 8 channel integrated circuit [47, 48] corresponds to the preamplifier/shaper and discriminator stages shown in fig. 5.2. It contains a common base bipolar input stage with charge integration at the collector. The shaper contains 4 integrators and two pole/zero cancellation stages. The output analog signal has 12.5 ns peaking time and a 15 ns falling time. The equivalent noise charge is at the level of 2000 electrons for a 10 pF input capacitance. The signal shaping for the TRDA and the somewhat faster shaping (7.5 ns peaking time) planned for the final electronics to be mounted on the TRT is shown in fig. 5.3. The successor [49] of the TRDA already has the faster shaping implemented.

The preamplifier/shaper is followed by two Schmitt triggers (comparators with hysteresis), which guarantee a minimal output pulse width of 5 ns. In order to avoid high swing signals close to the sensitive inputs, a differential, low amplitude,

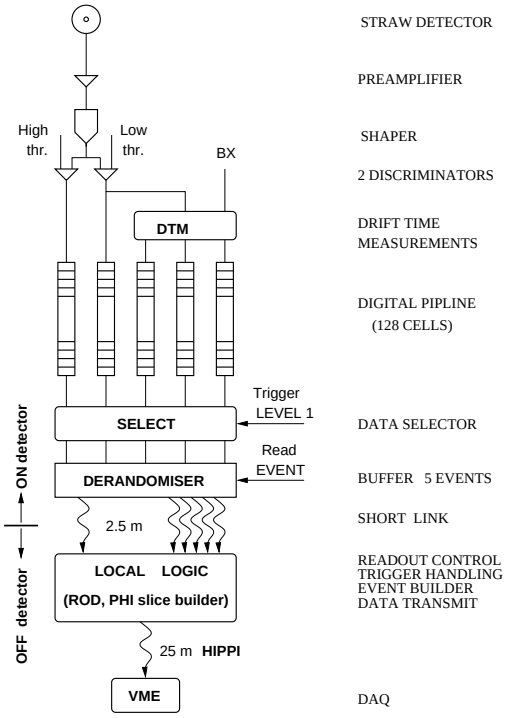

Figure 5.2: Complete chain of front-end electronics and readout system from the straws to the VME module readout by the DAQ. The details for one readout channel are emphasised.

current-sensitive interface was chosen. The information from low-threshold and high-threshold discriminators is ternary encoded in order to save output pins. This ternary interface encodes the values of low and high-threshold outputs according to table 5.1, which shows that the total value of the current in both pins of the ternary interface is constant.

The TRDA is an 8-channel chip produced in the PLESSEY bipolar process. It is packaged in a 44 pin PLCC package; power consumption is 12.5 mW/channel. During the testing of the prototype TRDA chips ceased operating at a slow rate with around 20% of the chips non-functional at the end of the testbeam period in 1996. Examination of failed chips showed that a short track between an input bond pad and its protection diode had been vaporised by high-energy electrical discharges. Test inputs verified that the following circuitry was still operational. A low value external resistor would have prevented this problem but was omitted to save space. Such a resistor is implemented for the successor [49] of the TRDA.

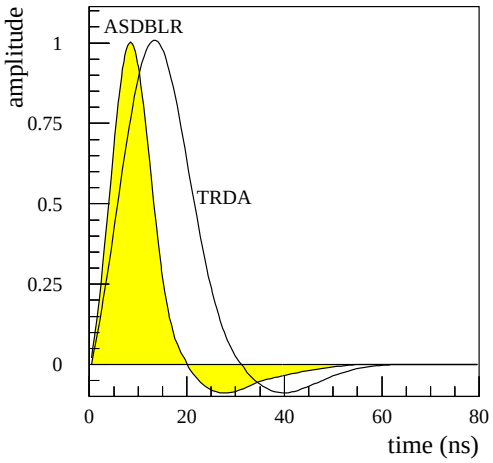

Figure 5.3: The signal shaping for the TRDA chip as used in the testbeam and the signal shape as planned for the final electronics (ASDBLR).

State	True current	Complement current
no event	1	3
low threshold only	2	2
high and low threshold	3	1

Table 5.1: Ternary interface state assignment for the TRDA chip. The currents are given in units of 200 μA.

5.2.3 Transition Radiation Detector Service (TRDS) chip

This 8 channel chip [50] receives the ternary signals from one TRDA and decodes and converts them to standard CMOS signals. It contains two 5-bit DAC's to set the low and high thresholds for the TRDA discriminators. For the standard gas gain, the low threshold can be varied from around 0 to 1 keV and the high threshold from 0 to 9 keV. The scales are linear and can be varied in steps of 1/32 of the maximum setting. There is a possibility to mask bad channels in the TRDS and to generate test pulses which are injected to the TRDA inputs. The test-pulse amplitude is adjustable with a three bit resolution. Test pulses can be generated separately for even and odd channels. The TRDS was produced in the ESS 2 μm CMOS process and packaged in a 68 pin PLCC package. It has a power consumption of 7.5 mW/channel.

5.2.4 Drift-Time Measuring ReadOut Chip (DTMROC)

The 32-channel DTMROC [51] receives low and high-threshold signals from the TRDS. These signals, which can be as short as 5 ns, are latched synchronously with the BX clock. The chip also measures the drift-time using a Delay Locked Loop (DLL). The DLL supplies a 3 bit Gray encoded word which represents the time since the last rising edge of the BX clock. The contribution of the DTMROC to the Gaussian resolution of the drift-time measurement is thus 0.90 ns ($\frac{25\text{ns}}{2^3\sqrt{12}}$), contributing a constant term of about 50 μm to the overall drift-time accuracy. The data from the low and high-threshold discriminator and the drift-time measurement (5 bits/straw and clock cycle) are written to a digital pipeline. The pipeline is 128 BX clock cycles long, allowing for a total trigger level-1 latency of 3.2 μs. The level-1 trigger signal activates internal circuitry and the data from three time slices, corresponding to the tagged event, are transferred from the pipeline to a so-called derandomiser. The derandomiser can store up to five events. The readout of the data output is organised on three serial outputs running at 20 MHz, and is activated when the Output Enable signal is transmitted from the back-end electronics.

The DTMROC was produced in the AMS 1.0 μm CMOS process. 32 channels are packaged in a 84 pin PLCC package with a power consumption of 7 mW/channel.

5.2.5 Front-end boards

The basic readout unit for the prototype is formed from four TRDA chips, four TRDS chips and one DTMROC placed on one front-end board as seen in fig. 5.4. The analog TRDA integrated circuits are placed on one side of the readout board while the digital TRDA and DTMROC chips are placed on the other side. In this way the sensitive analog input lines from the straws are protected as much as possible from the digital transmission lines.

The front-end boards are placed directly on the detector prototype and serve 32 straws. Eight front-end boards form a group which is connected to one so-called roof board. The roof board distributes power and services to front-end boards and collects the readout lines.

5.2.6 Back-end electronics

The data from two roof boards, corresponding to 16 front-end boards or 512 straws, are collected on a so-called Local Logic board, which controls the readout protocol. The state of the derandomiser and the available buffer space are checked by the trigger logic which provides a BUSY signal to the central trigger logic before the derandomiser in the DTMROC or the buffers on the Local Logic boards become full.

A DAQ system developed at CERN was used [52]. In addition to the standard DAQ modules the modules specific to the TRT prototype were:

- A Trigger Delay Module (TDM), which receives signals from the external trigger logic and synchronises them with an on-board generated 40 MHz clock to emulate the LHC clock cycle in the SPS conditions. The phase between the

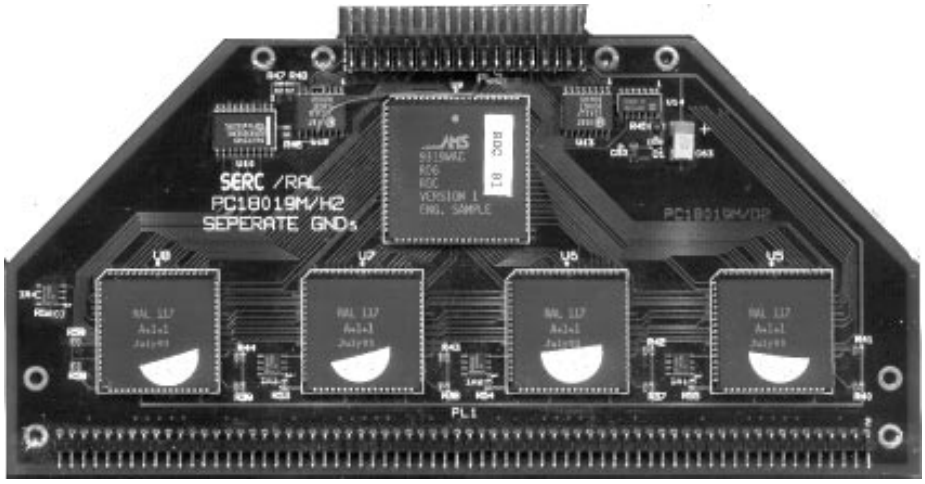

Figure 5.4: A front-end board from the TRT prototype. The 32 channel DTMROC is seen in the top with four 8 channel TRDS chips below. The four TRDA chips are on the other side of the board. 32 straws are connected to the pins in the bottom of the image and the connecter in the top fits into a roof board.

external trigger and the clock is measured with a 4 bit precision (1.6 ns per bin) and transmitted to the Local Logic together with the level-1 trigger signal. This provides a measurement of the offset in time between the beam particle and the rising edge of the 40 MHz clock on an event by event basis. The trigger is delayed to match the front-end pipeline length and delivered together with the clock signal to the front-end boards.

- A Slow Control Module (SCM), which mediates all slow control and parameter loading as well as the Local Logic programming and initialisation.

5.3 Testbeam setup

The sector prototype described above was tested in the H8 beamline at the CERN SPS during several periods in 1995 and 1996. The beamline was equipped with a precise beam telescope, consisting of three silicon microstrip detectors, two standard beam chambers, a Cherenkov counter, and a preshower detector together with a small electromagnetic calorimeter (lead-glass array or RD3 prototypes of the ATLAS liquid argon electromagnetic calorimeter [53]). With this detector configuration, an electron/pion separation at the level below 10^{-4} was achieved when necessary and beam particle tracks could be extrapolated to the sector prototype with an accuracy of 10 μm. The total amount of material in front of the detector was approximately 11% of a radiation length.

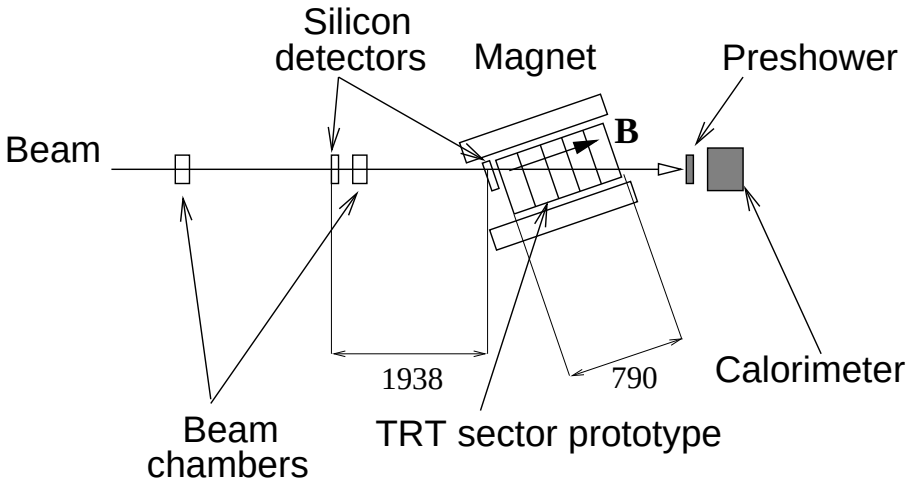

Figure 5.5: Top view of the TRT prototype setup in the 1995 testbeam run. The solenoidal magnet containing the prototype was rotated by 19° with respect to the beamline. All distances are in mm.

In the 1995 testbeam run the detector was placed in a small solenoidal magnet with a maximum field of 0.8 T. The magnet was, as seen in fig. 5.5, rotated by 19° with respect to the beamline to achieve maximum bending of the beam particles. The sector prototype was thus placed in a configuration similar to that at a pseudorapidity $\eta = 1.8$ at the LHC.

In the 1996 testbeam run the beamline was equipped with a large superconducting dipole magnet, with which testbeam measurements of the sector prototype were carried out in a magnetic field of up to 1.56 T. The layout of the testbeam setup and some of the most important geometric parameters are shown in fig. 5.6. In this setup the straws are oriented almost parallel to the magnetic field corresponding to the layout in ATLAS at a pseudorapidity $\eta \sim 0$.

The setups described above have been used extensively to evaluate the TRT sector prototype performance using beams of electrons and pions of energies with 20–200 GeV, with and without magnetic field, and also using tagged photon beams, where the photon was forced to convert in front of the prototype.

5.4 Track reconstruction and alignment

For the studies of pion rejection a simplified tracking algorithm which did not make use of the drift-time information from the straws was used. A straw has a (low-threshold) hit if the low threshold discriminator fired at any time during the three time slices read out for an event. For single particles crossing the detector the simpler track reconstruction algorithm, using no drift-time information from the straws, gives

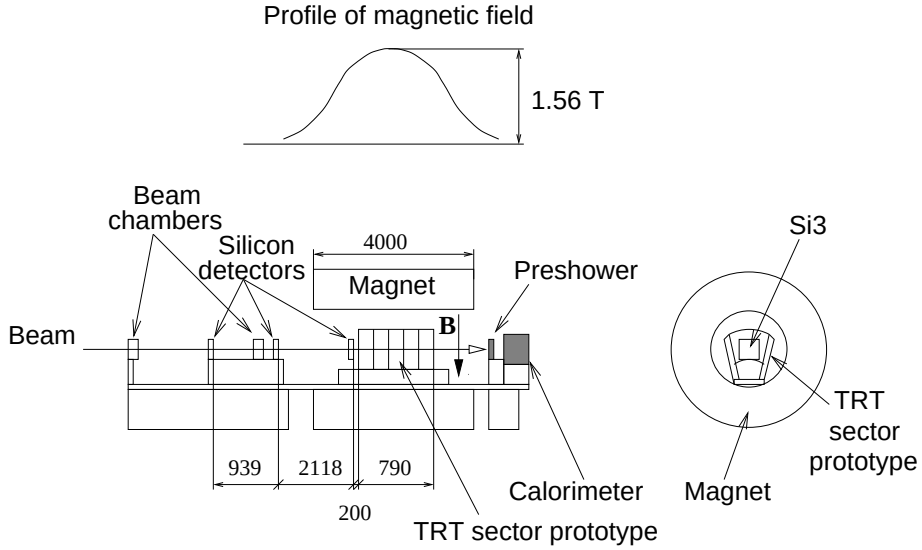

Figure 5.6: Side view (left) and downstream view (right) of the TRT prototype setup in the 1996 testbeam run at the H8 beamline of the CERN SPS. All distances are in mm. The sector prototype inside the dipole magnet is enlarged to improve visibility.

no loss in rejection power compared to an optimal tracking algorithm. Tracking studies with the prototype including drift-time information are presented in [54].

The alignment of the straws was done by extrapolating the tracks reconstructed using the beam telescope to each layer of straws. For all straws with a hit in the layer the position of the extrapolated track contributed to a straw profile. After normalising the profile of each straw to the profile of the beam, the position of the 4 mm wide and nearly square profile was fitted with a function of the type

$$f(x) = A \exp\left[-\frac{1}{2}\left(\frac{x - x_0}{\sigma}\right)^8\right] \tag{5.1}$$

where x_0 is the position of the fitted straw centre, A the straw efficiency and σ the half width of the profile with a value $\sigma \simeq 2$ mm. The alignment correction for a straw was determined as the difference between the position calculated from the geometry of the TRT prototype and the centre x_0 of the fitted straw profile.

Due to the narrow profile of the beam (1 cm) only one alignment correction could be determined with sufficient statistics for each layer of 16 straws. Therefore, straws which were at the edge of the beam, and thus impossible to align properly, were given the same alignment correction as the straw in the same layer placed fully inside the beam.

Using the aligned positions of the straws the distance from the centre of straws

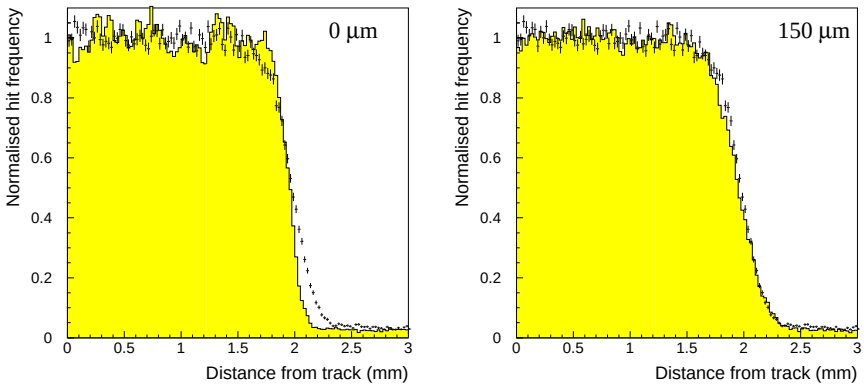

Figure 5.7: Distance from the track reconstructed with the beam telescope to all the hits in the detector for data (points with error bars) and the Monte Carlo (shaded histogram). The two figures are with a perfect straw position in the Monte Carlo (left) and with a 150 μm Gaussian spread in the un-aligned positions of the straws inside each layer (right).

with a hit to the extrapolation of the track reconstructed with the beam telescope was then calculated. This calculated distance plotted for all hits in the detector and for many events, is shown in fig. 5.7. Hits in straws above 2 mm from the beam telescope track are mainly from δ-rays emitted by the primary particle. Comparisons was made to the Monte Carlo with a Gaussian spread introduced to the un-aligned positions of the straws inside each layer. In the figure is shown the results from a 0 μm spread (perfect straw positioning inside the layers) and a 150 μm spread. The best fit is for a spread of 150 μm which can be understood as a $\sim$ 100 μm contribution from the construction and a $\sim$ 100 μm contribution from straw bending.

A parabolic fit accounting for the effect of the magnetic field was made to the hits found by the tracking algorithm and only reconstructed tracks with parameters matching the direction and momentum of the beam particles were selected for further analysis. The track parameters from the beam telescope were not used in the track fit. The number of hits along the reconstructed track, before and after matching to the beam parameters, is shown in fig. 5.8.

5.5 Beam purity

In the analysis of particle identification it was crucial to have a good identification of electrons and pions given by detectors separate from the TRT prototype. The beam entering the H8 beamline was a secondary beam produced by directing the 450 GeV beam extracted from the SPS into a target which produced a secondary mixed beam

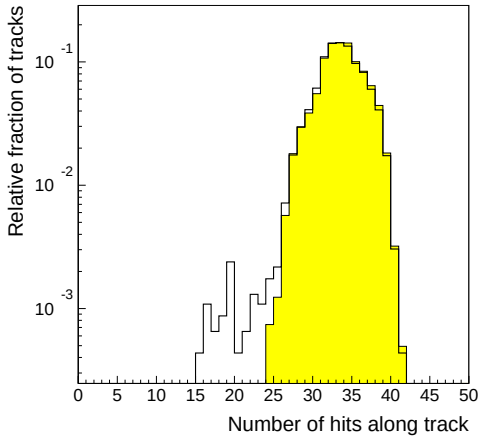

Figure 5.8: The number of hits on the reconstructed tracks in the TRT prototype before (open) and after (shaded) matching to the beam parameters (magnetic field of 0.8 T).

of mainly charged pions and photons (from π^0 decays).

A pion beam was obtained by inserting a lead plate to absorb the photons followed by magnetic optics to select particles of equal energy. As will be shown below the beam had an electron contamination of below 1.4%.

An electron beam was obtained by inserting a copper plate into the beamline where e^+e^- pairs are formed in photon conversions. The magnetic optics following the converter again selected particles of equal energy. The optics was optimised for particles with production point at the copper plate, but still the electron beam had a pion contamination of nearly 50%.

For both the electron and the pion beam external particle identification was required to obtain cleaner electron and pion samples. Three devices were present for this in the testbeam: far upstream a Cherenkov detector suitable for electron/pion separation up to energies of 50 GeV; behind the TRT prototype a presampler; and just behind that a lead glass calorimeter. The presampler was simply a scintillator with a lead plate placed just in front of it. The signals in the Cherenkov counter, the lead glass calorimeter and the preshower are shown in fig. 5.9 for 20 GeV electrons and pions.

In fig. 5.10 is shown a scatter plot of the signal in the Cherenkov counter and the lead glass calorimeter for a mixed beam of 20 GeV electrons and pions. The regions used for the selection of electron and pion samples are indicated.

The efficiency of finding electrons using the particle identification cuts for pions ε_e and the efficiency for finding pions using the particle identification cuts for electrons

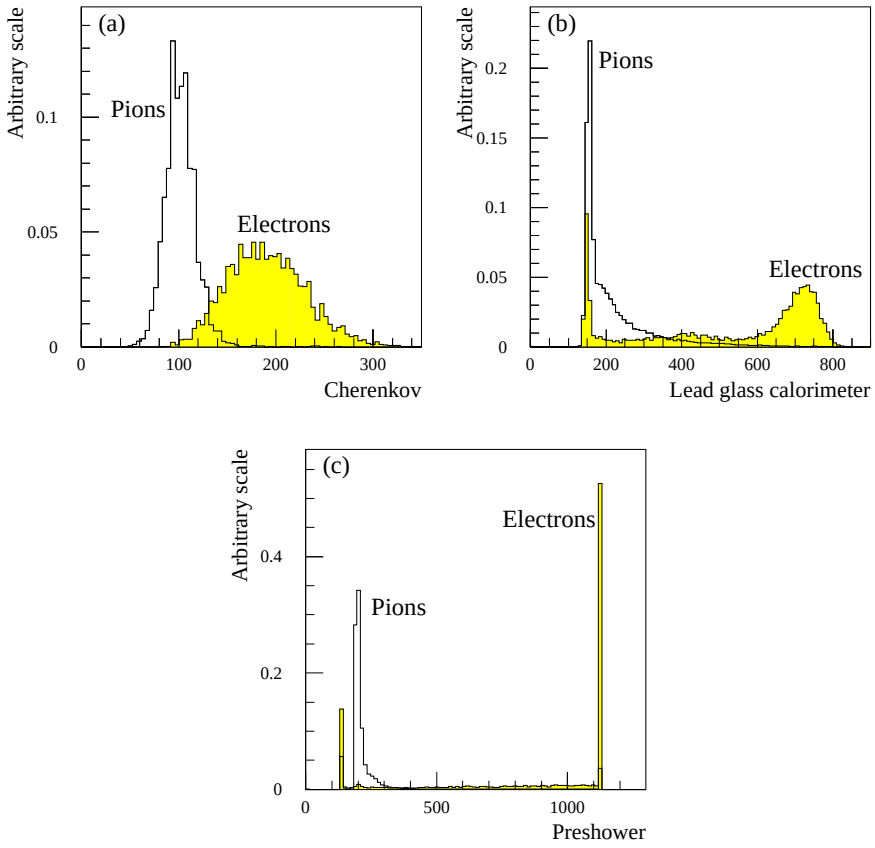

Figure 5.9: The signals of 20 GeV pions and electrons in the ADC's from the Cherenkov counter (a), the lead glass calorimeter (b) and the preshower (c).

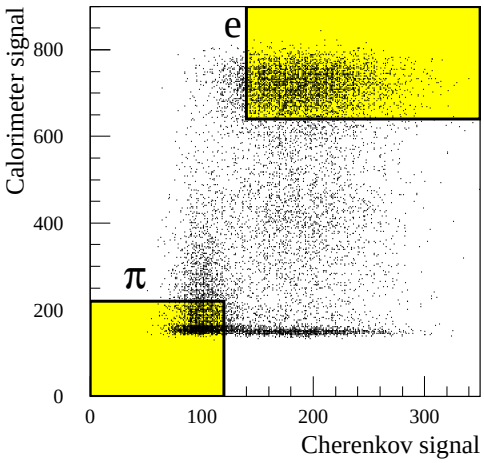

Figure 5.10: A scatter plot of the signal in the Cherenkov counter and the lead glass calorimeter for a mixed beam of 20 GeV electrons and pions. Electrons and pions for the electron identification analysis were taken from the shaded regions.

ε_π are the two important numbers to determine.

ε_e is best measured in a beam of dominantly electrons and an upper limit can be calculated assuming the signals in the Cherenkov counter and the calorimeter give independent measurements. The efficiency for finding electrons when making cuts for pions is

$$\varepsilon_e = \varepsilon_{Ch}\varepsilon_{Cal} \tag{5.2}$$

with ε_{Ch} and ε_{Cal} the efficiencies for the Cherenkov counter and the calorimeter. Measuring the efficiencies is easy in a beam containing only electrons but unfortunately such a beam was not available.

Four different selection criteria can be defined:

A Pion identification cuts in both the Cherenkov counter and the calorimeter.

B Pion identification cut in the Cherenkov counter and electron identification cut in the calorimeter.

C Electron identification cut in the Cherenkov counter and pion identification cut in the calorimeter.

D Electron identification cuts in both the Cherenkov counter and the calorimeter.

With X_e and X_π defined as the number of electrons and pions after the selection criteria X the total number of particles X_{total} is given as

$$X_{total} = X_e + X_\pi = xX_e \quad \text{, where } x > 1. \tag{5.3}$$

Since the cuts on the Cherenkov counter and the calorimeter are independent

$$\varepsilon_{\mathrm{Cal}} = \frac{\mathrm{C_e}}{\mathrm{C_e} + \mathrm{D_e}} = \frac{1}{1 + \frac{\mathrm{D_e}}{\mathrm{C_e}}}. \tag{5.4}$$

The fraction of pions in region D will be lower than in region C, so $\frac{c}{d} > 1$ using the notation from (5.3). Inserting this in (5.4) results in an upper limit on the efficiency

$$\varepsilon_{\mathrm{Cal}} = \frac{1}{1 + \frac{c\mathrm{D}}{d\mathrm{C}}} < \frac{1}{1 + \frac{\mathrm{D}}{\mathrm{C}}}. \tag{5.5}$$

However, the large number of particles in region A on fig. 5.10 indicate a large contamination of pions in the electron beam and (5.5) will be a pessimistic estimate.

The analysis of $\varepsilon_{\mathrm{Ch}}$ and $\varepsilon_\pi < \varepsilon_{\mathrm{Cal}}(\pi)\varepsilon_{\mathrm{Ch}}(\pi)$ are similar to the calculation of $\varepsilon_{\mathrm{Cal}}$ and the results are

$$\varepsilon_{\mathrm{e}} < \varepsilon_{\mathrm{Cal}}(\mathrm{e})\varepsilon_{\mathrm{Ch}}(\mathrm{e}) \; < 0.21 \cdot 0.025 \qquad = 5.1 \cdot 10^{-3} \tag{5.6}$$

$$\varepsilon_\pi < \varepsilon_{\mathrm{Cal}}(\pi)\varepsilon_{\mathrm{Ch}}(\pi) < 0.00064 \cdot 0.054 = 3.5 \cdot 10^{-5}. \tag{5.7}$$

An upper limit on the amount of electrons in the pion beam before the particle identification, is given by the fraction of events passing selection criteria D in the pion beam scaled with the fraction of electrons actually passing this selection criteria (estimated from the electron beam). The results are that the pion beam at the most contains 1.4% electrons and the electron beam at the most contains 60% pions.

After the external cuts both beams will be pure to below the level of 10^{-4} which is sufficient for the electron identification studies where rejections below $5 \cdot 10^{-3}$ are never reached. The results are summarised in table 5.2

	Maximum fraction before selection	Maximum fraction after selection
electrons in pion beam	0.014	$7.3 \cdot 10^{-5}$
pions in electron beam	0.603	$2.1 \cdot 10^{-5}$

Table 5.2: The purity of the beams used for electron identification studies before and after the identification criteria in the Cherenkov counter and the calorimeter was applied.

5.6 The simulation of transition radiation detectors

An analytical approach to the creation and absorption of transition radiation as presented in chapter 3 can give knowledge about the main parameters for building a detector for tracking and particle identification with transition radiation. However, the complexity of the physics involved makes it impossible in an analytical way to

calculate the performance and fine-tune the parameters of such a transition radiation detector directly. The solution is to construct a model that in a detailed way can be used for Monte Carlo simulations of the ATLAS detector and testbeam modules. The detailed simulation of transition radiation and energy absorption in the gas is described here while the general simulation framework for the testbeam will be described in section 5.7 for the ATLAS detector in section 6.1.

5.6.1 Simulation of the transition radiation spectrum

In the GEANT$\tilde{3}$.21 [55] framework, transition radiation is not simulated by default, but is instead implemented as a separate software module called for each step of a charged particle as it is traced by GEANT through the detector. At each point the particle has a spectrum of transition radiation associated. This is a simplification as the transition radiation photons should in principle be treated as independent particles. At the LHC electrons down to an energy of 0.5 GeV are considered in a magnetic field below 2 T. With absorption distances below a few cm, the approximation that the photons follow the charged particle is justified. The simulation of the generation and absorption of transition radiation is specific for the medium the charged particle traverse:

Radiator Upon leaving the radiator the transition radiation spectrum is calculated. For a radiator with foils, the effective thicknesses of the foils and the air gaps are calculated from the crossing angle between the particle and the foils. For a fibre type radiator the thickness is the same independent of particle direction. The generated transition radiation spectrum is then calculated from the angular integration of (3.26)[1]. As the emission angles are small these are ignored and all the radiation is treated as if going in the forward direction.

Detection gas When leaving a volume with sensitive gas the spectrum of absorbed radiation is calculated from the absorption length in fig. 3.10. The mean number of photons absorbed by the gas is then given by integrating the absorption spectrum, and the actual number of photons is taken from a Poisson distribution with this mean. The energy of each photon is taken by random from a normalised distribution of the absorption spectrum and the coordinate of each energy deposition taken randomly along the path the particle through the gas.

All media In all materials the transition radiation spectrum is modified by absorption. For the internal materials in the transition radiation detector (polypropylene, Kapton, carbon fibre, air and the sensitive gas) the spectrum is modified according to the measured absorption length as shown in fig. 3.7. In other materials the absorption is based on a simple rescaling by the radiation length of the absorption for mylar.

The continuous creation and absorption of transition radiation in many layers of a detector is simulated by in each new medium adding and subtracting from the transition radiation spectrum already associated to the charged particle.

[1] The actual calculations is done along the lines described in [56] for a regular stack.

The semi-classical approach where the transition radiation spectrum is first calculated as a continuous energy deposition and then quantised during the absorption to describe individual photons is identical to the approach taken for the photo absorption ionisation model (section 3.4.2).

As a simplification foils with irregularities in the spacing and fibre radiators are simulated as foils with regular spacing following (3.26). The lower efficiency from the irregular spacing of the boundaries is implemented as a relative performance[2]. The foils used in the TRT has a relative performance around 0.9 and the fibre radiator used in the barrel TRT a relative performance around 0.8. A detailed calibration of the relative performance for TRT foils is done in section 5.7.2.

As an alternative to the use of a relative performance, the irregularities in the radiator can be fully simulated following the formula in [56]. The radiator in the tested implementation was a foil radiator with regular foil thickness but with variable spacing between the foils. The spacings are assumed to follow a Γ distribution

$$f(x) = \frac{\beta^\alpha x^{\alpha-1} \exp(-\beta x)}{\Gamma(\alpha)}, \tag{5.8}$$

where Γ is the Euler gamma-function. The average distance between the foils and the root mean square deviation are given as

$$<x> = \frac{\alpha}{\beta} \tag{5.9}$$

$$\text{rms} = \frac{<x>}{\sqrt{\alpha}}. \tag{5.10}$$

Regular foils correspond to $\alpha = \infty$. In fig. 5.11 the Γ distribution is shown for different values of α.

In fig. 5.12 the transition radiation spectrum for different values of α is shown. It can be seen that the main effect of including irregularities in the foil spacing is to reduce the absolute level of the energy emitted thus justifying the simplified model where the energy spectrum is just scaled with a normalisation constant to reproduce the spectrum from foils with irregular spacings. However, it should be noted that the curves actually cross around 12 keV. With only a small fraction of the transition radiation with energy above 12keV ever absorbed this is, however, of minor importance.

In the limit $\alpha \to \infty$ (regular spacings) the dependence of the emission angle θ of the transition radiation can be integrated analyticly thus saving orders of magnitude in computation time. This is the reason why the default Monte Carlo model use the simplified approach with a relative performance. In section 5.8.3 it will on the basis of the testbeam data be concluded that this simplification cannot explain the discrepancies observed between the Monte Carlo model and the data.

[2]To make it easier and faster in simulations to change the relative performance, it is in the simulation code implemented as an *absorption* efficiency of identical value in the gas. This is, however, only a technical difference and it should still be interpreted as a relative performance related to the production of transition radiation.

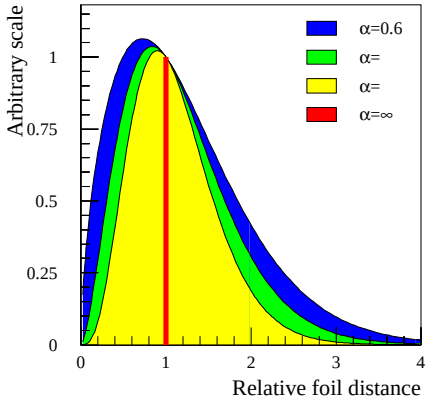

Figure 5.11: The distribution in foil distance around the mean for different values of α in a Γ distribution. Regular foil spacings corresponds to $\alpha = \infty$.

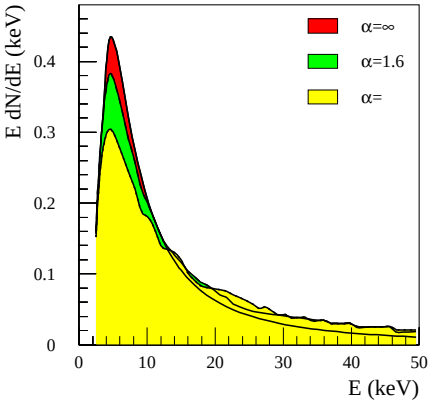

Figure 5.12: The energy spectrum of transition radiation from a stack of foils with irregular spacing. Regular foil corresponds to $\alpha = \infty$. Note how the curves cross at approximately 12 keV.

5.6.2 Energy absorption in a straw

The ionisation from charged particles crossing a straw is calculated using the photo absorption ionisation (PAI) model described in section 3.4.2. With the absorption cross section $\frac{\mathrm{d}\sigma}{\mathrm{d}\omega}$ taken from (3.38), the mean number of ionisations per unit length in the gas is calculated as a numerical integration

$$\left\langle \frac{\mathrm{d}N}{\mathrm{d}x} \right\rangle = \int_0^\infty \mathrm{d}\omega n_\mathrm{e} \frac{\mathrm{d}\sigma}{\mathrm{d}\omega}. \tag{5.11}$$

Starting from the entry point of the particle to the straw the distance x_i to the next ionisation is calculated as a random step

$$x_i = -\left\langle \frac{\mathrm{d}N}{\mathrm{d}x} \right\rangle^{-1} \log U_i \tag{5.12}$$

where U_i is a random number from a uniform distribution with $0 < U_i < 1$. The energy of each ionisation is taken as a random energy from the normalised distribution of the energy loss (3.37). In this way the fluctuations in both energy and position of the energy loss are simulated.

5.6.3 Electronics response

To simulate the response of the electronics the energy deposition of all charged particles and all transition radiation in a straw is taken into account. From the coordinates

of the individual energy depositions in the straw the arrival time at the wire is calculated and a table with energy deposition as a function of the time built up.

If a large charge arrives at the wire at the same time it will to some extent cancel the field from the wire thus giving a smaller gas amplification. This effect, the space charge effect, was measured on a single straw with analog readout in the testbeam. In fig. 5.13 the reduction of the recorded signal amplitude is shown as a function of the energy deposition for several different values of the gas gain. It can be seen that the space charge effect increases with increased deposited energy and increased gas gain.

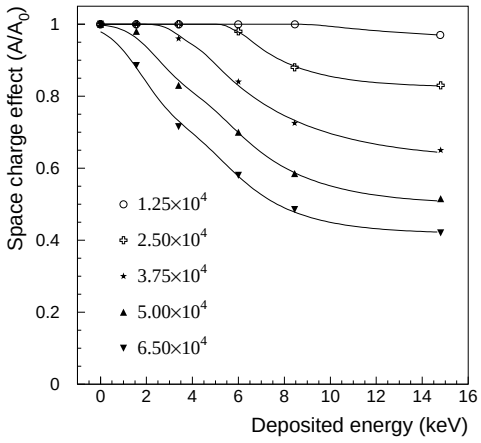

Figure 5.13: The space charge effect measured on a single straw in the testbeam. The relative amplitude of the signal is shown as a function of the deposited energy for several different values of the gas gain. The curves show the functional description of the space charge effect in the Monte Carlo.

For the Monte Carlo simulation an empirical fit with an exponential function was made to the data points. To assure a smooth transition to the region with low deposited energy where there is no space charge effect the exponential was folded with a Gaussian distribution. The relative amplitude recorded is thus parameterized as

$$\frac{A}{A_0} = 1 - \frac{\alpha}{2}\left[\mathrm{erfc}\left(-\frac{E-E_0}{\sigma}\right)\right. \\ \left. - \exp\left(\frac{\tau^2\sigma^2}{2} - \tau(E-E_0)\right)\mathrm{erfc}\left(\sigma\tau - \frac{E-E_0}{\sigma}\right)\right] \qquad (5.13)$$

where erfc is the error function, E the deposited energy, E_0 the point where the curve would cross unity in absence of the smooth transition, α the saturation value at high

deposited energies, τ the parameter controlling how fast the saturation is reached and finally σ the width of the Gaussian used in the folding. In fig. 5.13 it is seen that the empirical function nicely reproduces data. For other values of the gas gain the parameters in (5.13) are interpolated with the parameters from the closest lying gas gains. The model was tested with data from the sector TRT prototype with the results presented in section 5.8.4.

The signal recorded on the wire is as the last step in the simulation convoluted with the shaping function of the readout electronics as shown in fig. 5.3. With the final analog shape of the signal registered the periods where the high and low digital thresholds are passed are determined. The timing information (drift-time measurement) of the low threshold is stored with a precision of 0.5 ns.

5.7 The Monte Carlo model of the testbeam

A detailed Monte Carlo model using GEANT, has been developed to simulate the TRT prototype and the complete beamline. It makes use of the same software modules as the simulation of the TRT in the ATLAS Inner Detector providing as accurate as possible a calibration for the performance studies of the final ATLAS detector.

5.7.1 The modules in the testbeam simulation

A realistic simulation of the signals in the TRT prototype has to include not only a detailed model of the prototype but also a simulation of the other elements in the beamline. This is the only way to ensure that effects from material upstream and small effects from the alignment procedure are taken into account. As it was shown in section 5.5 the purity of the beams are so good that the electron and pion data can be assumed to be completely clean samples. For this reason the particle identification devices have not been simulated[3]. An event display of a simulated 20 GeV electron coming down the beamline and bent in the magnetic field is shown in fig. 5.14. The particle continuing in a straight line is an emitted photon and the small wiggle inside the second TRT module a δ-ray.

The silicon beam telescope

The silicon beam telescope consists of several individual silicon modules. Each module has two sensitive planes of 300 μm thick silicon with a 50 μm mylar window placed on each side of the double plane. The modules are 3.2×3.2 cm^2 and are assumed to be divided into parallel x or y strips with a width of 50 μm.

[3] The Cherenkov counter is so far upstream that any secondary particles created in the material of the counter bend out of the beam by the focusing magnets before reaching the TRT prototype. The calorimeter including the preshower is well behind the prototype and will not affect the other detectors.

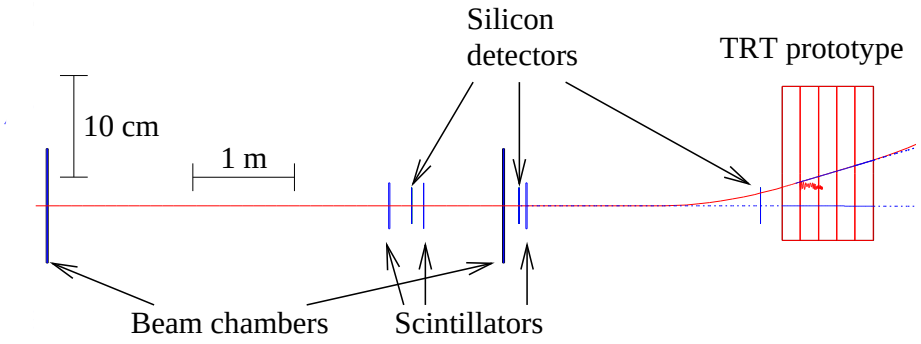

Figure 5.14: An event display of a simulated 20 GeV electron coming down the beamline and bent in the magnetic field. The particle continuing in a straight line is an emitted photon and the small wiggle inside the second TRT module prototype a δ-ray. Note the factor 10 difference in the horizontal and vertical scale.

Beam chambers

A rudimentary simulation of the H8 beam chambers has been implemented mainly to account for the 1% radiation length of material of each chamber. For this reason the beam chambers are just simulated as 10×10 cm^2 2 cm thick slabs of air with a 890 μm Al plate in the middle serving as the sensitive area. For flexibility, hits are stored with 100 μm precision in the x and y coordinate (instead of the 300 μm actual beam chamber precision). In the electron identification analysis the beam chambers were not used in the reconstruction of simulated data.

Counters

The testbeam setup includes several scintillator counters, mainly for triggering. While the counters are not used after the preliminary event selection, their presence contributes to the overall material in front of the TRT prototype. The counters in the simulation have a CH material composition with a density of 1.032 which is a good approximation for standard organic scintillators.

TRT prototype

The TRT prototype has been implemented in the simulation with great care following the geometry and material composition in the prototype as described in section 5.1. In the material description the radiator is simulated as CH_2 with a density taking into account the relative volume of the foil with respect to the air in the radiator. The straw signal is simulated as described in section 5.6 with parameters for foil thickness, anode wire radius etc. taken from the parameters of the prototype. In fig. 5.15 is shown a view along the straws in the first TRT prototype module. The

interchanging layers of straws and radiator can be seen as well as the positioning of the straws inside each layer minimising the layer-to-layer correlations in the drift-time measurements of the hits.

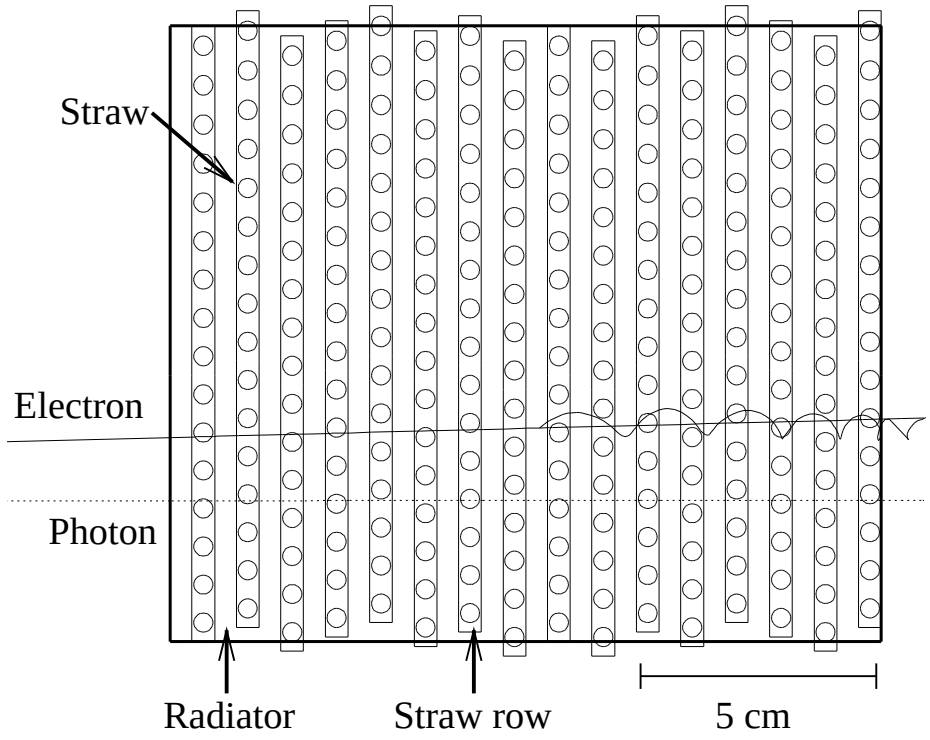

Figure 5.15: The first sector of the TRT prototype.

Material distribution

The material included in the simulation matches the amount and distribution in the beamline to an accuracy better than the 10% uncertainty in the actual amount of material present. The material in the simulation for the 1996 testbeam run including the prototype and all detectors in front of it is summarised in table 5.3.

5.7.2 Calibrating the Monte Carlo model

The probability per straw to observe a high-threshold hit on the reconstructed track as a function of the threshold in keV is shown in fig. 5.16 for pions and electrons in a 1.56 T magnetic field. The testbeam measurements are represented as horizontal bands with a width corresponding to the measurement errors. The discriminator

Testbeam part	X_0 (%)	λ (%)
5 TRT sectors	8.67	3.73
3 Silicon detectors	2.03	0.43
2 Beam chambers	2.00	0.48
3 scintillators	4.87	2.30
Air	2.10	0.86
Total	19.70	7.80

Table 5.3: The amount of material in the simulation of the testbeam in 1996 measured in radiation lengths (X_0) and absorption lengths (λ).

threshold was at the time the data was taken calibrated to a 5% accuracy using data taken with a 5.9 keV ^{55}Fe X-ray source.

For pions, the high-threshold hit probability is measured to be $4.93 \pm 0.07\%$, which corresponds to a value of 6.00 ± 0.06 keV for the high threshold, in excellent agreement with the ^{55}Fe measurements. Once this scale is fixed, the simulation can be compared to the data from electrons which produce transition radiation. The Monte Carlo model used for the production of transition radiation is valid for an ideal radiator with perfectly regular foil spacings and foil thicknesses. In reality, the prototype radiator geometry is not perfectly regular, and a tunable overall reduction factor was applied to the amount of transition radiation produced. This factor reflects the relative radiator performance with respect to an ideal radiator, and was found to be $88.4 \pm 2.2 \pm 2.0\%$ for a 6 keV threshold, as shown in fig. 5.16. The first quoted error is statistical and the second one is an estimate of the systematic error, based on the analysis of data taken at different periods during the testbeam run in 1996. This measured relative radiator performance was found to be stable as a function of the choice of GEANT cutoffs used in the Monte Carlo model.

The measured and predicted pion efficiencies at a fixed electron efficiency of 90% are shown in fig. 5.17 as a function of the high threshold. Data taken in a 1.56 T magnetic field are compared to simulations with relative radiator performances of 80% and 90%. This figure shows that the relative radiator performance varies from $\sim 80\%$ for a threshold around 4.5 keV to $\sim 90\%$ for a threshold above 6 keV. The shape of the transition radiation spectrum is therefore not reproduced accurately enough by the simulation. More detailed comparisons between measured and predicted transition radiation spectra and spectra can be found in [57].

5.8 Electron identification

All results reported here were obtained with beams of 20 GeV pions and electrons. Electron identification using transition radiation makes use of the difference in the energy deposited in the straws by electrons and by charged pions, which are the main background source to electrons at the LHC. For electrons, the tail above 5–7 keV is dominated by transition radiation hits; for pions it is mostly due to δ-rays. The pion

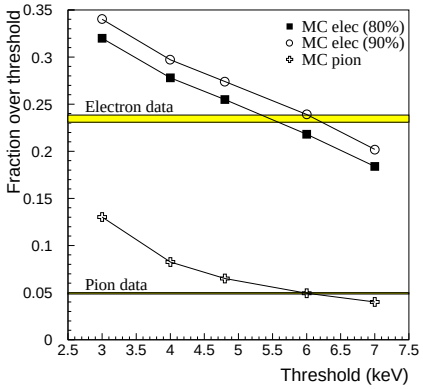

Figure 5.16: Probability to observe a high-threshold hit in a straw crossed by a pion or electron track as a function of the value chosen for the high threshold. The results are shown as horizontal bands for the data, which were taken at a fixed threshold of approximately 6 keV, and as curves for the Monte Carlo simulations. For the simulation of electrons, the results are shown for relative radiator performances of 80% and 90% (see text).

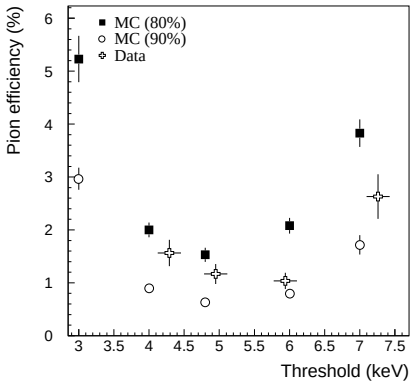

Figure 5.17: Pion efficiency at a fixed electron efficiency of 90% as a function of the high threshold. Results from measurements in a 1.56 T magnetic field are compared with Monte Carlo predictions for relative radiator performances of 80% and 90%.

rejection is calculated by counting the number of high threshold hits on reconstructed tracks for pions and electrons.

The distribution of high-threshold hits on the reconstructed tracks is expected to follow a binomial law. This is illustrated in fig. 5.19, where a fit has been performed to the electron and pion data of fig. 5.18. The distributions follow the binomial law across several orders of magnitude and do not display any poorly understood tails.

By requiring more than a certain number of high-threshold hits along the track the efficiency for misidentifying pions as electrons is measured as a function of the electron efficiency. In fig. 5.20 is shown the result of applying this procedure to the distributions from fig. 5.18, which were obtained with data taken in a 0.8 T field and with a high-threshold discriminator setting of 6 keV. For an electron efficiency of 90%, the measured pion efficiency is around 1.2%, corresponding to a rejection factor of 80 against pions.

The high-threshold setting for the TRDA chip can be varied and the pion rejection depends to some extent on the value chosen. In fig. 5.21 the pion efficiency for a fixed electron efficiency of 90% is shown as a function of the setting of the high-threshold

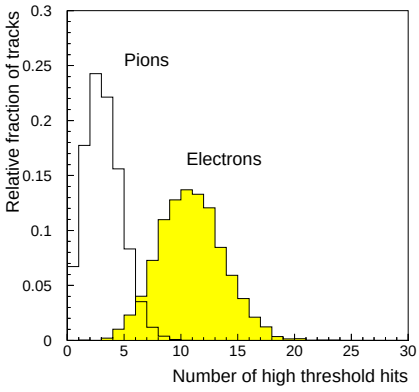

Figure 5.18: The distribution in the number of high-threshold hits (above 6 keV) on reconstructed tracks from 20 GeV pions and electrons in a magnetic field of 0.8 T.

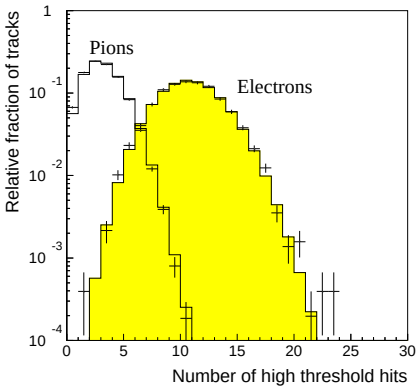

Figure 5.19: Distribution of the number of high-threshold hits for pions and electrons in a magnetic field of 0.8 T. The crosses represent the data and the histograms a fit of the data to a binomial distribution.

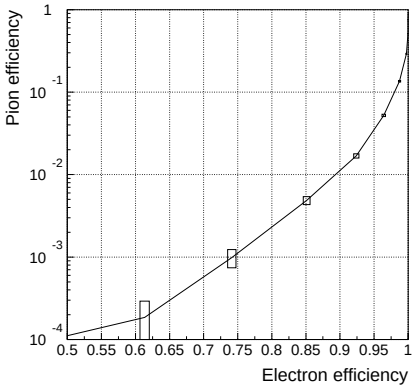

Figure 5.20: Pion versus electron efficiency, obtained as a function of the number of high-threshold hits, as shown in fig. 5.18, required on reconstructed tracks.

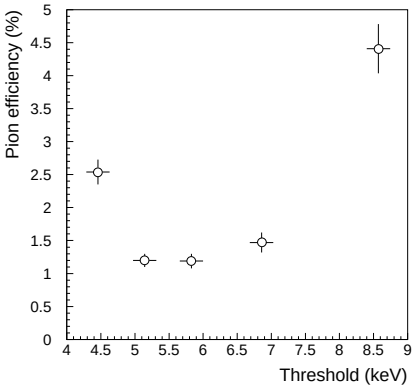

Figure 5.21: The pion efficiency as a function of the discriminator threshold for a fixed electron efficiency of 90%, and for 20 GeV pions and electrons in a 0.8 T magnetic field.

discriminator. The electron identification performance is seen to be quite stable for thresholds between 5 and 7 keV. Further results reported in this paper for pion efficiencies are given for a threshold of 6 keV and an electron efficiency of 90%.

5.8.1 Effect of the detector length

The pion efficiency depends strongly on the total length of the detector. In fig. 5.22 is shown the pion efficiency as a function of the length of the prototype traversed by the beam particles. The pion rejection improves by approximately a factor two for each additional 150 mm of detector length.

If the readout electronics in a given layer of the prototype has ceased to operate this layer cannot provide any additional pion rejection. In fig. 5.22 this effect can be seen at the length of around 680 mm where the rejection power stays constant for three consecutive straw layers corresponding to two nonfunctional layers. All results presented from data taken with one or more nonfunctional layers, have been corrected, making use of the exponential dependence of pion efficiency as a function of the detector length.

5.8.2 Effect of the magnetic field

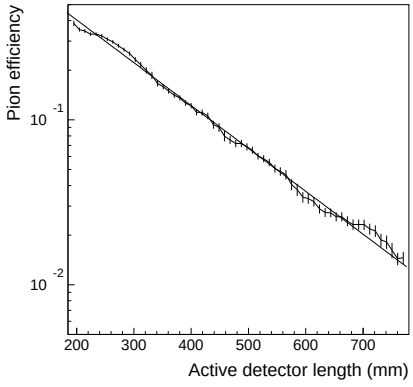

Figure 5.22: The efficiency for identification of pions with an electron efficiency of 90% as a function of the length of the prototype traversed by the beam particles. The error bars are strongly correlated from point to point.

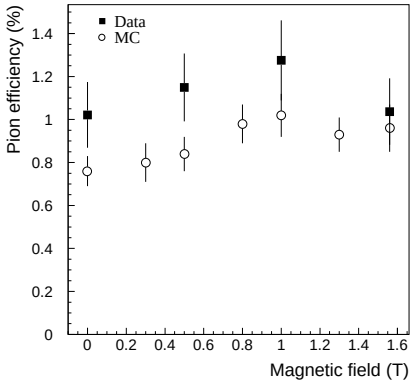

Figure 5.23: The pion efficiency at fixed electron efficiency of 90% as a function of the magnetic field in the prototype.

A good understanding of the behaviour of the TRT prototype in a high magnetic fields is of importance, since the ATLAS TRT will operate in a field of 1–2 T. In the

setup of 1996 it was possible to attain a maximum field of 1.56 T. For four different values of the magnetic field the pion efficiency was evaluated for a fixed electron efficiency of 90% as shown in fig. 5.23. The difference between the simulation and the data is less than the variations caused by the systematic uncertainty in the calibration of the relative radiator performance. For 20 GeV beams of electrons and pions no significant change of the performance as a function of the magnetic field was observed.

5.8.3 Effect of changing the straw density

For data taken in 1996, where the beam was perpendicular to the straws, it was possible to test the influence of the straw density in each layer on the electron identification performance. This was done by moving the prototype by ±6 cm and ±12 cm in the vertical direction, as shown in fig. 5.24.

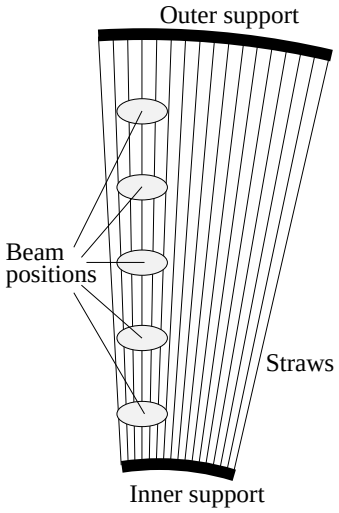

Figure 5.24: A single straw layer with the different positions of the beam used to test the influence of the straw density in the layers on the electron identification performance.

The relative radiator performance was for each position of the prototype determined as described in section 5.7.2 with the results including statistical errors shown in fig. 5.25. In principle the relative performance should only depend on the properties of the radiator, and thus not on the straw density in the layers, but the data shows a significant drop in the relative performance with an increased distance between the straws. The probability that the value of the relative performance is constant and the behaviour seen in fig. 5.25 just a statistical fluctuation is below 10^{-3}. As the signal from pions is unaffected by changing the straw density the reason for the discrepancy has to be found in the simulation of the absorbed transition radiation spectrum.

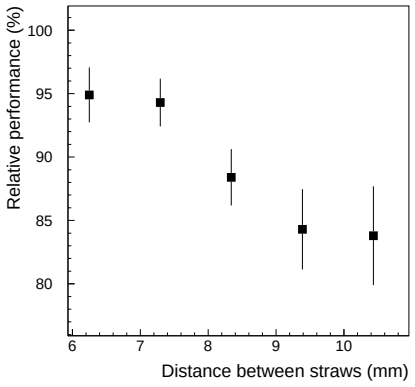

Figure 5.25: The best match to data of the relative radiator performance for the prototype as a function of the straw density from data in a 1.56 T field. The straw density is expressed as the distance between adjacent straws in a layer at the position of the beam.

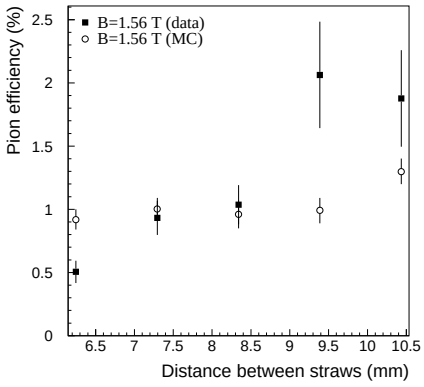

Figure 5.26: Pions rejection for different straw densities in a magnetic field of 1.56 T.

The formula for foils with irregular spacing as described in section 5.6.1 was implemented in the simulation to investigate if the difference between the data and the simulation was caused by the simplified simulation of the prototype foils as regular foils (see section 5.7.2). The absorbed transition radiation spectrum with the more detailed simulation was very similar to the simplified approach, thus providing no further explanation.

The dependence of the pion efficiency on the straw density in a 1.56 T field, as seen in fig. 5.26, is slightly different for the data and the simulation reflecting the difference of the single straw response described above. The same effect is seen for data taken in no magnetic field. For the simulation points in fig. 5.26 the relative performance of the prototype foils was kept fixed at the calibrated value of 88.4% for the central detector position with a threshold of 6 keV.

5.8.4 Effect of the gas parameters

The parameters of the gas also influence the electron identification performance. The tracking performance of the detector can be improved by lowering the xenon concentration and thereby get a faster gas or by increasing the gas gain from the nominal value of $2.5 \cdot 10^4$. The degradation in pion rejection from increasing the gain by 60% is a factor 1.8 as shown in fig. 5.27 where the data and the Monte Carlo simulations are compared. Space charge effects around the wire reduce the

effective gain for the highest energy depositions with an increased gas gain causing a larger effect as shown in section 5.6.3. The lower effective gas gain for large energy depositions reduces the signal from transition radiation photons thus causing a worse electron identification performance at high gas gains.

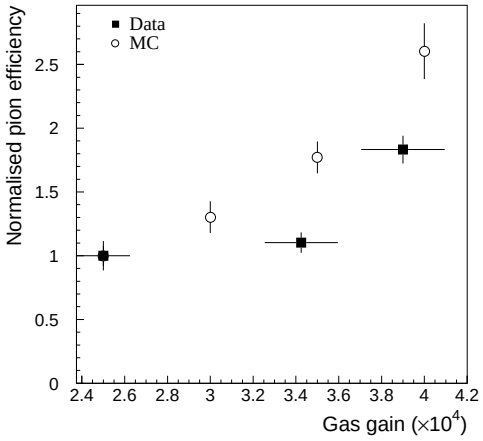

Figure 5.27: The pion efficiency at a fixed electron efficiency of 90% as a function of the gas gain. For both the data (filled squares) and the Monte Carlo simulation (open circles) the pion efficiency is normalised to the efficiency at the nominal gas gain of $2.5 \cdot 10^4$.

Two gas mixtures were tried, the standard 70% Xe, 20% CF_4, 10% CO_2 and a mixture with 40% Xe, 50% CF_4, 10% CO_2 in no magnetic field. Compared at the high threshold of 6 keV the pion efficiency increases by a factor 8 from 1.2% with 70% Xe to 9.6% with 40% Xe. This fits well with an extrapolation of the results from xenon concentrations between 50% and 70% presented in [44].

5.9 Summary of performance

A prototype of the Transition Radiation Tracker (TRT) of the ATLAS detector has been built. The geometry and materials of this prototype and the characteristics of its readout electronics are close to those foreseen for the operation of the TRT detector at the LHC.

The prototype has been tested over a wide range of operating conditions and has shown reliable and stable performance. Results on the electron identification performance have been presented in this chapter and show that, for an electron efficiency of 90%, a pion efficiency of $\sim 1\%$ can be achieved over a detector length of 780 mm.

The performance was measured to be stable as a function of the discriminator threshold (from 5 to 7 keV) and of the magnetic field (from 0 to 1.6 T). In contrast, the performance was found to be quite sensitive to the choice of gas gain and to the amount of xenon gas in the straws.

Although detailed Monte Carlo simulations have been shown to accurately describe the measured straw performance in terms of drift-time measurement accuracy and efficiency, the simulation of the transition radiation cannot predict the measured electron identification performance without introducing normalisation factors, which reflect the limited knowledge of the exact geometry of the foil radiator and also of the exact energy spectrum of produced and absorbed X-ray photons. On average, the measured radiator performance was found to be almost 90% of that expected from a perfectly regular radiator.

The above results can be used to evaluate more quantitatively the expected electron identification performance of the TRT at the LHC, as described in detail in [4]. The expected pion efficiency, at a fixed electron efficiency of 90%, varies from 0.5% to 8% (respectively 1.6% to 16%) over the different regions of the TRT detector, at low (respectively high) luminosity.

Chapter 6

ATLAS Monte Carlo simulations

Simulation tools are important for the design of a detector and for the development of the algorithms that will be used for reconstruction. Detector simulations have developed from a simple state into the detailed models used today where essentially all known physical processes involving the interaction between particles and matter are included.

In this chapter the Monte Carlo simulations of the ATLAS detector will be described. The emphasis will be on the physics processes and the algorithms involved while the actual software implementation will not be treated.

6.1 Simulation

Every detector simulation has to start with a description of the detector geometry. For the ATLAS detector almost every detail is included in the detector description. Taking the TRT as an example the carbon fibre shells of the modules, the straw walls, the gas composition inside and outside the straws, and the wires are all included. However, some simplifications are used in the materials which do not act as active detecting elements. For both the support structure, the cooling and the electronics, the materials are assumed to have a flat distribution in the φ coordinate. Neither are misalignments of detector elements included in the detector geometry.

The GEANT 3.21 [55] environment is used for the geometry description and the full detector simulation including the tracing of the particles and the electronics response of the active detector elements.

For the Inner Detector the most important physics processes simulated are multiple scattering, continuous energy loss, bremsstrahlung for electrons, conversions for photons and nuclear interactions for the hadrons. To get accurate results from a GEANT simulation it is thus necessary to have both the correct distribution and composition of the materials.

In the calorimeters the description of the shower processes are the most important. The showers are simulated by following all the particles created in the showering process. Particles are traced down to an energy of 100 keV at which point they stop and deposit their remaining energy. For electromagnetic showers the physics processes of pair production and bremsstrahlung are rather simple whereas the nuclear processes involved in hadronic showers are complicated and are not understood in as great detail. In particular the fluctuations in the response of the hadronic calorimeter are difficult to simulate with sufficient accuracy.

For each sub-detector there is a model of how the ionisation in the active detector element is changed into the digital output of the readout electronics. This step is called the digitisation phase and a description of the TRT signal collection can be found with the description of the testbeam Monte Carlo model in section 5.7. The simulated data should at this point be equivalent in format to the data that will eventually be recorded with the ATLAS detector. The simulation of noisy and dead channels in the electronics is also a part of the digitisation phase.

The simulation of the detector is important during the design phase to develop a detector with an optimal discovery potential within the constraints from technology, survivability and finances. When the final detector is taking data the simulations become important for calibration and understanding of the data.

The reconstruction step in a detector simulation involves the reconstruction of the kinematic information and particle identification. For the Inner Detector and the muon system, tracks are reconstructed from the hits in the individual detector elements. In the calorimeter cells with deposited energy are grouped together in clusters. At a later stage in the reconstruction all information can be combined to obtain the kinematic information of the event. Only the reconstruction in the Inner Detector will be treated in this chapter.

6.2 Pattern recognition in the Inner Detector

Pattern recognition is a widely used term for all kind of processes where specific information is extracted from a large set of individual measurements. The part of the brain that analyses the information from the eye is probably one of the most advanced pattern recognition systems known. The eye has three different sensor types used during daytime which provides the brain with a highly segmented colour image. From this the eye can at the first level extract information like lines and coloured areas and at a deeper lying level recognising objects as faces or letters.

Pattern recognition systems developed for finding tracks in detectors are often evaluated by visual inspection making use of the eyes outstanding pattern recognition capabilities. A discussion of visualisation methods suited for the eye can be found in [58].

For the ATLAS Inner Detector it is a problem to find all the tracks. As an example of the task for the pattern recognition a Higgs particle decaying to two b-quarks is shown in fig. 6.1. The two jets from the b-quark fragmentation are clearly recognisable in the TRT as are many individual tracks. The tracks cannot be seen

in the silicon detectors for two reasons: the number of hits on each track compared to the TRT is lower and the presentation is not optimal for the human eye[1].

Some clear definitions are necessary for a discussion of pattern recognition:

Hit A detection channel with an output signal above some threshold. In the silicon detectors the small cluster of channels with energy above threshold created by a charged particle or noise. In the TRT a straw with an energy deposition above the low threshold. With the drift-time included it is called a drift-time hit.

Occupancy The fraction of detector channels with a hit in a local area.

Efficiency The probability for a hit in a channel where the active detection area is crossed by a charged particle.

Noise level The fraction of channels in a local area with hits caused by electronic noise.

Shared hits Hits created by a combination of several charged particles or a combination of noise and a charged particle.

Space-point The combination of two hits, in the two different projections of a silicon layer with a stereo-angle, to form a hit in three dimensions.

Raising the abstraction level and looking at the reconstruction of tracks the following definitions are used:

Track The group of hits created by a single charged particle. Also used as a short form for the reconstructed parameters of a charged particle.

Pattern recognition The process of finding the tracks.

Track fitting After finding the track with the pattern recognition an optimal fit can be made with the positions of all hits on the track to extract the track parameters.

Wrong hit An extra hit associated to a track which is not created by the charged particle giving rise to the other hits on the track.

Double counting When one charged track is reconstructed as two tracks with almost identical parameters and sharing most of the hits. One or both tracks will have wrong and/or missing hits.

Track segment A group of hits which contains only a small part of all the hits created by a given charged particle.

[1] The tracks would be much easier to see in the silicon layers if the central part of the detector was shown in an (r, φ) projection with a highly compressed radial scale.

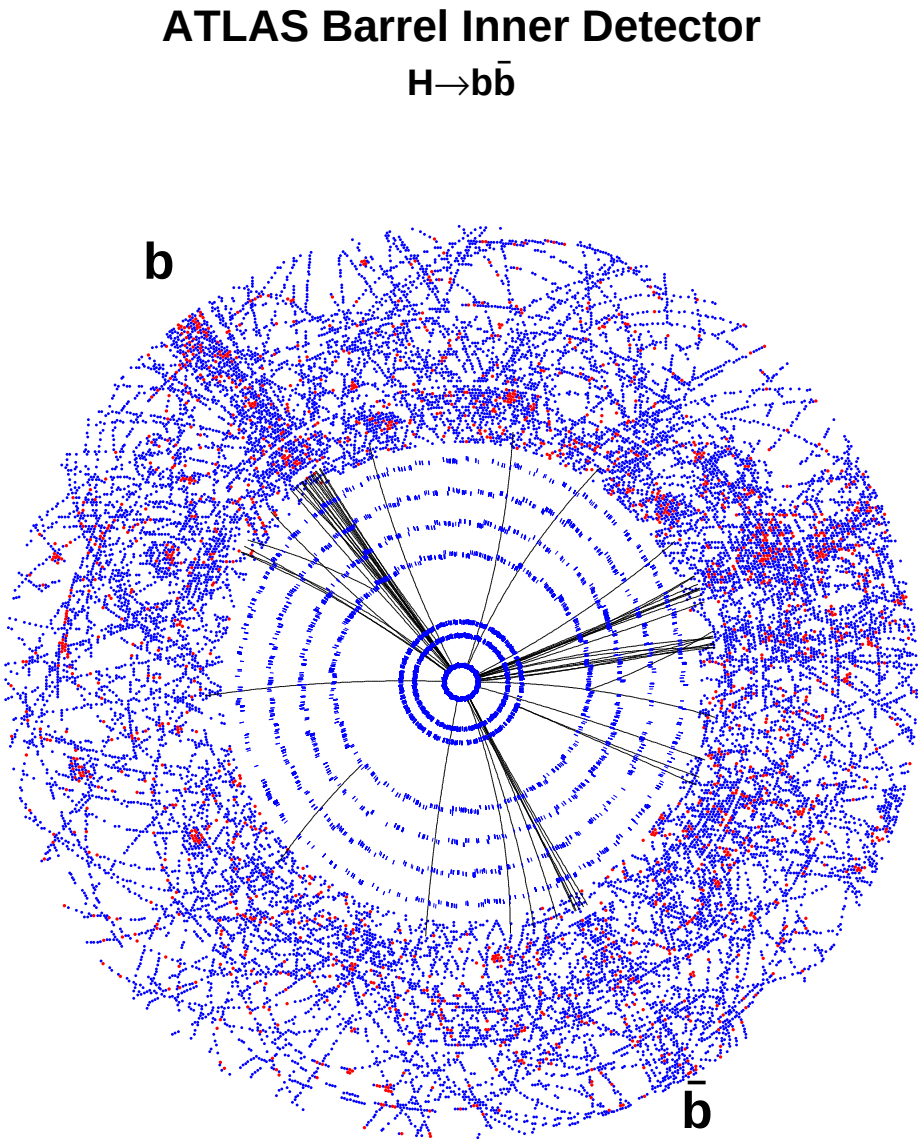

Figure 6.1: An event display of the barrel part of the Inner Detector with the decay of a Higgs particle to b-quarks at high luminosity. The two jets from the b-quark fragmentation are clearly visible. The inner part of the figure shows the hits in the silicon detectors with the reconstructed tracks superimposed. The outer part of the figure shows the hits in the barrel TRT.

Fake tracks A reconstructed track where the parameters do not match the parameters of any simulated charged track. In other places often defined as a track with above a certain fraction of wrong hits. Fake tracks mostly consist of several track segments randomly lining up.

Reconstructed tracks are in a solenoidal field described by the five parameters of a helix. The most commonly used parameterization is the Perigee representation where all five parameters and the corresponding 5×5 error matrix is given at the point where the track is closest to $(x, y) = (0, 0)$ in the transverse plane. The parameters are given as:

$\boldsymbol{d}$ Transverse impact parameter. Its sign is defined as positive when the φ angle of the point of closest approach is equal to $\varphi_0 + \frac{\pi}{2}$. See fig. 6.2.

$\boldsymbol{z_0}$ z-coordinate of the track at the point of closest approach to origo in the transverse plane.

$\boldsymbol{\varphi_0}$ The φ angle of the tangent to the track at the point of closest approach to origo in the transverse plane. See fig. 6.2.

$\boldsymbol{T}$ The slope $\cot(\theta)$ of the track.

$\boldsymbol{1/p_T}$ The inverse p_T of the track (Negative for tracks with negative charge).

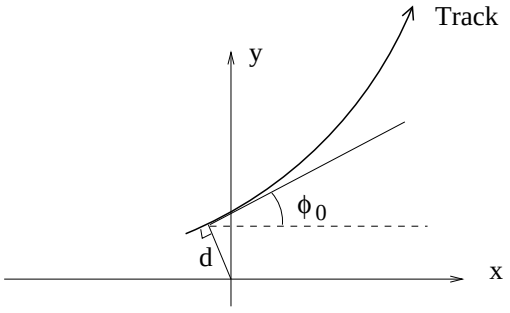

Figure 6.2: The definition of the impact parameter d and φ_0 in the track parameterization. The illustrated track has positive impact parameter.

Each bunch crossing at the LHC will at high luminosity create many hundred charged particles within the pseudorapidity coverage of the tracker. To avoid high occupancy in the tracker the detecting elements must have a high granularity such as pixel detectors which have been chosen for the three innermost silicon layers of the ATLAS detector. The occupancy in the innermost pixel layer is estimated to reach $4.4 \cdot 10^{-4}$ at high luminosity while the occupancy for the innermost silicon strip layer will reach $6.1 \cdot 10^{-3}$.

For the TRT the situation is quite different. Due to the larger area in (η, φ) covered by a single straw the occupancy is much higher but the number of hits on each

track is also high which for the pattern recognition performance more than outweighs the high occupancy. In fig. 6.3 the occupancy in the TRT at high luminosity is shown. It is seen that the highest occupancies ($\sim 40\%$) are in the innermost layers of the barrel detector and the wheels at the highest rapidities in the end-cap detectors. In both cases it is caused by the layers reaching close to the beampipe where the track density is higher. The TRT has the lowest occupancy of around 13% in the outermost layers of the barrel TRT. The innermost layers in the barrel TRT do, as described in section 4.4.2, only have active wires for $|z| > 40$ cm which gives an acceptable occupancy for those layers.

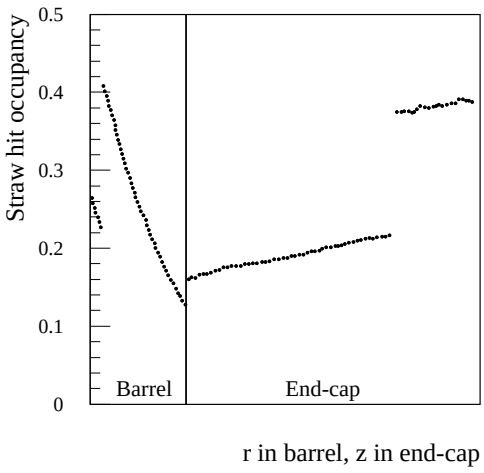

Figure 6.3: The occupancy in the TRT at high luminosity. The x-axis denotes increasing radius in the barrel detector and increasing z in the end-cap wheels.

When the occupancy in a detector rises the most sensitive parameter is the rate of fake tracks since the probability of segments of different tracks lining up rises sharply with the occupancy. In section 6.2.2 details will be given on the rate of fake tracks in the TRT and the evolution with luminosity.

6.2.1 Pattern recognition methods

For the reconstruction in the ATLAS detector several different methods have been developed for the pattern recognition based on different philosophies.

The XKALMAN pattern recognition starts the pattern recognition with a Hough transform of all hits in the TRT. The Hough transform will be explained in section 6.3.1. Here it will only be mentioned that the histogramming method takes advantage of the many hits on each track in the TRT to find tracks as spikes in a 2-dimensional $(\varphi_0, 1/p_{\mathrm{T}})$ distribution. From each track candidate found in the TRT a

Kalman filtering method [59, 60] is used to propagate the track candidate parameters through the silicon detectors, layer by layer towards the primary vertex. Effectively the Kalman filter method combines the pattern recognition and the track fitting into one step; the full track information from all already associated hits are used to propagate the track parameters including the error matrix to the next layer. Multiple scattering effects and the possibility to have kinks on the track from the emission of hard bremsstrahlung photons are taken into account. In the final stage, the track is propagated back into the TRT and the drift-time information of the straw hits used in the fit.

The IPatRec algorithm takes advantage of the low occupancy in the outermost layers of the silicon detectors. Within a narrow road connecting a seed from an electromagnetic cluster and the primary vertex all hits are selected and space points formed. The 3-D hits are divided into four partitions according to the distance from the primary vertex and track candidates created in a combinatorial search through the space-points in three different partitions. For each track candidate the track is propagated into the remaining detectors and fitted tracks passing quality cuts on the number of silicon detector hits and the χ^2 of the track are accepted. The TRT hits are included in the final stage of the track fit by a histogramming method in a narrow road around the reconstructed helix of the track.

More details on the XKalman and IPatRec algorithms can be found in [4] and references therein. Other pattern recognition algorithms have been developed for more or less specific problems. The algorithm for finding electrons from photons converting at radii above 40 cm will be described in section 6.3.1 as the development of this algorithm was of major importance for the π^0 rejection described in section 7.8.1.

6.2.2 Fake tracks in the TRT

The precision of the tracking parameters and fake track rates are the most important performance parameters of a tracking system. The parameter precision enters directly into the physics reach of the detector through the resolutions of mass, lifetime, secondary vertices etc. while a low fake track rate is essential to ensure a reliable tracking system. At the trigger level the rate of fake tracks will have a direct impact on the physics as a large rate will raise the level-2 trigger rate above an acceptable level.

The study presented here concerns the performance of the level-2 trigger in the TRT. At high luminosity the level-2 trigger in the electromagnetic calorimeter or the muon system will provide a trigger road of the size $(\eta, \varphi) = (0.20, 0.18)$ and within this road the Inner Detector level-2 trigger will search for tracks with high transverse momentum[2]. The tracks found inside the road can be separated in three groups:

Physics Tracks from the main physics event that the trigger tries to select, like the electrons in a $H \rightarrow ZZ \rightarrow e^+e^-l^+l^-$ decay.

Pile-up Tracks from minimum bias events. These tracks are at the trigger level an irreducible background rising linearly with the luminosity.

[2] At low luminosity there will also be a special J/Ψ trigger for B-physics studies.

Fake Tracks which are a random association of track segments creating tracks with parameters not matching any physics or pile-up tracks.

The important point for a tracker is to keep the rate of fake tracks well below the rate of pile-up tracks. In this way the large uncertainties that will necessarily be in the fake track rate, which is of a combinatorial origin, will not affect the performance of the detector.

The algorithm used for the pattern recognition is described in detail in [61]. It consist of the same Hough transform as used in the XKALMAN procedure but instead of continuing with the Kalman filtering method to include hits from the silicon detector it performs directly a fine-tuning of the reconstructed track in the TRT including the drift-time information of the hits. The code assumes implicitly that all tracks have a negligible impact parameter. If the level-2 trigger code in the Inner Detector will be able to combine the information in the TRT and the silicon detectors within the time allowed for a level-2 trigger is at the present not clear. This study represents a worst case scenario where it will not be possible to combine the information and the TRT and silicon detectors have to be treated separately.

The TRT pattern recognition code was modified to work inside a trigger road of size $(\eta, \varphi) = (0.20, 0.18)$ on the face of the calorimeter [62]. The histogramming algorithm works in the two natural projections for the TRT; (r, φ) for the barrel TRT and (z, φ) for the end-cap TRT. With the assumption of a negligible impact parameter and $p_{\mathrm{T}} > 2$ GeV tracks will be straight lines in both the (r, φ) and the (z, φ) projection. In fig. 6.4 the selected straws from a trigger road in the barrel TRT are shown and in fig. 6.5 the same for a trigger road in the end-cap part of the TRT.

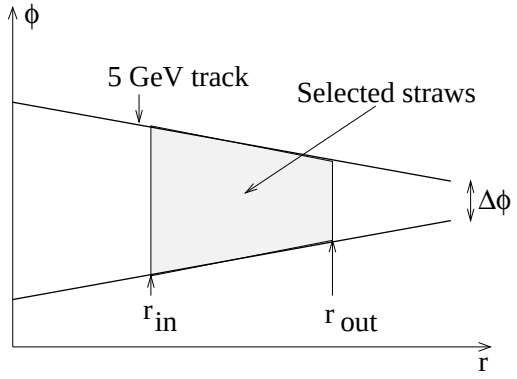

Figure 6.4: The straws selected from a trigger road in the barrel part of the TRT shown in the (r, φ) projection.

Three different sets of data were simulated: pile-up events containing only minimum-bias events, 20 GeV muons superimposed on top of the pile-up and 20 GeV electrons with pile-up superimposed. The Inner Detector layout used was the so

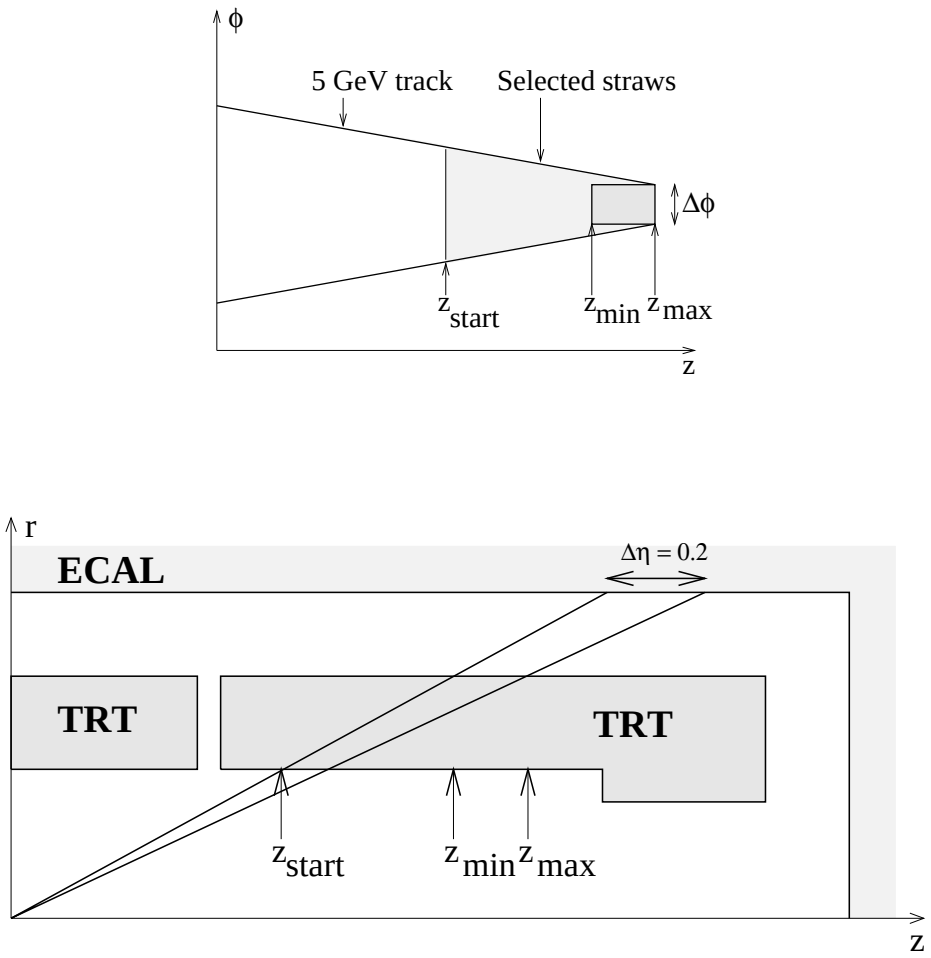

Figure 6.5: The straws selected from a trigger road in one of the end-cap parts of the TRT shown in an (z, φ) and (z, r) projection.

called *Panel layout* described in [2]. For the TRT the main difference was an inner radius of the barrel detector of 63 cm compared to the 56 cm in the current layout as presented in section 4.4.2.

The following definitions of fake track rate and track efficiency were used:

Fake track rate Probability to find one or more tracks in a trigger road containing pile-up i.e. no tracks from a physics event. Real tracks reconstructed from the pile up are subtracted from the rate.

Electron/muon efficiency Probability to find one or more tracks in a trigger road containing pile-up and one single lepton.

After assuring that the total track length within the TRT and the reconstructed pseudorapidity are compatible with the defined road, the main cut variables to maintain the lepton efficiency and decrease the fake rate were

$$\mathrm{h/t} = \frac{\#\text{ hits in crossed straws}}{\text{total }\#\text{ crossed straws}}, \tag{6.1}$$

$$\mathrm{d/h} = \frac{\#\text{ hits within drift-time road}}{\#\text{ hits in crossed straws}}, \tag{6.2}$$

where the drift-time road is defined as a 600 μm wide road in rφ around the fitted track. This corresponds to roughly twice the drift-time resolution at; at low luminosity the drift-time resolution is 140 μm; at high luminosity 180 μm.

Only tracks with $p_{\mathrm{T}} > 5$ GeV were considered and the real tracks in the pile-up subtracted to give the fake track rate from randomly aligned track segments with low transverse momentum in the TRT. The subtraction was done by comparing the reconstructed φ_0, p_{T} and η to the Monte Carlo truth information of the tracks in the pile-up.

The cuts on the track quality were adjusted to keep an efficiency for 20 GeV muons of 99% when all tracks with transverse momentum above 5 GeV were accepted. The fake rates plotted as a function of the luminosity are shown in fig. 6.6 for four different regions in pseudorapidity. It can be seen that the fake rates are well below the rate of tracks from pile-up events in most regions of the TRT.

In the transition region between the barrel and end-cap TRT ($|\eta| \sim 0.9$), where tracks pass through both parts of the TRT, it was impossible to attain a muon reconstruction efficiency of 99%. If instead the fake rate was fixed at the level of the real tracks in the pile-up the muon efficiency was as low as 70% at high luminosity.

By modifying the layout of the barrel TRT to have a minimum radius of 57 cm the average number of hits on muon tracks with transverse momentum of 5 GeV, increased from 22 to 28 in the worst part of the transition region. Since simulations with pile-up in several alternative layouts are demanding on computing time the different layout options were only studied without pile-up. However, comparisons with the fake rate studies in the layout with 63 cm inner radius of the barrel TRT suggested that the extra 6 hits on the tracks would bring the fake rate to an acceptable level at or below the rate of real tracks from the pile-up.

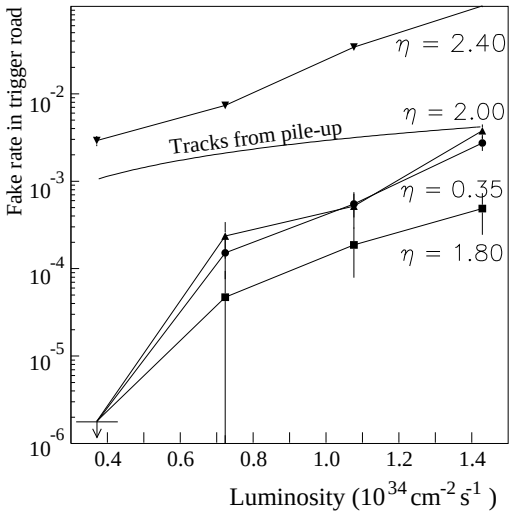

Figure 6.6: The fake rate inside a trigger road of size $(\eta, \varphi) = (0.20, 0.18)$ as a function of luminosity and pseudorapidity for a fixed efficiency of 99% for 20 GeV muons. The curved line is the rate of tracks from the pile-up in the end-cap region. See the text for a discussion of fake rates for $|\eta| \sim 0.9$.

In the present layout of the Inner Detector the detector has been improved at the two worst points in the *Panel layout*. The inner radius of the barrel TRT has, as a consequence of the fake rate study, been lowered to 56 cm to achieve better pattern recognition in the transition region from $0.65 < |\eta| < 1.2$. As suspected from the studies described above it was in [4] shown that the improvement of the transition region resulted in a fake rate well below the rate of real tracks in the pile-up.

In the redesign of the Inner Detector during 1995 the MSGC detectors[3] were replaced by silicon detectors. While the MSGC layers were placed in between the wheels of the end-cap TRT and behind the last TRT wheel, the silicon detectors are all placed at lower radius than the TRT. The change of the design gave room for a slightly longer end-cap TRT which results in an improved level-2 pattern recognition of the TRT at large pseudorapidities.

6.3 Conversion identification

Photons convert at positions corresponding to the material distribution in the Inner Detector of ATLAS and hence the conversion points are a direct measure of the material in the detector. For a small fraction x of material measured in units of radiation length along the photon path $\frac{7}{9}x$ of the photons will convert[4]. While the

[3] Micro Strip Gas Chamber detectors.

[4] The value 7/9 is correct within 10% for photon energies above 200 MeV

conversions are a part of the basic process in the electromagnetic calorimeter they are in nearly all situations a problem for a tracker and hence a tracker design with a minimum amount of material is desirable. For the design of the ATLAS Inner Detector the distribution in the conversions at the pseudorapidity $\eta = 0.3$ is shown in fig. 6.7. The individual silicon layers and the carbon fibre support structures of the TRT can clearly be seen as spikes in the distribution.

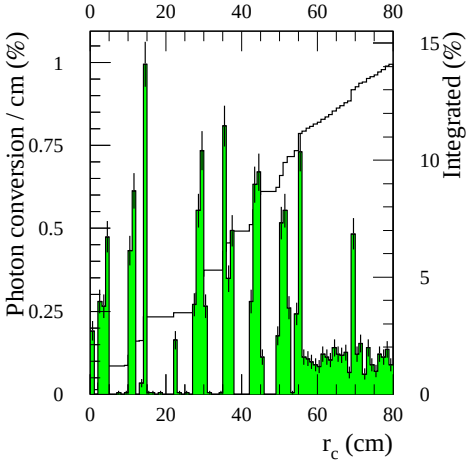

Figure 6.7: Distribution of conversions in the Inner Detector at $|\eta| = 0.3$. The left-hand scale shows the fraction of photons converting per cm at a given radius and the right-hand scale the integrated fraction.

With the photon conversions unavoidable the identification of them becomes important for several physics channels. A non-exhaustive list of areas are:

γ/π^0 separation The separation of photons in samples of converted and non-converted photons improves the γ/π^0 separation. The reconstructed parameters of conversions can provide further γ/π^0 separation for the converted photon sample. Details can be found in section 7.8.1.

γ/jet separation The main sample of hadronic events surviving the jet rejection in the calorimeter has a π^0 or η meson carrying the main part of the energy. Thus a good γ/π^0 separation is important to obtain a clean photon signal.

b-tagging The individual electrons from a photon conversion can create fake secondary vertices destroying the b-tagging capabilities. A veto on these electrons from the reconstruction of the conversions could improve the b-tagging power of algorithms depending on secondary vertex identification.

Lepton b-tagging Apart from secondary vertex identification the identification of leptons with relatively low p_{T} can be used for b-tagging. B-hadron decays

contain one or more leptons in a large fraction of the decays while this is not the case for light quark and gluon jets. A veto on early conversions is required to be able to reject jet events in the background where a photon from a π^0 decay converts.

$Z \to e^+e^-$ rejection If m_H is close to m_Z a rejection factor of around 500 is required on electrons in order to keep the $H \to \gamma\gamma$ decay clearly visible above the $Z \to e^+e^-$ background. The rejection is based on rejecting all events with a high transverse momentum track pointing towards the electromagnetic cluster. Such a process will also reject all $H \to \gamma\gamma$ events with one of the photons converting in the beampipe or the first pixel layer and conversion identification is required to regain these lost $H \to \gamma\gamma$ events.

Calorimeter calibration Several methods are possible for the calibration of the energy scale in the electromagnetic calorimeter. The E/p method calibrates the calorimeter energy with the transverse momentum measurement of electrons. The quality and the time required for a calibration depends on the purity of the isolated electrons [63]. Converted photons are a large background in the isolated electron sample which transition radiation identification can not reject. With conversion identification it is estimated that the background from converted photons will be well below the rate of real electrons in an isolated electron sample [4].

$A \to \tau\tau$ identification A decay of a pseudoscalar Higgs particle will be observed in the decay channel $A \to \tau\tau$. The τ-jets in the decay can be identified by selecting jets with few charged particles to identify the 3-prong τ decays. In this connection a veto on electrons from conversions can prove important for keeping a high τ-efficiency.

The conversion identification have so far only been tried out with full simulation in a few of the areas mentioned above.

Converted photons can be divided into two groups depending on the radius r_c where the conversion takes place. For late conversions with $r_c > 40$ cm the electrons are only reconstructed in the TRT as described in section 6.3.1 and the reconstructed conversion has no accurate slope $\cot\theta$ information. For early conversions with $r_c < 40$ cm the electrons have at least two space points each in the silicon tracker to measure the slope of the photon.

6.3.1 Pattern recognition in the TRT

Conversions with a conversion radius above 40 cm represents a special problem for pattern recognition programs as they will have either zero or just a few hits in the silicon detectors. The tracks from conversions also have a large impact parameter

$$d = \frac{\sqrt{1 + (r_c C)^2} - 1}{C}, \tag{6.3}$$

where r_c is the radius of conversion and $C = \frac{B}{p_T}$ the curvature signed with the charge of a track in the solenoid with magnetic field B. As an example a 1 GeV electron from a conversion at 50 cm will have an impact parameter of 7 cm. The standard pattern recognition programs are unsuitable for conversion identification as they have the implicit assumption of a impact parameter below a few cm.

A special pattern recognition program for late conversions has been developed. The implementation of the Hough transform is based on ideas developed for the first available pattern recognition program in the TRT [61] but many modifications and new ideas were required to optimise the code for identification of the electrons from late conversions.

For a conversion at a radius r_c the φ at a given radius r is given as

$$\varphi = \sin^{-1} u + \varphi_0 \tag{6.4}$$

with

$$u = \frac{Cr}{2} \frac{1 + \left(\frac{r_c}{r}\right)^2}{\sqrt{1 + r_c^2 C^2}}. \tag{6.5}$$

In fig. 6.8 the two electron tracks with transverse momentum of 10 GeV and 40 GeV from a photon with transverse momentum of 50 GeV converting at a radius of 50 cm, is shown in the (r, φ) projection. It can be seen how the tracks are no longer straight lines in this projection as was the case for tracks with infinitesimal impact parameter.

In the end-cap where the TRT measures (z, φ) and not (r, φ) as in the barrel TRT the radial coordinate can further be expressed through the z coordinate as

$$r^2 = \frac{1}{C^2} \left(4\sqrt{1 + r_c^2 C^2} \sin^2 \left(\frac{\alpha C}{2} \right) + \left(\sqrt{1 + r_c^2 C^2} - 1 \right)^2 \right) \tag{6.6}$$

with

$$\alpha = z \tan \theta \tag{6.7}$$

and θ the polar angle of the converted photon.

The starting point for the pattern recognition is a reconstructed electromagnetic cluster in the calorimeter. Straws in the TRT are selected to allow the reconstruction of tracks with $p_T > 0.5$ GeV from conversions with $r_c > 40$ cm and the conversion point (φ_c, η_c) inside a road of size $(\eta, \varphi) = (0.5, 0.5)$ centred around the direction of the reconstructed cluster. The straws selected for a road in the barrel TRT with $\varphi_c = 0.0$ are shown in fig. 6.9.

For each selected straw with a hit, the drift distance l calculated from the drift-time is translated into a coverage of the drift-time hit in φ

$$\left.\begin{matrix} \left[\varphi_w - \frac{l+\delta_l}{r}, \varphi_w - \frac{l-\delta_l}{r}\right] \\ \text{and } \left[\varphi_w + \frac{l-\delta_l}{r}, \varphi_w + \frac{l+\delta_l}{r}\right] \end{matrix}\right\} \quad \text{if } l \geq \delta_l, \tag{6.8}$$

$$\left.\left[\varphi_w - \frac{l+\delta_l}{r}, \varphi_w + \frac{l+\delta_l}{r}\right]\right\} \quad \text{if } l < \delta_l, \tag{6.9}$$

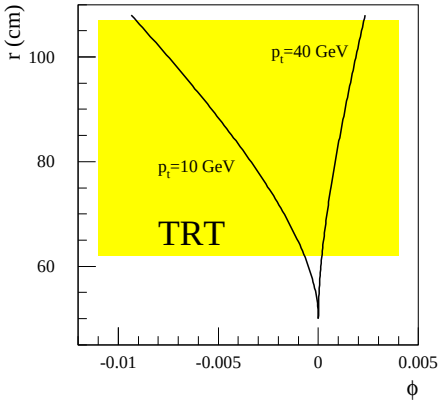

Figure 6.8: The tracks in the (r, φ) projection of the electrons from a photon converting at a radius of 50 cm.

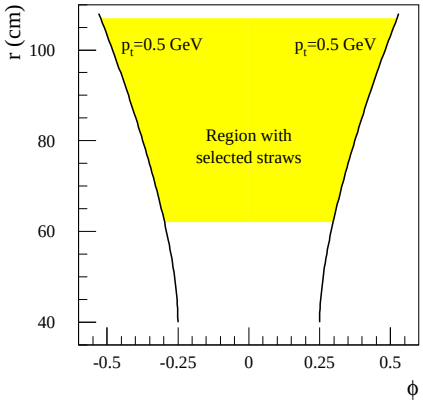

Figure 6.9: All straws inside the shaded region are selected for finding the tracks from late conversions in the barrel TRT. The road is centred around the position of the reconstructed cluster in the calorimeter.

where φ_w is the position of the wire and r the radius. In the end-cap the radius is taken as $r = z \tan\theta$ with z the position of the straw and $\tan\theta$ taken from the position of the electromagnetic cluster defining the road. The distance $\delta_l = 300$ μm is approximately twice the drift-time resolution. The ambiguity in the hit coordinate if $l \geq \delta_l$ is handled by treating each of the two possibilities as a hit but only allowing one of them to be used on a track.

The possible combinations of the three track parameters (r_c, C, φ_0) that will position a given hit on the track defines a volume in the (r_c, C, φ_0) parameter space of thickness $2\delta_l$ in the φ_0 direction. If the volumes defined by all selected hits are superimposed in the parameter space tracks will be defined by the points where most volumes overlap. In a mathematical language a *Hough transform* is performed on all selected drift-time hits and a function $h(r_c, C, \varphi_0)$ defined describing the number of overlapping volumes in the parameter space. The pattern recognition can then be understood as finding all local maxima of the function h.

The parameter space is searched by defining a grid in r_c and C with a grid size of 6 cm along the r_c coordinate and $7 \cdot 10^{-5}$ along the curvature coordinate.

Selecting a point in the (r_c, C) grid is equivalent to look at the intersection of a line along the φ_0 coordinate and all the volumes defined by the hits. In practise the intersection points are calculated using (6.4) to transform the spatial (r, φ) coordinates of the hits into the position on the φ_0 axis as

$$\varphi' = \varphi + \sin^{-1} u(r) \tag{6.10}$$

where the values $\sin^{-1} u(r)$ are taken from a *look-up table* prepared during the initialisation phase. The φ' coordinate where a drift-time hit starts its coverage is given a weight $w = +1$ while the endpoint in the coverage is given the weight $w = -1$. The number of hits on a track with a given φ_0 is then given as

$$n_{\rm hit}(\varphi_0) = n_{2\pi} + \sum_{\varphi_i < \varphi_0} w_i, \tag{6.11}$$

where $n_{2\pi}$ is the number of hits which covers the $0/2\pi$ border on the φ_0 axis. The sum in (6.11) is easily calculated by sorting all the drift-time hit borders φ'_i in ascending order and calculating the running sum of the associated weights w_i. Track candidates occur where $n_{\rm hit}(\varphi_0)$ attains a local maximum which is above some defined cutoff. The sorting method to find the φ_0 coordinate of the tracks is a continuous search in φ_0 thus not requiring a binning to be defined. Avoiding a binning has the advantage that an optimal precision is reached without having many empty bins and the disadvantage that sorting of an array with several thousand elements is required. For the first point selected in the $(r_{\rm c}, C)$ grid the array of φ' coordinates to be sorted is not ordered and the sorting time will develop as $N \log N$ where N is the total number of hits in the search. Moving from one curvature to the next only make a few of the hits change order, and the sorting time to reorder the array will, using an insertion sort method, be almost linear in N. Details about sorting algorithms can be found in [64].

Each track candidate identified during the scanning of the parameter space is given a weight proportional to $\frac{n_{\rm hit}}{n_{\rm cross}}$ where $n_{\rm cross}$ is the average number of crossed straws for a track with a given conversion radius and the track candidates are sorted in descending order of the weight. Passing through the list of track candidates a track is accepted if it has greater than five hits which are not already used by tracks with a higher weight. In this way the algorithm selects the best tracks and at the same time limits double counting. The number of independent hits required on a track is determined by a balance between double counting and track efficiency.

The algorithm described so far is used directly in the barrel TRT while the situation in the end-cap TRT is slightly more complicated since the straws crossed by a track not only depend on the three parameters $(r_{\rm c}, C, \varphi_0)$ but also on the polar angle of the parent photon. For all straws with a hit the α value of the straw is calculated using (6.7) and the shift in the φ coordinates of the hits calculated as

$$\varphi' = \varphi + \sin^{-1} u(r(\alpha)) \tag{6.12}$$

with the look-up table containing the values of $\sin^{-1} u(r(\alpha))$. In this way only the simple calculation of α needs to be performed for each hit while the time consuming calculation in (6.12) is required only once during the initialisation phase.

For each track found by the pattern recognition, fine-tuning is performed to get the optimal parameters $(r_{\rm c}, C, \varphi_0)$ of the track. The hits with coordinates (r, φ) on a track are mapped onto a plane as

$$(x, y) = (r, r \sin(\varphi - \varphi_0^{\rm PR})) \tag{6.13}$$

where φ_0^{PR} is the value of φ_0 obtained from the pattern recognition. Each point is assigned an error $\delta y = r\,\delta\varphi$ where $\delta\varphi$ is the width of the φ interval for the drift-time hit as defined in (6.8) and (6.9). A parabolic least squares fit of the type

$$y = Ax^2 + Bx + D \tag{6.14}$$

is made to the points and the refitted parameters are according to (6.4) extracted as

$$\varphi_0 = \varphi_0^{\mathrm{PR}} + B \tag{6.15}$$

$$C = \frac{2A}{\sqrt{1 - 4AD}} \tag{6.16}$$

$$r_{\mathrm{c}} = \sqrt{\frac{D}{A}} \tag{6.17}$$

Performance figures for the pattern recognition will be given after the presentation of the conversion algorithm in the next section since the code is so tightly connected to the identification of conversions.

6.3.2 The conversion algorithm

The algorithm for reconstructing conversions is relatively simple. It is assumed that all the primary photons have zero impact parameter, thus ignoring the beam spread of 15 μm in the transverse plane. No interesting areas with high energy photons from secondary vertices have yet been found. A conversion is, with this constraint, fully defined with the parameter set

$$\mathcal{C} = (r_{\mathrm{c}}, z_{\mathrm{c}}, \varphi_{\mathrm{c}}, T, C_1, C_2) \tag{6.18}$$

where the first three parameters define the conversion point in polar coordinates, T is the slope $\cot\theta$ of the photon and C_i the curvature of the two electrons signed with the charge. The parameters, $\mathcal{P}_i^{\mathrm{C}}$, of the electrons making up the conversion are uniquely given as

$$d_i = \frac{\sqrt{1 + r_{\mathrm{c}}^2 C_i^2} - 1}{C_i} \tag{6.19}$$

$$\varphi_i = \varphi_{\mathrm{c}} - \sin^{-1}\left(a_i r_{\mathrm{c}} + \frac{b_i}{r_{\mathrm{c}}}\right) \tag{6.20}$$

$$z_i = z_{\mathrm{c}} - \frac{2T}{C_i}\sin^{-1}\left(\frac{C_i\sqrt{\frac{r_{\mathrm{c}}^2 - d_i^2}{1 + C_i d_i}}}{2}\right) \tag{6.21}$$

$$T_i = T \tag{6.22}$$

$$1/p_{\mathrm{T}_i} = \frac{C_i}{B}, \tag{6.23}$$

where B is the magnetic field and

$$a_i = \frac{C_i}{2(1 + C_i d_i)} \tag{6.24}$$

$$b_i = d_i(1 - a_i d_i). \tag{6.25}$$

The reconstructed conversion is obtained as a χ^2 fit to the track parameters, $\mathcal{P}_i^{\mathrm{PR}}$, from the pattern recognition. The χ^2 is defined as

$$\chi^2 = \sum_{i=1}^{2} (\mathcal{P}_i^{\mathrm{PR}} - \mathcal{P}_i^{\mathrm{C}}) \mathrm{W}_i (\mathcal{P}_i^{\mathrm{PR}} - \mathcal{P}_i^{\mathrm{C}})^{\top} \tag{6.26}$$

which is minimised by varying the conversion parameters $\mathcal{C}$ as defined in (6.18). W_i is the inverse error matrix of the track with parameters $\mathcal{P}_i^{\mathrm{PR}}$. It is assumed that the individual track fits from the pattern recognition are uncorrelated. The minimisation of the 10 parameters with 6 degrees of freedom is performed with the MINUIT package [65].

Since a MINUIT fit is quite time consuming a preselection is made on the basis of the distance between the 2 tracks in the transverse plane. The distance is calculated at the radius of the hit closest to the primary vertex on the two tracks. The time consumed for conversion finding is at high luminosity in any case much lower than the time spent in the pattern recognition.

With the detector design as presented in the Inner Detector TDR [4] 10.6% of all photons with 50 GeV in transverse momentum convert below a radius of 40 cm. This fraction varies only slowly with the photon momentum. For $\mathrm{H} \to \gamma\gamma$ events this leads to at least one conversion in 20% of the events. Since the conversion electrons curve in the magnetic field, the cluster width in the $r\varphi$ direction is larger for converted photons leading to a worse energy resolution. To some extent this loss can be regained by an improved resolution in the position of the primary vertex from converted photons (section 7.3).

The identification of conversions has been tested mainly on a sample of photons and π^0's simulated with transverse momentum of 50 GeV over all pseudorapidities. This is close to the average p_{T} of photons expected from triggered $\mathrm{H} \to \gamma\gamma$ decays.

The efficiency and fake rates for conversions are normalised to conversions with $r_{\mathrm{c}} < 80$ cm and $|z_{\mathrm{c}}| < 280$ cm. Outside this region, the efficiency for finding conversions decreases quickly to zero as the amount of the Inner Detector crossed decreases.

The efficiency is almost flat across the Inner Detector volume, with an exception of conversions taking place close to the transition region between the barrel and end-cap TRT. The track search is performed down to a transverse momentum of 0.5 GeV, below which tracks begin to loop; tracks are found with high efficiency down to $p_{\mathrm{T}} \sim 1$ GeV. For photons with 50 GeV p_{T} this leads to a loss of 2% in efficiency. The distributions of the efficiency for recovering converted photons are shown in fig. 6.10 and fig. 6.11. The fall at large radii is mainly caused by conversions lost in the transition region between the barrel and end-cap TRT.

The efficiency as a function of the transverse momentum of the lowest energy conversion electron $p_{\mathrm{T}_{min}}$ is independent of this for $p_{\mathrm{T}_{min}}$ greater than 1 GeV. Early

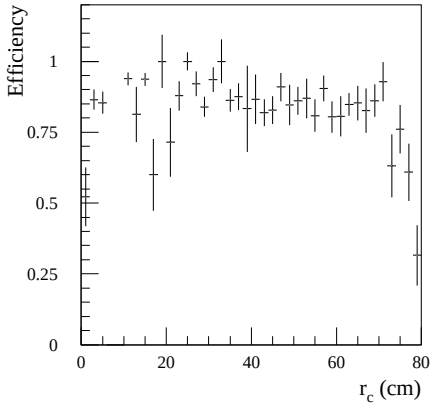

Figure 6.10: The efficiency for reconstructing converted photons with 50 GeV p_{T} as a function of the conversion radius.

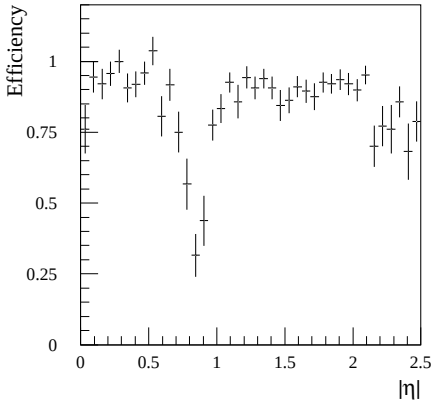

Figure 6.11: The efficiency for reconstructing converted photons with 50 GeV p_{T} as a function of the pseudorapidity of the photon.

conversions have a reconstruction efficiency integrated over η of 85%. The efficiency to reconstruct the high-p_{T} electron in this study is 95%.

How well the photon is reconstructed depends strongly on the radius of conversion r_{c}. Various reconstructed parameters for converted photons with 50 GeV transverse momentum (integrated over all pseudorapidities) are summarised in table 6.1. The resolution in transverse momentum is shown both before the conversion fit and after, where the photon p_{T} before the fit is simply defined as the summed p_{T} of the two reconstructed electrons. It can be seen how the χ^2 fit improves the p_{T} resolution by approximately 20%. The tails in the p_{T} resolution are measured as the fraction of the reconstructed photons with the p_{T} in the conversion fit above 2σ from the true value.

r_{c} (cm)	$\sigma(p_{\mathrm{T}})/p_{\mathrm{T}}$ before fit	$\sigma(p_{\mathrm{T}})/p_{\mathrm{T}}$ after fit	Tails outside $\pm 2\sigma$	$\sigma(r_{\mathrm{c}})$ (cm)	$\sigma(\varphi_0)$ (mrad)	$\sigma(z_0)$ (cm)
0–20	0.051	0.040	0.46	0.88	0.17	0.03
20–40	0.17	0.14	0.20	1.03	0.10	0.54
40–60	0.31	0.23	0.15	4.09	0.96	-
60–80	0.28	0.23	0.09	4.29	1.16	-

Table 6.1: Resolution at high luminosity of reconstructed parameters of converted photons with 50 GeV p_{T}.

Reconstructed momentum distributions after the conversion fit are in fig. 6.12 shown separately for r_{c} below 40 cm and r_{c} above 40 cm which more or less cor-

responds to the tracks reconstructed with XKALMAN (section 6.2) or the pattern recognition working in the TRT separately (section 6.3.1). It can be seen how the inclusion of hits from the silicon tracker and the longer track in the magnetic field greatly improves the p_{T} resolution. The long tails towards low reconstructed p_{T} is caused by the electrons emitting bremsstrahlung in the material of the Inner Detector. For isolated electrons it is possible, to some extent, to correct for this using the position of the electromagnetic cluster but this will not be possible for the electrons from converted photons.

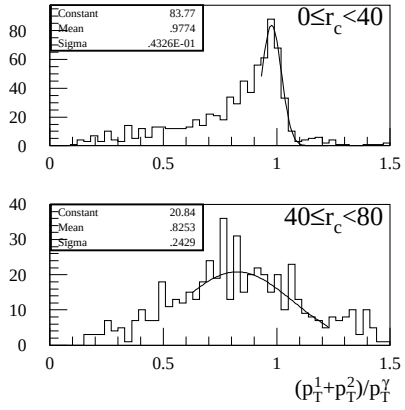

Figure 6.12: The reconstructed transverse momentum of the reconstructed conversions relative to the transverse momentum of the original photons with a transverse momentum of 50 GeV.

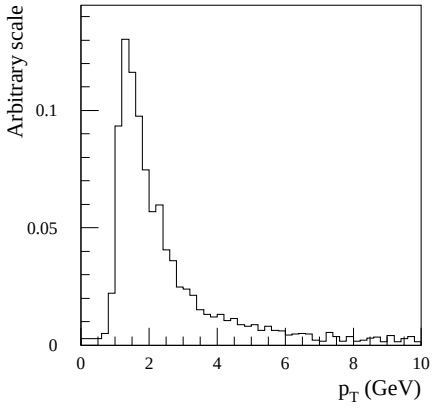

Figure 6.13: The distribution in transverse momentum of the fake conversions found at high luminosity.

Total efficiencies for finding reconstructed conversions are meaningful only when a comparison is made with the number of fake conversions identified in the presence of pile-up. Fake conversions arise mainly from pairs of uncorrelated charged pions, and it is desirable that this rate should be well below the rate of real conversions from π^0 decays in the pile-up.

The strongest handle to reject fake conversions is the number of transition radiation hits on the tracks. This is especially true for tracks crossing the end-cap TRT, where the transition radiation yield is higher than in the barrel TRT. The rate of fake conversions is defined as the rate of conversion candidates in pile-up events at full luminosity where true conversions in the pile-up have been subtracted. Rates are normalised to a road size of $(\eta, \varphi) = (0.20, 0.20)$ and are shown in table 6.2. No cut was applied on the transverse momentum of the reconstructed conversions except the implicit cut of 0.5 GeV p_{T} on the individual tracks in the pattern recognition. The transverse momentum of the fake conversions are peaked towards low momentum as shown in fig. 6.13.

$\lvert\eta\rvert$	Efficiency	Rate in pile-up	Fake rate
0.0–0.6	0.87	$2.3 \cdot 10^{-3}$	$5.7{\cdot}10^{-3}$
0.6–1.2	0.70	$2.8 \cdot 10^{-3}$	$12.1{\cdot}10^{-3}$
1.2–1.8	0.85	$4.5 \cdot 10^{-3}$	$< 0.7{\cdot}10^{-3}$
1.8–2.4	0.85	$3.3 \cdot 10^{-3}$	$9.5{\cdot}10^{-3}$

Table 6.2: Efficiencies and fake rates for conversions. The rates are normalised to a road size of $(\eta, \varphi) = (0.20, 0.20)$.

In the region $1.2 < |\eta| < 1.8$, where the TRT has its best performance, the conversion fake rate is at a satisfactory level far below the conversion rate in the pile-up. Opposed to this the situation in the other pseudorapidity regions is not at all as good. The effect of this relatively high fake rate on the physics performance has not yet been evaluated. As most fake conversions have low transverse momentum the most critical area will be b-tagging where the identification of low energy converted photons is required.

Chapter 7

The Higgs to two photon decay channel

The identification of a Higgs particle in the mass region from 80 GeV to 130 GeV will be a challenge for the LHC. The dominant decay will be $H \to b\bar{b}$ but with the large background of QCD-jets this channel will only be possible to observe through associative production as HW and $Ht\bar{t}$.

As described in section 2.6.1 a better decay mode will be the rare decay $H \to \gamma\gamma$ with a branching ratio around 10^{-3}. The theory describing the decay can be found in section 2.3.3 and the dominant production mechanism through gluon fusion in section 2.2.1.

The $H \to \gamma\gamma$ decay has to be observed above a large background of irreducible photon-photon background. The invariant mass distribution of the photon-photon background will vary smoothly across the mass range from 80–130 GeV. A Higgs particle has thus to be discovered as a slight bump on top of a well calibrated background.

In this chapter the main focus will be on the mass resolution of the $H \to \gamma\gamma$ signal and γ/π^0 separation. The mass resolution is determined solely by the quality of the detector as the natural Higgs width below the threshold of the $H \to W^+W^-$ decay is of the order 1 MeV, which is much narrower than any obtainable mass resolution. Good mass resolution is important to concentrate as much as possible of the signal into a narrow peak, which will be easier to observe above the continuum background.

7.1 Mass resolution of signal

The Higgs mass is determined from the energy of the two photons and their directions as

$$m_H^2 = 2E_1E_2(1 - \cos\alpha) \tag{7.1}$$

$$\cos\alpha = \cos(\varphi_1 - \varphi_2)\sin\theta_1\sin\theta_2 + \cos\theta_1\cos\theta_2, \tag{7.2}$$

where α is the angle between the two photons, and φ_i and θ_i the azimuthal and polar angle of the individual photons. A simple error propagation gives that the error on the Higgs mass is

$$\frac{\Delta m_{\mathrm{H}}}{m_{\mathrm{H}}} = \frac{1}{2}\left(\frac{\Delta E_1}{E_1} \oplus \frac{\Delta E_2}{E_2} \oplus \frac{\Delta\alpha}{\tan(\alpha/2)}\right). \tag{7.3}$$

As both the energy and the angular resolution of the calorimeter are dominated by the sampling term, in the energy range for the photons from a $\mathrm{H} \to \gamma\gamma$ decay, the resolution is given as

$$\frac{\Delta m_{\mathrm{H}}}{m_{\mathrm{H}}} \propto \left(\frac{a_E}{\sqrt{E}} \oplus \frac{a_E}{\sqrt{E}} \oplus \frac{a_\theta}{\sqrt{E}}\right) \sim \frac{a}{\sqrt{m_{\mathrm{H}}}}, \tag{7.4}$$

where $E \sim m_{\mathrm{H}}/2$ is a typical energy of the photons. It is thus expected that the width of the reconstructed Higgs will raise proportionally with $\sqrt{m_{\mathrm{H}}}$.

The angle between the photons can be expressed through the pseudorapidities as

$$\cos\alpha = \frac{\cos(\varphi_1 - \varphi_2)}{\cosh\eta_1 \cosh\eta_2} + \tanh\eta_1 \tanh\eta_2. \tag{7.5}$$

From information on the primary vertex position the directions are computed as

$$\eta_i = \sinh^{-1}\left(\frac{z_i - z_0}{r_i}\right), \tag{7.6}$$

with (r_i, z_i) the position of the cluster in the second sampling of the calorimeter.

For the analysis on the mass resolution approximately 1000 $\mathrm{H} \to \gamma\gamma$ events at high luminosity with a Higgs mass of 100 GeV were simulated[1].

The Higgs mass resolution as a function of the primary vertex accuracy is shown in fig. 7.1. The mass resolution improves linearly with the vertex resolution down to a vertex resolution of 1 cm. With better accuracy than this, the Higgs mass resolution is totally dominated by the energy measurements in the calorimeter.

The main reason for improving the Higgs mass resolution is to improve the significance of a possible Higgs signal. The significance is defined as $\mathfrak{S} = S/\sqrt{B}$ with S and B the number of signal and background events inside a given mass bin. If B instead is defined as the background density (events/GeV), S as the total signal, and the mass resolution of the signal assumed to be Gaussian with a resolution σ, the significance in a bin $m_{\mathrm{H}} \pm \delta m$ is given as

$$\mathfrak{S} = \frac{S\int_{-\delta m}^{\delta m} \mathrm{N}(0,\sigma)}{\sqrt{2\,\delta m\, B}}, \tag{7.7}$$

with $\mathrm{N}(0,\sigma)$ a Gaussian of mean 0 and width σ. The maximum of (7.7) is at $\delta m = 1.4\sigma$ with the value

$$\mathfrak{S}_{\max} = 0.70\frac{S(1-t)}{\sqrt{B\sigma}}, \tag{7.8}$$

[1] Pile-up was added as a Poisson distribution of minimum bias events with a mean of 24, 32 and 40 events in the silicon/pixel detectors, the TRT and the calorimeters.

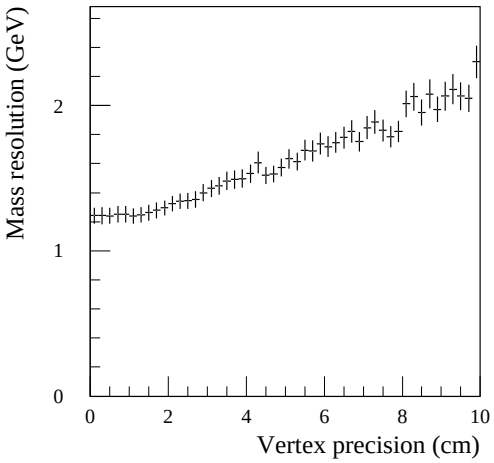

Figure 7.1: The Higgs mass resolution as a function of the resolution of the primary vertex. With the beam spot resolution of 5.6 cm the Higgs mass resolution is 1.7 GeV.

where the variable t is introduced to note the fraction of events in non-Gaussian tails.

From (7.8) it is clear that the optimal bin width to use is 2.8 times the mass resolution. The significance scales linearly with the fraction of events not entering the non-Gaussian tails and scales with the square root of the mass resolution.

and the significance scales with the square root of the mass resolution. Non-Gaussian tails in the mass resolution will to first order reduce the absolute value of the significance but not change the optimal bin size.

7.2 Methods for primary vertex determination

The primary vertex is with the parameters of the beam spot alone defined with a precision of 5.6 cm along the beam axis. The precision can be improved using the shower development in the calorimeter. The method is to reconstruct the barycentre of the shower in the first and second sampling of the calorimeter. The direction of the photon is found from simple pointing between the two positions [3].

In events with converted photons the position of the primary vertex can be identified from the reconstructed conversion.

A third method is to identify the position of the primary vertex from the charged tracks of the event underlying the $H \to \gamma\gamma$ decay. These particles are from initial and final state radiation and share the main vertex with the Higgs particle. At low luminosity this method is quite simple, only a few other primary vertices are present in the detector; at high luminosity there will be on average 23 additional primary vertices from the pile-up events and the situation is more complicated. The task is

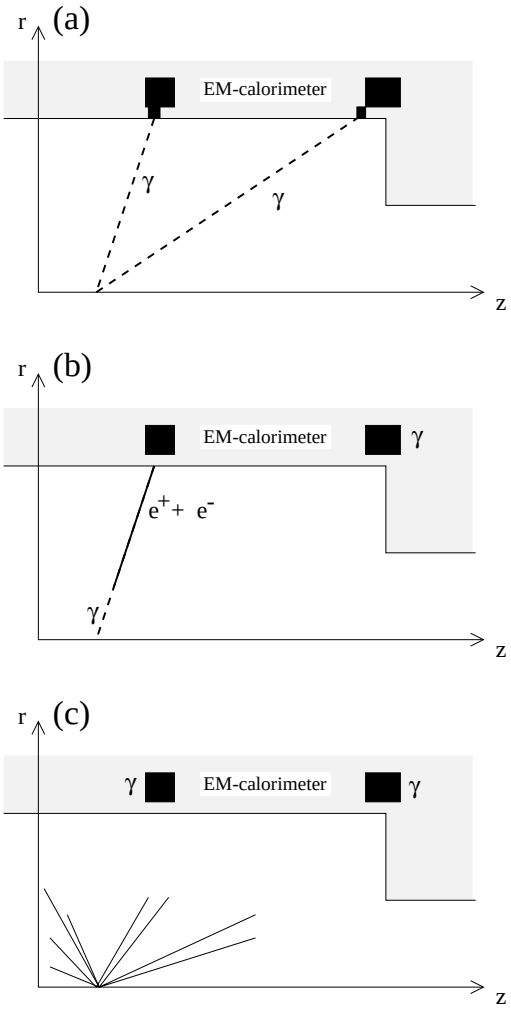

Figure 7.2: An illustration of primary vertex identification in H $\rightarrow \gamma\gamma$ events. In (a) the vertex is identified from pointing in the calorimeter, in (b) from the reconstruction of a converted photon and in (c) from the tracks in the underlying events.

to pick up the correct primary vertex. All three vertex reconstruction methods are illustrated in fig. 7.2.

7.3 Conversions

The method described in section 6.3 was used for the reconstruction of conversions. For locating the primary vertex only conversions with an accurately reconstructed pseudorapidity are of interest. This limits the usable conversions to those with hits from the silicon detectors on the tracks.

Conversions were reconstructed in roads $(\Delta\eta, \Delta\varphi) = (0.5, 0.5)$ around the identified clusters in the calorimeter and accepted if they had reconstructed transverse momentum above 20 GeV. The cut on p_{T} effectively rejected all background from conversions arising from photons in π^0 decays of the pile-up. The position of the primary vertex was calculated as

$$z_0 = z_c - r_c T_c. \tag{7.9}$$

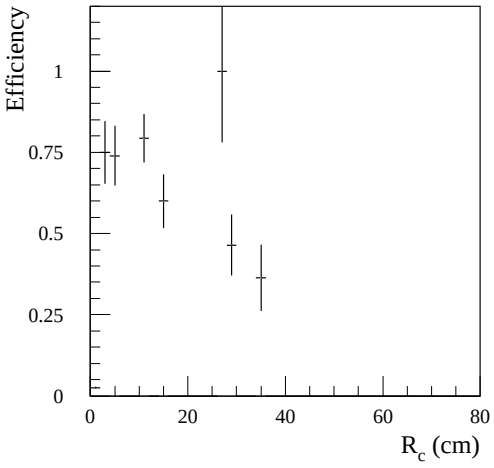

Figure 7.3: The efficiency for reconstructing conversions with hits in the silicon detectors as a function of the conversion radius.

For the conversions in the Higgs events with pile-up there is a reconstruction efficiency of $55\% \pm 3\%$ for conversion radii below 40 cm. The resolution as a function of the conversion radius is shown in fig. 7.3. The low efficiency is mainly from conversion radii close to 40 cm; in general conversion searches, where silicon hits on the tracks are not required, these conversions can be found with much larger efficiency as shown in fig. 6.10. Resolution plots for the reconstructed conversions are shown

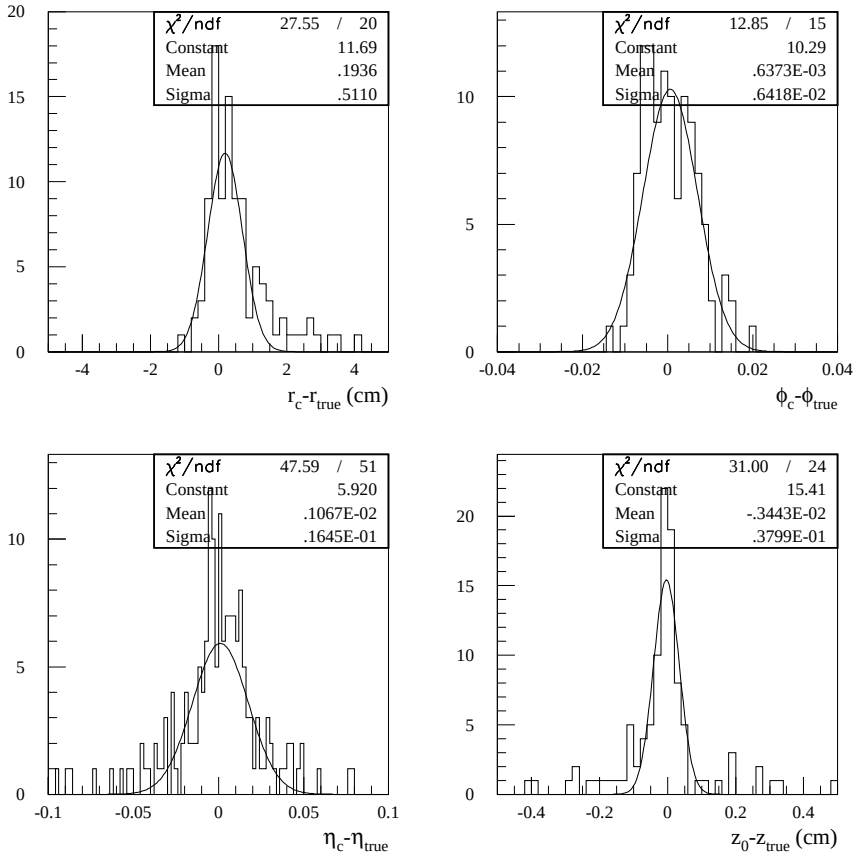

Figure 7.4: The resolution in conversion radius r_c, φ, η and primary vertex position z_0 for reconstructed conversions with $r_c < 40$ cm.

in fig. 7.4. Figures with much better statistics, and for conversions reconstructed in the full Inner Detector, can be found in section 6.3. However, they have been made for 50 GeV p_T single photons and not with the photons from $H \to \gamma\gamma$ events.

7.4 Global track reconstruction

Several variables can be taken into account for the identification of the $H \to \gamma\gamma$ vertex through reconstruction of all charged tracks in the event. The general idea is that the Higgs vertex has more activity than the minimum bias vertices present in the same event. As a first step in this analysis a simple toy Monte Carlo was made to identify appropriate measures to distinguish the primary vertices. No inefficiencies

were included at this stage and only tracks with $p_{\mathrm{T}} > 0.5$ GeV and $|\eta| < 2.5$ were selected. Possible parameters for identifying the correct vertex are:

Track count Counting the number of charged tracks above a p_{T} cutoff of the order of 0.5 to 4.0 GeV reveal an excess of high p_{T} tracks for the Higgs events.

Maximal p_{T} The primary vertex is selected as the vertex with the track of highest transverse momentum associated. A slightly better variable to use for the selection is the scalar p_{T} sum of the three particles with highest p_{T} from a vertex.

Thrust From the reconstructed transverse momentum of the Higgs a transverse thrust with respect to the Higgs axis is defined as

$$T = -\frac{\sum p_{\mathrm{T}}^{i} \cos \alpha_i}{\sum p_{\mathrm{T}}^{i}} \tag{7.10}$$

where the sum is over all tracks from a specific primary vertex and α the angles in the transverse plane between the particles and the reconstructed Higgs.

p_{T} balance The p_{T} balance for charged particles along the reconstructed Higgs direction

$$p_{\mathrm{T}}^{B} = -\sum p_{\mathrm{T}}^{i} \cos \alpha_i \tag{7.11}$$

with the same definitions as in (7.10). The value of p_{T}^{B} can either be used alone or compared to the reconstructed p_{T} of the Higgs in the event.

Integrated probability distributions for several of the variables mentioned above are shown in fig. 7.5. Distributions shown are for single Higgs events and minimum bias events; the distributions will overlap much more when in average 23 background events are superimposed and compared to the Higgs distribution.

7.4.1 The algorithm

The implemented global tracking algorithm selects the $\mathrm{H} \to \gamma\gamma$ vertex using the variable **Maximal p_{T}** and either the **Track count** or **p_{T} balance** variables. As a first step the data was analysed and two 2-dimensional histograms filled. One for the value of the variables at the correct Higgs vertex position and the other for all remaining vertex positions. In each bin of the histogram the *quality* of the Higgs vertex was calculated as

$$Q_{ij} = \frac{\mathrm{H}_{ij}}{\sqrt{\mathrm{B}_{ij}}} \tag{7.12}$$

where i and j are the indices in the Higgs histogram H and background vertex histogram B.

The important point in the reconstruction of the $\mathrm{H} \to \gamma\gamma$ vertex is to select the correct vertex, and not so much the precision in the position of the selected vertex.

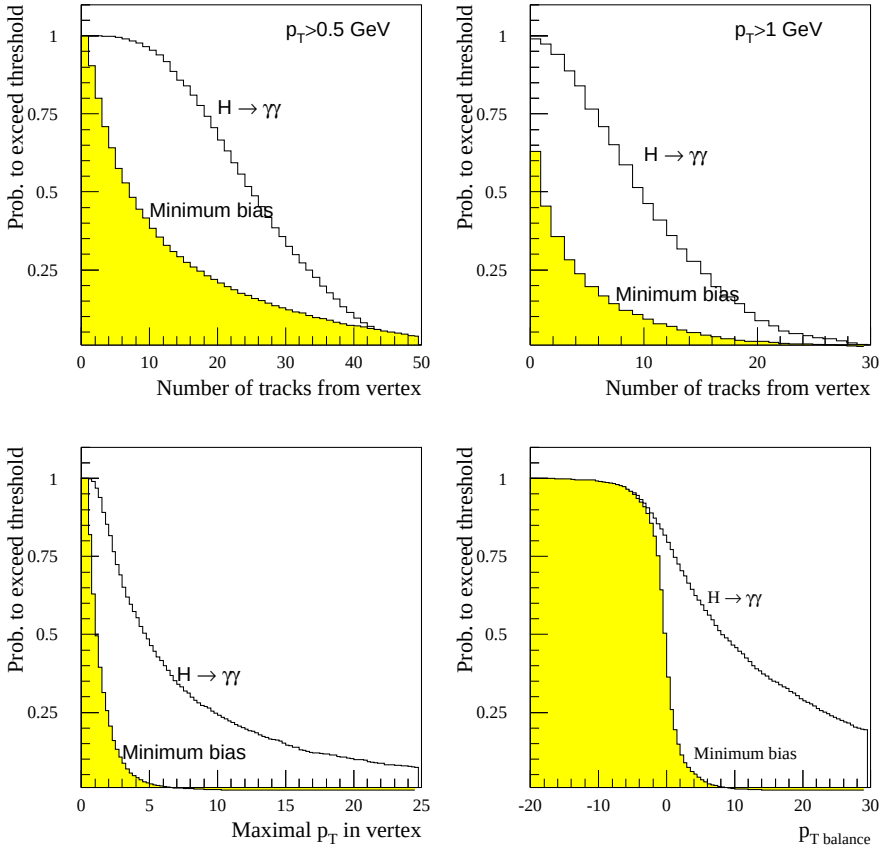

Figure 7.5: The probability to exceed a given threshold for tracks from the primary vertex of $H \to \gamma\gamma$ and minimum bias events. The probability is shown for the number of tracks with $p_T > 0.5$ GeV and $p_T > 1.0$ GeV, the maximal p_T from the vertex and the p_T balance along the reconstructed Higgs direction.

For this reason a scanning algorithm was constructed which in steps of 250 μm steps through all possible primary vertex positions, and at each point decides if the position can contain the Higgs vertex. The method gives a vertex resolution of 120 μm which is more than adequate for the Higgs mass resolution. It should be pointed out that no attempt was made to reconstruct all the primary vertices in the events.

At each possible vertex position the quality is calculated from (7.12). If the quality is above a lower cutoff value the vertex position enters into the Higgs mass fit. Using the variables **Maximal p_T** and **p_T balance** gives a plot for the quality of the vertices as shown in fig. 7.6.

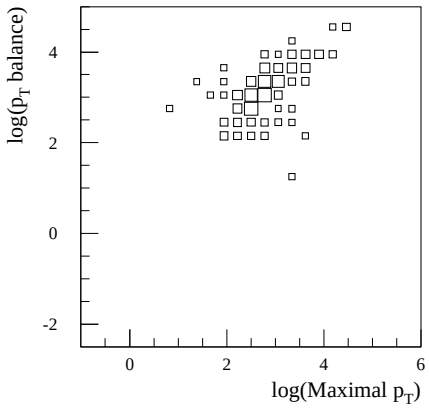

Figure 7.6: Vertex positions with the variables **Maximal p_T** and **p_T balance** inside the region with boxes are selected with a weight proportional to the size of the box.

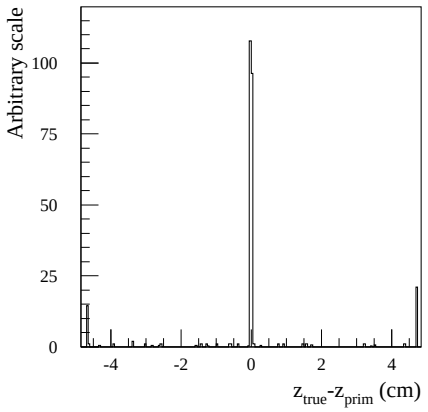

Figure 7.7: The resolution of the primary vertex for events where one or more primary vertices were identified. 80% of the weight is in the central peak. The spikes in the sides are from underflow and overflow.

For each event the algorithm returns zero, one or more candidates for the Higgs vertex. In case of zero candidates the vertex information is taken from the beam spot or the calorimeter. For one vertex candidate the Higgs mass is simply calculated using this position. For more than one vertex the Higgs mass is calculated with a weight for each vertex corresponding to the quality from (7.12). The total weight from all the accepted vertices in a single event is normalised to unity. This method of weighting, in case of several vertex candidates in one event, is better than simply choosing the vertex with the highest weight. An example of the distribution of the weight in the events with at least one vertex selected is shown in fig. 7.7. I can be seen that a large fraction of the weight enters into the correct position of the H $\rightarrow \gamma\gamma$ vertex. The long tails are from situations where a wrong vertex is selected.

7.4.2 Results

The main problem of the algorithm are events where a wrong primary vertex is selected with a large weight since this contributes to the tails in the Higgs mass distribution. Events with zero selected vertices at do not harm the mass resolution in comparison with using the calorimeter or beam spot information only. A high value for the cutoff on the quality (7.12) gives many events with zero vertices found; a low value of the cutoff returns the Higgs vertex in nearly every event but also many wrong vertex positions with similar or higher weights. Both effects are shown in fig. 7.8.

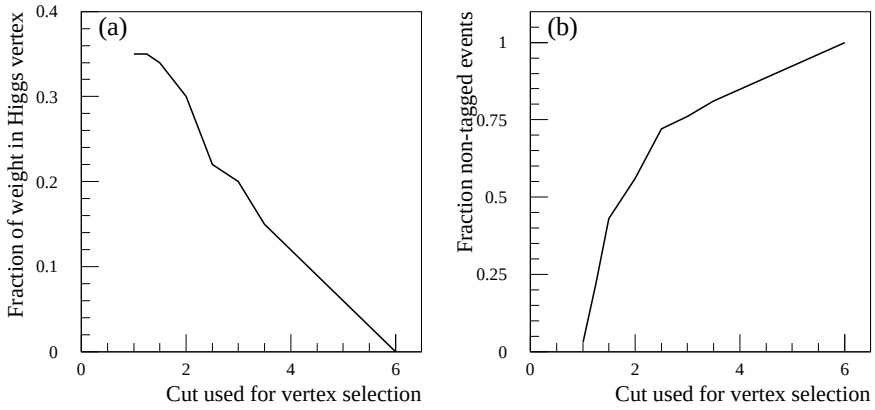

Figure 7.8: The fraction of the total weight that enters into the correct Higgs vertex as a function of the cutoff used for selecting vertex candidates. In (b) the fraction of events with no vertex selected as a function of the cutoff.

At high luminosity and without using the calorimeter pointing the optimal point for the Higgs signal significance, as defined in (7.8), is for a high value of the quality cut where a Higgs vertex candidate is found in 44% of the events and 30% of the weight enters into the correct Higgs vertex (or 68% of the weight in the events where at least one vertex is selected).

The optimisation of the cutoff is shown in fig. 7.9 for two different situations. The solid lines shows the situation where the calorimeter is used for the determination of the vertex position in case zero vertices are selected; the dashed lines shows the situation where just the average beam spot position is used. As expected, the global tracking is much more important for the case where the calorimeter pointing is not used. The significance of the Higgs signal is given as the relative improvement compared to the situation where no pointing information is used. The global tracking method has its best performance where the relative significance reaches its maximum.

At low luminosity with much fewer background vertices a larger efficiency for picking the correct vertex is of course possible.

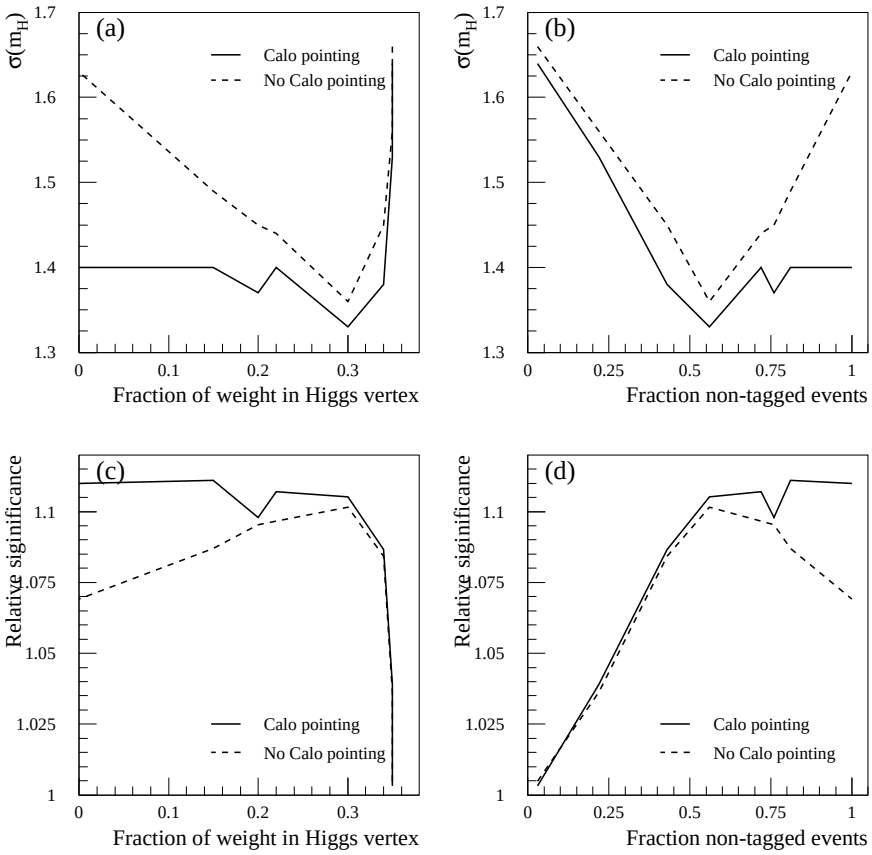

Figure 7.9: Effect of changing the cutoff used to select the correct candidates for the $H \to \gamma\gamma$ vertex. In (a) the Higgs mass resolution is shown as a function of the weight in the correct Higgs vertex and in (b) the mass resolution as a function of the fraction of events with zero selected vertices from the global tracking. In (c) and (d) the significance of the Higgs signal is normalised to the situation where no pointing information is used. The optimal cutoff to use is where the significance reaches its maximum. In each figure is shown results where the calorimeter pointing is used in the events with zero selected vertices (solid lines) and where only the beam spot position is used (dashed lines).

7.4.3 Uncertainties in the underlying physics

The main uncertainty in the primary vertex determination method described above is the model describing the Higgs production. The physics responsible for the Higgs vertex to be any different from the minimum bias vertices is the transverse energy flows in the initial state radiation and the effect of multiple interactions.

The two gluons in the gluon fusion process creating the Higgs will be a part of the initial state radiation. In PYTHIA as the two gluons are a part of a virtual parton cascade inside each proton. The hard scattering prevents the virtual cascade from being re-absorbed by the partons again and instead time-like partons are created from the remaining part of the virtual cascade. With a mass of the Higgs particle of 100 GeV the Higgs particle obtains in this process a transverse momentum of the order of 50 GeV which cancels the scalar sum of the remaining partons in the cascade. It should be noted that it is the scalar sum and hence a low transverse momentum of the Higgs does not imply that the event had no initial state radiation.

In the PYTHIA simulation the evolution of the initial stage radiation is controlled by a parameter κ which defines the maximum virtuality of the space-like cascades in the initial state radiation as

$$Q^2_{\max} = \kappa^2 Q^2 \tag{7.13}$$

where $Q^2 = m_{\mathrm{r}}^2$ for a resonance of mass m_{r} and $Q^2 = (m_{\mathrm{t}1}^2 + m_{\mathrm{t}2}^2)/2$ for $2 \to 2$ processes[2].

When two partons interact, there is a finite probability that another pair of partons will interact as well in the same proton-proton collision. This is called multiple interactions and should not be confused with pile-up which is multiple interactions in a bunch crossing but in different proton-proton collisions. The existence of multiple interactions have been controversial but has now been identified clearly in analysis from H1 at HERA in γp collisions [66] and in the analysis of $\gamma/\pi^0 + 3$jet events from the CDF detector at the Tevatron [67]. In the CDF analysis is was shown that 14% of all inelastic proton-proton collisions have multiple interactions at $\sqrt{s} = 1.8$ TeV.

To look into the uncertainties in the simulation of the Higgs vertex selection two different models for the multiple interactions has been tested [68]. In the first model all proton-proton collisions are treated in the same way and the number of parton interactions follows a Poisson distribution. In the more advanced model the protons are simulated with a parton distribution as a double Gaussian i.e. a narrow and dense core which can be understood as a resolved valence quark and a wider less dense distribution around it. The distribution in the number of multiple interactions now depends on how central the collision is; for a central collision the multiple interaction rate is higher than for a peripheral collision. An event with a low cross section compared to the inelastic cross section will be most likely in a central collision which gives a bias where seldom events have a larger probability for multiple interactions.

In [68] it was shown that jet events from UA1 at $\sqrt{s} = 630$ GeV favours the model with a double Gaussian distribution. With the recent articles published from

[2] In PYTHIA $\kappa^2 = 1$ as default for resonance production; the value can be changed in subroutine `PYSSPA`. For $2 \to 2$ processes the default value is $\kappa^2 = 4$ and is controlled by PARP(67).

CDF and D0 on the confirmation of multiple interactions, results on the structure of these events could be expected quite soon. At the Tevatron it is also possible to look at the underlying event structure of W events but they are mainly produced in quark fusion events while the minimum bias events they should be compared to are dominantly from gluon fusion processes. For this reason the comparison will have problems with systematic errors.

Particle level simulations of minimum bias events and Higgs events were performed to evaluate the uncertainty in the identification of the Higgs vertex from the uncertainties in the theoretical description. The sensitivity to the level of initial state radiation was evaluated by varying the κ parameter from (7.13) in the interval from half to the double of the default value. The value best describing the level of initial state radiation is strongly believed to be within those limits.

In another simulation the two models describing multiple interactions were compared. The first model has a uniform density of the protons while the second model as described above have hard partons inside a wider Gaussian distribution. The effect of changing between the two models is for minimum bias and $H \to \gamma\gamma$ events shown in fig. 7.10 for the number of tracks with transverse momentum above 0.5 GeV and in fig. 7.11 for the maximum p_T from the vertex. As expected it is mostly the spectrum of low p_T particles that is affected, such that the track counting with the p_T limit of 0.5 GeV is strongly affected while the maximum p_T of a charged track from the vertex is almost unaffected by the choice of model.

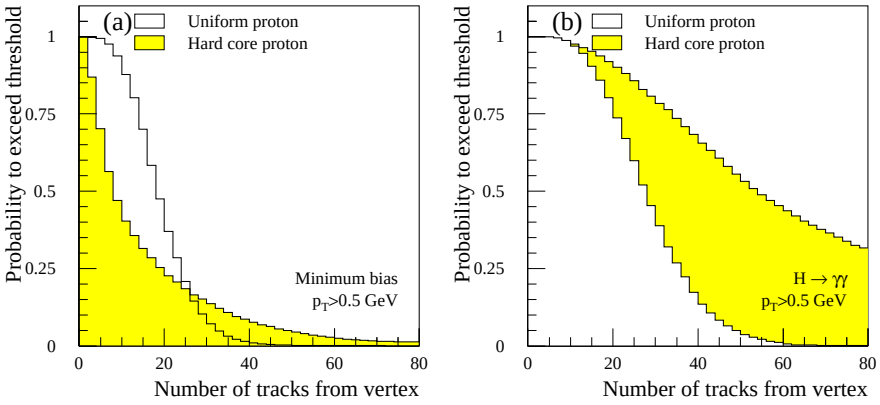

Figure 7.10: The probability for a minimum bias event (a) or $H \to \gamma\gamma$ event (b) to have above a given number of charged tracks from the primary vertex with $p_T > 0.5$ GeV as a function of the threshold. The distributions are shown both with the assumption of a homogeneous proton (white) and a proton with a hard core (shaded).

In the comparisons between the different models, the thresholds on the number

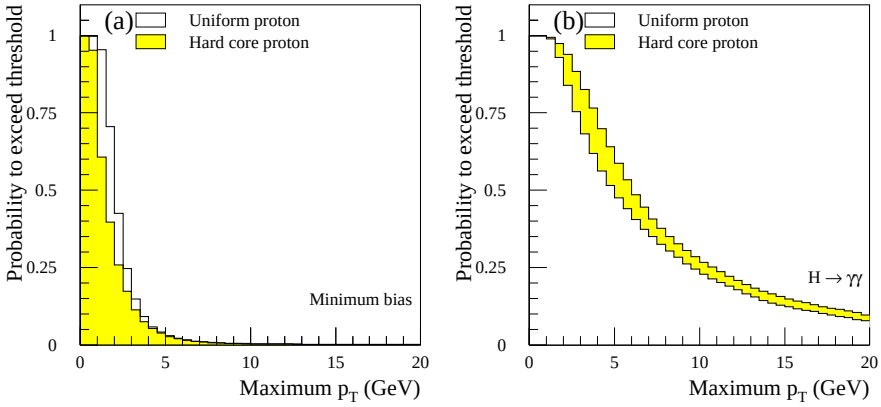

Figure 7.11: The probability for a minimum bias event (a) or $H \rightarrow \gamma\gamma$ event (b) to have a charged track with p_T above a given threshold as a function of the same threshold. The distributions are shown both with the assumption of a homogeneous proton (white) and a proton with a hard core (shaded).

of tracks and maximum p_T were varied in a systematic way to keep the probability for the minimum bias events to reach above both thresholds constant. In this way, it is expected that the fraction of minimum bias vertices misidentified as $H \rightarrow \gamma\gamma$ vertices are kept constant in a full simulation, while the fraction of correctly selected $H \rightarrow \gamma\gamma$ vertices varies.

Setting the maximum virtuality of the initial state radiation to half the default value results for a fixed probability to accept the minimum bias events, in a 25% reduction of the $H \rightarrow \gamma\gamma$ efficiency while a doubling of the maximum virtuality causes a 10% increase in the $H \rightarrow \gamma\gamma$ efficiency. As the probability for the minimum bias events to get accepted was kept constant it can be expected that the weight falling outside the central peak in fig. 7.7 will remain constant for the different models of the underlying event. For the $H \rightarrow \gamma\gamma$ events used for the full detector simulation 30% of the weight entered into the correct primary vertex and based on the arguments above the theoretical uncertainty from initial state radiation is estimated to be $^{+3}_{-8}$% on this value.

The events entering into the full simulation of $H \rightarrow \gamma\gamma$ events with pile-up were simulated with the uniform proton model for the $H \rightarrow \gamma\gamma$ events and with the hard core model for the superimposed minimum bias events. As seen from fig. 7.10 and fig. 7.11 this results in a pessimistic estimate in the power of global tracking to improve the $H \rightarrow \gamma\gamma$ significance. Using the uniform proton model for both the $H \rightarrow \gamma\gamma$ and minimum bias events results in an insignificant change of the results from the full simulation. On the other hand the use of the hard core model changes the $H \rightarrow \gamma\gamma$ distribution in the number of tracks from the vertex radically and the

probability to select the correct $H \to \gamma\gamma$ rise by 65% when the probability to select a wrong vertex is kept constant. For the full simulation this means that the total weight entering into the correct $H \to \gamma\gamma$ vertex raise from 30% to 50%.

To summarise, the theoretical uncertainties in the kinematics of minimum bias and $H \to \gamma\gamma$ events are large for the particles with the lowest transverse momentum. The theoretical uncertainty in the model for initial state radiation is of minor importance compared to the uncertainties in the description of multiple interactions. The full simulations used for the primary vertex selection was performed with a pessimistic set of parameters and can thus be taken essentially as a lower limit in the power of finding the correct primary vertex with global tracking. Simulations performed at particle level indicate that the weight entering into the correct $H \to \gamma\gamma$ vertex will be in the interval from 23% to 55%, with 14% of the weight entering into wrong vertex positions as determined from the full detector simulation of $H \to \gamma\gamma$ events with pile-up corresponding to high luminosity.

7.5 Calibration of cluster energies

An important part of the reconstruction in the calorimeter is the calibration of the energy scale. This calibration tells how the measured amount of ionisation in the liquid argon is translated into the energy of the incoming particle. It depends on the number and distribution of the samplings in the calorimeter, the cluster size used to collect the energy, the amount of material in front of the calorimeter etc. The calibration of the final calorimeter can be done for electrons with either a comparison of the energy in the EM-cluster with the reconstructed p_{T} of the track in the Inner Detector or through the decay of a known resonance like $Z \to e^+e^-$.

For most physics studies at the LHC a calibration with electrons will be sufficient for both electrons and photons. For the $H \to \gamma\gamma$ decay channel there will, however, be a significant gain in the mass resolution for a special energy calibration.

The idea for the $H \to \gamma\gamma$ decay is to use the energy collected in a $(\Delta\eta, \Delta\varphi) = (0.075, 0.125)$ window for non-converted photons and in a $(\Delta\eta, \Delta\varphi) = (0.075, 0.175)$ for converted photons with separate energy calibrations. Converted photons produce wider showers especially in the φ direction where the magnetic field bend the electron tracks and by collecting the energy in an highly asymmetric window $(\Delta\eta, \Delta\varphi) = (0.075, 0.175)$, a better energy resolution can be achieved. The special calibration of converted and non-converted photons separately will have to rely on the difference to the electron calibration observed in testbeam measurements and Monte Carlo simulations.

As shown in section 6.3.2 it is possible to identify conversions with a high efficiency and a low rate of fake conversions. That converted photons are not identified if the conversion radius is above 80 cm or at $|z| > 280$ cm is fully acceptable as those conversions will open up very little and in almost all respects look like non-converted photons. There is a potential gain in further sub-dividing the sample of converted photons into separate samples depending on the reconstructed conversion radius with separate energy calibrations for each sub-sample, the limited amount of

events simulated did not allow such an analysis.

As will be seen in the following section the separation of the photons in the $H \to \gamma\gamma$ events into a converted and non-converted sample actually provides the main improvement in the $H \to \gamma\gamma$ signal significance using the information from the Inner Detector.

7.6 Influence on Higgs mass resolution and significance

With the different methods for finding the primary vertex developed it is easy to compare the power of them. The significance of a Higgs signal is determined by the mass resolution and the amount of signal events outside a $\pm 1.4\sigma$ window as shown in section7.1.

As a reference point results, with vertex information taken from the average position of the beam spot only, will be used. This is the worst case scenario with a mass resolution of 1.66 GeV and with 75% of the events inside the signal peak. The last number should be compared to the 84% expected from a perfect Gaussian. Events with one or both photons in a crack of the calorimeter are excluded from the analysis, i.e. the accepted regions in η for reconstructed clusters are $0.08 < |\eta| < 1.37$ and $1.52 < |\eta| < 2.45$.

Some selected mass distributions in the high luminosity case can be found in fig. 7.12.

High luminosity			
Method used	Resolution (GeV)	Fraction in peak	Relative significance
Beam constraint	1.66	0.75	1.00
Calorimeter	1.54	0.74	1.01
Calorimeter & Conversions	1.40	0.77	1.11
Calorimeter & Global	1.57	0.74	1.01
Calo, Conv & Global	1.40	0.77	1.11
Beam & Conversions	1.63	0.80	1.07
Beam & Global	1.67	0.76	1.01
Beam, Conv & Global	1.42	0.77	1.10
True vertex	1.40	0.72	1.04
True vertex & Conversions	1.27	0.76	1.15

Table 7.1: The Higgs mass resolution and the relative significance of a signal using different methods to identify the primary vertex. Evaluated at high luminosity. See the text for further comments.

In table 7.1 the results are summarised for a large set of different conditions at high luminosity:

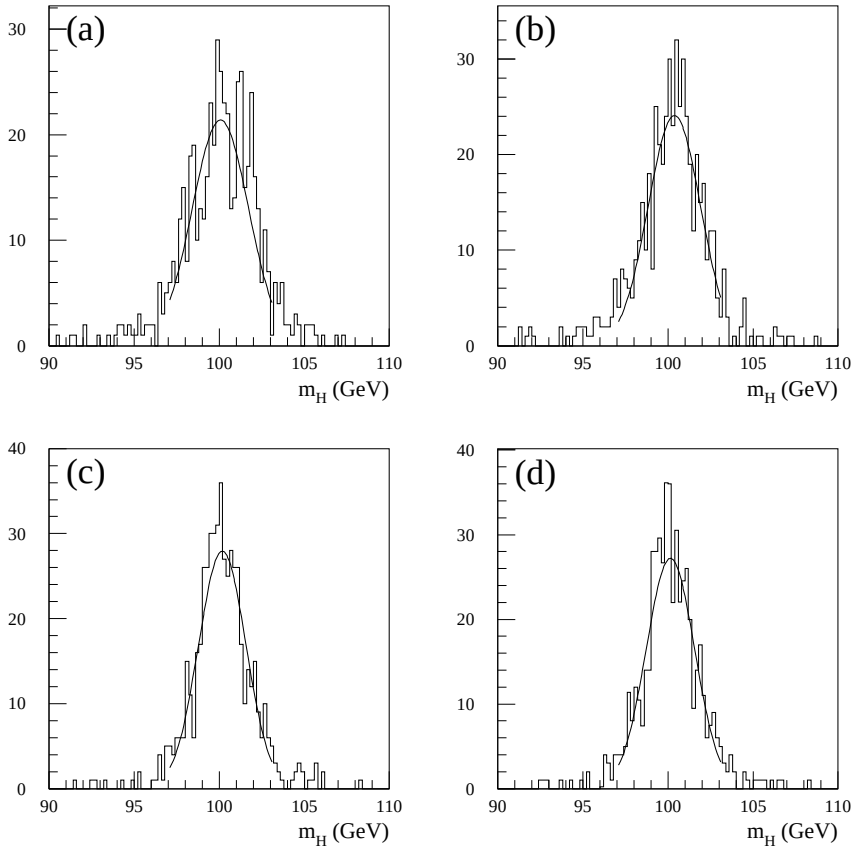

Figure 7.12: Distribution of the reconstructed Higgs mass at high luminosity for the options **Beam constraint** (a), **Calorimeter** (b), **Calorimeter & Conversions** (c) and **Beam, Conv & Global** (d). The values of the fits can be found in table 7.1.

Beam constraint A primary vertex position of (0,0,0) used in all positions. Conversions are not identified.

Calorimeter The pointing from the calorimeter used but conversions are not identified.

Calorimeter & Conversions Same as above but identified conversions are used both for pointing and for separate energy calibrations.

Calorimeter & Global Global track reconstruction used in addition to the calorimeter pointing.

Calo, Conv & Global All information available used for both energy calibration and primary vertex determination.

Beam & Conversions The beam constraint and information from conversions used. No pointing from the calorimeter.

Beam & Global The beam constraint and global track reconstruction used. Conversions are not identified.

Beam, Conv & Global All information except the pointing from the calorimeter used.

True vertex The true vertex position used.

True vertex & Conversions The true vertex information used and identified conversions used for separate energy calibration.

In the high luminosity case, the calorimeter performance alone can be compared to the situation with adding information from the Inner Detector. The main improvement is from identifying conversions such that an independent energy calibration can be done for converted and non-converted photons in the calorimeter. It is seen that the best performance achievable using only the global track reconstruction (row **Beam, Conv & Global**) and using only the calorimeter (row **Calorimeter & Conversions**) for pointing are nearly equal. However, combining the two methods (row **Calo, Conv & Global**) gives no further improvement.

That the same significance of the Higgs signal is achievable at high luminosity with the calorimeter pointing having a worse resolution than expected, confirms the robustness of the ATLAS detector for finding a Higgs particle in the $H \to \gamma\gamma$ decay channel.

The uncertainties in the kinematics of the underlying event was treated by artificially changing the amount of events where the Higgs vertex was identified correctly from the global tracking. Varying it the interval from 23% to 55%, which was estimated to be the maximum uncertainty in section 7.4.3, changes the relative significance for the combined pointing with $^{+4.0\%}_{-0.5\%}$ for the most optimal pointing with and without the calorimeter pointing. The important point is that the estimate from the full simulation on the influence of the signal significance using global tracking is a pessimistic estimate.

In the multiple interaction model with a hard core proton the upper bound for the option with pointing from the calorimeter, conversions and global tracking (row **Calo, Conv & Global** in table 7.1) is 1.14 in the relative significance or nearly the same as using the true vertex position (row **True vertex & Conversions**). The option with pointing from the calorimeter and from conversions (row **Calorimeter & Conversions**) is clearly unaffected by the treatment of multiple interactions.

As a conclusion the combined approach using both the calorimeter and the Inner Detector for pointing is clearly better than using the calorimeter alone when the hard core proton model is considered for multiple interactions.

Inside the ATLAS collaboration a fast simulation program of the ATLAS detector is under development which will include the resolutions and correlations in the tracking parameters and the track finding efficiencies[3]. The program will be an important tool to continue the study of the significance of the $H \to \gamma\gamma$ signal as the particle level simulations directly from the Monte Carlo do not give enough information on the problems with global track reconstruction, and the full simulation is too slow for simulating the many different kinematic models of the underlying event.

Low luminosity

Method used	Resolution (GeV)	Fraction in peak	Relative significance
Beam constraint	1.66	0.82	1.00
Calorimeter	1.25	0.72	1.06
Calorimeter & Conversions	1.15	0.76	1.18
Calorimeter & Global	1.15	0.69	1.08
Calo, Conv & Global	1.04	0.77	1.26
Beam & Conversions	1.44	0.78	1.08
Beam & Global	1.15	0.70	1.08
Beam, Conv & Global	1.04	0.77	1.25
True vertex	1.14	0.69	1.08
True vertex & Conversions	1.03	0.77	1.26

Table 7.2: The Higgs mass resolution and the relative significance of a signal using different methods to identify the primary vertex. Evaluated at low luminosity. See the text for further comments.

At low luminosity the improvement in the $H \to \gamma\gamma$ significance is much better than at high luminosity. The results in table 7.2 are obtained with only the Higgs event in the simulation. For the purpose here the situation is quite close to the low luminosity case where only a few overlapping events are expected in the silicon and pixel detectors. The effect of adding pointing from the global tracking now adds 7% to the significance compared to using only the calorimeter for pointing, and 16% when using only the beam spot constraint. From this it is seen that the global tracking

[3] This will be an upgrade of the present ATLFAST program, which only parameterizes the calorimeter and the muon detectors.

is essential in the search for $H \to \gamma\gamma$ decays at low luminosity. Some selected mass distributions can be found in fig. 7.13.

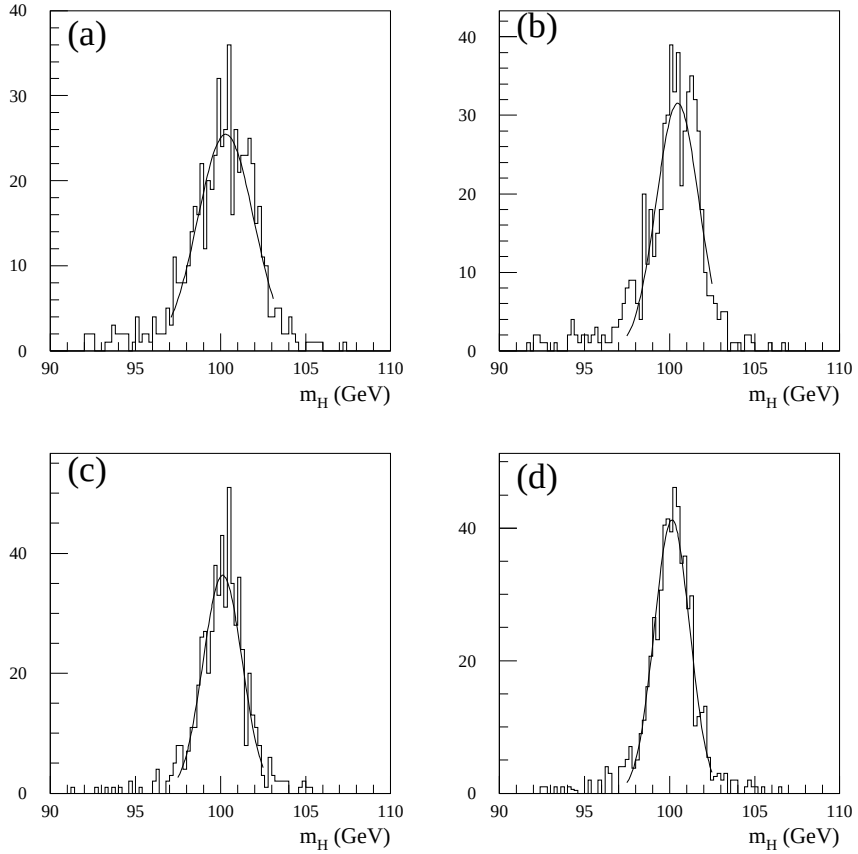

Figure 7.13: Distribution of the reconstructed Higgs mass at low luminosity for the options **Beam constraint** (a), **Calorimeter** (b), **Calorimeter & Conversions** (c) and **Beam, Conv & Global** (d). The values of the fits can be found in table 7.2.

7.7 Irreducible two photon background

In the previous sections the background to the $H \to \gamma\gamma$ decay has been treated as a flat background of an unknown level; only relative improvements in the significance was considered. To calculate the absolute level of the significance the different backgrounds has to be evaluated.

The irreducible background to the detection of $H \to \gamma\gamma$ comes from production

of real photon pairs. The most important processes are the Born ($q\bar{q} \to \gamma\gamma$), box ($gg \to \gamma\gamma$) and bremsstrahlung ($gq \to q\gamma \to q\gamma\gamma, gg \to jj\gamma\gamma$) processes as shown in fig. 7.14.

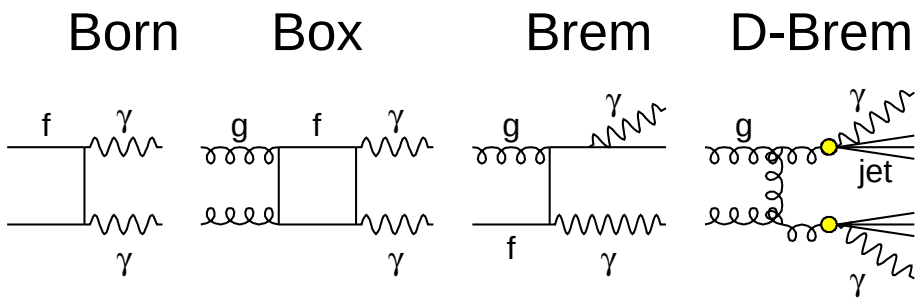

Figure 7.14: Irreducible backgrounds to the two photon decay of a Higgs boson from the Born, box, and quark bremsstrahlung processes.

The most efficient way to reduce the background from real photons, keep a reasonable amount of the Higgs signal, and have a tolerable trigger rate [69] is to require both photons to have $|\eta| < 2.5$ and for the photons ordered in decreasing E_{T}, $E_{\mathrm{T}}^1 > 40$ GeV and $E_{\mathrm{T}}^2 > 25$ GeV. A cut on the transverse energy balance

$$E_{\mathrm{T}}^{\mathrm{bal}} = \frac{E_{\mathrm{T}}^1}{E_{\mathrm{T}}^2 + E_{\mathrm{T}}^2} < 0.7 \tag{7.14}$$

to reduce the quark bremsstrahlung background was also proposed in [69] but in [70] it was clearly shown that such a cut in fact reduce the significance of the Higgs signal and should be avoided.

The background from the quark bremsstrahlung processes was, using a semi-analytical model, in [70] determined to be below 35% of the sum of the Born and the box process and almost independent of the transverse energy of the first photon as seen in fig. 7.15.

The invariant mass spectrum, $m_{\gamma\gamma}$, for the irreducible background is shown in fig. 7.16. The individual contributions from the Born and box processes are shown and the total is estimated as the sum of the two with an additional 35% added from the quark bremsstrahlung processes. A photon identification efficiency of 80% was taken into account (see section 7.8).

The complexity of the box process has so far prevented a full next-to-leading order calculation of the irreducible background. For the calculated processes the K-factor is close to unity and it is generally believed to be lower than the factor 1.5 for the gluon fusion Higgs production (see section 2.2.1). Ignoring K-factors will thus give a pessimistic but consistent estimate of the significance of observing the Higgs particle in the $H \to \gamma\gamma$ channel.

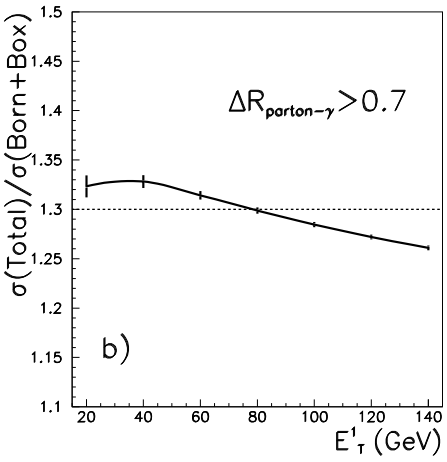

Figure 7.15: The ratio between the cross section of the quark bremsstrahlung processes and the sum of the Born and box processes for photon-photon production as the function of the maximum transverse energy of the two photons. From [70].

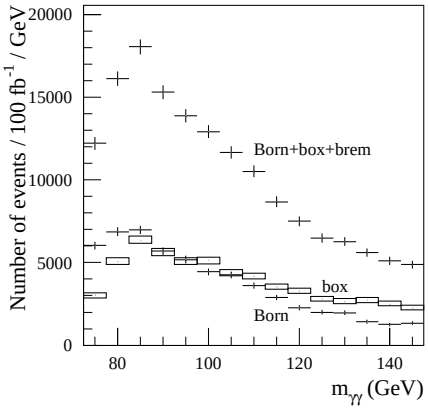

Figure 7.16: The invariant mass spectrum of the irreducible background to the $H \to \gamma\gamma$ decay. The sum of the Born, box and quark bremsstrahlung contributions are shown along with the individual contributions of the Born and box term.

7.8 Reducible QCD-jet background

As already mentioned, the background from QCD-jets has a cross section many orders of magnitude above the $H \to \gamma\gamma$ cross section. Applying the same kinematic cuts to jet-jet and jet-γ events as to the irreducible background, gives a rate $2 \cdot 10^2$ respectively 10^3 higher than the irreducible background. A large data sample of 10^6 di-jet events was generated with PYTHIA and fully simulated to estimate the rejection power of jets.

The rejection of the jet-jet and jet-γ background has strongly affected the design of the calorimeter and to some extent the Inner Detector. A detailed description of the analysis on the 10^6 fully simulated di-jets can be found in [71]; only a summary is given here. The photon identification criteria was:

- Below 500 MeV of transverse energy in the hadronic calorimeter in a window of size $(\Delta\eta, \Delta\varphi) = (0.2, 0.2)$ behind the electromagnetic cluster. This rejects the majority of the hadronic jets.

- An isolated electromagnetic cluster where above 90% of the energy in the 7×7 cluster was required to be within the 3×5 cluster. The larger cluster size in the φ direction was motivated by the photons which convert and create wider clusters in the direction where the magnetic field open the electron pairs.

- A narrow shower profile compatible with the energy deposition of a single particle.
- Above a large fraction of the total cluster energy deposited in the four most energetic calorimeter cells. Again this favours clusters created by single particles.

A rejection factor for individual jets of 1200 was found on the di-jet sample for jets with $E_{\mathrm{T}} > 17$ GeV and 2500 for jets with $E_{\mathrm{T}} > 40$ GeV with a photon efficiency of 90%.

Uncertainties in the level of the background after the rejection cuts are from [71]:

- A factor two in the PYTHIA simulation mainly from the uncertainty in structure functions and higher order corrections.
- A factor two per jet from the detector simulation where the rejection depends critically on the details of the hadronic interactions, the shower simulation and the material description.
- A factor 1.5 per jet from the approximation that the jet events can be treated as isolated π^0's after the isolation criteria (see text below).

Added in quadrature this gives an uncertainty in the jet-jet rejection of a factor 4 and the jet-photon of a factor 3. The large uncertainties demands that the reducible background is well below the irreducible background to assure that the significance of the $\mathrm{H} \to \gamma\gamma$ signal is not affected.

The composition of the jets surviving the photon identification cuts is shown in table 7.3. It can be seen that in around 80% of the remaining jets scalar mesons decaying to photons carry the major part of the energy.

Jet composition	Fraction of events
single $\pi^0 \to \gamma\gamma$	0.59
multiple $\pi^0 \to \gamma\gamma$	0.14
$\eta, \eta' \to \gamma\gamma, \omega \to 2\gamma, 3\gamma$	0.06
quark bremsstrahlung	0.12
prompt photons	0.04
electrons from b, W, Z decays	0.04
others	0.01

Table 7.3: The composition of the jets surviving the identification cuts of isolated photons. From [71].

As the number of simulated jets did not allow a study of the rejection obtainable including the preshower and the Inner Detector, specific studies have been made on data sets of single π^0's with pile-up corresponding to high luminosity added. The next section will focus especially on the role of the Inner Detector in the π^0 rejection.

7.8.1 Single π^0 rejection

To reduce the background from jet-jet and jet-γ events to the $H \to \gamma\gamma$ signal well below the level of the irreducible background it is necessary to provide a rejection of π^0's on top of the jet rejection provided by the calorimeter. The standard algorithm for this is based on the shower shape in the η-strips of the calorimeter. The rejection power obtainable is limited by converted photons which, even in the non-bending η direction, have slightly broader shower profiles in the calorimeter thus faking the π^0 showers. This degradation in π^0 rejection can be more than regained by including the information from reconstruction in the Inner Detector as shown below.

If a primary photon converts, the reconstructed transverse momentum in the tracker is close to the transverse energy in the corresponding electromagnetic cluster; for a π^0 with a converted photon, the reconstructed transverse momentum of the photon generally will be below the total transverse energy in the cluster, which includes energy from the conversion plus the non-converted photon. The ratio of these two is shown in fig. 7.17. It can be used to discriminate between photons and π^0's: for photons, the ratio is peaked at 1, with an r.m.s. which reflects the resolution; for π^0's, the ratio is fairly flat between 0 and 1, as a consequence of the energy sharing between the two photons in the π^0 decay.

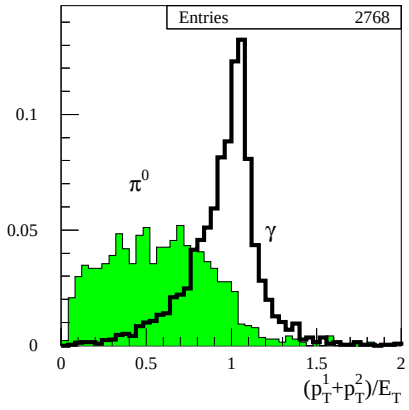

Figure 7.17: Ratio of the reconstructed conversion p_T to the total EM-cluster E_T for photons and π^0's at low luminosity.

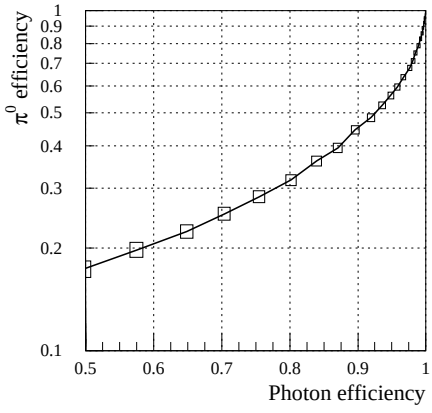

Figure 7.18: π^0 efficiency as a function of photon efficiency for different cuts on the ratio of conversion p_T to E_T in the EM-cluster.

The rejection which can be achieved against π^0's is shown in fig. 7.18. For a 90% photon efficiency, it is possible to achieve a π^0 rejection of 2.4 without using the η strips in the calorimeter.

The use of the Inner Detector without information from the η-strips of the calorimeter is inefficient and a combined method for π^0 rejection is necessary. As a first step in a combined analysis all photon candidates with an identified conversion

were selected. This was done with an average efficiency across the Inner Detector of 85%.

For early conversions, the transverse momentum resolution of the conversions is good and gives the dominant rejection for π^0's; for later conversions, the essential information provided by the Inner Detector is that a conversion has taken place such that the selection criteria in the calorimeter can be changed.

An mistake made earlier [3] was to reject all events with more than one identified conversion pointing towards the EM-cluster. The naïve interpretation would be that two identified conversions are from a π^0 with both photons converted. For several reasons this is bad as extra conversions can have several other sources:

- Double counting of the real conversion. This happens in more than 10% of the reconstructed conversions. As explained in section 6.3.2 the double counting rate is correlated to the conversion efficiency and to some extent unavoidable.
- In around 1% of all events there will be an extra reconstructed conversion with $p_{\mathrm{T}} > 5$ GeV either from the pile-up or as a fake conversion (see table 6.2).
- Shower type events where an electron from the photon conversion emits a hard bremsstrahlung photon which subsequently converts. Around 1% of the events with a converted photon have additional conversions in a cascade.

Based on the reconstructed conversion radius and pseudorapidity, the data are divided into sub-samples. The π^0 rejection is optimised in each sub-sample keeping the efficiency for identified conversions in the photon sample at 90%. Results are summarised in table 7.4 and table 7.5. The fraction of 50 GeV p_{T} photons and π^0's with at least one converted photon, and the fraction actually identified are shown, followed by the rejection of π^0's with identified conversions for an efficiency of 90% of photons with identified conversions. The rejection is defined as the reciprocal value of the π^0 efficiency.

r_{c} (cm)	π^0 rejection	Conversion fraction
0-20	6.3	0.056
20-40	3.3	0.056
40-60	3.1	0.057
60-80	2.7	0.043
0-80	3.4	0.212

Table 7.4: The π^0 rejection at 50 GeV p_{T} for a fixed efficiency of 90% to select reconstructed photon conversions. The third column shows the fraction of photons that convert in each radial interval.

The rejection of π^0's using the calorimeter only is shown in fig. 7.19 for transverse momenta of 25, 50 and 80 GeV. For a transverse momentum of 50 GeV the improvement in the π^0 rejection from adding the conversion identification in the Inner Detector is summarised in table 7.6. The rejection of the two samples with and

	Photons		π^0's		
$\|\eta\|$	converted	identified	converted	identified	π^0 rejection
0.0-0.6	0.15	0.14	0.30	0.26	5.0
0.6-1.2	0.22	0.16	0.38	0.25	6.3
1.2-1.8	0.28	0.25	0.51	0.42	2.9
1.8-2.4	0.24	0.21	0.42	0.36	2.8
0.0-2.4	0.21	0.19	0.40	0.32	3.4

Table 7.5: The fraction of 50 GeV p_{T} photons and π^0's with at least one converted photon and the fraction actually identified. The last column gives the rejection of π^0's with identified conversions for an efficiency of 90% of photons with identified conversions.

without identified conversions is given and the fraction of π^0 events in each sample. In the last two columns first the π^0 rejection from using the calorimeter alone, where the converted and non-converted events are not separated and then the optimal result where the conversion information from the Inner Detector was used[4]. Averaged over all pseudorapidities a 10% increase in the π^0 rejection is observed from using the Inner Detector information as well.

	No conversions		Conversions		Calorimeter	Combined
$\|\eta\|$	fraction	rejection	fraction	rejection	π^0 rejection	π^0 rejection
0.0-0.6	0.74	3.9	0.26	5.0	3.9	4.1
0.6-1.2	0.75	3.8	0.25	6.3	3.2	4.2
1.2-1.8	0.58	3.2	0.42	2.9	2.8	3.1
1.8-2.4	0.64	3.1	0.36	2.8	3.2	3.0
0.0-2.4	0.68	3.5	0.32	3.4	3.2	3.5

Table 7.6: The improvement observed in the π^0, with a fixed photon efficiency of 90% rejection, from including the identification of conversions in the Inner Detector. The rejection on the sample of π^0's with and without identified conversions are shown separately.

7.8.2 Final estimate of reducible background

Assuming that the π^0 rejection can provide a factor 3 of rejection on the jets surviving the photon identification is quite conservative as the rejection of multiple π^0's and other scalar mesons can be assumed to be higher than the rejection of single π^0's.

The rejection factor for individual jets will thus raise at least to 3600 jets with $E_{\mathrm{T}} > 17$ GeV and 7500 for jets with $E_{\mathrm{T}} > 40$ GeV at the expense of the photon

[4]Obviously the cuts are not optimal for the combined method for $1.8 < |\eta| < 2.4$ where the combined approach gives a worse result.

efficiency falling to 80%. An ongoing study on a new and larger jet sample, with the most recent detector design of the calorimeter and the reconstruction of conversions included, shows a total rejection of 5600 for the jets with $E_{\mathrm{T}} > 17$ GeV with the photon efficiency kept at 80%. However, the analysis is not yet final and the numbers will not be used here.

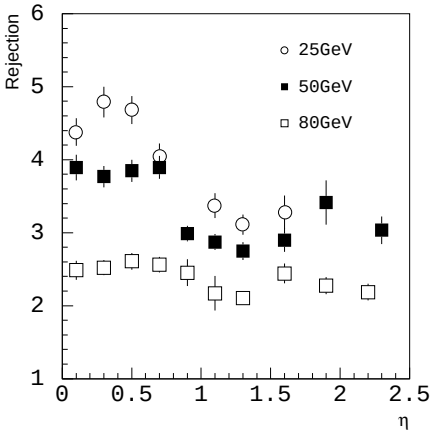

Figure 7.19: π^0 rejection for a fixed photon efficiency of 90% as a function of pseudorapidity for 25, 50 and 80 GeV transverse momentum. Only the calorimeter information was used. From [3].

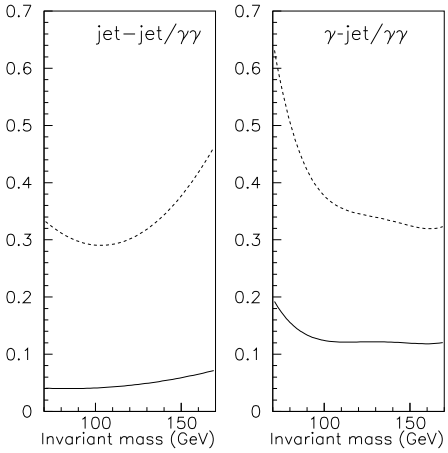

Figure 7.20: The estimated rate of the jet-jet and jet-γ backgrounds relative to the irreducible $\gamma\gamma$ background as a function of the invariant mass of the pair. From [3].

In fig. 7.20 is shown the estimated rate of the jet-jet and jet-γ background relative to the irreducible $\gamma\gamma$ background as a function of the invariant mass of the pair. There is assumed to be no correlation between the rejection of the two jets in the jet-jet events. It can be seen that the reducible background is at a level where it will be below the irreducible background even taken into account the uncertainties from the theory and the simulation mentioned above.

7.9 Signal significance

The significance of the Higgs signal in the two photon decay channel is given from the expected number of signal and background events. As shown in section 7.6 the highest significance is obtained with a mass bin of width $\pm 1.4\sigma(m_{\mathrm{H}})$.

To save the already limited statistics in the data-set with tracks in the Inner Detector fully analysed (section 7.6), the kinematic cuts of $E_{\mathrm{T}}^1 > 40$ GeV and $E_{\mathrm{T}}^2 > 25$ GeV was loosened to $E_{\mathrm{T}} > 20$ GeV for both photons. This gave an optimal Higgs mass resolution of a 100 GeV Higgs of 1.40 GeV at high luminosity which is somewhat

higher than the most recent result of 1.31 GeV [72] performed with larger statistics but with just a parameterized conversion identification. The different kinematic cuts on the photons fully account for the observed difference in the mass resolution.

The mass resolution for masses different from 100 GeV was taken from a fast simulation of the ATLAS detector with the calorimeter resolution parameterized[5]. A normalisation factor of 1.11 was applied to all mass resolutions from the fast simulation, to obtain the same resolution of 1.31 GeV as in the full simulation for $m_{\mathrm{H}} = 100$ GeV. The mass resolution was seen to closely follow the square root dependence of the Higgs mass given by (7.4).

The accepted Higgs events has contributions from the dominant gluon fusion process, the vector boson fusion process, and the associative production processes WH, ZH and $\mathrm{t\bar{t}H}$. The requirement of the decay photons to be isolated leads to a lower efficiency for the Higgs events in the associative production. The WH and ZH associative production contributes to the number of accepted signal events with approximately 10% while the contribution from $\mathrm{t\bar{t}}$ is at or below 5%[6].

An efficiency of 80% for each photon was used with the exception of the $m_{\mathrm{H}} = 90$ GeV bin where the efficiency was reduced to 72%. The reduced efficiency arises from the extra electron rejection required to avoid the $\mathrm{Z} \to \mathrm{e^+e^-}$ resonant background [4, 73].

A summary of the Higgs mass resolution, the number of signal and background events, and the total significance $S/\sqrt{B}$ after one year at high luminosity is shown in table 7.7. If a 5σ effect is required to claim a discovery a Higgs with mass above approximately 105 GeV will be discovered within one year. It was in section 2.4 seen that the upper limit for Higgs searches at LEP2 will be at 95 GeV and just to achieve a small overlap with the $\mathrm{H} \to \gamma\gamma$ decay at the LHC will take three years at high luminosity.

m_{H} (GeV)	$\sigma(m_{\mathrm{H}})$ (GeV)	$\mathrm{H} \to \gamma\gamma$	Born	box	$\sum$ irreducib	$\sum$ reducib	$\sum$ bckgrnd	$S/\sqrt{B}$
80	1.11	560	15804	37147	50149	9528	59677	2.3
90	1.20	624	15360	30860	41662	7083	48744	2.9
100	1.31	1013	18825	35096	47380	7581	54961	4.3
110	1.35	1163	15829	29449	39756	6361	46117	5.4
120	1.46	1271	13450	22716	30666	4907	35573	6.7
130	1.56	1266	11690	20278	27376	4380	31756	7.1
140	1.59	1146	11214	16820	22706	3633	26339	7.1

Table 7.7: Summary of the $\mathrm{H} \to \gamma\gamma$ signal after one year at high luminosity (100 fb^{-1}). For different values of the Higgs mass, the mass resolution, the number of expected events, and the signal significance is given. The Higgs signal significance reaches above 5 within one year for $m_{\mathrm{H}} > 105\ GeV$.

[5] The ATLFAST simulation used for this is described in further detail in chapter 8.

[6] It seems that the $\mathrm{t\bar{t}H}$ associative production is double counted in [70] through production in PYTHIA with both subprocess 3 and subprocess 121.

At low luminosity the Higgs mass resolution is better as shown in table 7.2. This results in a smaller background as a narrower mass bin can be used. In table 7.8 the results are summarised for an integrated luminosity after three years at low luminosity (30 fb^{-1}). It can be seen that a discovery defined from a 5σ level will not be possible in the H $\to \gamma\gamma$ channel alone during the low luminosity period at the LHC. Together with the H $\to$ b$\bar{\text{b}}$ channel a discovery should be possible though.

m_{H} (GeV)	$\sigma(m_{\text{H}})$ (GeV)	H $\to \gamma\gamma$	Born	box	$\sum$ irreducib	$\sum$ reducib	$\sum$ bckgrnd	$S/\sqrt{B}$
80	0.88	168	3764	8847	11944	2269	14213	1.4
90	0.95	187	3658	7350	9923	1687	11609	1.7
100	1.04	304	4484	8359	11284	1806	13090	2.3
110	1.07	349	3770	7014	9469	1515	10984	3.3
120	1.16	381	3203	5410	7304	1169	8472	4.2
130	1.24	380	2784	4830	6520	1043	7563	4.4
140	1.26	344	2671	4006	5408	865	6273	4.3

Table 7.8: Summary of the H $\to \gamma\gamma$ signal after three years at low luminosity (30 fb^{-1}). For different values of the Higgs mass, the mass resolution, the number of expected events, and the signal significance is given.

7.10 Summary of the H $\to \gamma\gamma$ decay channel

The H $\to \gamma\gamma$ decay mode of a standard model Higgs boson is the most promising detection channel for a Higgs boson in the mass range $90 < m_{\text{H}} < 130$ GeV. The signal of two isolated photons is clear but both the irreducible photon-photon background and the reducible jet-jet and jet-photon backgrounds are much larger than the signal.

It was shown that the crucial points for the detection are a good mass resolution to achieve as narrow a mass peak as possible and a high rejection power of QCD-jets faking photons.

The mass resolution can be improved with a separate calibration of the energy scale in the electromagnetic calorimeter for converted and non-converted photons giving rise to a 10% higher significance of a 100 GeV Higgs particle.

A determination of the primary vertex position along the beam axis improves the mass resolution through a better measurement of the angle between the two photons. Three methods to measure the position of the primary vertex was compared: pointing in the calorimeter, reconstruction of converted photons and global tracking where all charged tracks in the event are reconstructed. The significance of the Higgs signal improves by an additional 3–7% depending on the description of the underlying event. This theoretical uncertainty affecting the global tracking pointing method was reviewed and it was concluded that the results presented from a full detector simulation are pessimistic estimates.

After the standard rejection of QCD-jets in the calorimeters the reducible background consists mainly of jets where a single π^0 carry the main part of the energy. The role of the Inner Detector in the rejection of these π^0 events was analysed. At high luminosity and with a photon efficiency of 90% the overall rejection factor of π^0 events with transverse momentum of 50 GeV is 3.2 using the presampler in the calorimeter alone, while a combined method using the identification of conversions in the Inner Detector gives a rejection factor of 3.5.

A pessimistic estimate of the total significance of a Higgs signal shows it will be possible to have a clear identification within one year at high luminosity for a Higgs mass above 105 GeV. The improved QCD-jet rejection from the combined π^0 rejection will improve the absolute significance by less than 1%; more importantly it reduces the uncertainty from the many unknown factors in the rate and rejection of the QCD-jets.

The ATLAS detector was shown to be robust for the detection of the $H \to \gamma\gamma$ decay. If either the performance of the calorimeter pointing is reduced or the difference between the underlying events for the gluon fusion Higgs production and the minimum bias events are less than expected, the Higgs signal efficiency will only be marginally effected.

Chapter 8

Identification of a heavy Higgs

The identification of a Standard Model Higgs particle with a mass above 650 GeV will not be possible in the golden decay channel $H \rightarrow ZZ \rightarrow l^+l^-l^+l^-$: the cross section is too low to observe the four lepton decay mode with its low branching ratio of. As seen in fig. 2.6 the vector boson decays are dominant for Higgs masses above 300 GeV, hence the only alternatives to the four lepton decay are decay channels with a higher branching ratio in the vector boson decays.

The analysis presented here will focus on a 1 TeV Higgs which, as described in detail in section 2.5, is close to or above the upper theoretical limit for a standard model Higgs particle. The branching ratios for a 1 TeV Standard Model Higgs particle can be found in table 8.1

Decay	Branching ratio
$H \rightarrow W^+W^-$	0.624
$H \rightarrow W^+W^- \rightarrow 4j$	0.296
$H \rightarrow W^+W^- \rightarrow l\nu jj$	0.144
$H \rightarrow W^+W^- \rightarrow l^+\nu l^-\bar{\nu}$	0.029
$H \rightarrow ZZ$	0.309
$H \rightarrow ZZ \rightarrow 4j$	0.151
$H \rightarrow ZZ \rightarrow l^+l^-jj$	0.029
$H \rightarrow ZZ \rightarrow l^+l^-\nu\bar{\nu}$	0.008
$H \rightarrow ZZ \rightarrow l^+l^-l^+l^-$	0.001
$H \rightarrow t\bar{t}$	0.067

Table 8.1: The dominant branching ratios for a 1 TeV standard model Higgs particle.

The simulation of the physics events was done with PYTHIA 5.7 [74] using the CTEQ(2L) structure functions. The fast analysis program ATLFAST [75] was used

for the analysis. ATLFAST is a parameterization of the ATLAS detector allowing studies of physics processes in ATLAS without a the full and time consuming detector simulation. From the output of a physics event generator ATLFAST deposits the energy of the stable particles on a grid in (η, φ) with a resolution corresponding to the basic resolution of the ATLAS detector. The deflection in the solenoidal field is taken into account for charged particles. With a given cone size the program finds clusters of cells with energy above a threshold inside the cone and label them as jets if the summed energy inside the cone pass an adjustable threshold. In the case of overlapping cones the energy of the shared cells are shared according to the jet energy. Isolated electrons and muons are identified and the energies of jets, electrons and muons smeared according to parameterizations calibrated with full simulations of the ATLAS detector. The ATLFAST program was modified to allow the reconstruction of jets with different cone sizes simultaneously and to include the calculation of jet invariant masses.

Comparisons between simulations with ATLFAST and full detector simulations can be found in [75, 76]. In general the agreement is good but special care should be taken in situations where pile-up can have a strong influence on the results.

8.1 Reducible backgrounds

The reducible backgrounds to a signal of a heavy Higgs particle are from processes with a large transverse momentum in the hard scattering process. Even with a requirement of very high energy jets in the final state, the QCD-jet production still has by far the largest cross section. Other processes that require special attention are $t\bar{t}$, jW and jZ production. To reduce the time required for the simulation in PYTHIA a general cut was placed on the transverse momentum in the hard scattering process, ensuring that events with a transverse momentum in the hard scattering below this cut were never simulated. While a too low cut would cause the simulation of a large number of events that eventually would be rejected, a too large cut would introduce a bias in the simulated events and cause a too low prediction in the size of the background.

Samples of $t\bar{t}$ and jW events were simulated with different values of the p_T cut in the hard scattering. In fig. 8.1a the $t\bar{t}$ and jW cross sections from the simulation are shown as a function of the p_T cut, while the same cross section is shown in fig. 8.1b after requiring a jet with transverse energy above 350 GeV transverse and an isolated lepton with transverse momentum above 100 GeV. It can be seen that for a p_T cut on the hard scattering above 350 GeV the cross sections after the identification cuts are strongly biased. Except for the simulations of the Higgs signal all simulations concerning the identification of a heavy Higgs are made with a p_T cut of 300 GeV. It is estimated that this at the most adds a 10% systematic uncertainty to the level of the background.

The main tools to reject the reducible background are lepton identification, jet identification, forward tag jets, and a low amount of tracks outside the jets from the vector bosons. All the methods will be described in detail in connection with the different Higgs decay channels described below.

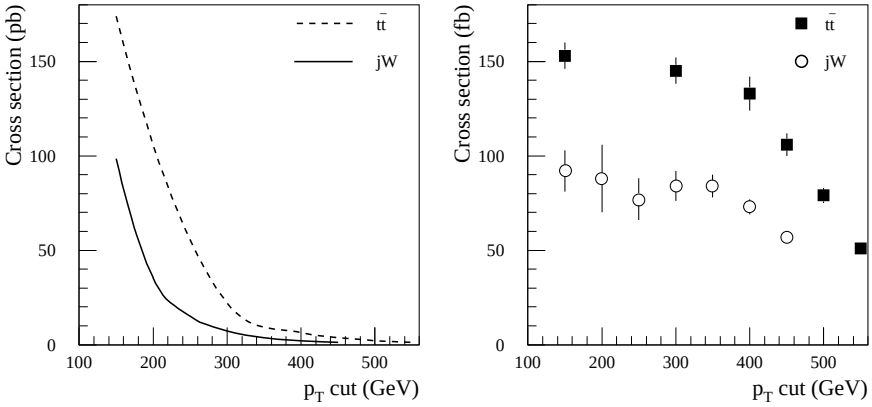

Figure 8.1: The cross sections of the $t\bar{t}$ and jW backgrounds as a function of the p_T cut on the hard scattering in the simulation. In (a) before any identification and in (b) after the identification of a jet with transverse energy above 350 GeV and an isolated lepton with $p_T > 100$ GeV.

8.2 Irreducible vector boson background

The irreducible backgrounds to the vector boson decays of a heavy Higgs particle are from vector boson pair production. The irreducible background can be divided into a group with pairs of longitudinal polarised vector bosons in the final states and another group where either one or both final state vector bosons are transverse polarised.

8.2.1 $V_L V_L$ background

The production of final states with longitudinal polarised vector bosons can to the lowest order be described accurately by the effective W approximation (section 2.2.2) using the diagrams from fig. 2.14 for the vector boson interaction. There are interference effects between the different diagrams and some of the individual diagrams diverge for large centre of mass energies, $\sqrt{\hat{s}}$, in the hard scattering. For this reason it is not possible to distinguish the different processes and in fact the sum of all should be regarded as the signal of a heavy Higgs particle.

To implement the full matrix element in a simulation is not trivial, and it is only for the s-channel Higgs in the $VV \to VV$ scattering (fig. 2.14e), that a detailed description of the virtuality of the incoming vector bosons and the $\hat{s}$ dependent width of the Higgs state is treated correctly in the PYTHIA simulation.

All $VV \to VV$ processes can also be included in PYTHIA but in a somewhat simpler framework where it is possible to treat the cancellations between the different diagrams [74]. Based on the simulation of in total 1 600 000 $VV \to VV$ events with

different treatment of the vector boson scattering the uncertainties in the total cross section will be discussed in section 8.8. The simulations were performed with a 100 GeV cut on the p_T of the hard scattering to avoid the divergence at $p_T = 0$ from the photon propagator in the VV $\rightarrow$ VV scattering (fig. 2.14b).

8.2.2 $V_T V_{L/T}$ background

The cross section for W^+W^-/ZZ events produced in vector boson fusion, where at least one of the bosons are transverse polarised, is almost independent of the Higgs model and the Higgs mass [30]. A trick to compute the background from $W_T W_{L/T}$ states is thus to compute the total WW cross section from vector boson fusion with a low Higgs mass of 100 GeV where the $W_L W_L$ final state has a cross section much below the $W_T W_{L/T}$ final state. For LHC energies this has been done in [31] where the background from $W_T^+ W_{L/T}^-$ events produced in vector boson fusion is estimated to be below 10% of the signal cross section with $m_H = 1$ TeV[1]. Based on this result the background from transverse polarised vector boson states produced in vector boson fusion will be ignored in the further analysis.

8.2.3 Continuum VV background

Pairs of vector bosons are also produced in quark fusion processes giving rise to a spectrum of vector boson pairs with a relatively low invariant mass. The background is the most serious background to the $H \rightarrow ZZ^*$ Higgs signal in the region below the threshold for a Higgs decay to two real Z bosons.

A total of 1 000 000 events of vector bosons was simulated with PYTHIA with a p_T cut in the hard scattering of 300 GeV to study this background.

8.3 Simulated events

The total number of events simulated in different event classes can be found in table 8.2. To avoid any bias of the simulated events from unaccounted leptons in cascade decays, all decay channels have been left open for the $t\bar{t}$, jW, QCD-jet (jj) and continuum VV simulations. The cut on the transverse momentum of the hard scattering was 300 GeV for the background simulation and 100 GeV for the VV $\rightarrow$ VV scattering simulations.

8.4 The four jet channels

The decay of a heavy Higgs in the hadronic decay channels $H \rightarrow W^+W^- \rightarrow$ 4j and $H \rightarrow ZZ \rightarrow$ 4j has a branching ratio of nearly 50%. The problem for this decay channel is the background from QCD-jets with a high cross section. The standard methods

[1] The kinematic cuts used in [31] are not identical to the cuts used in the results presented here but so close that the conclusion is still valid.

Process	Cross section (pb)	Number simulated
$H \to W^+W^-$	0.0548	200 000
$H \to W^+W^- \to l\nu jj$	0.0163	200 000
$H \to ZZ$	0.0274	200 000
$t\bar{t}$	22.0	3 500 000
jW	33.6	5 000 000
VV continuum	0.59	1 000 000
QCD-jets (jj)	$1.15 \cdot 10^5$	4 000 000
$VV \to WW \to l\nu jj$		
② s-channel H, $m_H = 1$ TeV	0.0211	200 000
③ All, $m_H = 1$ TeV	0.0379	200 000
④ All, $m_H = 100$ GeV	0.0018	200 000
⑤ No H	0.0234	200 000
$VV \to ZZ \to l^+\nu l^-\bar{\nu}$		
② s-channel H, $m_H = 1$ TeV	0.0010	200 000
③ All, $m_H = 1$ TeV	0.0018	200 000
⑤ No H	0.0010	200 000

Table 8.2: The number of simulated events for signal and background studies in the detection of a heavy Higgs signal. The Higgs signal processes are only simulated in the vector boson fusion channel. The cut in transverse momentum on the hard scattering process was 300 GeV for the background processes and 100 GeV for the $VV \to VV$ processes.

of jet rejection through identification of isolated leptons or a requirement on a large missing transverse energy cannot be applied in the case of the four jet decays of a Higgs boson.

8.4.1 Vector boson reconstruction

The two vector bosons in the four jet decay are reconstructed from the energies deposited in the calorimeters. The two vector bosons will be nearly back-to-back with a high boost along the vector boson direction and the two jets from each vector boson decay will thus be close together and appear as sub-jets inside jets with a large cone size. The event structure is illustrated in fig. 8.2.

The first step in the reconstruction is to identify two high energy jets with the energy collected in a large cone of radius 0.5[2] centred on the jet axis. The jets are quite central and as shown in fig. 8.3 a selection inside the region $|\eta| < 2.5$ maintains nearly the full signal. The transverse energy distribution of the jet with highest transverse energy is shown in fig. 8.4 for the Higgs signal together with the

[2] All directions where $\sqrt{(\varphi - \varphi_c)^2 + (\eta - \eta_c)^2} < r$ will be within a cone of radius r and with centre (φ_c, η_c).

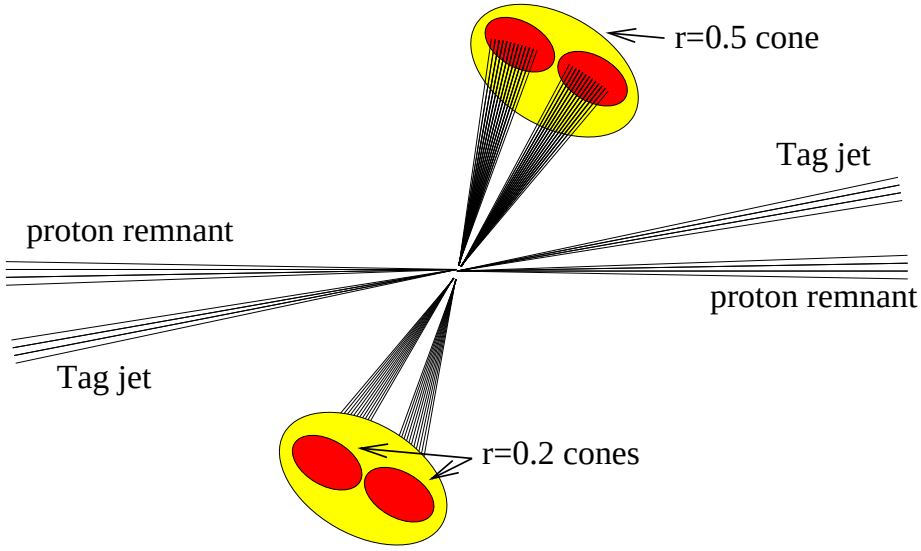

Figure 8.2: The structure of a Higgs event with the Higgs decaying to two vector bosons which in turn decay hadronicly. The central region contains two large-cone jets from each vector boson each with two sub-jets from the fragmentation of the quarks in the vector boson decay. Tag jets (section 8.4.2) and the proton remnants are seen in the forward region.

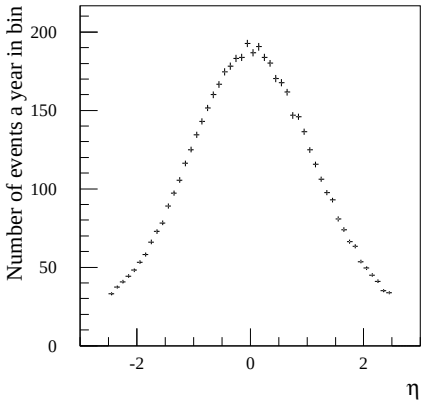

Figure 8.3: The pseudorapidity distribution of the jet with highest transverse energy in $H \rightarrow W^+W^- \rightarrow 4j$ events before any kinematic cuts.

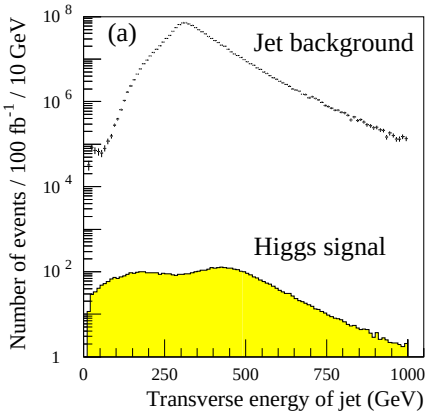

Figure 8.4: The transverse energy distribution of the jet with highest transverse energy in $H \rightarrow W^+W^- \rightarrow 4j$ and QCD-jet events before any kinematic cuts.

background from QCD-jets. The number of events with transverse energy below 300 GeV in the jet sample is strongly biased by the simulation technique[3]. The significance of the signal has a broad maximum for a cut on the jet transverse energy in the interval from 300–400 GeV and the central value of 350 GeV was chosen for the cut.

In a second iteration jets are reconstructed with the energy collected in more narrow cones of radius 0.2. The purpose is to look for two individual sub-jets inside each of the high energy jets, caused by the independent fragmentation of the two quarks in the vector boson decay. For the $H \rightarrow W^+W^- \rightarrow 4j$ events the search for sub-jets with transverse momentum above 50 GeV in both W jets retain 75% of the events, while it keeps 13% of the QCD-jet background. The significance of the signal is almost unaffected by changing the cut in the region from 50 to 125 GeV.

The invariant mass of the large-cone jets are reconstructed by treating each cell of the calorimeter inside the jet cone as a massless 4-vector; the squared mass of a jet is then

$$m_j^2 = (\sum_i P_i)^2, \tag{8.1}$$

with

$$P_i = (\sqrt{p_{x_i}^2 + p_{y_1}^2 + p_{z_i}^2}, p_{x_i}, p_{y_i}, p_{z_i}) \tag{8.2}$$

the massless 4-vectors of each cell inside the jet. The mass distribution for W jets reconstructed using ATLFAST is shown in fig. 8.5. The resolution is 7.9 GeV and no systematic shift is observed. This should be compared to a resolution of (7.7 ± 0.4) GeV for a full simulation of a small sample of $H \rightarrow W^+W^- \rightarrow 4j$ events at high luminosity [3].

8.4.2 Tag jets

As described in section 2.2 the Higgs production for a heavy Higgs is through gluon fusion and vector boson fusion. The Higgs events produced in vector boson fusion are despite the lower cross section the interesting events for the identification of a heavy Higgs particle. As illustrated in fig. 8.6 the quarks that emit the vector bosons will generate jets in the forward direction. The forward jets can be used as tag jets for the vector boson fusion events and strongly reduce the background.

In the ATLAS detector hadronic calorimeters will cover the region down to $|\eta| = 4.9$. Details on the calorimeter design can be found in section 4.3. The tag jets will have a transverse momentum of the order of $m_W/2$. In table 8.3 the effect of requiring either one or two tag jets is shown. The jets are required to have $2.5 < |\eta| < 5.0$ and to be in opposite forward regions for the two jet case.

The probability p for a single tag jet in the forward or the backward direction of the detector is the same. If the two tag jets in double tag events are uncorrelated

[3] This bias does not affect the final results as shown in section 8.1.

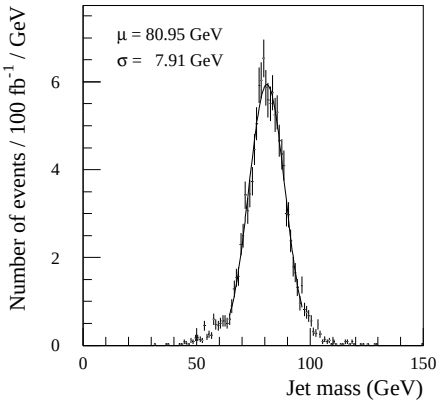

Figure 8.5: The mass distribution of reconstructed W-jets in $H \to W^+W^- \to 4j$ decays using the ATLFAST program.

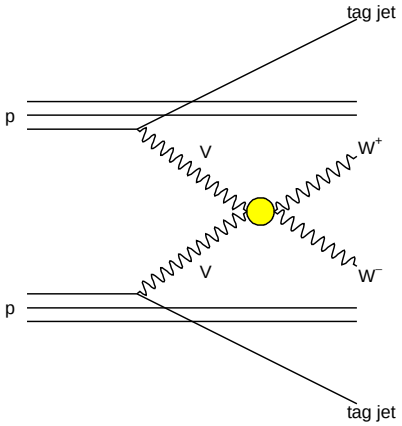

Figure 8.6: An illustration of tag jets created in Higgs production through vector boson fusion. The hard scattering process can be any of the processes in fig. 2.14.

E_T cut (GeV)	Efficiency 1 tag jet (%)		Efficiency 2 tag jets (%)	
	$H \to W^+W^-$	jj	$H \to W^+W^-$	jj
15	85.7±0.7	34.2 ±0.6	36.7±0.4	0.37±0.02
20	82.0±0.7	28.8 ±0.6	31.5±0.4	0.25±0.02
30	71.8±0.6	1.96±0.04	20.6±0.3	0.12±0.01
50	49.3±0.5	1.09±0.04	8.2±0.2	0.04±0.01

Table 8.3: The efficiency of requiring tag jets in the forward regions for $H \to W^+W^- \to 4j$ and QCD-jet events for different values of the E_T cut on the tag jets. Efficiencies are relative to the amount of events left after the identification cuts on the central jets.

the probability for a double tag is p^2 while the probability for a single tag, in either the forward or the backward direction, is $1-(1-p)^2$ and not p as a would be the naïve expectation.

From the tag jet efficiencies for single and double tag jets listed in table 8.3 it is seen that the Higgs events have uncorrelated tag jets while the QCD-jet events show a positive correlation. The Higgs events have uncorrelated tag jets since the quarks emitting the vector bosons are uncorrelated (see fig. 8.6).

8.4.3 Significance of signal

In table 8.4 the effect of all the kinematic cuts are listed for the $H \to W^+W^- \to 4j$ signal and the dominant QCD-jet background. The number of events expected in one year at high luminosity (100 fb^{-1}) is shown and the efficiency of each cut with respect to the preceding cuts.

Cut type (GeV)	H # / 100 fb^{-1}	(%)	jj # / 100 fb^{-1}	(%)
-	5483±12	-	-	-
$E_T^{jet} > 350$	2828±9	52	$4.6{\cdot}10^8 \pm 1.6{\cdot}10^6$	-
$2 \times E_T^{jet} > 350$	1050±5	37	$1.9{\cdot}10^8 \pm 6.6{\cdot}10^6$	41
$E_T^{sub} > 50$	791±5	75	$2.4{\cdot}10^7 \pm 2.3{\cdot}10^5$	13
$\lvert m_{jet} - m_W \rvert < 15$	703±4	89	$1.0{\cdot}10^7 \pm 1.5{\cdot}10^5$	42
$2 \times \lvert m_{jet} - m_W \rvert < 15$	540±4	77	$2.4{\cdot}10^6 \pm 7.4{\cdot}10^5$	24
$E_T^{tag} > 30$	387±3	72	$5.4{\cdot}10^5 \pm 3.5{\cdot}10^4$	23
$2 \times E_T^{tag} > 30$	111±2	29	$2.9{\cdot}10^4 \pm 2.9{\cdot}10^3$	5.3

Table 8.4: Efficiency of applying identification cuts for the $H \to W^+W^- \to 4j$ decay and the QCD-jet background. The first column for the signal and the background gives the expected number of events after one year at high luminosity. The second column is the efficiency relative to the number of events passing all preceding cuts.

Based on these cuts it can be seen that it will not be possible to observe the signal of a heavy Higgs particle in the decay channel $H \to W^+W^- \to 4j$. The $H \to ZZ \to 4j$ could be included by extending the mass cut on the jets to the interval 65 GeV $< m_{jet} <$ 105 GeV, but this would just increase the QCD-jet background far more than the gain in signal from the $H \to ZZ \to 4j$ channel.

A veto on tracks or jets outside the two large-cone jets in the central region, as described for the $H \to W^+W^- \to l\nu jj$ channel, could provide a large rejection of the QCD-jets while keeping a substantial part of the signal. An analysis showed it possible at the most to reject the QCD-jet background with a factor 15 which is not enough to make a discovery of the Higgs particle in the hadronic channel possible. Instead decay channels where at least one of the vector bosons have a fermionic decay has to be used in the Higgs search.

8.5 The $H \rightarrow W^+W^- \rightarrow l\nu jj$ channel

In section 8.4 it was shown that the decay of a heavy Higgs boson to four jets will not be possible to observe above the large background from QCD-jet production. In the decay channel $H \rightarrow W^+W^- \rightarrow l\nu jj$ it is possible to reduce this background through lepton identification and a requirement on a large missing transverse energy from the neutrino in W decay. Other reducible backgrounds are the $t\bar{t}$ and jW processes.

The event topology is similar to the four jet case in fig. 8.2 but with one of the large-cone jets replaced by a lepton and an invisible neutrino.

8.5.1 Vector boson reconstruction

The jet identification requires a jet with transverse energy above 350 GeV inside a large cone with radius 0.5 and two sub-jets inside the large-cone jet with transverse energy above 50 GeV inside a cone size of 0.2. In addition the jet mass as calculated in (8.1) is required to be within 15 GeV of the W mass.

The two fermions are identified in the event by requiring an isolated electron or muon with a transverse momentum above 100 GeV in the central region $|\eta| < 2.5$ and a missing transverse energy above 100 GeV. The efficiency of the cuts are 23% for the $H \rightarrow W^+W^- \rightarrow l\nu jj$ signal when applied to the events passing jet identification and assuming a 90% efficiency for lepton identification after the isolation criteria is passed.

The background sample of QCD-jet events used for the analysis of the $H \rightarrow W^+W^- \rightarrow 4j$ decay was re-analysed for the $H \rightarrow W^+W^- \rightarrow l\nu jj$ channel. Requiring a real isolated lepton leaves a nearly clean $t\bar{t}$ sample and it would thus be double counting to include this in the background along with the separately simulated $t\bar{t}$ events. On the other hand, there is a low probability to misidentify a QCD-jet as an electron. As a conservative estimate, a rejection factor on QCD-jets of 10^4 is assumed based on an analysis with full simulation at much lower jet and electron energies [4].

The results of all identification cuts are summarised in table 8.8, where the number of events passing for an LHC year at high luminosity (100 fb^{-1}) and the efficiency of the individual cuts with respect to the events passing all preceding cuts, are shown. The efficiency of the first cut on the transverse jet energy is not calculated as it depends entirely on the cut on the transverse energy in the hard scattering process as described in section 8.1. As expected the requirement of an isolated lepton is very effective in reducing the background.

8.5.2 Tag jets

The identification cuts in the central region did not reduce the background sufficiently and tag jets as described in section 8.4.2 has to be required. In table 8.5 is shown the effect of requiring a single or double tag of jets in the forward and backwards regions with $3 < |\eta| < 5$ using different cuts on the transverse energy of the tag jets.

E_T cut (GeV)	Efficiency 1 tag jet (%)			Efficiency 2 tag jets (%)		
	H	$t\bar{t}$	jW	H	$t\bar{t}$	jW
15	85.1±0.6	35.8±0.4	29.0±0.5	36.4±0.3	4.0±0.1	2.4±0.1
20	81.3±0.6	30.2±0.4	23.8±0.4	31.6±0.3	2.8±0.1	1.6±0.1
30	71.4±0.6	21.2±0.3	16.1±0.3	21.0±0.3	1.3±0.1	0.7±0.1
50	49.9±0.3	12.1±0.2	8.8±0.2	8.5±0.0	0.4±0.0	0.2±0.0

Table 8.5: The efficiency of requiring tag jets in the forward regions for the signal $H \rightarrow W^+W^- \rightarrow l\nu jj$ and for the background samples $t\bar{t}$ and jW. Efficiencies are relative to the amount of events left after the identification cuts on the central jets. Effects of pile-up are not taken into account.

Rejecting background through a requirement of tag jets in the forward region sensitive to the pile-up creating both real and fake jets in the forward regions. With a full GEANT simulation of the Higgs events and pile-up at high luminosity is was in [77] shown that the rate of jets originating from the pile-up with a transverse energy above 30 GeV is below 2% in one hemisphere. This means that a background event with no tag jets has a 4% probability (two hemispheres) to pick up a tag jet from the pile-up while a background event with one tag jet has a 2% probability to pick up a second jet from the pile-up (pile-up jet has to be in the opposite hemisphere of the real tag jet). With the numbers for the $t\bar{t}$ and jW background from table 8.5 with a cut on the transverse energy of 30 GeV it can be seen that this seriously affects the rejection using two tag jets; the $t\bar{t}$ efficiency rise from 1.3% to 1.8% and the jW efficiency rise from 0.7% to 1.1%.

In principle a clean discovery within one year at high luminosity should be possible with the rejection achieved against the reducible background, but the signal to background ratio is a problem. The background cannot be accurately calibrated as the signal is not a clear peak on top of a flat background. With the above numbers an uncertainty in the background level of 30% will be able to fake a discovery. Some calibration can be done by specifically looking at the events not surviving the cut confining the jet mass to the W mass. For the Higgs signal and the $t\bar{t}$ and jW backgrounds the mass spectrums for the central jet with the highest E_T are shown in fig. 8.7. All other central identification cuts and the requirement on two tag jets have been applied. It can be seen that both the $t\bar{t}$ and the JW backgrounds are peaked as the signal around the W mass and hence a calibration looking at the side-bands to the W mass peak will have a limited value.

8.5.3 Jet and track veto

Events with Higgs particles produced through vector boson fusion can be separated into four regions centred around the two tag jets and the two vector bosons in the decay as shown in fig. 8.2 and fig. 8.6. To the lowest order, there will be no colour flow between the regions, as they are not connected by any quarks or gluons carrying colour charge. The lack of colour flow between the jets developing causes the number

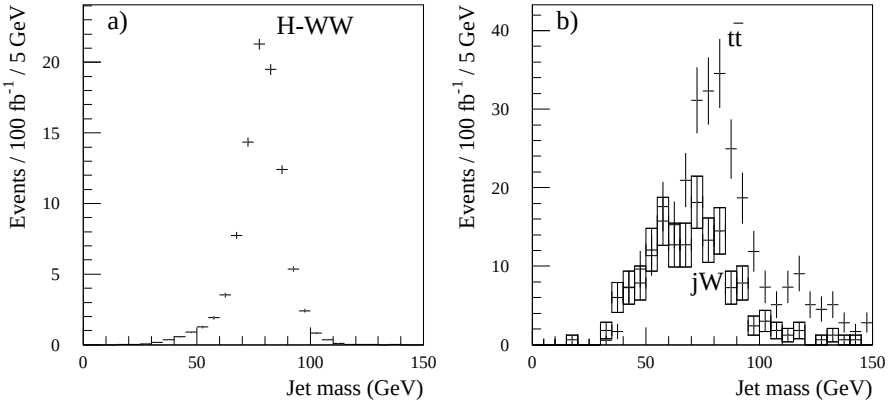

Figure 8.7: The mass spectrum of the central jets in events surviving the central identification cuts and have two tag jets. In (a) the Higgs signal and in (b) the $t\bar{t}$ (crosses) and jW (boxes) backgrounds.

of tracks outside the four regions to be low.

For QCD type events created through quark and gluon fusion processes there will in general be colour flow between all the jets in the events, creating particles in the regions between the jets as well.

Vetoing events with a large number of particles in the central region and outside the two large-cone jet can be used to reject backgrounds like $t\bar{t}$, jW and QCD-jet events which all have colour flow between the final state jets. Higher order QCD processes will to some extent disturb the clean picture described above as the partons produced in the higher order interaction can connect the outgoing jets in the vector boson fusion process and thus create a colour flow between them. The higher order QCD processes are not directly simulated by PYTHIA but are instead effectively included in the initial and final state radiation. This approximation causes a quite large uncertainty in the power of a track counting veto.

Up to 90% of all vector boson fusion events will have colour flow between the different final state jets [78], but in most cases the Q^2 transfer in these colour strings will be low and only allow few particles with relatively low p_{T} to be created. Counting only particles between the jets above a p_{T} threshold, has thus the potential to increase the power of a track veto.

A track counting veto is not trivial at high luminosity LHC conditions. Only charged tracks can be reconstructed and only in the central pseudorapidity region $|\eta| < 2.5$. That it is possible was demonstrated in section 7.4, where it was shown with a full detector simulation that tracks with transverse momentum of a few GeV could be assigned to specific primary vertices with a high efficiency at high luminosity.

In fig. 8.8 is shown the distribution in the number of charged tracks, with p_{T}

above 3 and 4 GeV respectively, for the Higgs signal and the $t\bar{t}$ background after all other identification cuts. Only tracks outside the large-cone jet in the central region are counted.

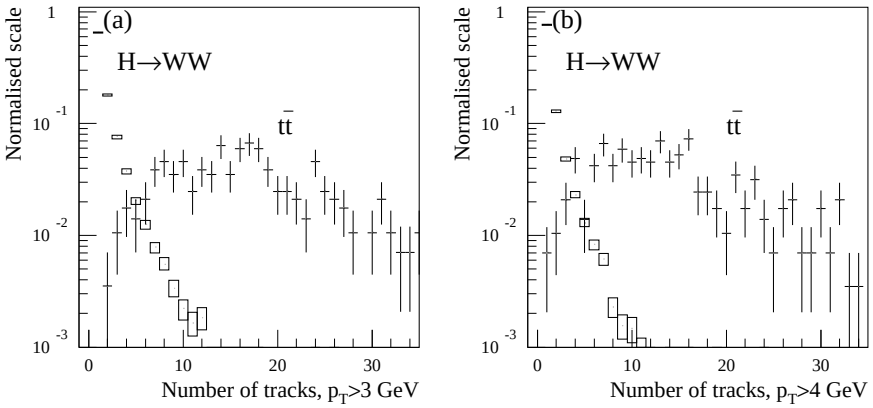

Figure 8.8: The distribution for the Higgs signal (boxes) and the $t\bar{t}$ background (crosses) in the number of tracks with $|\eta| < 2.5$ and outside the jet in the central region. The cut on transverse momentum was 3.0 GeV in (a) and 4.0 GeV in (b).

The Higgs events with regions empty of particles can also be identified by looking for low energy jets in the calorimeter outside the high energy central jet. The method has the advantage compared to the track counting method that it registers neutral tracks as well. However, there is no way in the calorimeter to distinguish between a jet from the pile-up or a jet from the hard interaction, which makes the method sensitive to pile-up unless a quite high threshold is used on the transverse energy of the required jets. In fig. 8.9 is shown the distribution in the number of jets with $|\eta| < 2.5$ and a transverse energy cut on the jet energy of 20 GeV respectively 50 GeV for the Higgs signal and the $t\bar{t}$ background.

The effect of a jet veto is summarised in table 8.6 and the effect of a track veto in table 8.7. A tracking efficiency of 95% has been taken into account. On average the pile-up will at high luminosity have 3.5 (0.9) charged tracks with $p_T > 3$ (4) GeV. To allocate the few tracks from the pile-up to primary vertices different from the Higgs vertex will not be a problem. For this reason pile-up is not considered to degrade the track veto significantly.

8.5.4 Significance of signal

To both retain some statistics and maximising the signal to background ratio two tag jets with $E_T > 30$ GeV and a track veto for tracks with $p_T > 4$ GeV in the central region has been required. The number of events after a year at high luminosity is

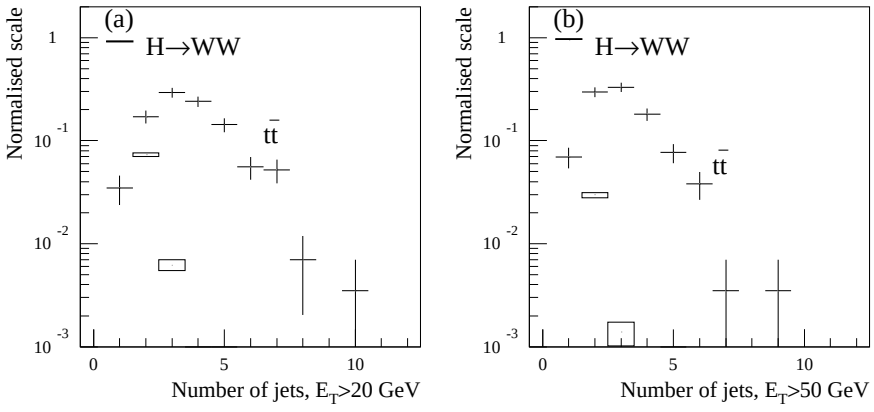

Figure 8.9: The distribution in the number of jets with $|\eta| < 2.5$ in the Higgs signal (boxes) and $t\bar{t}$ background (crosses). A transverse energy threshold of 20 GeV (a) and 50 GeV (b) was used.

Jet veto (GeV)	H eff. (%)	$t\bar{t}$ eff. (%)	jW eff. (%)	S/N
$E_T > 20$	85.3	2.44	15.6	4.4
$E_T > 30$	92.0	3.48	18.9	3.8
$E_T > 50$	96.9	6.97	33.6	2.1

Table 8.6: A veto on further jets outside the jet with the highest E_T and with $|\eta| < 2.5$. The $H \to W^+W^- \to l\nu jj$ signal and the $t\bar{t}$ and jW backgrounds are shown. The last column contains the signal to background ratio after the jet veto.

Track veto (GeV)	H eff. (%)	$t\bar{t}$ eff. (%)	jW eff. (%)	S/N
$p_T > 3$	77.9	< 1.0	11.7	6.8
$p_T > 4$	66.8	< 1.0	7.0	8.0

Table 8.7: The efficiency of a veto on any charged track excluding the identified lepton outside the jet with the highest E_T and with $|\eta| < 2.5$. The $H \to W^+W^- \to l\nu jj$ signal and the $t\bar{t}$ and jW backgrounds are shown. The last column shows the signal to background ratio after the track veto.

shown and the efficiencies relatively to all preceding cuts are shown in the summary table 8.8. After including the track veto the situation is favourable with 62 Higgs events expected a year with a background of 9 events from jW production and below 3 events from $t\bar{t}$ production. Systematic corrections to this estimate will be discussed in section 8.8 and the final numbers will be given in section 8.9.

8.6 The H → ZZ→ $l^+l^-\nu\bar{\nu}$ channel

The H → ZZ decay channels where one of the vector bosons are required to decay to electrons or muons has the potential for a clean signal using the requirement of a pair of leptons with an invariant mass close to m_Z. The disadvantage is the branching ratio which for the H → ZZ→ $l^+l^-\nu\bar{\nu}$ channel is 18 times lower than the branching ratio for the H → W^+W^- → lνjj decay. The decay with two neutrinos on one side of the event creates a large missing transverse energy. In fig. 8.10 the missing transverse energy is shown for the H → ZZ→ $l^+l^-\nu\bar{\nu}$ signal and the dominant $t\bar{t}$ and jZ backgrounds after the requirement of two isolated leptons with transverse momentum above 100 GeV.

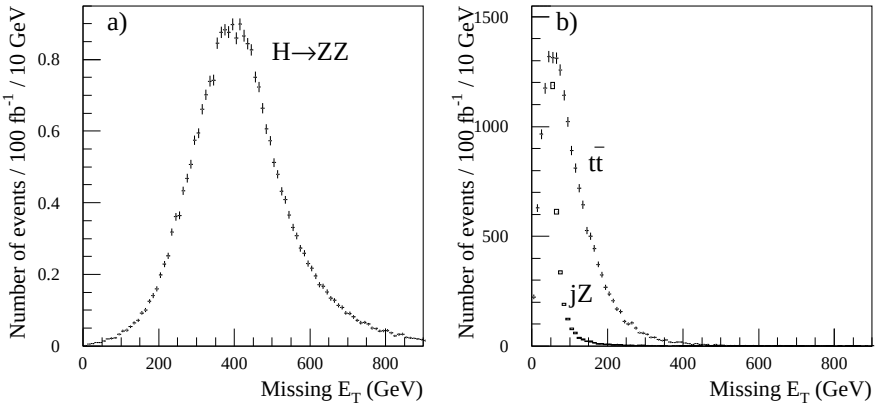

Figure 8.10: The missing transverse momentum in H → ZZ→ $l^+l^-\nu\bar{\nu}$ events (a) and the dominant $t\bar{t}$ and jZ backgrounds in (b) after a requirement on two isolated leptons with $p_T > 100$ GeV.

In table 8.9 the effect of all identification cuts are shown. An efficiency for the identification of already isolated leptons of 90% has been assumed. The constraint of the lepton pair mass to m_Z has a large effect caused by the good di-lepton mass resolution of the ATLAS detector and the fact that most lepton pairs in the $t\bar{t}$ and jW events are fake pairs with large separation. With an efficiency of 80% for the signal it reduces the jZ background by a factor six and eliminates the $t\bar{t}$ and jW backgrounds.

Cut type (GeV)	H # / 100 fb^{-1}	(%)	$\bar{\text{tt}}$ # / 100 fb^{-1}	(%)	jW # / 100 fb^{-1}	(%)
-	1633±4	-	-	-	-	-
$E_{\text{T}}^{\text{jet}} > 350$	818±3	50	503408±1489	-	1644243±3323	-
$\lvert m_{\text{jet}} - m_{\text{W}} \rvert < 15$	606±2	74	200985±941	40	380443±1598	23
$E_{\text{T}}^{\text{sub}} > 50$	591±2	98	190895±917	95	353865±1541	93
$p_{\text{T}}^{\text{lep}} > 100$	453±2	77	22796±301	12	14254±293	4
$E_{\text{T}}^{\text{miss}} > 100$	381±2	84	12927±86	57	10355±80	73
$E_{\text{T}}^{\text{tag}} > 30$	272±2	71	3149±43	24	2015±35	19
$2 \times E_{\text{T}}^{\text{tag}} > 30$	80±1	29	179±10	5.6	113±7	5.6
Track veto $p_{\text{T}} > 4$	62±1	78	< 3	< 1.6	14±2	12
Cut type (GeV)			jj # / 100 fb^{-1}	(%)	WW continuum # / 100 fb^{-1}	(%)
$E_{\text{T}}^{\text{jet}} > 350$			$4.6 \cdot 10^8 \pm 1.0 \cdot 10^6$	-	32303±63	-
$\lvert m_{\text{jet}} - m_{\text{W}} \rvert < 15$			$4.4 \cdot 10^7 \pm 3.2 \cdot 10^5$	10	17898±47	55
$E_{\text{T}}^{\text{sub}} > 50$			$3.9 \cdot 10^7 \pm 3.0 \cdot 10^5$	89	15311±43	86
$p_{\text{T}}^{\text{lep}} > 100$			$3.9 \cdot 10^3 \pm 30$	0.01	2983±18	19
$E_{\text{T}}^{\text{miss}} > 100$			83±4	2	2227±15	75
$E_{\text{T}}^{\text{tag}} > 30$			22±2	26	228±5	21
$2 \times E_{\text{T}}^{\text{tag}} > 30$			2±1	10	4±1	2
Track veto $p_{\text{T}} > 4$			-	-	-	-

Table 8.8: Efficiency of applying identification cuts for the $\text{H} \rightarrow \text{W}^+\text{W}^- \rightarrow \text{l}\nu\text{jj}$ decay and the dominant background channels. The efficiencies are relative to the number of events passing all preceding cuts. Pile-up effects on the tag requirement has been taken into account. For the QCD-jet events (jj) a probability of 10^{-4} to identify a jet as an electron has been assumed.

Cut type (GeV)	H # / 100 fb^{-1}	(%)	VV continuum # / 100 fb^{-1}	(%)	$\bar{t}t$ # / 100 fb^{-1}	(%)
-	74.32±0.17	-	-	-	-	-
$p_T^{lep1} > 100$	57.72±0.14	78	14252±40	-	374216±1219	-
$p_T^{lep2} > 40$	43.04±0.13	75	2238±15	16	40856±552	11
$E_T^{miss} > 200$	39.95±0.12	93	579±8	26	5180±113	13
$\lvert m_{ll} - m_Z \rvert < 5$	31.77±0.11	80	89±3	15	< 1.5	-
$E_T^{tag} > 30$	22.16±0.10	70	12.9±1.0	14	< 1.5	-
$2 \times E_T^{tag} > 30$	6.36±0.04	29	< 1.2	-	< 1.5	-
Cut type (GeV)			jZ # / 100 fb^{-1}	(%)	jW # / 100 fb^{-1}	(%)
$p_T^{lep1} > 100$			85732±126	-	445438±1219	-
$p_T^{lep2} > 40$			50781±95	59	2780±552	0.6
$E_T^{miss} > 200$			123±5	0.2	589±113	21
$\lvert m_{ll} - m_Z \rvert < 5$			16.4±1.7	13	< 2.1	-
$E_T^{tag} > 30$			3.8±0.9	23	< 2.1	-
$2 \times E_T^{tag} > 30$			2.0±0.6	53	< 2.1	-

Table 8.9: Efficiency of applying identification cuts for the H → ZZ→ l⁺l⁻νν̄ decay and the dominant background channels. The efficiencies are relative to the number of events passing all preceding cuts. An electron identification efficiency after the isolation requirement of 90% has been assumed.

The total number of signal events per year is well below the number of events in the $H \rightarrow W^+W^- \rightarrow l\nu jj$ channel but the background is almost absent. The rejection obtained with the requirement of two tag jets is limited by the effects of pile-up.

Replacing the requirement on tag jets with a track veto in the central region gives 12 signal events in a year with a background of 23 events totally dominated by the vector boson continuum. The significance is slightly worse with these cuts but will be valuable as a cross check on the jZ background.

8.7 The $H \rightarrow ZZ \rightarrow l^+l^-jj$ channel

The $H \rightarrow ZZ \rightarrow l^+l^-jj$ decay is the last decay channel that will be treated for the heavy Higgs particle. It has a branching ratio four times larger than the $H \rightarrow ZZ \rightarrow l^+l^-\nu\bar{\nu}$ but lacks the possibility of a requirement of a large missing transverse momentum which will make the identification more sensitive to the jZ background.

The decay is identified from the lepton pair, as described in section 8.6, and the large-cone jet in the opposite direction with two sub-jets and the jet mass constrained to m_Z, as described in section 8.4. The results are summarised in table 8.10.

It should not be impossible to find the Higgs in the $H \rightarrow ZZ \rightarrow l^+l^-jj$ channel but clearly the signal will not be very good. Both the significance and the signal to background ratios are low compared to the $H \rightarrow ZZ \rightarrow l^+l^-\nu\bar{\nu}$ and $H \rightarrow W^+W^- \rightarrow l\nu jj$ channels. The channel allows a full reconstruction of the event but with the few events left after the identification cuts this has no real interest.

8.8 Uncertainties in the size of signal and background

Both the signal and the background has theoretical uncertainties. Some of the uncertainties can be reduced through calibration with LHC data, others require theoretical developments to reduce.

The power of the different identification criteria in the simulated events have uncertainties mainly related to the effects of pile-up. In none of the simulations presented here pile-up has been added but several other independent studies have been made of the effects.

The following sections will estimate the size of the different uncertainties and with this taken into account a final estimate on the significance and the signal to background ratio of a Higgs signal will be given in section 8.9.

8.8.1 Structure functions

The ambiguous choice of structure functions used for the simulation introduces an uncertainty in the production cross section. The production of heavy objects requires the x values of the incoming partons to be large. The structure functions are best

Cut type (GeV)	H # / 100 fb^{-1}	(%)	VV continuum # / 100 fb^{-1}	(%)	$\bar{\text{t}}$t # / 100 fb^{-1}	(%)
-	396.0±2.3	-	-	-	-	-
$p_{\text{T}}^{\text{lep1}} > 100$	300.6±1.9	76	14252±40	-	374216±1219	-
$p_{\text{T}}^{\text{lep2}} > 40$	213.6±1.6	71	2238±15	16	40856±552	11
$\lvert m_{\text{ll}} - m_{\text{Z}} \rvert < 5$	160.6±1.4	75	512±7	23	42±17	0.1
$E_{\text{T}}^{\text{jet}} > 350$	55.98±0.80	35	126±3	25	< 1.5	-
$\lvert m_{\text{jet}} - m_{\text{W}} \rvert < 15$	36.96±0.65	66	62.2±2.5	49	< 1.5	-
$E_{\text{T}}^{\text{sub}} > 50$	35.64±0.62	96	59.7±2.5	96	< 1.5	-
$E_{\text{T}}^{\text{tag}} > 30$	25.46±0.53	71	5.8±0.8	10	< 1.5	-
$2 \times E_{\text{T}}^{\text{tag}} > 30$	7.57±0.29	30	< 0.6	-	< 1.5	-
Cut type (GeV)			jZ # / 100 fb^{-1}	(%)	jW # / 100 fb^{-1}	(%)
$p_{\text{T}}^{\text{lep1}} > 100$			85732±126	-	44543 8±1219	-
$p_{\text{T}}^{\text{lep2}} > 40$			50781±95	6	2780±552	0.6
$\lvert m_{\text{ll}} - m_{\text{Z}} \rvert < 5$			35983±80	71	< 2.1	-
$E_{\text{T}}^{\text{jet}} > 350$			15216±51	42	< 2.1	-
$\lvert m_{\text{jet}} - m_{\text{W}} \rvert < 15$			914±13	6	< 2.1	-
$E_{\text{T}}^{\text{sub}} > 50$			840±12	92	< 2.1	-
$E_{\text{T}}^{\text{tag}} > 30$			148±5	18	< 2.1	-
$2 \times E_{\text{T}}^{\text{tag}} > 30$			5.9±0.9	4	< 2.1	-

Table 8.10: Efficiency of applying identification cuts for the $\text{H} \rightarrow \text{ZZ} \rightarrow \text{l}^{+}\text{l}^{-}\text{jj}$ decay and the dominant background channels. The efficiencies are relative to the number of events passing all preceding cuts. An electron identification efficiency after the isolation requirement of 90% has been assumed.

measured at large x thus making the extrapolation to the LHC energy relatively certain.

In [79] the cross section for a 1 TeV Higgs and the major backgrounds were evaluated using PYTHIA with several different structure functions. For the signal the variation was less than 5% and for the backgrounds less than 10%, making the uncertainty from structure functions small compared to other uncertainties.

8.8.2 jW cross section

The dominant jW background to the $H \to W^+W^- \to l\nu jj$ signal is simulated from the $2 \to 2$ matrix elements $f_1\bar{f}_2 \to gW$ and $f_1 g \to f_2 W$ with additional jets created in the initial and final state radiation. This may lead to uncertainties in the rate of multi-jet events.

For the analysis of $W + nj$ data at CDF the VECBOS Monte Carlo model was used for comparisons. VECBOS simulates the $W + nj$ states directly by including the matrix elements for direct creation of a vector boson together with multiple partons. It was shown, that the Monte Carlo for Tevatron energies underestimate the cross section for W production with one or more jets by 30%, while the cross sections for W production with two or more jets is overestimated by 10% [80]. For the study jets were counted with $E_T > 15$ GeV and $|\eta| < 2.4$.

In [81] the PYTHIA Monte Carlo and VECBOS Monte Carlo (with parameters as in [80]) were compared at LHC energies and it was shown that the jW cross sections were almost identical but with the PYTHIA cross section falling slowly with respect to the VECBOS cross section as a function of the primary jet energy.

It seems clear that PYTHIA for the analysis presented here to some extent underestimates the jW background. A conservative estimate is that the cross section is underestimated by 50%. It is assumed that the jZ background is underestimated as well, even though there is no experimental evidence from the Tevatron for this.

8.8.3 $VV \to VV$ cross section

As explained in section 8.2 the $VV \to VV$ signal events were simulated only in the s-channel Higgs transfer channel. The standard simulation ① is compared to four different scenarios in the simplified model where the incoming vector bosons are assumed to be on the mass shell and the width of the Higgs a simple Breit-Wigner shape.

① The standard simulation with a 1 TeV Higgs mass and a correct treatment of the incoming vector bosons and the Higgs width. Only the s-channel Higgs transfer is included.

② The same simulation as above but now in the simplified model.

③ All $VV \to WW$ diagrams included and a Higgs mass of 1 TeV.

④ All $VV \to WW$ diagrams included and a Higgs mass of 100 GeV.

⑤ The un-physical situation where the Higgs is not included but neither any other model to prevent the divergences in the Standard Model.

In table 8.11 the number of events expected for a year at high luminosity after the central jet cuts and after the requirement of a double jet tag, is compared between the different simulation models. By comparing ① and ② it can be seen that the correct treatment of the incoming vector bosons and the Higgs width predicts a lower cross section. It can also be seen by comparing ② and ③ that there is a cancellation between the different scatter diagrams and the total VV → WW signal will be below the signal expected from the Higgs s-channel. This is not the case in the VV → ZZ channel.

	$W^+W^- \to l\nu jj$		$ZZ \to l^+l^-\nu\nu$	
Simulation type	Central cuts	2 tag jets	Central cuts	2 tag jets
① Standard, $m_H = 1$ TeV	381±2	80±1	31.8±0.1	6.36±0.04
② s-channel H, $m_H = 1$ TeV	739±3	166±1	39.3±0.1	8.78±0.06
③ All, $m_H = 1$ TeV	586±4	126±1	49.2±0.2	9.67±0.08
④ All, $m_H = 100$ GeV	0.8±0.0	0.16±0.01	0.3±0.0	0.04±0.00
⑤ No H	272±2	64±1	18.2±0.1	3.35±0.04

Table 8.11: The number of events for an integrated luminosity corresponding to one year at high luminosity for five different simulation models of VV → VV scattering (see text for details).

As the best estimate for the VV → VV signal with a 1 TeV Higgs particle is taken the detailed s-channel simulation ①. In the $H \to W^+W^- \to l\nu jj$ channel the cross section is corrected with the 24% reduction in the signal from the cancellation between the diagrams as evaluated from the simplified model. In the same way the cross section in the $H \to ZZ \to l^+l^-\nu\bar{\nu}$ channel is increased by 10%.

The precision in the Higgs signal cross section is clearly not satisfactory and theoretical developments are required to get improved predictions for the number of signal events surviving the identification cuts. As a Higgs mass of 1 TeV stretches the Standard Model to the limit, and maybe even beyond, no high precision in the expected cross sections and kinematics of the VV → VV processes are to be expected.

8.8.4 Tag jets

The identification of tag jets is sensitive to pile-up as minimum bias events have a large activity in the forward regions. Backgrounds such as jW can from the pile-up pick up either one or two fake tag jets.

The effect on the efficiency of adding pile-up was treated in section 8.5, where it was shown to have a substantial influence on the background rates. As the study in [77] also includes a requirement of at least one cell in the cluster to have $E_T > 6$ GeV a slight reduction in the Higgs signal efficiency is also expected. With the tag jets required to have $E_T > 30$ GeV the reduction will be insignificant.

A full simulation of the background rejection using tag jets would improve the precision in the estimates but the computing power involved in such a study makes it unrealistic to perform in the near future.

8.8.5 Colour flow in Pythia

The description of the colour flow in the Higgs events produced through vector boson fusion in PYTHIA is not satisfactory. Only the lowest order diagrams where there is no colour flow between the spectator quarks and the central jets are implemented. With the relatively high cut on transverse momentum used in the central track veto the consequences of this simplified description should not be large, but a better understanding of the implications is desirable.

8.9 Final estimate of a heavy Higgs signal

All different decay channels of a heavy Higgs particle have been analysed and it can be concluded that the only realistic channels available for a Higgs mass of 1 TeV are the $H \to W^+W^- \to l\nu jj$, $H \to ZZ \to l^+l^-\nu\bar{\nu}$ and $H \to ZZ \to l^+l^-jj$ channels: the channels with more jets will drown in the QCD-jet background and the $H \to ZZ \to l^+l^-l^+l^-$ channel has a too low rate.

A pessimistic estimate on the significance and the signal to background ratio after one year at high luminosity of the different channels is given in table 8.12. Following the discussion in section 8.8 the jW and jZ backgrounds were increased by 50% above the PYTHIA predicted cross section and the Higgs cross section modified to account for the cancellation between the different vector boson scattering diagrams (section 8.8.3). Only the $H \to W^+W^- \to l\nu jj$ will thus for sure be visible after one year at high luminosity while the visibility of the $H \to ZZ$ channels will depend on the level of the jZ background. In any case the two HZZ channels will be able to confirm a discovery in the $H \to W^+W^- \to l\nu jj$ channel.

Decay	Signal # / 100 fb^{-1}	Background # / 100 fb^{-1}	$S/\sqrt{B}$	S/B
$H \to W^+W^- \to l\nu jj$	47	21	10.3	2.2
$H \to ZZ \to l^+l^-\nu\bar{\nu}$	7.0	< 4	3.5	1.8
$H \to ZZ \to l^+l^-jj$	8.3	8.9	2.8	0.9

Table 8.12: The final pessimistic estimates for the discovery of a Standard Model Higgs particle with $m_H = 1$ TeV after 1 year at high luminosity. Both the significance $S/\sqrt{B}$ and the signal to background ratio S/B are given.

In table 8.11 it can be seen that with a low mass Higgs particle (below a few hundred GeV) the scattering of longitudinal vector bosons is insignificant. Thus the discovery of a Higgs boson in the at the moment most favoured mass region around 115 GeV (see section 2.4), would make the measurement of longitudinal polarised

vector boson scattering important as it will confirm that the Higgs particle stabilises the electroweak sector of the Standard Model. Assuming that the jW background can be properly calibrated, an upper limit of 25% of the expected cross section with a 1 TeV Higgs can be set with 95% confidence level after one year at high luminosity. This corresponds to a cross section for longitudinal polarised W pair production of 12 fb.

A measurement of the relative branching ratios of $H \to W^+W^-$ and $H \to ZZ$ is interesting as it probes the SU(2) symmetry of the electroweak theory in the Higgs sector. The theory as seen in (2.60) and (2.60) predicts the $H \to W^+W^-$ branching ratio to be exactly twice the $H \to ZZ$ branching ratio in the limit of a heavy Higgs particle. To measure this factor with reasonable accuracy will obviously take several years of data to get sufficient statistics in the $H \to ZZ$ channel.

In [82] some effort was devoted to the study of the mass peak from a 1 TeV Higgs particle. In the $H \to W^+W^- \to l\nu jj$ the mass can be reconstructed (with a two-fold ambiguity) from constraining the pair of the lepton and the missing transverse energy vector to the W mass. Without a simulation model that at the same time can treat the mass dependent width and the cancellations between the different $VV \to VV$ diagrams the use of the mass peak in the estimation of the significance of the Higgs signal seems speculative. For lower Higgs masses down to around 600 GeV where the $H \to W^+W^- \to l\nu jj$ channel would still be observable such a study makes more sense.

Chapter 9

Summary

If the Higgs boson is not discovered at LEP2 it has to have a mass in above 95 GeV. On the other hand the Standard Model will break down if the Higgs mass is above 1 TeV. A global fit to the measurements from LEP2 and the Tevatron favours a Higgs mass for a Standard Model Higgs boson around 115 GeV but with a large uncertainty towards higher masses. Within the Standard Model it will be possible with the ATLAS detector at the LHC to discover the Higgs boson regardless of its mass within the allowed region.

A detailed study was presented on the identification of an intermediate mass Higgs boson in the $H \to \gamma\gamma$ decay channel. It was shown that the ATLAS Inner Detector plays a vital role both for the reconstruction of the photon-photon invariant mass and for the rejection of the reducible background.

A study of the identification of the heaviest imaginable Higgs particle with a mass around 1 TeV was performed with a fast simulation of the ATLAS detector. It showed that after one year with the LHC running at high luminosity it will be possible to identify the Higgs in the $H \to W^+W^- \to l\nu jj$ decay channel; with more data the $H \to ZZ \to l^+l^-\nu\bar{\nu}$ and $H \to ZZ \to l^+l^-jj$ decay channels will be observable as well.

The Higgs sector of the Standard Model cannot be tested fully just through a discovery of the Higgs boson. First of all the results has to fit together. An improved measurement of all electroweak parameters including the W and the top quark mass will improve the indirect measurement of the Higgs mass which has to be consistent with the directly reconstructed mass of the discovered Higgs boson.

The Higgs particle in the Standard Model prevents the cross section for the scattering of longitudinal vector bosons at high momentum transfers from diverging. Thus a measurement of this cross section will be another important point in the verification of the Higgs theory.

Any inconsistence in the above measurements will point towards a more complicated Higgs sector than the one described by the Standard Model. Both the description of the different alternative models to the Higgs theory and how to distinguish them experimentally are outside the scope of this thesis.

Other predictions of the Standard Model such as the branching ratios and the isotropic decay angle distribution of the Higgs scalar will in some cases be hard to confirm with data from the ATLAS detector. The limitation is the limited significance of the Higgs signal in some mass regions and the accessibility to only a few decay modes. A future linear e^+e^- collider with a centre of mass energy sufficient to produce the Higgs boson will for such studies be able to extent the measurements from the LHC.

A combined tracking and electron identification detector will be a part of the ATLAS Inner Detector. The design of this Transition Radiation Tracker (TRT) was described in detail. Results from a prototype of the TRT was analysed. They showed a well performing detector which will be stable under the operating conditions of the LHC. The Monte Carlo model for the production and detection of transition radiation describes the general performance of the detector but the absolute levels of pion rejection are not predicted correctly. An arbitrary normalisation constant in the radiator performance of around 90% is required for the Monte Carlo model to describe the data. The results obtained with the prototype and the subsequent calibration of the Monte Carlo model allows for a better prediction of the electron identification power of the TRT in the ATLAS detector.

It has in this thesis been shown that the tracking and electron identification capabilities of the ATLAS Inner Detector are essential parts of the ATLAS detector for Higgs physics.

For an intermediary mass Higgs particle, the electron identification power of the TRT will be important in the $\mathrm{H} \to \gamma\gamma$ decay channel. For the rejection of the QCD-jet background it was shown how the identification of converted photons from π^0 decays can improve the rejection by 10%. A well performing algorithm to reconstruct conversions relies heavily on the electron identification power of the TRT. In the special case of $m_\mathrm{H} \simeq m_\mathrm{Z}$ the electron rejection using tracking and transition radiation is essential for observing the signal.

The significance of the Higgs signal in the $\mathrm{H} \to \gamma\gamma$ decay channel depends on the level of the background and the photon-photon mass resolution. It was shown how the individual calibration of the energy scale in the calorimeter for converted and non-converted photons improve the significance of the signal by 10%. The determination of the primary vertex position will improve the significance by another 3–7%. The uncertainty in the prediction from the uncertainties in the model used for the underlying event to the Higgs particle was analysed.

The electron identification power of the TRT will also be important for b-tagging with soft leptons in the $\mathrm{H} \to \mathrm{b\bar{b}}$ decay channel.

For a heavy Higgs particle where the golden decay $\mathrm{H} \to \mathrm{ZZ} \to \mathrm{l^+l^-l^+l^-}$ is accessible the Inner Detector is important for obtaining a clean inclusive electron sample and for reconstructing the position of the primary vertex. Also the rejection of the $\mathrm{t\bar{t}}$ background with a b-tagging veto relies on the Inner Detector.

For the detection of a very heavy Higgs particle the Inner Detector is used in the identification of the electrons from W and Z decays. For the identification of the Higgs boson in the $\mathrm{H} \to \mathrm{W^+W^-} \to \mathrm{l\nu jj}$ decay channel it was also shown that a veto on charged tracks in the central rapidity region will be powerful for reducing the dominant jW background.

Acknowledgements

To work as a PhD student within particle physics is a teamwork with your results relying on the cooperation of many other people and hopefully with your own results usable by a large amount of people as well. Here I will only mention a few.

First of all, I would like to thank my supervisor Torsten Åkesson who has supported the work all the way along. His time is shared between many projects but still he has managed to guide my work at the right points with his many ideas.

I would like to thank all from the ATLAS TRT collaboration. *Step-by-step* I was introduced to both hardware and software connected to the testbeam and the general TRT development. In special I would like to thank Daniel Froidevaux and Anatoli Romaniouk. Their constructive criticism of my work has caused a significant improvement of the quality of this thesis.

From the ATLAS physics team I will mention Fabiola Gianotti and Jerome Schwindling who has given advice for my $H \to \gamma\gamma$ analysis. Stephen Haywood also deserves to be mentioned for the great energy he has put into the coordination of physics studies involving the Inner Detector.

From Lund, I would like to thank all my colleagues at the Department of Elementary Particle Physics. The PhD students, Magnus Söderberg, Oxana Smirnova and Helen Korsmo have been great company both in Lund and at CERN. Especially, I will remember many long lunches on the different restaurants in Lund. Torbjörn Sjöstrand from Theoretical Physics has been a great help always ready to help me with the understanding of Higgs physics and its implementation in the PYTHIA event generator.

I am grateful for the funding of my PhD studies from the Swedish Natural Science Research Council and the Danish Research Academy.

Thanks to Sverker Almehed, Daniel Froidevaux, Frank Paige, Anatoli Romaniouk and Torsten Åkesson who have provided comments for different parts of the thesis.

Finally I would like to thank my fiancée Caroline who has been a great support during all four years. I hope no one will ever charge us for the busy internet connection between Lund and Melbourne. I regard is as remarkable that she even took on her the job of proofreading this thesis.

Bibliography

[1] T. Akesson et al. Electron Identification with a Prototype of the Transition Radiation Tracker for the ATLAS experiment. *Submitted to Nucl. Instrum. Meth.*, 1997.

[2] ATLAS collaboration[1]. ATLAS Technical Proposal. (CERN/LHCC/94-43), 1994.

[3] ATLAS collaboration. ATLAS Calorimeter Performance Technical Design Report. (CERN/LHCC/96-40), 1996.

[4] ATLAS collaboration. ATLAS Inner Detector Technical Design Report volume 1. (CERN/LHCC/97-16), 1997.

[5] ATLAS collaboration. ATLAS Inner Detector Technical Design Report volume 2. (CERN/LHCC/97-17), 1997.

[6] G. Flügge. Future Research in High Energy Physics. In N. Ellis and M. B. Gavela, editors, *1993 European School of High Energy Physics*, Yellow reports. CERN 94-04, 1994.

[7] F. Mandl and G. Shaw. *Quantum field theory.* John Wiley & Sons, 1984.

[8] Z. Kunszt, S. Moretti, and W. J. Stirling. Higgs production at the LHC: An update on cross-sections and branching ratios. *Z. Phys.*, C74:479, 1996.

[9] M. Spira, A. Djouadi, D. Graudenz, and P. M. Zerwas. Higgs boson production at the LHC. *Nucl. Phys.*, B453:17–82, 1995.

[10] G. L. Kane, W. W. Repko, and W. B. Rolnick. The effective $W^{\pm}, Z^0$ approximation for high-energy collisions. *Phys. Lett.*, 148B:367, 1984.

[11] S. L. Glashow, D. V. Nanopoulos, and A. Yildiz. Associated production of Higgs bosons and Z particles. *Phys. Rev.*, D18:1724–1727, 1978.

[1] All ATLAS documentation is available from the ATLAS WWW pages at the address http://www.cern.ch/Atlas.

[12] H. Baer, B. Bailey, and J. F. Owens. $O(\alpha_s)$ Monte Carlo approach to W+ Higgs-boson associated production at hadron supercolliders. *Phys. Rev.*, D47:2730–2734, 1993.

[13] Z. Kunszt. Associated production of heavy Higgs boson with top quarks. *Nucl. Phys.*, B247:339, 1984.

[14] Duane A. Dicus and Scott Willebrock. Higgs boson production from heavy-quark fusion. *Phys. Rev.*, D39:751–757, 1989.

[15] Michael Spira. HIGLU and HDECAY: Programs for Higgs boson production at the LHC and Higgs boson decay widths. hep-ph/9610350, 1996.

[16] Jens Lyng Petersen. Elementarpartikelfysik. The Niels Bohr Institute, Copenhagen, 1993. Lecture notes in particle physics.

[17] Levan R. Surguladze. Quark mass effects in fermionic decays of the Higgs boson in $O(\alpha_s^2)$ pertubative QCD. *Phys. Lett.*, B341:60–72, 1994.

[18] Bernd A. Kniehl. Two loop $O(\alpha_s^2)$ correction to the H $\rightarrow$ b anti-b decay rate induced by the top quark. *Phys. Lett.*, B343:299–303, 1995.

[19] Bernd A. Kniehl. Status of higher order corrections in the standard electroweak theory. *Int. J. Mod. Phys.*, A10:443–464, 1995.

[20] J. F. Gunion, H. E. Haber, G. L. Kane, and S. Dawson. *The Higgs Hunters Guide*. Addison-Wesley, 1990.

[21] Bernd A. Kniehl. Higgs phenomenology at one loop in the standard model. *Phys. Rept.*, 240:211–300, 1994.

[22] ALEPH collaboration. Search for the Standard Model Higgs Boson in e^+e^- Collisions at $\sqrt{s}$=161, 170 and 172 GeV. *Subm. to Phys. Lett., B*, 1997.

[23] L3 collaboration. Search for the Standard Model Higgs Boson in e^+e^- Interactions at $161 \leq \sqrt{s} \leq 172$ GeV. *Subm. to Phys. Lett., B*, 1997.

[24] OPAL collaboration. Search for the Standard Model Higgs Boson in e^+e^- Collisions at $\sqrt{s} = 161$ GeV. *Phys. Lett.*, 393B:231–244, 1997.

[25] E. Accomando et al. Higgs physics. In *Physics at LEP2*, volume 1 of *Yellow reports*. CERN-96-01, 1996.

[26] Paolo Gambino. Two-loop heavy top effects on precision observables and the Higgs mass. hep-ph/9703264, 1997.

[27] A. Wagner. Summary of experimental results, 1997. Summary talk at the International Europhysics Conference on High Energy Physics, Jerusalem, Israel.

[28] Thomas Hambye and Kurt Riesselmann. Matching conditions and Higgs mass upper bounds revisited. *Phys. Rev.*, D55:7255–7262, 1997.

[29] Urs M. Heller, Markus Klomfass, Herbert Neuberger, and Pavlos Vranas. Numerical analysis of the Higgs mass triviality bound. *Nucl. Phys.*, B405:555–573, 1993.

[30] J. Bagger, V. Barger, K. Cheung, J. Gunion, T. Han, G. A. Ladinsky, R. Rosenfeld, and C.-P. Yuan. Strongly interacting WW system: Gold plated modes. *Phys. Rev.*, D49:1246–1264, 1994.

[31] J. Bagger, V. Barger, K. Cheung, J. Gunion, T. Han, G. A. Ladinsky, R. Rosenfeld, and C.-P. Yuan. CERN LHC analysis of the strongly interacting WW system: Gold plated modes. *Phys. Rev.*, D52:3878–3889, 1995.

[32] X. Artru, G.B. Yodh, and G. Mennessier. Practical theory of the multilayered transition radiation detector. *Phys. Rev.*, D12(5):1289–1306, 1975.

[33] L. Fayard. Transition radiation. In *Lectures given at l'Ecole Joliot Curie, Carcans, France, September 26-30, 1988.* LAL-88-55, 1988.

[34] Boris Dolgoshein. Transition radiation detectors and particle identification. *Nucl. Instrum. Meth.*, A252:137–144, 1986.

[35] Boris Dolgoshein. Transition radiation detectors. *Nucl. Instrum. Meth.*, A326:434–469, 1993.

[36] A. H. Walenta, J. Fischer, H. Okuno, and C. L. Wang. Measurement of the ionization loss in the region of relativistic rise for noble and molecular gases. *Nucl. Instrum. Meth.*, 161:45, 1979.

[37] R. M. Barnett et al. Review of particle physics. *Phys. Rev.*, D54:1, 1996.

[38] W. W. M. Allison and J. H. Cobb. Relativistic charged particle identification by energy loss. *Ann. Rev. Nucl. Part. Sci.*, 30:253–298, 1980.

[39] D. Barberis et al. A comparative study of reduced layouts of the ATLAS Inner Detector. *ATLAS internal note*, (INDET-NO-188), 1997.

[40] Hans Danielsson. *A central rapidity straw tracker and measurements on cryogenic components for the Large Hadron Collider.* PhD thesis, Department of Physics, Lund University, 1997.

[41] T. Akesson et al. The ATLAS TRT straw proportional tubes: Performance at very high counting rate. *Nucl. Instrum. Meth.*, A367:143–153, 1995.

[42] T. Akesson et al. Study of straw proportional tubes for a transition radiation detector / tracker at LHC. *Nucl. Instrum. Meth.*, A361:440–456, 1995.

[43] J. T. Shank et al. Test beam performance of a tracking TRD prototype. *Nucl. Instrum. Meth.*, A309:377–385, 1991.

[44] T. Akesson et al. Particle identification performance of a straw transition radiation tracker prototype. *Nucl. Instrum. Meth.*, A372:70–84, 1996.

[45] Ruth Nünnerich. Transition radiation yield in various materials for the ATLAS detector. Universität-Gesamthochschule Siegen, Fachbereich Physik, 1996. Diplomarbeit.

[46] V. Bondarenko et al. Kapton straw chambers for a tracking transition radiation detector. *Nucl. Instrum. Meth.*, A327:386–392, 1993.

[47] Martin Millmore. RAL internal note RAL-118, 1992.

[48] David White. RAL internal note RAL-161, 1994.

[49] B. Bevensee, F. M. Newcomer, R. Van Berg, and H. H. Williams. An amplifier-shaper-discriminator for the ATLAS Transition Radiation Tracker. *IEEE Trans. Nucl. Sci.*, 43:1725–1731, 1996.

[50] John Dowdell. RAL internal note RAL-117, 1992.

[51] Henrik Carling and Magnus Thulesius. Technical Specification of the RD6 Drift Time Measuring Read-Out Chip. Revision 3. Lund University internal report LUNFD6(NFFL-7097), 1995.

[52] S. Buono et al. Software engineering techniques and CASE tools in RD13. *Nucl. Instrum. Meth.*, A352:383, 1994.

[53] D. M. Gingrich et al. Performance of a large scale prototype of the ATLAS accordion electromagnetic calorimeter. *Nucl. Instrum. Meth.*, A364:290–306, 1995.

[54] T. Akesson et al. Tracking with a prototype of the Transition Radiation Tracker for the ATLAS experiment. *To be published.*

[55] CN division Application Software group. GEANT Detector Description and Simulation Tool. CERN Program Library Long Writeup W5013, 1993.

[56] G. M. Garibian, L. A. Gevorgian, and C. Yang. The calculation of X-ray transition radiation generated in regular and irregular-layered media. *Nucl. Instrum. Meth.*, 125:133, 1975.

[57] Wolfgang Funk. A systematic study of the particle identification performance in the Transition Radiation Tracker (TRT) of ATLAS. *ATLAS internal note*, (INDET-NO-157), 1997.

[58] H. Drevermann, D. Kuhn, and B. S. Nilsson. Event display: Can we see what we want to see? In C. E. Vandoni, editor, *1995 CERN School of Computing*, Yellow reports. CERN 95-05, 1995.

[59] Pierre Billoir. Track fitting with multiple scattering: A new method. *Nucl. Instr. Meth.*, A225:352, 1984.

[60] R. K. Bock, H. Grote, D. Notz, and M. Regler. *Data analysis techniques for high-energy physics experiments*, chapter 3. Cambridge, 1990.

[61] Igor Gavrilenko. Pattern recognition in TRD/Tracker (TRD/T). *ATLAS internal note*, (INDET-NO-016), 1992.

[62] Ulrik Egede, Torsten Akesson, Daniel Froidevaux, and Igor Gavrilenko. Fake tracks in the ATLAS straw detector. *ATLAS internal note*, (INDET-NO-083), 1994.

[63] Ulrik Egede. Electron identification with the ATLAS detector at the Large Hadron Collider. Department of Physics, Lund University, 1996. Thesis for the degree of filosofie licentiat, CERN-THESIS-97-003.

[64] W. Press, B. Flannery, S. Teukolsky, and W. Vetterling. *Numerical Recipes, the art of scientific computing.* Cambridge University Press, 1989.

[65] F. James. *MINUIT Function Minimization and Error Analysis.* CERN, 1994.

[66] S. Aid et al. Jets and energy flow in photon - proton collisions at HERA. *Z. Phys.*, C70:17–30, 1996.

[67] F. Abe et al. Double parton scattering in anti-p p collisions at $\sqrt{s} = 1.8$ TeV. *Phys. Rev.*, D56:3811–3832, 1997.

[68] Torbjorn Sjostrand and Maria van Zijl. A multiple interaction model for the event structure in hadron collisions. *Phys. Rev.*, D36:2019, 1987.

[69] L. Fayard and G. Unal. Search for Higgs decay into photons with EAGLE. *ATLAS internal note*, (PHYS-NO-001), 1992.

[70] Vincent Tisserand. *Optimisation du detecteur ATLAS pour la recherche du boson de Higgs se desintegrant en deux photons au LHC.* PhD thesis, Université Paris XI Orsay, 1997.

[71] Fabiola Gianotti and Irene Vichou. γ/jet separation with the ATLAS detector. *ATLAS internal note*, (PHYS-NO-078), 1996.

[72] S. Simion. Higgs mass resolution. Transparencies presented at H $\rightarrow \gamma\gamma$ meeting in the ATLAS collaboration meeting 10/9-1997.

[73] Silvia Schuh. Higgs hunting with a transition radiation tracker. Institut für Kernphysik, Technische Universität Wien, 1995. Diplomarbeit.

[74] Torbjorn Sjostrand. High-energy physics event generation with PYTHIA 5.7 and JETSET 7.4. *Comput. Phys. Commun.*, 82:74–90, 1994.

[75] Elzbieta Richter-Was. ATLFAST 1.0: A package for particle-level analysis. *ATLAS internal note*, (PHYS-NO-079), 1996.

[76] D.Cavalli and S.Resconi. Comparison between full simulation and fast simulation of ATLAS. *ATLAS internal note*, (PHYS-NO-100), 1997.

[77] Pierre Savard. PhD thesis, University of Montreal, 1998. Not yet published.

[78] Torbjörn Sjöstrand, 1997. Private communications.

[79] Elzbieta Richter-Was. Standard Model and Minimal Supersymmetric Standard Model Higgs rates and backgrounds in ATLAS. *ATLAS internal note*, (PHYS-NO-048), 1995.

[80] F. Abe et al. Properties of jets in W boson events from 1.8 TeV $\bar{p}p$ collisions. *Submitted to Phys. Rev. Lett.*, 1997.

[81] M.Cobal, D.Costanzo, and S.Lami. VECBOS: A lowest order matrix element calculation to simulate direct QCD W + n jet events. *ATLAS internal note*, (PHYS-NO-084), 1996.

[82] S. Zmushko, D. Froidevaux, and L. Poggioli. $H \rightarrow W^+W^- \rightarrow l\nu jj$ and $H \rightarrow ZZ \rightarrow l^+l^-jj$ particle level studies. *ATLAS internal note*, (PHYS-NO-103), 1997.